SORBONNE UNIVERSITÉ

École doctorale Sciences Mécaniques, Acoustique, Électronique, et Robotique de Paris (ED 391)
Institut Jean le Rond d'Alembert (UMR 7190)

---

# Buckling and packing of beams and plates inside solid and liquid cavities

---

Par JIAYU WANG

Thèse de doctorat de MÉCANIQUE

Dirigée par SÉBASTIEN NEUKIRCH Et ARNAUD ANTKOWIAK

Présentée et soutenue publiquement le 16/10/2025

Devant un jury composé de :

| | |
|---|---|
| **Camille DUPRAT**, *Professeure, Institut Polytechnique de Paris* | Présidente |
| **Fabian BRAU**, *Professeur, Université libre de Bruxelles, Belgique* | Rapporteur |
| **Keith SEFFEN**, *Professeur, University of Cambridge, U.K.* | Rapporteur |
| **Florence BERTAILS-DESCOUBES**, *Directrice de Recherche, Inria Grenoble* | Examinatrice |
| **Benoît ROMAN**, *Directeur de recherche, CNRS et ESPCI-Paris* | Examinateur |
| **Emmanuel TRÉLAT**, *Professeur, Sorbonne Université* | Examinateur |
| **Arnaud ANTKOWIAK**, *Professeur, Sorbonne Université* | Directeur de thèse |
| **Sébastien NEUKIRCH**, *Directeur de recherche, CNRS* | Directeur de thèse |

“天下之至柔，驰骋天下之至坚。无有入无间，吾是以知无为之有益。”
“天下莫柔弱于水，而攻坚强者，莫之能胜。其无以易之。
弱之胜强，柔之胜刚，天下莫不知，莫能行。”

《道德经》——老子

*« The gentlest thing in the world overcomes the hardest thing in the world.*
*That which has no substance enters where there is no space.*
*This shows the value of non-action. »*
*« Nothing in the world is as soft and yielding as water.*
*Yet for dissolving the hard and inflexible, nothing can surpass it.*
*The soft overcomes the hard; the gentle overcomes the rigid.*
*Everyone knows this is true, but few can put it into practice. »*

The *Tao Te Ching*, Laozi

# Abstract

This PhD thesis investigates the buckling and packing behavior of slender structures, such as beams and plates, when confined within solid or liquid cavities. These packing phenomena arise in various contexts, including cable deformation in the drilling industry, endoscope-artery interaction in vascular surgery, and DNA coiling within viral capsids. While most existing studies focus on solid confinement, elastic structures at small scales can also be confined by liquid cavities due to dominant capillary effects. In such cases, elasto-capillary interactions lead to phenomena such as the wrinkling of liquid-infused membranes.

To understand these behaviors, we analyze the packing of an inextensible elastic beam (Elastica) in two-dimensional settings, under both rigid and liquid confinements. Numerical simulations were developed to incorporate geometric constraints and self-contact, and theoretical models were formulated to predict system responses. These predictions show strong agreement with simulation results. Furthermore, the stability of the identified equilibria is examined through analytical methods.

The study primarily focuses on the geometric configurations and force responses during deformation. We developed an analytical approach to obtain the scales of the horizontal and vertical applied forces as the compaction ratio is increased. Although hysteresis is observed, the models capture the overall behavior reliably. In both solid and liquid cavities, the early stages of confinement exhibit ordered and homogenous packing. At higher confinement levels, systems with liquid interfaces transition into inhomogeneous configurations. These findings align with experimental observations of liquid-infused membranes and can be interpreted with a phase transition approach.

Overall, this work extends the classical understanding of beam confinement between rigid boundaries to include elasto-capillary interactions in liquid environments. The models and insights presented here contribute to the broader understanding of packing phenomena under diverse confinement types, particularly those involving liquid interfaces.

# Résumé

Cette thèse de doctorat étudie le comportement de flambement sous contrainte des structures élancées, telles que les poutres et les plaques, lorsqu'elles sont confinées dans des cavités solides ou liquides. Ces phénomènes de confinement apparaissent dans divers contextes, notamment la déformation des câbles dans l'industrie du forage, l'interaction entre un endoscope et une artère en chirurgie vasculaire, ou encore l'enroulement de l'ADN dans les capsides virales. Alors que la plupart des études existantes se concentrent sur les confinements solides, les structures élastiques peuvent également être confinées par des interfaces liquides, à petite échelle, lorsque les effets capillaires dominent. Dans ce cas, les interactions élasto-capillaires engendrent des phénomènes tels que le plissement de membranes imprégnées de liquide.

Afin de comprendre ces comportements, nous analysons le confinement d'une poutre élastique inextensible (Elastica) en 2D, sous des confinements rigides et liquides. Des simulations numériques ont été développées pour prendre en compte les contraintes géométriques et l'auto-contact, et des modèles théoriques ont été formulés pour prédire la réponse du système. Ces prédictions montrent une bonne concordance avec les résultats des simulations. En outre, la stabilité des équilibres identifiés est analysée par des méthodes théoriques.

Nos études portent principalement sur les configurations géométriques et les réponses en force pendant la déformation. Nous développons une approche analytique qui permet d'obtenir les lois d'échelle des forces horizontales et verticales appliquées sur la poutre en fonction du confinement qui lui est imposé. Bien qu'un phénomène d'hystérèse soit observé, les modèles décrivent fidèlement le comportement global du système. Dans les cavités solides et liquides, les premières étapes du confinement présentent une réponse ordonnée et homogène du système. À des niveaux de confinement plus élevés, les systèmes à interfaces liquides évoluent vers des configurations hétérogènes. Ces observations sont cohérentes avec les expériences menées sur les membranes imprégnées de liquide, et peuvent être interprétées à l'aide de la théorie des transformations de phase.

Ce travail étend les compréhensions du confinement d'une poutre entre parois rigides aux interactions élasto-capillaires dans des environnements liquides. Les modèles et les résultats présentés apportent un éclairage nouveau sur les phénomènes de confinement sous différentes formes, en particulier ceux impliquant des interfaces liquides.

# Acknowledgement

This thesis marks the culmination of my journey as a PhD student. Looking back, I still remember hoping for a mind filled with knowledge, the courage to explore the unknown, and, most importantly, an inquisitive heart for science. Much like the Scarecrow, the Tin Woodman, and the Lion meeting Dorothy in *The Wonderful Wizard of Oz*, I was fortunate to find advisors who encouraged me to embark on the road, accompanying and helping me all along the way. I have come to understand that the PhD title (the "Magicien Oz") does not in itself grant intelligence, courage, or an inquisitive mind; rather, it is the journey and the people I met along the way that have shaped me. To them, I would like to express my sincere gratitude.

First and foremost, I wish to express my deepest gratitude to Sebastien Neukirch and Arnaud Antkowiak for accepting me as their student. I have truly enjoyed working with them, and this work would not have been possible without Sebastien's patient guidance and Arnaud's encouraging words, which carried me through the most challenging phases of my research. What I have learned from them was precious not only scientifically but also on a personal level. Their exemplary approaches as researchers and professors have been, and will continue to be, a constant source of inspiration and motivation for me.

I would like to thank Florence Bertails-Descoubes and Benoit Roman, the members of my "comité de suivi", for their invaluable advice and support. Their annual reassurance that I was on track and progressing at a good pace greatly boosted my confidence and alleviated my stress. I am also grateful that they agreed to serve as the examiners of my defense. My sincere thanks extend to all the jury members for their time, generosity, and thoughtful engagement with my work. I am especially indebted to the reviewers, Fabien Brau and Keith Seffen, for reading this long dissertation with such care, for their insightful feedback, and for validating my efforts with such generous praise. I warmly thank Camille Duprat for presiding over the jury, and Emmanuel Trélat for managing the videoconference (and also thanks for the optimization class for my doctoral course requirement). My thanks to all jury members for our stimulating discussions and their remarks, which provided new perspectives that I truly cherished.

Looking back, I feel incredibly moved by the eight years I spent at Sorbonne University, beginning as an undergraduate student. These years are filled with memories that will stay with me forever. My heartfelt thanks go to the University for giving me the chance to pursue higher education, and to ED SMAER for the doctoral contract and the essential support that made this thesis possible. I am also deeply grateful to the Department of Mechanics (UFR d'ingénierie), where I met so many generous and passionate professors who guided me from my undergraduate studies through to graduation. A special and emotional note of thanks goes to Hélène Dumontet. As head of the undergraduate program, she accepted me into the department through CMI program, and supported me with sincere kindness. Her sudden passing just before the beginning of my PhD was heartbreaking. I will always remember her warmth, her strength, and the inspiration she gave me. My sincere gratitude also goes to Corrado Maurini and José-María Fullana, the heads of my master's program, for their help and support throughout my studies and especially during my search for a PhD position. I could not have reached this point without their help. José is now the head

of the doctoral school, and together with his predecessor, Djmedo Kondo, I thank them for their dedication to the well-being of PhD students. I would like to acknowledge Jean-Camille Chassaing, who guided me during my bachelor's and master's degrees and helped me navigate my studies and internships. His trust in me opened the door to my first teaching experiences, something I will always be grateful for. For the subject of teaching, my warm thanks also go to Régis Wunenburger, Jose-Maria Fullana, Hélène De Maleprade, Jean-Loïc Le Carrou, Jean-François Krawczynski for their guidance. Their support made my time as a tutor deeply meaningful and enjoyable.

I feel truly fortunate to have spent three years at Institut d'Alembert, surrounded by all the great and kind people, many of whom I have already mentioned. I would also like to thank Stéphanie Deboeuf for her insightful discussions and for sharing her experimental perspective on the confined elastica problem; Andrés A. León Baldelli for introducing me to the Pareto problem and our discussions on stability analysis; and Basile Radisson for his reading and correcting my manuscript and sharing with me his experience as a researcher. My thanks extend to the permanent members with whom I interacted: Claire Lestringant for discussions on homogenization, Sophie Dartois for presenting the slicing machine, Lucas Frérot for discussions about numerical contact, and Suzie Protière for showing the usage of silicone rubbers. I am grateful to Jean-François Egea for preparing the experimental equipment (although the experiential part is not shown in the thesis). I would like to thank the managers of the lab, Simona Otarasanu, Catherine Dejancourt, Olivier Labbey, Célia Sakho, who patiently handled all the administrative documents required for my travels, conferences, and all the various procedures. And I would like to thank the director of the laboratory Pièrre-Yves Lagrée for his contribution in creating such a welcoming and supportive atmosphere in d'Alembert institut. To all the PhD students and postdocs I met: thank you, your daily greetings, spontaneous conversations, and shared moments brightened my workdays more than you can imagine. A very special thanks goes to Antonio, Krishan, Yvan, and Nathan, with whom I shared not only an office but also countless memories. They were the closest to me, literally and figuratively, and the first people I turned to whenever I had questions or simply needed company. Thanks to Patricia, Sophie, Eleonore, Anaëlle, Lila and Markus: I will never forget how you made the conferences that we participated together to be wonderful experiences. And to my Chinese colleagues, Guangjin, Fanshuo, Jieyun, Tian, Xiangbin, Bingbing, Zichen, Wei and Li, thank you for the comfort of your presence, it made me feel at home just by talking in my mother tongue.

I was lucky to receive help from many others along the way. My heartfelt thanks go to Paul Grandgeorge, whose work is the starting point of this thesis, for kindly introducing me his work and answering all my questions. I am deeply grateful to Natacha Krins for preparing the membranes and for initiating and organizing a collaborative internship between UFR d'ingénierie and UFR de chimie. I would like to thank our friends from PMMH, Jose Bico, Benoit Roman, Etienne Reyssat, Joo-Won Hong, Nathan Vani, for our numerous discussions, and also for providing me with plastic films for experimental tests. It has been a real pleasure to have such kind and supportive research buddies just across the campus.

Finally and most importantly, I would like to thank my family and friends. To my parents: thank you for your unconditional love and support, especially when I feel nervous and confused about my decisions and my future. Your belief in me sustained me throughout this journey. To my friends Yilin, Kejian, Nanxian, Pin, and Yuyao: thank you for pulling me away from my desk when I needed it most and helping me breathe again outside of my PhD work. Your companionship has kept me grounded and joyful.

In truth, there are so many people who have helped me that it is impossible to name them all without becoming verbose. As the story of Oz teaches us, the adventure did not end upon meeting the Wizard; the journey continues. All those I have met during my PhD, mentioned here or not, will remain a part of me and will be carried into the future with my gratitude.

# Contents

# Introduction

Slender structures such as beams and filaments, and thin structures such as membranes, are ubiquitous in both natural and engineered systems. When confined within narrow spaces, their ability to bend, twist, and coil gives rise to complex geometrical arrangements, collectively referred to as *packing phenomena*. Understanding how slender structures organize under confinement is essential for elucidating mechanisms encountered across physics, biology, materials science, and engineering. Representative examples include DNA packaging within viral capsids (Vetter, Wittel, and Herrmann, 2014), the deformation of cables in the drilling industry (Lubinski and Althouse, 1962; Miller et al., 2015), and fiber–crimper interactions in the textile industry (Hearle, 2014).

The specific behavior of a confined slender structure depends on multiple factors, including the geometry and stiffness of the confinement and the intrinsic properties of the structure itself. This thesis focuses on two-dimensional systems involving inextensible beams, or *Elastica*, particularly in configurations where the beam is confined inside a narrow tunnel.

Previous studies have investigated the buckling and post-buckling responses of rods and plates against a range of solid boundaries, including rigid walls (Domokos, Holmes, and Royce, 1997; Roman and Pocheau, 1999), compliant substrates (Manning and Bulman, 2005), and elastic supports such as spring-like walls (Chen and Wen, 2019; Katz and Givli, 2015). However, much less is understood about situations in which confinement is imposed not by solids, but by liquid interfaces.

Although liquid interfaces may at first appear too weak to confine solids, at small scales capillary forces can dominate elastic resistance, leading to striking deformation phenomena. The interplay between elasticity and capillarity, commonly referred to as *elasto-capillary effects*, has been shown to drive deformation across a wide range of systems (Bico, Reyssat, and Roman, 2018). Examples include the distortion of soft substrates by droplets (Style et al., 2017), the deformation and aggregation of wet fibers (Duprat et al., 2012; Py et al., 2007), the curling of soft textured sheets (Cappello et al., 2023) and the capillarity-induced crumpling of thin membranes (Huang et al., 2007).

Of particular interest here are systems in which liquid interfaces can actively trap slender bodies. One striking example is the natural "windlass" mechanism formed by spider silk winding around droplets, which imparts the thread with remarkable extensibility (Elettro et al., 2016; Schulman et al., 2017; Vollrath and Edmonds, 1989). Similarly, in the experimental work of Grandgeorge et al. (2018), a thin porous polymer membrane covered by a liquid film exhibited extraordinary stretchability, accommodating large contractions without sagging. In both cases, liquid interfaces act as confinements, storing slender structures in so-called fiber or surface reservoirs. These reservoirs can be recruited on demand, granting the system exceptional deformability. A deeper understanding of such mechanisms not only sheds light on biological phenomena, such as the deformability of white blood cells (Guillou et al., 2016), but also offers inspiration for the design of synthetic stretchable materials, with potential applications in smart textiles and biomedical devices.



Despite the differences between solid–solid and liquid–solid packing, this thesis develops theoretical and numerical frameworks for both classes of confinement and highlights the commonalities and distinctions between them.

### Organization and content of the manuscript

This thesis consists of three parts:

**Part I** introduces the theoretical and methodological framework. Chapter 1 presents fundamental notions of optimization, stability, and bifurcation, together with related numerical methods. Simple examples from elasticity and capillarity illustrate the application of these concepts. Chapter 2 introduces the numerical solver used throughout the thesis, with emphasis on discretization strategies and their implementation. A convergence study is provided to compare different discretization schemes. Chapter 3 addresses the numerical treatment of contact conditions, and provides two examples that illustrate the implementation of beam-to-beam contact. Finally, Chapter 4 introduces two concepts central to later discussions: phase transitions and configurational forces.

**Part II** investigates solid–solid packing, focusing on the responses of an Elastica confined between rigid walls. Two boundary conditions are considered, depending on the placement of the clamped ends: the wall-attached configuration (Chapter 5) and the centered configuration (Chapter 6). For the wall-attached case, attention is given to the deformation process and overall system responses under different models. For the centered case, additional emphasis is placed on bifurcation and stability analyses. Chapter 7 compares the behaviors of both configurations using the proposed semi-analytical models, providing a broader perspective on the problem of an Elastica confined in a rigid tunnel.

**Part III** turns to liquid–solid packing, motivated by experimental studies. Two systems are examined numerically in two dimensions: a drop–fiber system (Chapter 8) and a soaked membrane system (Chapter 9). For the drop–fiber problem, we first analyze the elasto-capillary buckling of a fiber inside a disk-shaped drop, and then extend the study to cases where the liquid interface is deformable. Parameter studies highlight the influence of material and geometrical properties, as well as the additional effects introduced by interface deformability. In the soaked membrane problem, modeled as a two-dimensional analogue of an Elastica confined between rigid walls, we examine the deformation process, force responses, and the phase transition phenomena observed experimentally. Both simulations and semi-analytical models are employed to capture these behaviors.



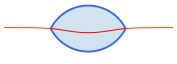

# Part I

# Theoretical background and methods



# Chapter 1

# Optimization, stability and bifurcation

In this chapter, we introduce the theoretical framework and numerical methods used for constrained continuous optimization problems. These problems are widely encountered in science, engineering, economics, and industry. Optimization theory, which traces its roots to the work of Euler and Lagrange on the calculus of variations, provides the conditions for optimality and forms a foundational component of the present work.

Moreover, optimality conditions are closely related to the determination of equilibrium stability. For this reason, a brief overview of stability and bifurcation theories is also provided. Finally, we present a few examples to illustrate the application of the theoretical concepts and numerical methods we have introduced.

Beginning with a brief history of the calculus of variations and Lagrangian mechanics, the content of this chapter is primarily based on established results and standard references in optimization, numerical methods, and stability theory. Key sources include textbooks and manuals such as the work of Nocedal and Wright (2006) and Luenberger and Ye (2008). The aim is to provide a concise summary of the concepts and tools relevant to the work presented in this thesis.

## 1.1 Variational approach and Lagrangian mechanics

Different from but consistent with Newtonian mechanics, which is based on vector quantities like force, momentum and acceleration, the Euler-Lagrange approach is based on the calculus of variation and the minimization of an integral scalar quantity.

The concepts of the *Lagrangian* and the *calculus of variations* are fundamental and appear frequently throughout the studies of this thesis. Here we introduce the history of the variational approach and the Lagrange method.

This integral variational approach was first championed by Gottfried Wilhelm Leibniz, at the same period of Newton's development of the differential approach to classical mechanics. During the 18th century, a student of Leibniz, Johann Bernoulli, developed the field of variational calculus which underlies the integral variational approach to mechanics. He solved the brachistochrone problem, which aims to find the path which has the shortest transit time between two points. The integral variational approach also underlies Fermat's principle in optics, which can be used to derive that the angle of reflection equals the angle of incidence, as well as Snell's law. Bernoulli developed the principle of virtual work which is used to describe equilibrium in static systems. Jean-Baptiste le Rond $\partial$'Alembert extended the principle of virtual work to dynamical systems. Bernoulli's student Leonhard Euler, a Swiss mathematician of the 18th century, developed the calculus of variations with full mathematical rigor. Joseph-Louis Lagrange, a student of Euler,



culminated the development of the Lagrangian variational approach to classical mechanics (Cline, 2017; Dugas, 1988; Lanczos, 2012).

The standard Lagrangian in Lagrangian mechanics is defined as the difference between the kinetic and potential energy, that is $L = T - V$. In optimization, the Lagrangian function defined in the method of Lagrange multipliers is also called Lagrangian for short, which defined as

$$\mathcal{L}(x, \lambda) = f(x) - \lambda\, g(x)$$

where $f(x)$ and $g(x)$ are respectively the objective and constraint function, and $\lambda$ is the Lagrange multiplier (Nocedal and Wright, 2006). Both Lagrangian are named after the great mathematician Joseph-Louis Lagrange in memory of his contributions to calculus of variations.

## 1.2 Theory of optimization

Here we present the theory for a general constrained optimization problem. The variables are defined as $\mathbf{x} = [x_1, x_2, ..., x_n]^T$, contained within a subset $\Omega$ of real domain $\mathbb{R}^n$. We would like to minimize a continuous function $f(\mathbf{x})$, the objective, under $m$ equality constraints $\mathbf{h}(\mathbf{x})$ and $p$ inequality constraints $\mathbf{g}(\mathbf{x})$. The objective $f(\mathbf{x}) : \mathbb{R}^n \to \mathbb{R}$, and constraints $\mathbf{h}(\mathbf{x}) : \mathbb{R}^n \to \mathbb{R}^m$, $\mathbf{g}(\mathbf{x}) : \mathbb{R}^n \to \mathbb{R}^p$ are all smooth real functions.

The formulation for this problem is

$$\begin{aligned} \min_{\mathbf{x}\in\Omega} \quad & f(\mathbf{x}) \\ \text{subject to} \quad & \mathbf{h}(\mathbf{x}) = \mathbf{0} \\ & \mathbf{g}(\mathbf{x}) \geq \mathbf{0} \end{aligned} \tag{1.1}$$

### 1.2.1 (First Order) Necessary Condition

The first order necessary condition of optimization problems, also called Karush-Kuhn-Tucker Condition, goes as follows:

> ***Karush-Kuhn-Tucker (KKT) condition.*** *Let $\mathbf{x}^*$ be a relative minimum point of problem (1.1), and suppose $\mathbf{x}^*$ is a regular point for the constraints. Then, there is a vector $\boldsymbol{\lambda} \in \mathbb{R}^m$ and $\boldsymbol{\mu} \in \mathbb{R}^p$ with $\boldsymbol{\mu} \geq \mathbf{0}$, such that*
>
> $$\nabla\mathcal{L} = \nabla f(\mathbf{x}^*) - [\nabla\mathbf{h}(\mathbf{x}^*)]^T\, \boldsymbol{\lambda} - [\nabla\mathbf{g}(\mathbf{x}^*)]^T\, \boldsymbol{\mu} = \mathbf{0} \in \mathbb{R}^n \tag{1.2}$$
>
> $$diag(\boldsymbol{\mu})\, \mathbf{g}(\mathbf{x}^*) = \mathbf{0} \in \mathbb{R}^n \tag{1.3}$$
>
> *where $\nabla f = [\partial f/\partial x_1, ..., \partial f/\partial x_n]^T$. $\nabla\mathbf{h}$ is a $m \times n$ matrix, with $[\nabla\mathbf{h}]_{ij} = \partial h_i/\partial x_j$, idem for $\nabla\mathbf{g}$. $diag(\boldsymbol{\mu})$ is a $p \times p$ diagonal matrix, with $\boldsymbol{\mu}$ in the diagonal.*

We also call a point $\mathbf{x}$ satisfying the KKT condition an equilibrium.

### 1.2.2 (Second Order) Sufficient Condition

An equilibrium is not necessarily an optimum. According to the optimization theory, the sufficient condition of a minimum goes as following:

> ***Second order sufficient condition.*** *If a point $\mathbf{x}^*$ satisfies constraints $\mathbf{h}(\mathbf{x}^*) = \mathbf{0}$ and $\mathbf{g}(\mathbf{x}^*) \geq \mathbf{0}$ and if there exist $\boldsymbol{\lambda}$, $\boldsymbol{\mu}$ such that*
>
> $$\boldsymbol{\mu} \geq \mathbf{0} \tag{1.4}$$
>
> $$diag(\boldsymbol{\mu})\, \mathbf{g}(\mathbf{x}^*) = \mathbf{0} \tag{1.5}$$
>
> $$\nabla\mathcal{L} = \nabla f(\mathbf{x}^*) - [\nabla\mathbf{h}(\mathbf{x}^*)]^T\, \boldsymbol{\lambda} - [\nabla\mathbf{g}(\mathbf{x}^*)]^T\, \boldsymbol{\mu} = \mathbf{0} \tag{1.6}$$



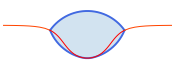

*and if the Hessian matrix*

$$\mathbf{H} = \nabla^2 \mathcal{L} = \nabla^2 f - \sum_{i=1}^{m} \lambda_i \nabla^2 h_i - \sum_{j=1}^{p} \lambda_j \nabla^2 g_j \in \mathbb{R}^{n \times n} \tag{1.7}$$

*is positive definite on the subspace*

$$\begin{aligned} M = \{\mathbf{y} \in \mathbb{R}^n \mid & \nabla \mathbf{h}(\mathbf{x}^*)\, \mathbf{y} = \mathbf{0} \in \mathbb{R}^n, \\ & \nabla g_j(\mathbf{x}^*) \cdot \mathbf{y} = 0,\ \forall j \in J_S,\ \nabla g_j(\mathbf{x}^*) \cdot \mathbf{y} > 0,\ \forall j \in J_W\} \end{aligned} \tag{1.8}$$

*where $J_S$ is the index set of all the strongly active constraints, and $J_W$ is the index set of all the weakly active constraints:*

$$J_S = \{j \mid g_j(\mathbf{x}^*) = 0,\ \mu_j > 0\}, \qquad J_W = \{j \mid g_j(\mathbf{x}^*) = 0,\ \mu_j = 0\}. \tag{1.9}$$

*Then $\mathbf{x}^*$ is a strict relative minimum point of the optimization problem*

*The positivity of $\mathbf{H}$ can be also described as $\mathbf{y}^T \mathbf{H}(\mathbf{x}^*)\mathbf{y} > 0,\ \forall\, \mathbf{y} \in M$.*

**Application of the projection** To explain how this condition applies in practice, we consider a relatively simple case in which all the constraints are strongly active, that is $J_W = \varnothing$, then the subspace $M$ writes

$$M_S = \{\mathbf{y} \in \mathbb{R}^n \mid \nabla \mathbf{h}(\mathbf{x}^*)\mathbf{y} = \mathbf{0},\ \nabla g_j(\mathbf{x}^*) \cdot \mathbf{y} = 0,\ \forall j \in J_S\}. \tag{1.10}$$

$M_S$ is the kernel, also known as the null space, of the matrix composed of $\nabla \mathbf{h}$ and $\nabla g_j$ ($j \in J_S$). We note the kernel as $\mathbf{K}$, an $n \times (n - m - p_s)$ matrix, where $p_s$ is the number of strongly active inequality constraints and $n$ the number of variables. Then $\mathbf{K}$ satisfies the relation

$$\underbrace{\begin{bmatrix} — & \nabla \mathbf{h} & — \\ — & \nabla g_j & — \end{bmatrix}}_{(m+p_s) \times n \text{ matrix}} \cdot \mathbf{K} = \mathbf{0} \in \mathbb{R}^{(m+p_s) \times (n-m-p_s)} \tag{1.11}$$

In practice, $\mathbf{K}$ can be calculated with numerical packages, for example `scipy.linalg.null_space`.

$\mathbf{K}$ can be considered as a transformation matrix, mapping from $\mathbb{R}^{n-m-p_s}$ to $\mathbb{R}^n$. Through matrix $\mathbf{K}$, any vector in $\mathbb{R}^{n-m-p_s}$ projected to $\mathbb{R}^n$ is in the subspace $M_S$. To put it another way, if $\mathbf{H}$ is positive definite on the subspace $M_s$, then

$$\widehat{\mathbf{y}}^T \mathbf{K}^T \mathbf{H} \mathbf{K} \widehat{\mathbf{y}} \geq 0, \qquad \forall\, \widehat{\mathbf{y}} \in \mathbb{R}^{n-m-p_s}. \tag{1.12}$$

Therefore, if all the eigenvalues of the projected Hessian matrix

$$\widehat{\mathbf{H}} = \mathbf{K}^T \mathbf{H} \mathbf{K} \in \mathbb{R}^{(n-m-p_s) \times (n-m-p_s)} \tag{1.13}$$

are positive, then $\mathbf{x}^*$ is a local minimum.

**Formulation as an optimization problem and the equivalence** We have stated that eigenvalues can be used to determine the positiveness of the projected Hessian matrix $\widehat{\mathbf{H}}$ and thus to verify if the second-order optimal condition is satisfied. It is also possible to determine the positivity of $\widehat{\mathbf{H}}$ through optimization problem formulation.

We define the optimization problem

$$\begin{aligned} \min \quad & \widehat{\mathbf{y}}^T \widehat{\mathbf{H}} \mathbf{y}, \quad \widehat{\mathbf{y}} \in \mathbb{R}^{n-m-p_s} \\ \text{subject to} \quad & ||\widehat{\mathbf{y}}|| = \widehat{\mathbf{y}}^T\, \widehat{\mathbf{y}} = 1 \end{aligned} \tag{1.14}$$

Recall that if $\widehat{\mathbf{y}}^T \widehat{\mathbf{H}} \widehat{\mathbf{y}} > 0,\ \forall\, \widehat{\mathbf{y}} \in \mathbb{R}^{n-m-p_s}$, then $\widehat{\mathbf{H}}$ is positive definite. Thus, if the objective at minimum is strictly positive, then $\widehat{\mathbf{H}}$ is strictly positive definite in space $\mathbb{R}^{n-m-p_s}$, and if the minimal objective is negative, then $\widehat{\mathbf{H}}$ is not positive definite and the solution is not a local minimum.

We can prove that this formulation is equivalent to the determination with eigenvalues. Following the normal process for analyzing optimization problems, we construct the Lagrangian

$$\mathcal{L} = \frac{1}{2}\left[\widehat{\mathbf{y}}^T\,\widehat{\mathbf{H}}\,\widehat{\mathbf{y}} - \lambda(\widehat{\mathbf{y}}^T\,\widehat{\mathbf{y}} - 1)\right] \tag{1.15}$$

The factor $\frac{1}{2}$ is added to simplify the notations, and it does not change the reasoning.

Using KKT conditions, the gradient of the Lagrangian should be zero at the minimum. Taking into account that $\widehat{\mathbf{H}}$ is symmetric, we have

$$\nabla\mathcal{L} = \widehat{\mathbf{H}}\,\widehat{\mathbf{y}} - \lambda\,\widehat{\mathbf{y}} = \mathbf{0} \quad \rightarrow \quad \widehat{\mathbf{H}}\,\widehat{\mathbf{y}} = \lambda\,\widehat{\mathbf{y}}, \quad \widehat{\mathbf{y}}^T\,\widehat{\mathbf{y}} = 1 \tag{1.16}$$

That is the definition of an eigenvalue $\lambda$ of $\widehat{\mathbf{H}}$, with $\widehat{\mathbf{y}}$ its corresponding eigenvector.

Then we apply the second-order sufficient condition,

$$\nabla^2\mathcal{L} = \widehat{\mathbf{H}} - \lambda\,\mathbb{I} \text{ is positive definite on the subspace } M = \{\widehat{\mathbf{x}} | \widehat{\mathbf{y}}^T\,\widehat{\mathbf{x}} = 0\} \tag{1.17}$$

where $\mathbb{I}$ is the identity matrix, and $(\lambda, \widehat{\mathbf{y}})$ satisfies the KKT condition.

Suppose $(\lambda_1, \lambda_2, \ldots, \lambda_{n-m})$ and $(\widehat{\mathbf{y}}_1, \widehat{\mathbf{y}}_2, \ldots, \widehat{\mathbf{y}}_{n-m-p_s})$ are the eigenvalues and their corresponding eigenvectors. Because $\widehat{\mathbf{H}}$ is a symmetric matrix, $\widehat{\mathbf{y}}_i$ are perpendicular to each other, that is $\widehat{\mathbf{y}}_i^T\,\widehat{\mathbf{y}}_j = \delta_{ij}$, where $\delta_{ij}$ is the Kronecker delta. This means $(\widehat{\mathbf{y}}_1, \widehat{\mathbf{y}}_2, \ldots, \widehat{\mathbf{y}}_{n-m-p_s})$ form a base in $\mathbb{R}^{n-m-p_s}$, and $\widehat{\mathbf{y}}_i^T\,\widehat{\mathbf{H}}\,\widehat{\mathbf{y}}_j = \lambda_i\,\delta_{ij}$, which are two important properties that we will use in the following reasoning.

Recall that each pair of $(\lambda, \widehat{\mathbf{y}})$ satisfies the KKT condition, we would like to use the second order condition to determine whether $\widehat{\mathbf{y}}$ is a minimum. Taking one eigenvalue $\lambda_i$ and its eigenvector $\widehat{\mathbf{y}}_i$, the Hessian for this solution is $\nabla^2\mathcal{L} = \widehat{\mathbf{H}} - \lambda_i\,\mathbb{I}$, and we would like to determine its positiveness in subspace $M = \{\widehat{\mathbf{x}} \in \mathbb{R}^{n-m-p_s} | \widehat{\mathbf{y}}_i^T\,\widehat{\mathbf{x}} = 0\}$, which is the subspace generated by the base $(\widehat{\mathbf{y}}_1, \ldots, \widehat{\mathbf{y}}_{i-1}, \widehat{\mathbf{y}}_{i+1}, \ldots, \widehat{\mathbf{y}}_{n-m-p_s})$. We project $\nabla^2\mathcal{L}$ to this subspace using the two properties that were described above

$$\mathbf{K}^T \cdot \nabla^2\mathcal{L} \cdot \mathbf{K} = \begin{bmatrix} \lambda_1 - \lambda_i, & & & & \\ & \ddots & & & \\ & & \lambda_{i-1} - \lambda_i, & & \\ & & & \ddots & \\ & & & & \lambda_{n-m} - \lambda_i \end{bmatrix} \tag{1.18}$$

where

$$\mathbf{K} = \begin{bmatrix} | & & | & | & & | \\ \widehat{\mathbf{y}}_1, & \ldots & \widehat{\mathbf{y}}_{i-1}, & \widehat{\mathbf{y}}_{i+1}, & \ldots & \widehat{\mathbf{y}}_{n-m-p_s} \\ | & & | & | & & | \end{bmatrix} \tag{1.19}$$

The projected matrix in (1.18) is diagonal, and we have the eigenvalues directly.

Suppose $\lambda_1$ and $\widehat{\mathbf{y}}_1$ are the smallest eigenvalue and its eigenvector, then all the eigenvalues of the matrix (1.18) are positive. Thus, the pair $(\lambda_1, \mathbf{y}_1)$ is a local minimum. If we take another eigenvalue, $\lambda_1 - \lambda_i$ must be negative, and $\widehat{\mathbf{y}}_i$ is not a local minimum. Consequently, only the eigenvector of the smallest eigenvalue is the minimum, and the objective $\widehat{\mathbf{y}}^T\,\widehat{\mathbf{H}}\,\mathbf{y}$ at this point is $\widehat{\mathbf{y}}_1^T\,\widehat{\mathbf{H}}\,\widehat{\mathbf{y}}_1 = \lambda_1$.

Recall that $\hat{\mathbf{H}}$ is positive definite if the objective at the minimum is positive. Therefore, the discussion of the positivity of $\hat{\mathbf{H}}$ is equivalent to discussing the positivity of its minimum eigenvalue.

## 1.3 Numerical optimization

The optimization theory gives the basic idea on how to find an optimum. Many optimization problems are highly nonlinear and numerical methods are required. In this part, we introduce two numerical methods, which are used in this thesis.



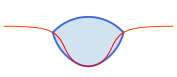

### 1.3.1 Sequential quadratic method

The sequential quadratic method, also called sequential quadratic programming (SQP), is based on quadratic programming, which deals with optimization problems with quadratic objective functions and linear constraints. SQP solves nonlinear constrained optimization problems in steps. At each step, the nonlinear problem is linearized and solved by quadratic programming to derive the direction leading to the final result.

Compared to the interior-point method that will be presented in the next part, one key point of the SQP method is the need to determine whether each inequality constraint is active or not. Indeed, a proper name of this SQP method is the active-set SQP method.

For better performance, there exist a number of variations of the active-set method, please refer to chapter 18 of (Nocedal and Wright, 2006). Here we explain the basic idea and our numerical scheme.

#### Description of the method

To initialize the algorithm, we provide an approximate solution $\mathbf{x}_0$, and the related guess of active inequality constraints. To explain the iterations, supposing at step $k$, the value of the variables $\mathbf{x}_k$ and the Lagrange multipliers are $(\boldsymbol{\lambda}_k, \boldsymbol{\mu}_k)$ are known, to find the step $\mathbf{p}$ towards the final solution, we linearize both the equality and inequality constraints of problem 1.1 to obtain

$$\begin{aligned} \min_{\mathbf{p}} \quad & f_k(\mathbf{x}_k) + \nabla f_k(\mathbf{x}_k)^T \mathbf{p} + \frac{1}{2} \mathbf{p}^T \nabla^2_{\mathbf{xx}} \mathcal{L}_k(\mathbf{x}_k)\, \mathbf{p} \\ \text{subject to} \quad & \nabla \mathbf{h}(\mathbf{x}_k)^T \mathbf{p} + \mathbf{h}(\mathbf{x}_k) = \mathbf{0} \\ & \nabla \mathbf{g}(\mathbf{x}_k)^T \mathbf{p} + \mathbf{g}(\mathbf{x}_k) \geq \mathbf{0} \end{aligned} \tag{1.20}$$

The new iterate is given by $(\mathbf{x}_k + \mathbf{p}_k, \boldsymbol{\lambda}_{k+1}, \boldsymbol{\mu}_{k+1})$, where $\mathbf{p}_k$, $\boldsymbol{\lambda}_{k+1}$ and $\boldsymbol{\mu}_{k+1}$ are the solution of the linearized problem. The solution of the original non-linear optimization problem is found by iterating until $|\mathbf{p}|$ goes under a certain criterion.

We again apply the KKT condition to this sub-problem. If $\mathbf{p}^*$ is a relative minimum of the problem, and $\boldsymbol{\lambda}^*$ and $\boldsymbol{\mu}^*$ are the related Lagrange multipliers of the linearized problem, then

$$\nabla^2_{\mathbf{xx}} \mathcal{L}_k\, \mathbf{p}^* + \nabla f_k - \boldsymbol{\lambda}^{*T} \nabla \mathbf{h}(\mathbf{x}_k) - \boldsymbol{\mu}^{*T} \nabla \mathbf{g}(\mathbf{x}_k) = \mathbf{0} \tag{1.21a}$$

$$\nabla \mathbf{h}(\mathbf{x}_k)^T \mathbf{p}^* + \mathbf{h}(\mathbf{x}_k) = \mathbf{0} \tag{1.21b}$$

$$\nabla \mathbf{g}(\mathbf{x}_k)^T \mathbf{p}^* + \mathbf{g}(\mathbf{x}_k) \geq \mathbf{0} \tag{1.21c}$$

$$\boldsymbol{\mu}^* \geq \mathbf{0} \tag{1.21d}$$

The system is linear with respect to the unknown step $\mathbf{p}$. We can also understand it as a Newton step of system (1.1).

Imagine we already know the indices of active inequality constraints, then these constraints can be treated as equality constraints. We use $\tilde{\mathbf{h}}$ to mark the equality constraints and the active inequality constraints. Then the above system can be written in matrix form

$$\begin{bmatrix} \nabla^2_{\mathbf{xx}} \mathcal{L}_k(\mathbf{x}_k) & -\nabla \tilde{\mathbf{h}}^T(\mathbf{x}_k) \\ -\nabla \tilde{\mathbf{h}}(\mathbf{x}_k) & \mathbf{0} \end{bmatrix} \cdot \begin{bmatrix} \mathbf{p} \\ \boldsymbol{\lambda} \end{bmatrix} = \begin{bmatrix} -\nabla f_k \\ \tilde{\mathbf{h}}(\mathbf{x}_k) \end{bmatrix}. \tag{1.22}$$

This linear system can be solved easily. Thus, the key to the SQP method is to find the indices of active inequality constraints. At each step, we check all the inequality constraints and their corresponding Lagrange multipliers to determine if each of them is active or not. After solving step (1.22), if an inequality constraint is violated, we set it active, which means it is treated as an equality constraint at the next step. If a Lagrange multiplier of inequality constraint is negative,



the corresponding constraint is set inactive, which means the Lagrangian multiplier is set to zero, and the constraint is not included in the next solving step.

For better convergence and stability of the algorithm, after solving equation (1.22) we adjust the step length with regard to inequality constraints. If $\mathbf{x}_k + \mathbf{p}_k$ violates one of the inequality constraints, we multiply the step by a coefficient $\alpha < 1$, such that $\mathbf{x}_{k+1} = \mathbf{x}_k + \alpha \mathbf{p}_k$. This strategy is called the *line search*, and $\alpha$ can be understood as the control of step length towards the minimum.

Please remark that the described scheme does not use the second-order stability condition, and we are basically using an iterative method for solving $\nabla \mathcal{L} = 0$ with constraints. For this reason, the solution found is not necessarily a minimum but an equilibrium.

Below we state the SQP algorithm used in our study in a simple form.

**Algorithm:**
Initial : choose an initial point $(\mathbf{x}_0, \boldsymbol{\lambda}_0, \boldsymbol{\mu}_0)$, and the related active set.
**Repeat** until a given maximal number of steps:
Evaluate $f_k, \nabla f_k, \nabla^2_{\mathbf{xx}} \mathcal{L}_k, \mathbf{h}(\mathbf{x}_k), \nabla \mathbf{h}(\mathbf{x}_k), \mathbf{g}(\mathbf{x}_k), \nabla \mathbf{g}(\mathbf{x}_k)$.
Solve 1.22 to obtain step $\mathbf{p}_k$ and Lagrange multipliers $\boldsymbol{\lambda}_{k+1}, \boldsymbol{\mu}_{k+1}$.
**if** $||\mathbf{p}_k|| \leq tol$ :
**break**
**else**
Evaluate $\mathbf{x}_k + \mathbf{p}_k$ to determine coefficient $\alpha$
Set $\mathbf{x}_{k+1} \leftarrow \mathbf{x}_k + \alpha\, \mathbf{p}_k$
Reset active set according to the value of $\mathbf{h}(\mathbf{x}_{k+1})$ and $\boldsymbol{\mu}_{k+1}$

### 1.3.2 Interior-point method

In our studies, we use the optimizer *IPOPT*, which is an implementation of a primal-dual interior-point algorithm with a filter line-search method for nonlinear programming, see the references of Byrd, Hribar, and Nocedal (1999), Wächter (2002), Andreas Wächter and Biegler (2004), Wachter and Biegler (2006). This is one of the variants of the interior-point methods. Although the use of this optimizer does not require advanced knowledge of interior-point methods, a basic understanding is necessary to set the parameters of the optimizer, and thus increase efficiency.

Interior-point methods can be seen as barrier methods or continuation methods. To explain this, we reformulate the problem 1.1 as

$$\begin{aligned} \min_{\mathbf{x},\mathbf{s}} \quad & f(\mathbf{x}) \\ \text{subject to} \quad & \mathbf{h}(\mathbf{x}) = \mathbf{0}, \qquad \mathbf{h} \in \mathbb{R}^p \\ & \mathbf{g}(\mathbf{x}) - \mathbf{s} = \mathbf{0}, \qquad \mathbf{g} \in \mathbb{R}^m \\ & \mathbf{s} \geq \mathbf{0} \end{aligned} \tag{1.23}$$

where $\mathbf{s}$ is a vector of slack variables.

The algorithm basically solves a sequence of barrier problems with a series of positive parameters $\{\mu_k\}$

$$\begin{aligned} \min_{\mathbf{x},\mathbf{s}} \quad & \varphi(s) = f(\mathbf{x}) - \mu_k \sum_{i=1}^{p} \ln(s_i) \\ \text{subject to} \quad & \mathbf{h}(\mathbf{x}) = \mathbf{0} \\ & \mathbf{g}(\mathbf{x}) - \mathbf{s} = \mathbf{0} \end{aligned} \tag{1.24}$$



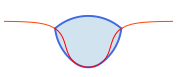

Thanks to the properties of the natural logarithm function, the term $\mu_k \sum_{i=1}^{p} \ln(s_i)$ prevents $\mathbf{s}$ becoming negative. When $\mu_k$ converges to zero, the solution of problem (1.24) converges to that of the initial problem (1.23).

To briefly explain the equivalence, we write out the first-order optimality condition for problem (1.24)

$$\nabla f - (\nabla \mathbf{h})^T \mathbf{y} - (\nabla \mathbf{g})^T \mathbf{z} = \mathbf{0} \tag{1.25a}$$
$$\mu_k \mathbf{S}^{-1}\mathbf{e} + \mathbf{z} = \mathbf{0} \tag{1.25b}$$
$$\mathbf{h}(\mathbf{x}) = \mathbf{0} \tag{1.25c}$$
$$\mathbf{g}(\mathbf{x}) - \mathbf{s} = \mathbf{0} \tag{1.25d}$$

where $\mathbf{y}$ and $\mathbf{z}$ are Lagrange multipliers, $\mathbf{S}^{-1}$ is a diagonal matrix whose diagonal composed by $s_i^{-1}$, $\mathbf{e} = [1, 1, ..., 1]^T$. And the KKT condition of the problem 1.23 is

$$\nabla f - (\nabla \mathbf{h})^T \mathbf{y} - (\nabla \mathbf{g})^T \mathbf{z} = \mathbf{0} \tag{1.26a}$$
$$\mathbf{S}\mathbf{z} - \mu\mathbf{e} = \mathbf{0} \tag{1.26b}$$
$$\mathbf{h}(\mathbf{x}) = \mathbf{0} \tag{1.26c}$$
$$\mathbf{g}(\mathbf{x}) - \mathbf{s} = \mathbf{0} \tag{1.26d}$$

where $\mathbf{S}$ is a diagonal matrix whose diagonal is the vector $\mathbf{s}$, and $\mu = 0$ is an added parameter. Note that the only difference is (1.25b) and (1.26b). We can multiply (1.25b) by $\mathbf{S}$, and the two equations coincide. This proves the problem (1.24) can be interpolated as the original problem when $\mu_k$ goes to zero.

The term "interior-point" comes to the fact that early barrier methods use directly the inequality constraints in the barrier function but not the slack variables $\mathbf{s}$. The initial point $\mathbf{x}_0$ is assumed to be feasible with respect to the inequality constraints and the barrier methods keep the iterates inside the feasible region. Most of the modern interior-point methods can start at any initial point even if it is not feasible, we only need to ensure $\mathbf{s}_0 \geq 0$ and $\mu_0 \geq 0$. This is one advantage of introducing slack variables.

In appendix A we list some important parameters that should be paid attention to.

## 1.4 Stability and bifurcation

In dynamic systems, the notion of stability is related to the stationary solutions, also known as the equilibria of the differential equations. If the system is able to return to the equilibrium after a small perturbation, then this state is stable, and if the system diverges away, then it is unstable.

When a system parameter passes through a certain value, the system changes qualitatively the number or type of equilibria, periodic orbits, or their stability, and we say the system undergoes a bifurcation. That means the critical thresholds where stability properties change are marked by the bifurcation points. For example, a stable solution may lose stability (Hopf bifurcation), or split into multiple equilibria (saddle-node bifurcation). Thus, the concept of stability and the bifurcation theory are fundamentally tied together.

Moreover, the stability and bifurcation analyses are also related to the optimization theory presented in section 1. Schulz and Pellegrino (2000) have shown how a mechanical system subjected to the unilateral constraints differs from the standard system, and how the KKT conditions in the optimization theory are applied in this case.

The concept of stability and bifurcation is important in a wide variety of contexts, including cell differentiation and pattern formation in multicellular organisms (Raj and Bose, 2024), the wave propagation in excitable media (Hagberg and Meron, 1998), the transition to turbulent flow



(Shimizu and Manneville, 2019), and also for the hydrodynamics in general (Charru, 2011). Notably, these notions not only apply to dynamical systems. The general bifurcation theory involves the study of differential equations and their asymptotic solutions, and naturally finds its applications in the domain of the mechanics of structures. For example, Groh, Avitabile, and Pirrera (2018) proposed the generalized path-following method combined with the finite element method, which determines the stability and bi-stability of structures and helps the design of functional structures.

In this section, we introduce the concept of stability in static system with the help of energy potential. Following that, the concept of bifurcation is also given within the static systems. We also include some general bifurcation theory and numerical methods for the bifurcation analysis.

### 1.4.1 Stability

The word 'stable' is used by everyone in daily life. In the Oxford English Dictionary, it is explained by *fixed or steady; not likely to move, change or fail.* Here we would like to discuss stability in the mechanical context.

In conservative systems, a stable equilibrium corresponds to a local minimum of the potential energy. We illustrate this notion in figure 1.1a: all the small balls are at an equilibrium state, but only the first two are stable in the general sense. Specifically, the first one is *asymptotically stable* (Seydel, 2010). With dynamical notions, if the initial state is stable, small perturbations remain small as the time approaches infinity. A more rigorous definition of stability (in the sense of Lyapunov) can be found in the reference Verhulst (1996).

While the definition and analysis of stability can be introduced within dynamical systems, it is also possible to check stability in static systems. In this case, a stable equilibrium is a local minimum of the potential energy. Then, the direct application of the optimization theory is a way of finding equilibria and their stability. From KKT conditions, one derives the system of equations for equilibrium, and the second-order sufficient condition provides the stability of an equilibrium. For complex systems, the solutions are often found by numerical methods, most of which require a discretized version of the continuous system. In this case, the basic principle of stability analysis does not change, examples of stability analysis of discretized systems can be found in the example in section 1.7. More examples and a more specified presentation can be found in reference Lazarus, Maurini, and Neukirch (2015).

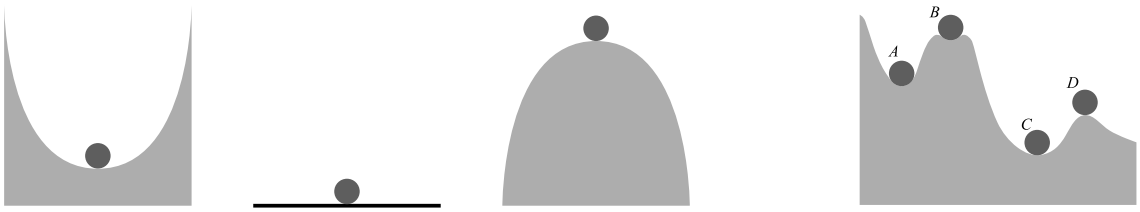


**(a) Equlibrium and stability** **(b) Domain of attraction**

We use figure 1.1b to add some remarks. There are four small balls, all at equilibrium state. $A$, $B$ and $C$ are stable, and $D$ is unstable.

- A stable state is at the local minimum, it is not assured to be the global minimum, for example the small ball $A$.
- The energy of an unstable state may also be lower than that of a stable state, for example, the small ball $A$ has higher energy than $D$.



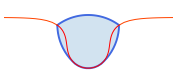

- The *domain of attraction*, defined by the set of all initial values which converge to the equilibrium, is different for each stable state. For example, the small ball $B$ has a small domain of attraction, we call this state a *weak equilibrium*.

### 1.4.2 Bifurcation

In general, the behavior of a physical system depends on a certain number of parameters, for example the behavior of a loaded column depends on the imposed load $P$ (shown in figure 1.2a). When these parameters change, the behavior of the system changes, and sometimes the change can be qualitative. For the loaded column, if the load is small enough, no significant deformation can be observed; when the load exceeds a certain value, known as the buckling threshold, the column buckles. If the load reaches a very large value, the column might even break.

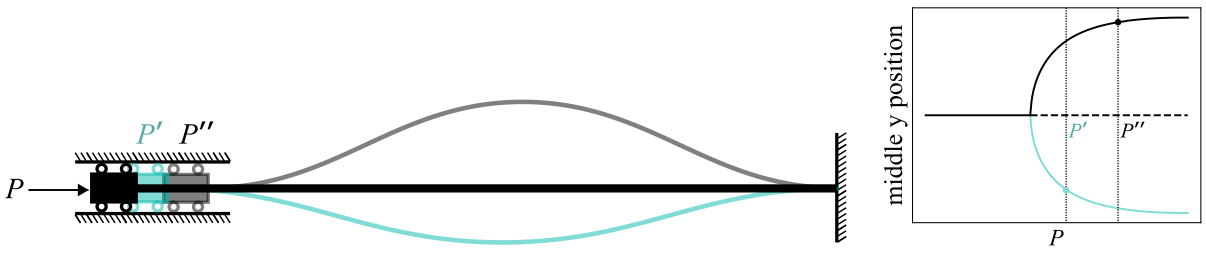


**(a) Illustration : loaded column** **(b) Bifurcation diagram**

**Figure 1.2: Example : loaded column**

It is important to understand how the system evolves as the relevant parameters are varied. Depending on the parameter values, both the number of equilibrium solutions and their stability may change. These behaviors are naturally captured and analyzed within the framework of bifurcation theory. The word 'bifurcation' is first introduced by the French mathematician and physicist Henri Poincaré. Now 'bifurcation' is used in a general way to indicate branching behaviors and changes in a system (Verhulst, 1996).

For a better visualization, we use a bifurcation diagram to show the evaluation of the system as one parameter changes. Figure 1.2b is a bifurcation diagram of the example of the loaded column. In this example, the parameter in question is the load $P$, and we choose the vertical position of the middle point as an indicator of the changes, but the choice is not unique. As we can see, when $P$ passes a certain value, the number of equilibrium solutions increases from one to three, which is the branching behavior. Moreover, although the non-buckled form of the column is still an equilibrium solution, it is no longer stable. In fact, this is a classical example of pitchfork bifurcation. Other types of bifurcation include saddle-node bifurcation, transcritical bifurcation, Hopf bifurcation, etc. Champneys et al. (2019) not only list different types of bifurcation but also provide several examples related to elasticity and deformation of materials and structures.

The bifurcation theory is closely related to discussions of stability, and it is a whole domain of study, having a variety of applications. For foundational and detailed expositions, please refer to Seydel et al. (1991), Seydel (2010), Strogatz (1994), and Verhulst (1996).

### 1.4.3 Continuation method

Most physical systems involve non-linear behaviors and possess intricate energy landscapes. Consequently, the related bifurcation diagrams may not be as simple as the one presented in figure 1.2b. In practice, the bifurcation diagram is usually drawn by a series of points, which are the numerical solutions as parameters change. To carry out the bifurcation analysis, one should ask

how to select and construct these points. *Continuation methods* can be used to generate such sequences of solutions and construct the branches. For this reason, these methods are also called *branch tracing* or *path following* methods. Here we present such methods and portions of this part closely follow the presentation in chapter 4 of the book of Seydel (2010), with adaptations made to fit the context of this thesis.

Continuation methods are also extremely useful for solving highly nonlinear problems. Usually, solvers converge badly if the initialization is far from the solution, a highly nonlinear solution that does not have an analytical approximation may be hard to find, but one can start from a point that is close to the linear approximation, and use the continuation method to reach the highly nonlinear solution.

Given the system of equations of the equilibrium $\mathbf{f}(\mathbf{y}, \lambda) = \mathbf{0}$ ($\mathbf{f} \in \mathbb{R}^n$), which could be obtained for example by applying KKT conditions on the discretized system. $\mathbf{y} = [y_1, ..., y_n] \in \mathbb{R}^n$ are the variables of the system and $\lambda \in \mathbb{R}$ is a parameter to be discussed.

The basic idea behind the continuation method is the predictor–corrector principle. One starts from a solution $\mathbf{y}_1$ with parameter $\lambda_1$, aiming to find the next point $\mathbf{y}_2$ with parameter $\lambda_2$ on the branch. Repeating this process, we will have a series of points from $\lambda_1$ to a targeted value of $\lambda$. Each step from $(\mathbf{y}_j, \lambda_j)$ to $(\mathbf{y}_{j+1}, \lambda_{j+1})$ is split into two parts:

$$(\mathbf{y}_j, \lambda_j) \xrightarrow{\text{predictor}} (\bar{\mathbf{y}}_j, \bar{\lambda}_j) \xrightarrow{\text{corrector}} (\mathbf{y}_{j+1}, \lambda_{j+1}).$$

The intermediate point $(\bar{\mathbf{y}}_j, \bar{\lambda}_j)$ is an initial guess of the next point, and can be seen as the initialization given to the solver to find the next step.

*Step length* is the distance between two points $(\mathbf{y}_j, \lambda_j)$ and $(\mathbf{y}_{j+1}, \lambda_{j+1})$ on the bifurcation path, and can be approximated by the predictor. In addition to equation $f(\mathbf{y}, \lambda) = \mathbf{0}$, we also need a relation that locates solution points on the branch, that is the *parametrization strategy* of the branch.

Predictor, corrector, parametrization strategy and step length control are the four important ingredients of continuation methods. The ingredients are not bonded and can be combined freely.

**Local parametrization** As we are searching branches for different values of parameter $\lambda$, the natural choice of continuation is to solve the system for a series of chosen values of $\lambda$, that is to parameterize the branch by $\lambda$, like what is shown in figure 1.3a. Indeed, any of the components $y_i\,(i = 1, ..., n)$ can be chosen as the fixed parameter to generate the branch, and this kind of parametrization is called local parametrization because it uses the variables and parameters of the system to parameterize the branch.

Suppose we use the $\lambda$ parametrization. For each $\lambda_j$, we want to find $\mathbf{y}_j$, solution of $\mathbf{g}(\mathbf{y}) = \mathbf{f}(\mathbf{y}, \lambda_j) = \mathbf{0}$. This also means that $\bar{\lambda}_j$ in the predictor is just $\bar{\lambda}_{j+1}$. For $\bar{\mathbf{y}}_j$, the simplest choice is $\mathbf{y}_j$. There are more sophisticated choices, but usually it works well when the increment in $\lambda$ is reasonable.

This strategy is often used when the main objective is to find a highly nonlinear solution for a given $\lambda$ value. However, it may fail or miss out some part of the branch when used to track a folded branch in the bifurcation diagram. Figure 1.3b illustrates one of such cases. To overcome this problem, we define the parameter of the next step $\lambda_{j+1}$ as a free variable, and add another equation to close the system.

**Arc-length or pseudo-arc-length continuation** In fact, the name *arc-length* comes from arc-length parametrization. As its name of suggests, the branch is parameterized by its length $s$, $\mathbf{y}$ and $\lambda$ are functions of $s$, such that $(\mathbf{y}_j, \lambda_j) = (\mathbf{y}(s_j), \lambda(s_j))$. To find the next point, the system to



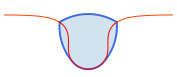

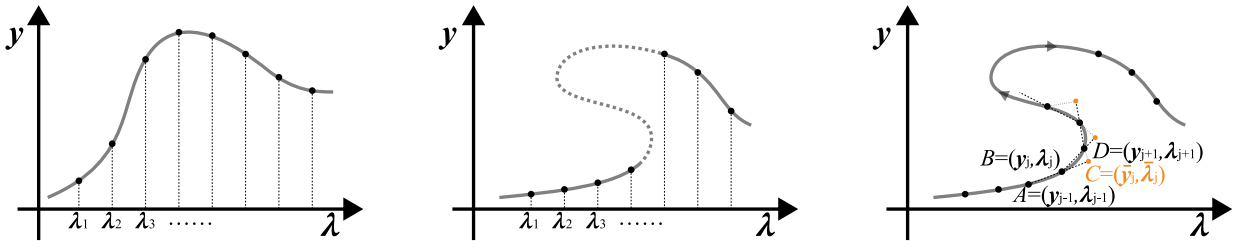


**(a)** **(b)** **(c)**

**Figure 1.3: Continuation methods and construction of points**

solve is

$$\mathbf{f}(\mathbf{y}, \lambda) = \mathbf{0} \tag{1.27a}$$

$$p(\mathbf{y}, \lambda, s) = ||\mathbf{y} - \mathbf{y}(s_j)||^2 + (\lambda - \lambda(s_j))^2 - (s - s_j)^2 = 0, \tag{1.27b}$$

where $s$ is given by the user, and the step length is $s - s_j$.

For pseudo-arc-length parametrization, the second equation is

$$p(\mathbf{y}, \lambda, s) = \zeta||\mathbf{y} - \mathbf{y}(s_j)||^2 + (1 - \zeta)(\lambda - \lambda(s_j))^2 - (s - s_j)^2 = 0, \tag{1.28}$$

where $0 < \zeta < 1$ is a tuning factor used to place the emphasis on $\mathbf{y}$ or $\lambda$. This is useful when the scales of the variables $\mathbf{y}$ and that of $\lambda$ are very different.

In the scope of this thesis, the term *arc-length continuation* is used in a general sense, such that the branch is not generated with local parametrization. Apart from the additional equation proposed by classical arc-length continuation and pseudo-arc-length continuation, there are other choices that can easily generate the sequence of points that well represent the branch.

Supposing we have already generated points $A = (\mathbf{y}_{j-1}, \lambda_{j-1})$, $B = (\mathbf{y}_j, \lambda_j)$, shown in figure 1.3c. Then we can calculate the predictor $C = (\bar{\mathbf{y}}_j, \bar{\lambda}_j)$ with

$$\mathbf{BC} = a \cdot \frac{\mathbf{AB}}{|\mathbf{AB}|} \tag{1.29}$$

where $a$ is a parameter related to step length control. We then try to find the next point $D = (\mathbf{y}_{j+1}, \lambda_{j+1})$ such that

$$\mathbf{AB} \cdot \mathbf{CD} = 0 \Leftrightarrow (\mathbf{y}_{j+1} - \bar{\mathbf{y}}_j)(\lambda_{j+1} - \bar{\lambda}_j) = 0 \tag{1.30a}$$

$$f(\mathbf{y}_{j+1}, \lambda_{j+1}) = 0. \tag{1.30b}$$

With all the previously presented theories and numerical methods about optimization, stability and bifurcation, in the following we illustrate their applications with some basic examples.

## 1.5 Example : planar Elastica

Led by Bernoulli and Euler, scientists created theories of the mechanics of rods and strings undergoing planar deformation since the seventeenth century and this domain of study still thrives nowadays.

Sophisticated models and theories can be found in articles, manuals and books, for example Antman (2005) and Bedford and Liechti (2020). Here we show the plane system of Elastica under

planar deformation. This model is a basic representation of slender rods, and is important for our models of confined structures.

In this example, we show how to derive the system of equations by constructing a Lagrangian and calculating its variation. Then we use the shooting method to solve the equations and use the continuation method to calculate branches.

The stability of the solutions is not discussed, interested readers can refer to for example the study of Levyakov and Kuznetsov (2010).

The setup is shown in figure 1.4. The Elastica is an inextensible beam of length $L$ and bending stiffness $EI$ is clamped at two ends. It deforms under displacement control $\Delta$ at one end.

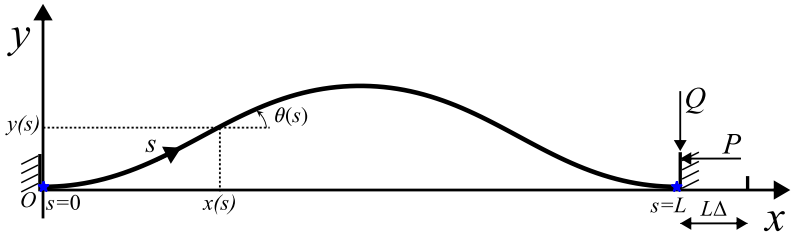


**Figure 1.4: Planar Elastica under compression**

$\kappa$, $\theta$, $x$, and $y$ are the curvature, the flexion angle, the horizontal and vertical positions of the Elastica, all of which are functions of $s$, the curvilinear coordinate. By definition, they are related by differential equations

$$x'(s) = \cos\theta(s), \qquad y'(s) = \sin\theta(s). \tag{1.31}$$

And the boundary conditions are

$$x(s=0) = 0, \qquad y(s=0) = 0, \qquad \theta(s=0) = 0, \tag{1.32a}$$
$$x(s=L) = L(1-\Delta), \qquad y(s=L) = 0, \qquad \theta(s=L) = 0. \tag{1.32b}$$

Using the energy minimization method, we start from the total energy of the system

$$\mathcal{E} = \int_0^L \frac{1}{2} EI\theta'^2(s)ds, \tag{1.33}$$

and build the Lagrangian with the differential equations from above

$$\mathcal{L} = \int_0^L \frac{EI}{2}\theta'^2(s) + n_x(s)\left[x'(s) - \cos\theta(s)\right] + n_y(s)\left[y'(s) - \sin\theta(s)\right] ds. \tag{1.34}$$

$n_x(s)$ and $n_y(s)$ are the Lagrange multipliers associated with the constraints (1.31). They have the dimension of forces. We choose to add these two differential equations to the Lagrangian because it is easier to apply the boundary conditions on $x$ and $y$.

Following the energy minimization method, the variation of the Lagrangian should be zero. We use $\bar{(\cdot)}$ to mark the variations of unknown variables, and the variation of the Lagrangian is

$$\bar{\mathcal{L}} = \int_0^L EI\theta'\bar{\theta}' + n_x\left[\bar{x}' + \bar{\theta}\,\sin\theta\right] + n_y\left[\bar{y}' - \bar{\theta}\,\cos\theta\right] ds.$$

As we only have fixed boundaries, the variations of the boundary conditions are all zero. Because of this, the derivative parts obtained with integration by parts vanish. Finally, the variation of the Lagrangian becomes

$$\bar{\mathcal{L}} = \int_0^L \left[\left(-EI\theta'' + n_x\sin\theta - n_y\cos\theta\right)\bar{\theta} - {n_x}'\bar{x} - {n_y}'\bar{y}\right] ds. \tag{1.35}$$



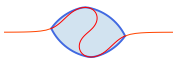

Canceling the factor before variation $\bar{x}$ and $\bar{y}$, we have ${n_x}'(s) = {n_y}'(s) = 0$, which means the $n_x$ and $n_y$ are constant. In fact, their physical meanings are the horizontal and vertical components of the internal force of Elastica, equal to the forces $P$ and $Q$ in figure 1.4. Then, the term before variation $\bar{\theta}$ gives the classical equation of Elastica

$$EI\theta''(s) = -P\sin\theta(s) + Q\cos\theta(s) \tag{1.36}$$

### 1.5.1 Dimensionless system

To generalize the solution and facilitate the numerical solving, we adimensionalize the system with length unit $L$ and force unit $EI/L^2$, and introduce the dimensionless quantities

$$\hat{\theta} = \theta \qquad \hat{s} = \frac{s}{L} \qquad \hat{x} = \frac{x}{L} \qquad \hat{y} = \frac{y}{L} \tag{1.37a}$$

$$\hat{\kappa} = \frac{d\hat{\theta}}{d\hat{s}} = \kappa L \qquad \hat{P} = \frac{P\,L^2}{EI} \qquad \hat{Q} = \frac{Q\,L^2}{EI} \tag{1.37b}$$

For the sake of simplicity, we omit the hat in the notation, and the variables presented in the following are all dimensionless variables.

Note that the non-dimensionalized version of the equations can be obtained by formally setting $L = 1$ and $EI = 1$. And the Elastica equation becomes

$$\theta''(s) = -P\sin\theta(s) + Q\cos\theta(s) \tag{1.38}$$

with equation (1.31) and boundary conditions

$$x(s=0) = 0, \qquad y(s=0) = 0, \qquad \theta(s=0) = 0, \tag{1.39a}$$

$$x(s=1) = 1-\Delta, \qquad y(s=1) = 0, \qquad \theta(s=1) = 0. \tag{1.39b}$$

### 1.5.2 Numerical implementation

**Minimization method** To solve the above system, we can use a global approach, meaning implement the problem into a numerical optimizer, for example IPOPT, with objective (1.33) and constraints (1.39) and (1.31). Through this way, we do not need the Elastica equation (1.38). Please note that the optimizers are only able to find the local minima, which are the stable equilibria, not all the equilibria.

**Shooting method** Another method is the *shooting method*. This name vividly describes the principle of the method. If we throw a ball from a fixed point towards a target, we need to find the right angle of shooting, such that the ball hits the target precisely. In practice, we usually do not succeed with a single shot, and we gradually adjust the shooting angle to achieve the goal. This illustrates the three main ingredients of the shooting method: unknowns to find (the shooting angle), integration (shooting), and adjustments.

In the example of planar Elastica, we want to find the right value of $P$, $Q$ and $\theta'(0)$, integrating the differential equations (1.31) and (1.38) with the boundary conditions on $s = 0$ can precisely 'shoot' the three boundary conditions on $s = 1$. This method is implemented in Python using the rootines `solve_ivp`[1] and `root`[2] of scipy package.

Different from the minimization method, this method can find all the equilibria, but their stability should be discussed. We use the shooting method to solve the problem and show how to find branches with the continuation method.

[1] `solve_ivp` solves initial value problems with numerical integration

[2] `root` finds a root of a system of nonlinear equations.

### 1.5.3 Bifurcation branches and mode 1/2

In this problem, the only control is the end displacement $\Delta$. Thanks to the shooting method, the unknowns of the system are reduced to $P$, $Q$, and $\kappa(0)$. The system parameter and the unknowns form the *global representation space* (GRS) (Domokos, 1994), and we search solutions in this space.

To solve the system for a fixed $\Delta$, we need to start from an initial guess. Because the solution is not unique, the final solution found by the numerical method depends on the initialization. If it is too far from any solution, the algorithm will not converge. For small $\Delta$, the linear approximation is still close to the real solution, but it is not the case for large $\Delta$. Thus, we use the local continuation method described in section 1.4.3 with the control parameter $\Delta$, gradually increasing $\Delta$ from a small value. We can use the linearized solution of any buckling mode as the initial state. Figure 1.5a and 1.5b show respectively the solutions bound by mode 1 and mode 2[3] initialization. Following this method, nonlinear solutions of any higher-order buckling mode can be obtained by choosing the appropriate initial state.

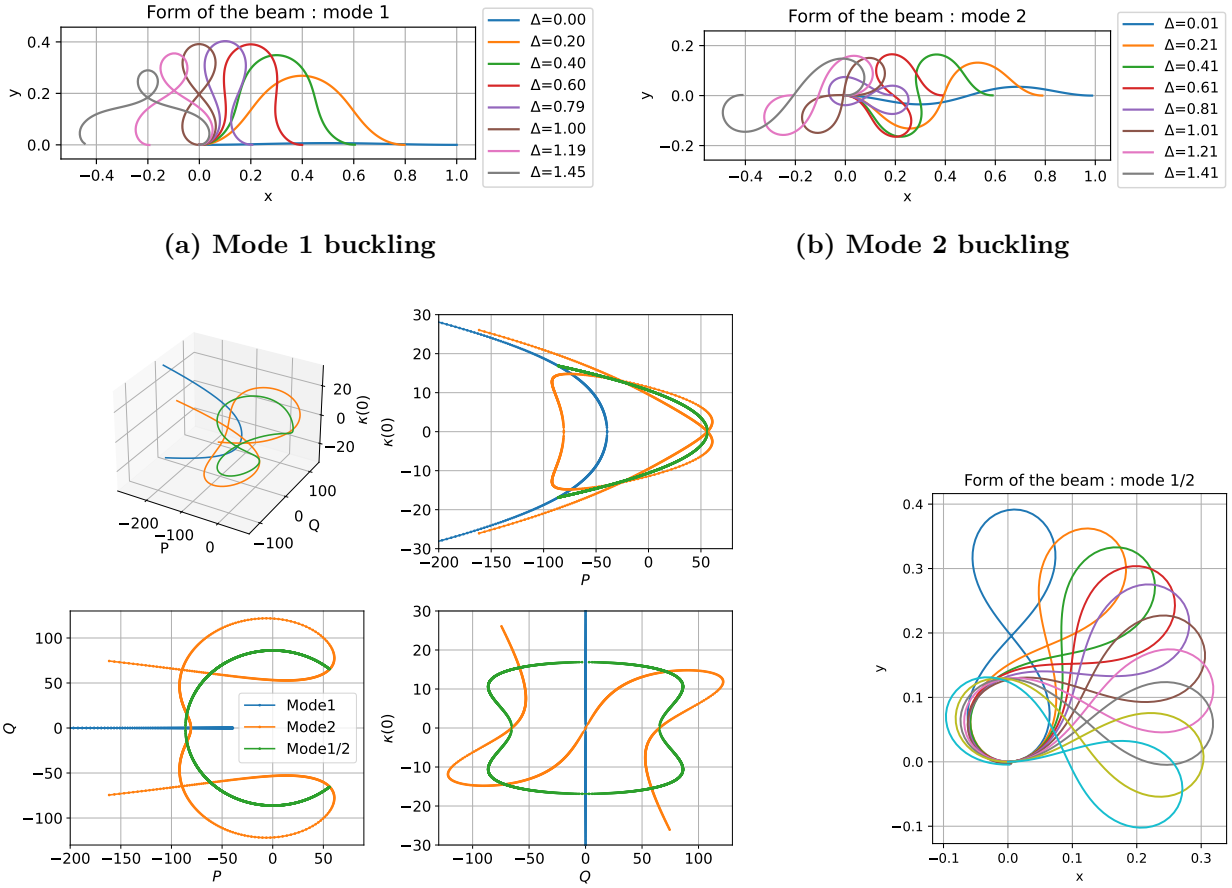


**(a) Mode 1 buckling**

**(b) Mode 2 buckling**

**(c) Bifurcation branches**

**(d) Mode 1/2**

**Figure 1.5: Solutions of the planar Elastica and the bifurcation branches.**

In a bifurcation diagram, there is a branch connecting the branches of mode 1 and mode 2, we call it mode 1/2 (Domokos, 1994). For mode 1/2, $\Delta = 1$, the two ends of the beam are joined together, and the beam forms the 8-shape. In fact, when we look at mode 1 and mode 2 at $\Delta = 1$, both look like 8 but with different orientations, one can imagine how this branch joins mode 1 and

[3]Mode 1 corresponds to the stable equilibrium of buckled Elastica, and mode 2 corresponds to the first unstable equilibrium. Other modes are defined in the same manner



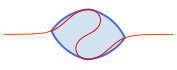

mode 2 by turning the 8 around.

Because the system parameter $\Delta$ is fixed to 1, we cannot use the local parametrization by $\Delta$. Thus, we apply the simplified arc-length continuation method described at the end of the section 1.4.3. In fact, the most difficult step is to find the first two points on the branch. To achieve this, we choose the solution of mode 1 at $\Delta = 1$ as the first point, then add random perturbations to this point and use the perturbed point to initialize the algorithm. The algorithm may fail to converge or find the first point again, so we repeat the random searching until another point on the mode 1/2 is found.

The solutions of mode 1/2 obtained by our continuation method are shown in figure 1.5d, where we observe well the turning 8 as expected. In figure 1.5c, we draw the branches in the global representation space $(P, Q, \kappa(0))$. All branches have certain sorts of symmetry, this is due to the symmetry of the problem itself, and it makes another good example of the pitchfork bifurcation. The branch for mode 1/2 connects those of mode 1 and mode 2, which also verifies our proposal made earlier.

## 1.6 Example: simple drop on a substrate

Here we give another example to illustrate the energy minimization method with functional variation. We consider a droplet of constant volume $V$ attached to a substrate, see figure 1.6. The system is described in 2D, assuming that there is a translation invariance along the $z$ direction. The surface energy of liquid-gaz, liquid-substrate, and substrate-gaz interfaces are marked by $\gamma_{lg}$, $\gamma_{ls}$, and $\gamma_{sg}$ respectively. The density of the liquid is noted $\rho$, and $g$ is the gravitational constant.

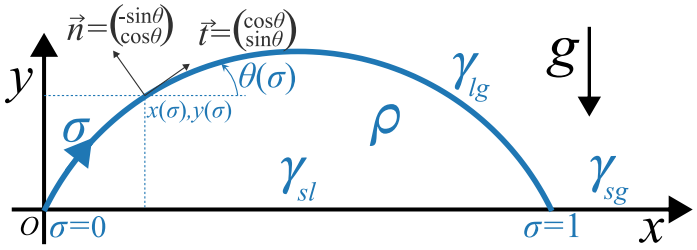


**Figure 1.6: Geometry description of a drop on a rigid substrate**

We would like to find the form of the interface using a curvilinear description of the geometry: $\theta(\sigma)$, $x(\sigma)$ and $y(\sigma)$, where $\sigma \in [0, 1]$ is the curvilinear coordinate. These functions are related by

$$\frac{dx}{d\sigma} = x'(\sigma) = \ell \cos\theta(\sigma), \qquad \frac{dy}{d\sigma} = y'(\sigma) = \ell \sin\theta(\sigma), \tag{1.40}$$

where $\ell$ is the actual total length of the interface, an unknown of the problem.

To find the geometry, we minimize the total energy of the system, that is the addition of the surface energy and the gravity energy

$$\mathcal{E} = \gamma_{lg}\ell - \Delta\gamma \int_0^1 x'\, d\sigma + \int_0^1 \frac{\rho g}{2} y^2\, x'\, d\sigma, \text{ where } \Delta\gamma = \gamma_{sg} - \gamma_{sl}, \tag{1.41}$$

under the volume constraint

$$V = \int_0^1 y(\sigma)x'(\sigma)d\sigma, \tag{1.42}$$

and the boundary conditions $x(0) = y(0) = 0$, and $y(1) = 0$.

With that, we build the Lagrangian

$$\begin{aligned}\mathcal{L} =&\gamma_{lg}\ell + \int_0^1 \left(-\Delta\gamma x' + \frac{\rho g}{2} y^2\, x'\right) d\sigma + \mu\left[V - \int_0^1 y\, x' d\sigma\right] \\ &+ \int_0^1 n_x(\sigma)\left[x' - \ell\cos\theta\right] - n_y(\sigma)\left[y' - \ell\sin\theta\right] d\sigma\end{aligned} \tag{1.43}$$

$n_x(\sigma)$, $n_y(\sigma)$ and $\mu$ are the Lagrange multipliers. We choose these notations because $n_x(s)$ and $n_y(s)$ have the same dimension as linear forces. We note that this energy has to be understood as per unit length along the $z$ direction.

Furthermore, we use $\bar{(\cdot)}$ to mark the admissible variations of the unknown variables. These variations should satisfy the boundary conditions $\bar{x}(0) = 0$, $\bar{y}(0) = 0$, and $\bar{y}(1) = 0$. And the variation of the Lagrangian is

$$\begin{aligned}\bar{\mathcal{L}} =& \left[\gamma_{lg} - \int_0^1 (\cos\theta + \sin\theta)\, d\sigma\right] \bar{\ell} + \left[-\Delta\gamma + n_x(1)\right] \bar{x}(1) \\ &+ \int_0^1 \left[\frac{d}{d\sigma}\left(\Delta\gamma - \frac{\rho g}{2} y^2 + \mu y - n_x\right) \bar{x} + \left(\rho g y x' - \mu x' - n'_y\right) \bar{y}\right. \\ &\left. + \left(n_x \ell\cos\theta - n_y \ell\sin\theta\right) \bar{\theta}\right] d\sigma\end{aligned} \tag{1.44}$$

At the minimum, the variation of the Lagrangian should be zero for any admissible variation $\bar{(\cdot)}$. Therefore, we require the factor of each variation to vanish:

$$n_x\cos\theta - n_y\sin\theta = 0, \tag{1.45a}$$

$$\Delta\gamma - \frac{\rho g}{2} y^2 + \mu y - n_x = \text{Cste} = 0, \qquad n_x(1) = \Delta\gamma, \tag{1.45b}$$

$$n'_y = \rho g y x' - \mu x' = \ell\left(\rho g y - \mu\right)\cos\theta, \tag{1.45c}$$

$$\gamma_{lg} = \int_0^1 \left(n_x\cos\theta + n_y\sin\theta\right) d\sigma. \tag{1.45d}$$

We differentiate equation (1.45b) with respect to $\sigma$:

$$n'_x = -\left(\rho g y - \mu\right) y' = -\ell\left(\rho g y - \mu\right)\sin\theta. \tag{1.46}$$

To further interpret the equations, we introduce the tangent vector $\vec{t} = (\cos\theta, \sin\theta)$ and the normal vector $\vec{n} = (-\sin\theta, \cos\theta)$ of the interface, which are also shown in figure 1.6. The two vectors are perpendicular, and they are related by

$$\frac{d\vec{t}}{d\sigma} = \frac{d}{d\sigma}\begin{pmatrix}\cos\theta \\ \sin\theta\end{pmatrix} = \begin{pmatrix}-\sin\theta \\ \cos\theta\end{pmatrix}\frac{d\theta}{d\sigma} = \theta'\,\vec{n}. \tag{1.47}$$

Introducing vector $\vec{N} = (n_x, n_y)$, then we can rewrite equations (1.45a), (1.45c), (1.45d), and (1.46) as

$$\vec{N}\cdot\vec{n} = 0, \tag{1.48a}$$

$$\gamma_{lg} = \int_0^1 \vec{N}\cdot\vec{t}\, d\sigma \tag{1.48b}$$

$$\frac{d\vec{N}}{d\sigma} = \begin{pmatrix}n'_x \\ n'_y\end{pmatrix} = \ell\left(\rho g y - \mu\right)\begin{pmatrix}-\sin\theta \\ \cos\theta\end{pmatrix} = \ell\left(\rho g y - \mu\right)\vec{n}. \tag{1.48c}$$



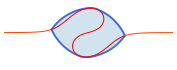

The first equation indicates that $\vec{N}$ is parallel to $\vec{t}$, and we can assume that $\vec{N} = f(\sigma)\,\vec{t}$, where $f(\sigma)$ is a scalar function. Differentiating this gives

$$\vec{N}' = f'(\sigma)\,\vec{t} + f(\sigma)\,\theta'\,\vec{n}.$$

By identification with equation (1.48c), we have $f'(\sigma) = 0$, which means $f(\sigma)$ is a constant. Apply this information to equation (1.48b), we have $f(\sigma) = \text{Cste} = \gamma_{lg}$, then

$$\vec{N} = \gamma_{lg}\,\vec{t}, \qquad \Rightarrow \qquad n_x = \gamma_{lg}\cos\theta, \quad n_y = \gamma_{lg}\sin\theta \tag{1.49a}$$

$$\gamma_{lg}\,\frac{\theta'}{\ell} = \rho g y - \mu. \tag{1.49b}$$

Finally, the whole system can be determined by $\theta(\sigma)$, $x(\sigma)$, $y(\sigma)$, $\ell$ and $\mu$. To do so, we solve three differential equations (1.40) and (1.49b), with four boundary conditions $x(0) = y(0) = y(1) = 0$ and (1.50), adding the volume constraint (1.42), the system is closed.

With equation (1.49a), we know that $\vec{N}$ is the surface tension along the interface. For equation (1.49b), we see the local curvature multiplied by $\gamma_{lg}$ on the left and the hydrostatic pressure on the right, which is *the Young–Laplace equation*. Setting equation (1.49a) at $\sigma = 1$ knowing the boundary value by (1.45b), we have

$$\Delta\gamma = \gamma_{lg}\cos\theta(1), \tag{1.50}$$

which is *the Young-Dupré law*.

This example shows that the classical laws of surface tension can be derived by variational approach. Comparing the right-hand side of equation of Elastica (1.36) and that of a drop (1.45a), we observe similar form. In fact, the interface can be seen as a slender structure that has no shear force and uniform tension $\gamma_{lg}$.

## 1.7 Example: hanging drop with gravity

Here we consider a droplet attached to a substrate and hanging down from the ceiling due to gravity, shown in figure 1.7. This is a classical problem, and has already been studied long ago. One can find detailed analysis from the studies of, for example, Michael and Williams (1976), Padday (1971), and Padday and Pitt (1973).

For notations and definitions, the perimeter of the attachment is fixed with radius $a$, the liquid-air surface tension is $\gamma$, and the mass density of the liquid is $\rho$. The system is in 3D.

In this example, we would like to show how to apply the optimization theory, stability analysis and continuation methods in the discretized system.

Considering the rotation symmetry, cylinder coordinates $(r, \psi, z)$ are used, and we only consider half of the drop. We use curvilinear description for the geometry of the drop $(\theta(s), R(s), Z(s))$, and they are related by differential equations

$$\frac{dR}{ds} = R'(s) = \cos\theta(s), \qquad \frac{dZ}{ds} = Z'(s) = \sin\theta(s). \tag{1.51}$$

It is also possible to rewrite the derivatives of $R$ with respect to $Z$ as expressions of $\theta(s)$:

$$\frac{dR}{dz} = \frac{dR}{ds}\frac{1}{dZ/ds} = \frac{\cos\theta}{\sin\theta} = \frac{1}{\tan\theta(s)} \tag{1.52a}$$

$$\frac{d^2R}{dz^2} = \frac{d}{dz}\frac{dR}{dz} = \frac{d}{ds}\left(\frac{dR}{dz}\right)\frac{1}{dZ/ds} = -\frac{\theta'(s)}{\sin^3\theta(s)} \tag{1.52b}$$

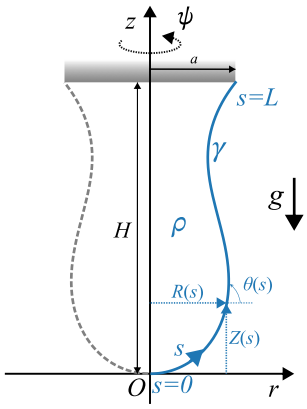


**Figure 1.7: Geometry description of a pending drop**

Note that the length of the interface $L$ and the height of the drop $H$ are all unknown. To find the geometry of the drop under the given conditions, we again use energy minimization method. The total energy is the sum of surface energy and gravity potential. The surface of air-liquid contact is

$$\mathcal{S} = \int_z \int_r \int_\psi r \, d\psi \sqrt{(dr)^2 + (dz)^2} = 2\pi \int_{s=0}^{L} R \, ds, \tag{1.53}$$

then the energy related to capillarity is $\mathcal{E}_{surf} = \gamma \mathcal{S}$. The gravity potential of the drop is

$$\begin{aligned} \mathcal{P}_{grav} =& -\rho g \int_z \int_\psi \int_r (H - z) \; (r \, dr \, d\psi dz) = -\rho g \pi \int_{z=0}^{H} (H - z) \, R^2(z) \, dz \\ =& -\rho g \pi \int_{s=0}^{L} [H - Z(s)] \; R^2(s) \sin\theta(s) ds, \end{aligned} \tag{1.54}$$

In conclusion, we would like to minimize the total energy of the system:

$$\begin{aligned} \mathcal{E} &= \mathcal{E}_{surf} + \mathcal{P}_{grav} \\ &= 2\gamma\pi \int_{s=0}^{L} R(s) \, ds - \rho g \pi \int_{s=0}^{L} (H - Z(s)) \, R^2(s) \sin\theta(s) ds \end{aligned} \tag{1.55}$$

with boundary conditions and fixed volume:

$$Z(s=0) = 0, \qquad R(s=0) = 0 \tag{1.56a}$$

$$Z(s=L) = H, \qquad R(s=L) = a \tag{1.56b}$$

$$V = \int_z \int_\psi \int_r r \, dr \, d\psi \, dz = \pi \int_{z=0}^{H} R^2(z) dz = \pi \int_{s=0}^{L} R^2(s) \sin\theta(s) ds. \tag{1.56c}$$

With the above definitions, the Lagrangian of the system is

$$\begin{aligned} \mathcal{L}(R, Z) =& \pi \int_{s=0}^{L} \left[ 2\gamma R - \rho g (H - Z) \, R^2 \sin\theta \right] \, ds \\ & - \int_{s=0}^{L} n_R (R' - \cos\theta) + n_Z (Z' - \sin\theta) \, ds - P \cdot \left( \pi \int_{s=0}^{L} R^2 \sin\theta ds - V \right) \end{aligned} \tag{1.57}$$

where $n_R$, $n_Z$ and $P$ are Lagrange multipliers.



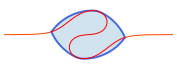

### 1.7.1 Discretization and the discretized system

To generate the numerical solutions, we adimensionalize the system with length unit $\sqrt{\frac{\gamma}{\rho g}}$ and force unit $\gamma\sqrt{\frac{\gamma}{\rho g}}$. And in the following, all variables are dimensionless. Note that the non-dimensionalized system can be obtained by formally setting $\gamma = 1$ and $\rho g = 1$ in the original system.

We discretize the interface with equal length, with fixed grid such that $s_0 = 0$ and $s_N = 1$, see figure 1.8, and project the fixed grid to the real length by multiplying the unknown interface length $L$.

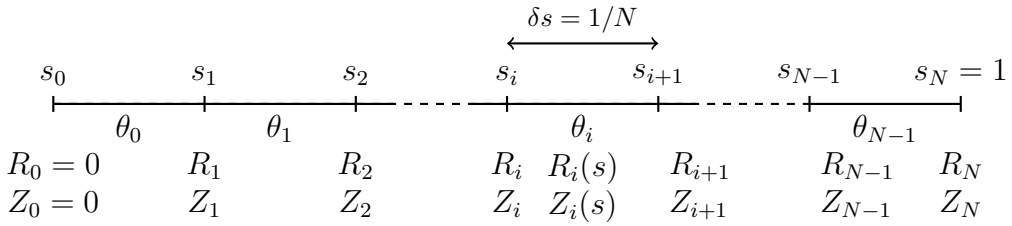


**Figure 1.8: Diagram of discretization**

In this discretized system, we have $3N + 1$ variables, that are $\theta_i$, $(i = 0, ..., N-1)$, $R_i$, $Z_i$ $(i = 1, ..., N)$, and $L$. One can rewrite the relations for the continuous system in their discretized form:

$$R(s) = R_i + \cos(\theta_i)\, L(s - s_i), \quad s \in [s_i, s_{i+1}]; \qquad \Rightarrow R_{i+1} - R_i = \cos(\theta_i)\, L\delta s \tag{1.58a}$$

$$Z(s) = Z_i + \sin(\theta_i)\, L(s - s_i), \quad s \in [s_i, s_{i+1}]; \qquad \Rightarrow Z_{i+1} - Z_i = \sin(\theta_i)\, L\delta s \tag{1.58b}$$

$$Z_0 = 0, \qquad R_0 = 0, \qquad R_N = a \tag{1.58c}$$

$$\mathcal{E}_{disc} = \pi \sum_{i=0}^{N-1} \left[ 2 \cdot \frac{R_i + R_{i+1}}{2} - \left( Z_N - \frac{Z_i + Z_{i+1}}{2} \right) \left( \frac{R_i + R_{i+1}}{2} \right)^2 \sin\theta_i \right] L\delta s \tag{1.58d}$$

$$\mathcal{V}_{disc} = \pi \sum_{i=0}^{N-1} \left[ \left( \frac{R_i + R_{i+1}}{2} \right)^2 \sin\theta_i \right] L\delta s \tag{1.58e}$$

### 1.7.2 Optimal conditions, equilibrium, and stability analysis

For the discretized system, we show how the system of equations and the stability analysis are implied by the optimal conditions.

We construct the Lagrangian $\mathcal{L}_{disc} = \mathcal{L}_{disc}(\theta_i, R_i, Z_i)$ of the discretized system

$$\begin{aligned} \mathcal{L}_{disc} =& \pi \sum_{i=0}^{N-1} \left[ 2 \cdot \frac{R_i + R_{i+1}}{2} - \left( Z_N - \frac{Z_i + Z_{i+1}}{2} \right) \left( \frac{R_i + R_{i+1}}{2} \right)^2 \sin\theta_i \right] L\delta s \\ & - \sum_{i=0}^{N-1} \left[ N_i^R (R_{i+1} - R_i - \cos(\theta_i)\, L\delta s) + N_i^Z (Z_{i+1} - Z_i - \sin(\theta_i)\, L\delta s) \right] \\ & - N_N^R (R_N - a) - P \left[ \pi \sum_{i=0}^{N-1} \left( \frac{R_i + R_{i+1}}{2} \right)^2 \sin(\theta_i)\, L\delta s - V \right] \end{aligned} \tag{1.59}$$

where $N_i^R$ and $N_i^Z$ $(i = 1, ..., N-1)$ are the Lagrange multipliers associated to (1.58a) and (1.58b). $N_N^R$ is the Lagrange multiplier associated to the boundary condition $R_n = a$.

To present this problem in the standard form in section 1.2, we put all the $3N+1$ variables in one vector, $\mathbf{x} = [\theta_i, R_i, Z_i, L]$. The vector $\mathbf{g}$ groupes all the equality constraints:

$$\mathbf{g} = [R_{i+1} - R_i - \cos\theta_i \, L\delta s, \; Z_{i+1} - Z_i - \sin\theta_i \, L\delta s, \; R_N - a, \; \mathcal{V}_{disc} - V] \, .$$

And all the Lagrange multipliers are put in a vector $\boldsymbol{\lambda} = \left[N_0^R, ..., N_{N-1}^R, N_0^Z, ..., N_{N-1}^Z, N_N^R, P\right]$. Then, one can apply directly the KKT condition in section 1.2.1 to obtain the system of equations satisfied by the equilibria. In the same way, a direct application of the second order condition of optimality gives the stability of a given equilibrium.

More precisely, an equilibrium $\mathbf{x}^*$ is a solution of

$$\nabla_{\mathbf{x}} \mathcal{L}_{disc}(\mathbf{x}^*) = \mathbf{0}, \qquad \mathbf{g}(\mathbf{x}^*) = \mathbf{0}. \tag{1.60}$$

To check the stability of $\mathbf{x}^*$, one should calculate the eigenvalues of the projected Hessian matrix $\mathbf{H}^* := \mathbf{K}\,\mathbf{H}\,\mathbf{K}^T$, with $\mathbf{H} = \nabla^2_{\mathbf{x}} \mathcal{L}_{disc}$. And $\mathbf{K}$ is the kernel of $\nabla_{\mathbf{x}} \mathbf{g}$. If all the eigenvalues are strictly positive, then the equilibrium is stable. If there exists any negative eigenvalue, the equilibrium is unstable, and the number of negative eigenvalue indicates the level of instability.

The derivatives are calculated by the algorithmic differentiation feature of CasADi in python, a detailed presentation of which is given in the next chapter.

### 1.7.3 Results and discussions

In figure 1.9 we show solutions for two chosen radius value, $a = 0.4$ and $a = 1.6$, representing results for relatively small and large radius.

For each radius value, we show the contact angle ($\theta(L) = \theta_{N-1}$), drop height ($H = Z(L) = Z_N$), and the Lagrange multiplier of volume constraint ($P$) as functions of volume $V$. Different colors indicate different stability index, which is the number of negative eigenvalues of $\hat{\mathbf{H}}^*$. Several solutions with the same value of $V$ are chosen and the corresponding forms of the drop are drawn below these diagrams.

To initialize the solver, we start from a small value of volume, such that the solution can be approximated by a spherical cap. Then the continuation method is used for solving larger values of volume. From the diagrams, we can see that the control parameter $H$ do not increase uniformly. Without using arc-length continuation, we cannot access the entire branch only by local continuation. This shows the utility of the arc-length continuation method.

From the diagrams, we can see that the branches turn around a certain value of $V$, and the index changes at each turning point of the branch. The forms of the drop shown below these diagrams reveal how the change of stability index reflects on the form of the drop.

This example proves the validity of our continuation and stability analysis approach.



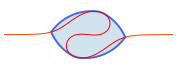

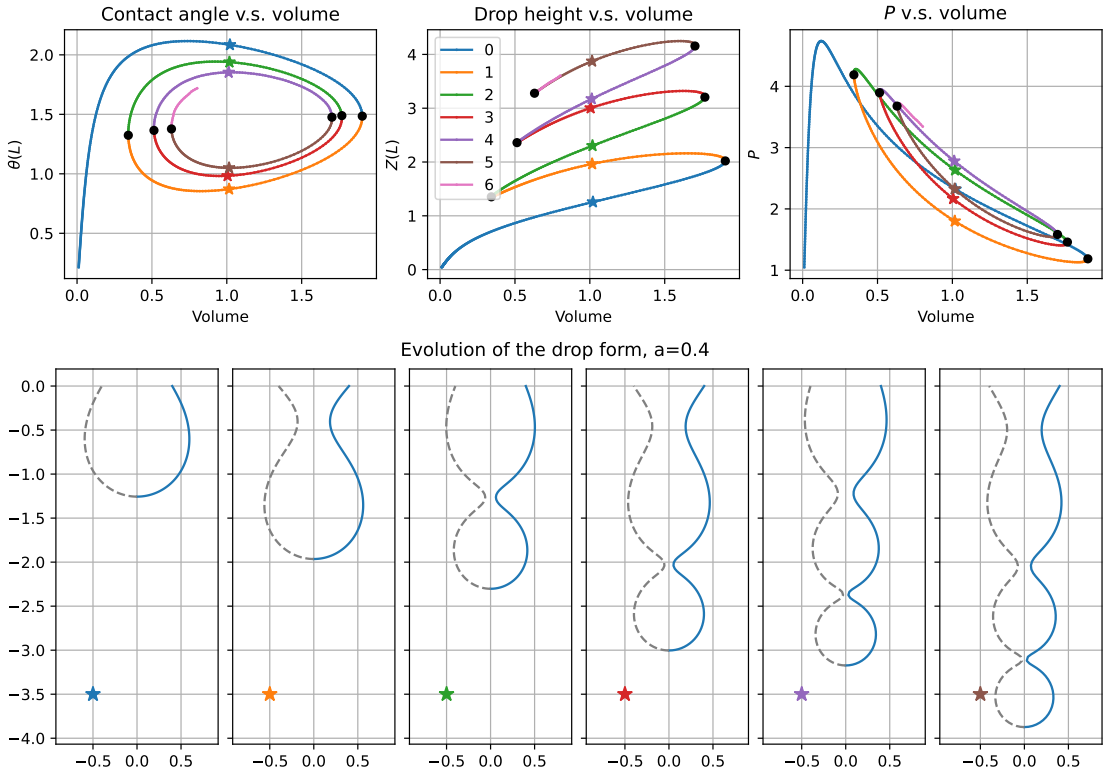


**(a)** $a = 0.4$

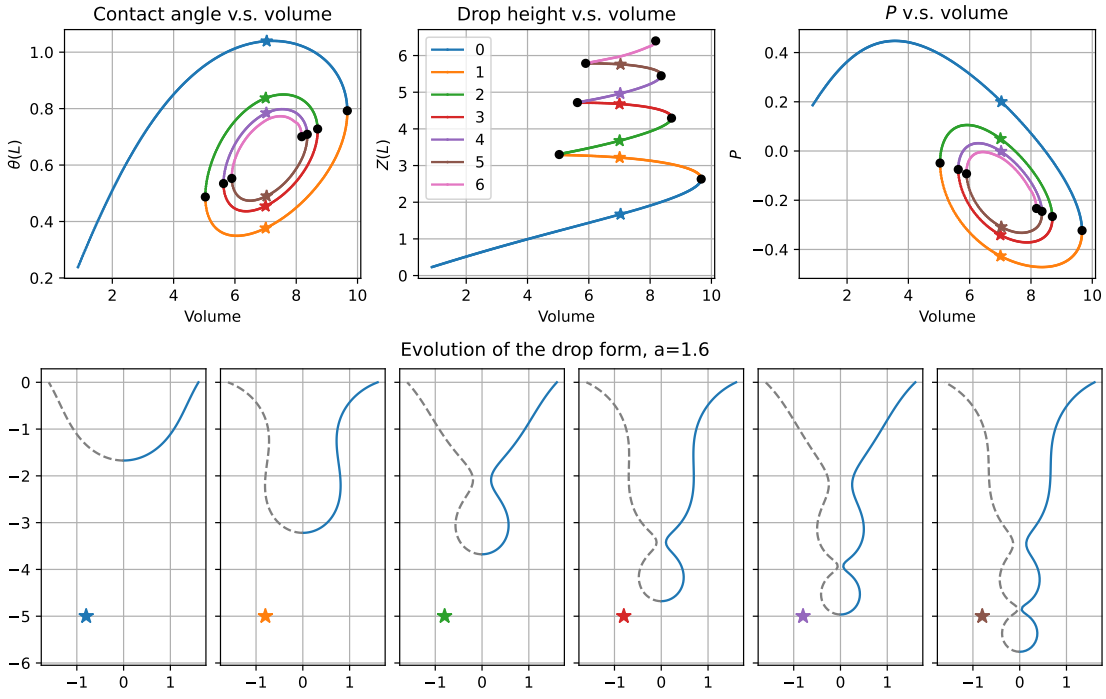


**(b)** $a = 1.6$

**Figure 1.9: Solving results of the pending drop problem for two fixed radius $a$.**

# Chapter 2

# Numerical configurations and convergence study

## 2.1 CasADi: an open-source tool

CasADi is an open-source tool for nonlinear optimization and algorithmic differentiation (AD) using a syntax borrowed from computer algebra systems (CAS), which explains its name (Andersson et al., 2019).

It is important to point out that CasADi is not a conventional AD tool, that can be used to calculate derivative information from existing user code with little to no modification. However, it is not a computer algebra system, also known as a symbolic computation system. While the symbolic core does include an increasing set of tools for manipulating symbolic expressions, these capabilities are very limited compared to a proper CAS tool.

At the core of CasADi is a symbolic framework implementing forward and reverse mode of AD on expression graphs to construct gradients, large-and-sparse Jacobians and Hessians. Users can construct symbolic expressions using a MATLAB inspired everything-is-a-matrix syntax.

The other features of CasADi include integrators, implicit functions, and it supports the creation of functions based on look-up table. Additionally, CasADi implements several routines for nonlinear and quadratic optimization problems, and interfaces to several famous optimizers, including IPOPT, which we mentioned earlier.

All of these features make CasADi a powerful tool to tackle initial value problems, optimal control problems, and optimization problems in general.

The notion of algorithmic differentiation (AD) is different from the classical numerical differentiation, for example

$$\begin{aligned} D_{+h}\, f(x) &= \frac{f(x+h) - f(x)}{h} \quad \text{(forward differentiation)}, \\ D_{\pm h}\, f(x) &= \frac{f(x+h) - f(x-h)}{2h} \quad \text{(centered differentiation)}. \end{aligned} \tag{2.1}$$

To understand the idea behind AD and the advantages of the method, in the following we explain the concept and illustrate it with a simple example. The next part is a brief introduction written with the help of Griewank and Walther (2008). For readers who want to have a better understanding of AD, please refer to the original reference.

### 2.1.1 Algorithmic differentiation

*Algorithmic differentiation* (AD), also called *automatic differentiation*, is a computational method used to evaluate derivatives of a given function. It differs from symbolic differentiation and nu-



merical differentiation. AD uses expression graphs rather than expression trees like symbolic differentiation. Moreover, symbolic differentiation is a subdomain of symbolic computation, focusing on returning mathematical expressions, which may be inefficient when the user's objective is only the value of the derivative. Compared to the numerical differentiation, AD does not introduce truncation errors, related to the value of $h$ in the differential scheme (2.1).

Here we give a simplified example to illustrate some basic ideas of AD. Suppose we have a program that calculates floating outputs $y$ from floating inputs $x$. To do so, the program needs to calculate a sequence of intermediate floating values. This sequence of calculation can be described by an evaluation trace, a record of a particular run of a given program, containing the sequence of intermediate floating values. Supposing the program calculates the function

$$y = f(x_1, x_2) = [\sin(x_1/x_2) + x_1/x_2 - e^{x_2}] \cdot [x_1/x_2 - e^{x_2}]\,, \tag{2.2}$$

then the related evaluation trace is shown in Table 2.1.

| | | | | | | |
|---|---|---|---|---|---|---|
| $v_{-1}$ | = | $x_1$ | = | 1.5000 | | |
| $v_0$ | = | $x_2$ | = | 0.5000 | | |
| $v_1$ | = | $v_{-1}/v_0$ | = | $1.5000/0.5000$ | = | 3.0000 |
| $v_2$ | = | $\sin(v_1)$ | = | $\sin(3.0000)$ | = | 0.1411 |
| $v_3$ | = | $e^{v_0}$ | = | $e^{0.5000}$ | = | 1.6487 |
| $v_4$ | = | $v_1 - v_3$ | = | $3.0000 - 1.6487$ | = | 1.3513 |
| $v_5$ | = | $v_2 + v_4$ | = | $01411 + 1.3513$ | = | 1.4924 |
| $v_6$ | = | $v_5 * v_4$ | = | $1.4924 * 1.3513$ | = | 2.0167 |
| $y$ | = | $v_6$ | = | 2.0167 | | |

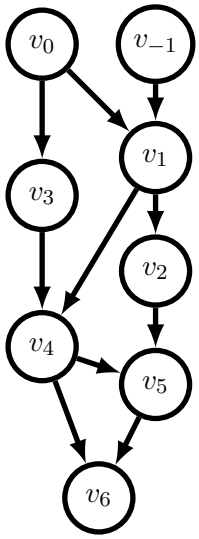


**Table 2.1: An evaluation trace of the example. Right: computational graph of the table.**

**Forward Mode** Suppose we want to differentiate $y$ with respect to $x_1$. To do so, we follow the evaluation trace from the inputs, differentiate each intermediate variable $v_i$ up to the output $y$. Table 2.2 illustrates this process. Each variable $v_i$ is associated with $\dot{v}_i = \partial v_i/\partial x_1$.

Using this method, we can obtain the derivative even if there are many more operations to calculate $y$ from $x_1$, and the total number of operations to evaluate $\partial y/\partial x_1$ is a small multiple of that for evaluating $y$.

This is the basic idea of the forward mode of AD. It is called *forward* because the derivatives $\dot{v}_i$ are calculated along with $v_i$, that is in the forward direction.

In the same manner, we can also calculate the partial derivative $\partial y/\partial x_2$, but if we want to have the two derivatives, it is more efficient to redefine $\dot{v}_i$ to be vectors and evaluate several partial derivatives at once.

**Reverse Mode** Another approach to evaluate the partial derivatives is the *reverse* or *adjoint mode*. As its name indicates, we do not calculate the derivatives of each intermediate variables with respect to input, but evaluate the sensitivity of an output variable with respect to each of the intermediate variables. To achieve this, the analysis must start backwards, that is, from the output variables. For our example, Table 2.3 shows the evaluation trace of reverse mode AD, which is called the reverse trace. For each step that leads to a new variable, we calculate the adjoint variable



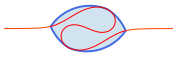

| | | | |
|---|---|---|---|
| $v_{-1} = x_1$ | $= 1.5000$ | $\dot{v}_{-1} = \dot{x}_1$ | $= 1$ |
| $v_0 = x_2$ | $= 0.5000$ | $\dot{v}_0 = \dot{x}_2$ | $= 0$ |
| $v_1 = v_{-1}/v_0$ | $= 3.0000$ | $\dot{v}_1 = (\dot{v}_{-1} - v_{-1}\dot{v}_0)/v_0$ | $= 1.0000/0.5000 = 2.0000$ |
| $v_2 = \sin(v_1)$ | $= 0.1411$ | $\dot{v}_2 = \cos(v_1)\dot{v}_1$ | $= -0.9900 * 2.0000 = -1.9800$ |
| $v_3 = e^{v_0}$ | $= 1.6487$ | $\dot{v}_3 = e^{v_0}\dot{v}_0$ | $= 1.6487 * 0.0000 = 0.0000$ |
| $v_4 = v_1 - v_3$ | $= 1.3513$ | $\dot{v}_4 = \dot{v}_1 - \dot{v}_3$ | $= 2.0000 - 0.0000 = 2.0000$ |
| $v_5 = v_2 + v_4$ | $= 1.4924$ | $\dot{v}_5 = \dot{v}_2 + \dot{v}_4$ | $= -1.9800 + 2.0000 = 0.0200$ |
| $v_6 = v_5 * v_4$ | $= 2.0167$ | $\dot{v}_6 = \dot{v}_5 * v_4 + v_5 * \dot{v}_4$ | $= 0.0200 * 1.3513$ $+1.4924 * 2.0000 = 3.0118$ |
| $y = v_6$ | $= 2.0167$ | $\dot{y} = \dot{v}_6$ | $= 3.0118$ |

**Table 2.2: Forward-Derived Evaluation Trace.**

| | | | | | |
|---|---|---|---|---|---|
| $v_{-1} = x_1$ | $= 1.5000$ | $\downarrow$ | $\uparrow$ | $\bar{x}_1 = \bar{v}_{-1}$ | $= 3.0118$ |
| $v_0 = x_2$ | $= 0.5000$ | $\downarrow$ | $\uparrow$ | $\bar{x}_2 = \bar{v}_0$ | $= -13.7239$ |
| $v_1 = v_{-1}/v_0$ | $= 3.0000$ | $\downarrow$ | $\uparrow$ | $\bar{v}_0 = -\bar{v}_1 * v_1/v_0 + \bar{v}_0$ | $= -1.5059 * 3.000/0.5000$ $-4.6884 = -13.7239$ |
| | | | | $\bar{v}_{-1} = \bar{v}_1/v_0$ | $= 1.5059/0.5000 = 3.0118$ |
| $v_2 = \sin(v_1)$ | $= 0.1411$ | $\downarrow$ | $\uparrow$ | $\bar{v}_1 = \bar{v}_1 + \bar{v}_2\cos(v_1)$ | $= 2.8437 + 1.3513 * (-0.9900)$ $= 1.5059$ |
| $v_3 = e^{v_0}$ | $= 1.6487$ | $\downarrow$ | $\uparrow$ | $\bar{v}_0 = \bar{v}_3 * v_3$ | $-2.8437 * 1.6487 = -4.6884$ |
| $v_4 = v_1 - v_3$ | $= 1.3513$ | $\downarrow$ | $\uparrow$ | $\bar{v}_3 = -\bar{v}_4$ | $= -2.8437$ |
| | | | | $\bar{v}_1 = \bar{v}_4$ | $= 2.8437$ |
| $v_5 = v_2 + v_4$ | $= 1.4924$ | $\downarrow$ | $\uparrow$ | $\bar{v}_4 = \bar{v}_4 + \bar{v}_5$ | $= 1.4924 + 1.3513 = 2.8437$ |
| | | | | $\bar{v}_2 = \bar{v}_5$ | $= 1.3513$ |
| $v_6 = v_5 * v_4$ | $= 2.0167$ | $\downarrow$ | $\uparrow$ | $\bar{v}_5 = \bar{v}_6 * v_4$ | $= 1.0000 * 1.3513 = 1.3513$ |
| | | | | $\bar{v}_4 = \bar{v}_6 * v_5$ | $= 1.0000 * 1.4924 = 1.4924$ |
| $y = v_6$ | $= 2.0167$ | $\downarrow$ | $\uparrow$ | $\bar{v}_6 = \bar{y}$ | $= 1$ |

**Table 2.3: Reverse-Derived Evaluation Trace.**



of every variable on the right-hand side $\bar{v}_i = \partial y/\partial \delta_i$, where $\delta_i$ is a new independent variable added to the right-hand side of the equation defining $v_i$, such that adding a small variation $\delta_i$ to $v_i$ will change the calculated numerical value of $y$ by $\bar{v}_i \delta_i$. For example, to calculate $\bar{v}_5$, we see that $v_5$ influence $y$ only by $v_6 = v_5 * v_4$, and $y = v_6$. Then $\bar{v}_5 = \partial y/\partial v_6 * \partial v_6/\partial v_5 = \bar{v}_6 * v_4$. As for $\bar{v}_4$, it is first used as an entry in step $v_5 = v_2 + v_4$ and then in step $v_6 = v_5 * v_4$. To calculate the final $\bar{v}_4$, we observe that $v_4$ is called in $v_5 = v_2 + v_4$ and then in $v_6 = v_5 * v_4$, which leads to $\bar{v}_4 = \partial y/\partial v_6 * \partial v_6/\partial v_4 + \partial y/\partial v_5 * \partial v_5/\partial v_4 = \bar{v}_6 * v_5 + \bar{v}_5$. In the table, $\bar{v}_4$ is calculated in two steps, following the reversed order of calculating $y$, and this presentation is used to show how we build the reverse mode AD from the output to the input with each evaluation of the intermediate variable, so the adjoint variable of some reused variables can be calculated incrementally. Different from the forward mode, with the reverse evaluation sequence, we not only have the partial differential of $x_1$, but also $x_2$. This is true even though there are a lot more inputs.

With this example, we can generate reverse AD for larger problems. For reverse mode AD, the total floating point operations of the added lines in reverse trace is a small multiple of that for the underlying code to evaluate $y$, but we can obtain the derivatives of all the input variables, while the forward mode AD needs nearly the same number of operations to evaluate the derivative for each variable. In many applications, the number of input variables are much larger than the output variables, and problems of one single objective depending on thousands and millions of operations are quite common. In this case, the reverse AD can provide an accurate set of first-order derivatives for a relatively low computational cost.

## 2.2 Discretization and convergence study

In this part we show and discuss the different discretization schemes used in our numerical simulations.

The deformation of slender structures like beams is the main topic of this thesis. For this reason, we choose to discuss different numerical schemes over the Planar Elastica example mentioned in section 1.5.

Recall that the Elastica is clamped at two ends and deforms under displacement control. We adimensionalize the system by bending stiffness $EI$ and Elastica length $L$. Formulating the problem as a constrained optimization problem, we can use the optimization theories and find the following system of equations

$$\theta'(s) = \kappa(s), \tag{2.3a}$$
$$\kappa'(s) = -P \sin\theta(s) + Q \cos\theta(s), \tag{2.3b}$$
$$x'(s) = \cos\theta(s), \tag{2.3c}$$
$$y'(s) = \sin\theta(s) \tag{2.3d}$$

with boundary conditions

$$x(0) = 0, \quad y(0) = 0, \quad \theta(0) = 0 \tag{2.4a}$$
$$x(1) = 1 - \Delta, \quad y(1) = 0, \quad \theta(1) = 0. \tag{2.4b}$$

Note that $P$ and $Q$ in 2.3b are respectively the Lagrange multipliers for boundary condition $x(1)$ and $y(1)$.

### 2.2.1 Rod discretization

The most basic discretization is to connect discrete points by straight lines. Thus, each edge has a constant angle $\theta_i$, and a more detailed definition is shown in figure 2.1. This is equivalent to approximating the continuous beam by rigid rods, so we call this *rod discretization*.



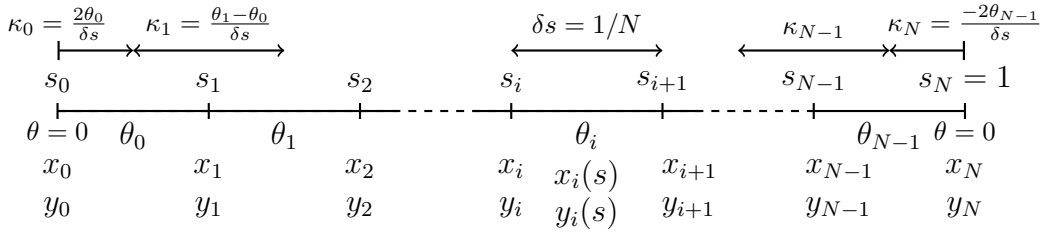


**Figure 2.1: Rod discretization**

We give some remarks on this discretization. First, the geometry of the system is defined by $\theta_i$, but only the curvature $\kappa$ appears in the energy definition. Therefore, we define

$$\kappa_i = \frac{(\theta_i - \theta_{i-1})}{\delta s}, \quad s \in [s_i - \delta s/2, s_i + \delta s/2], \qquad (i = 1, ..., N-1). \tag{2.5}$$

This is the derivative of $\theta_i$ calculated with the finite difference method. Each $\kappa_i$ is supposed to cover a scope of $\delta s$ centered by each node $s_i$, shown in figure 2.1.

Second, special treatments should be applied to the boundary conditions of $\theta$. We do not fix the first and last rod to be horizontal, but apply these conditions with $\kappa_0$ and $\kappa_N$. With the earlier definition of $\kappa_i\,(i = 1, ..., N-1)$, there are two parts of length $\delta s/2$ beyond the two extremities, where $\kappa$ is not defined. We use the boundary conditions on $\theta$ to define

$$\kappa_0 = \frac{2\theta_0}{\delta s}, \qquad s \in [s_0, s_0 + \delta s/2], \tag{2.6a}$$

$$\kappa_N = -\frac{2\theta_{N-1}}{\delta s}, \qquad s \in [s_N - \delta s/2, s_N]. \tag{2.6b}$$

To understand this, we add two spurious edges outside the domain of definition, with related angle $\theta_{-1}$ and $\theta_N$. Then $\theta(0) \approx (\theta_{-1} + \theta_0)/2 = 0$ and $\theta(s_N) \approx (\theta_{N-1} + \theta_N)/2 = 0$ gives the values of $\theta_{-1}$ and $\theta_N$, which can be used in the original definition of $\kappa_i$ and leads to the definition of $\kappa_0$ and $\kappa_N$.

With $\kappa_i$, we define the energy in the rod discretization as

$$\mathcal{E} = \frac{1}{2}\left\{\left(\frac{2\theta_0}{\delta s}\right)^2 \frac{\delta s}{2} + \left(\frac{-2\theta_{N-1}}{\delta s}\right)^2 \frac{\delta s}{2} + \sum_{i=1}^{N-1}\left(\frac{\theta_i - \theta_{i-1}}{\delta s}\right)^2 \delta s\right\}. \tag{2.7}$$

For $x_i$ and $y_i$, they are defined by equation (2.3c) and (2.3d) and the boundary conditions,

$$x_0 = 0, \quad x_{i+1} = x_i + \cos\theta_i, \qquad y_0 = 0, \quad y_{i+1} = y_i + \sin\theta_i, \qquad (i = 1, ..., N). \tag{2.8}$$

### 2.2.2 Super-Helices

The so-called *Super-Helices discretization* (Bertails et al., 2006) in 2D version relates discrete points by arcs of circle. More precisely, each edge has constant curvature $\kappa_i$, and $\theta_i$, $x_i$, $y_i$ (the local deflection and position) are defined at points. Different from the rod discretization, here $\kappa_i$ is used in the integrands to give the other kinematic variables, and we can directly express the energy of the system with $\mathcal{E} = \sum_i \frac{1}{2}\kappa_i^2 \delta s$.

We suppose the Elastica is equally separated into $N$ segments bounded by $N+1$ points (from $s_0 = 0$ to $s_N = 1$), see figure 2.2.

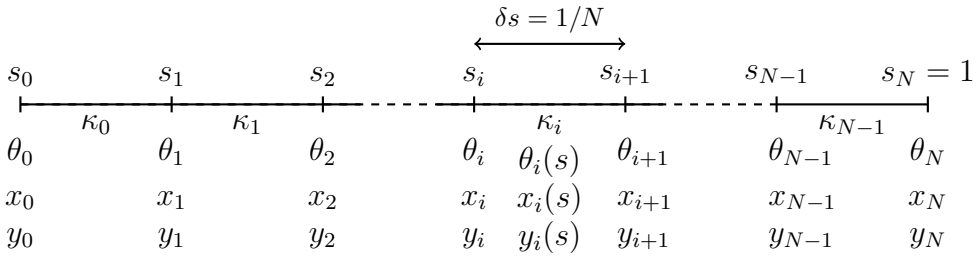


**Figure 2.2: Discretization Super-Helices**

The geometry can be recovered by numerical integration from the discretized curvature using equations (2.3a), (2.3c), and (2.3d).

As $\kappa_i$ is continuous per segment, the deflection $\theta$ is linear per segment, more precisely, from equation (2.3a):

$$\theta_i(s) = \theta_i + \int_{s_i}^{s'} \kappa_i \, ds' \qquad \rightarrow \qquad \begin{cases} \theta_i(s) = \theta_i + \kappa_i(s - s_i), & s \in [s, s_{i+1}] \\ \theta_{i+1} = \theta_i + \kappa_i \, \delta s \end{cases}, \tag{2.9}$$

where $\delta s$ is the length of each segment.

**Discretization variations** For equation (2.3c) and (2.3d), we have 3 different discretized versions. The first one is called the *trapezoidal integration*, as if $\cos\theta$ or $\sin\theta$ were linear on each segment, thus

$$x_{i+1} = x_i + \frac{1}{2}(\cos\theta_{i+1} + \cos\theta_i)\,\delta s, \qquad y_{i+1} = y_i + \frac{1}{2}(\sin\theta_{i+1} + \sin\theta_i)\,\delta s \tag{2.10}$$

The second one is called *Sinc integration*, derived from integrating equation (2.3c) and (2.3d) with $\theta_i(s)$ given by (2.9)

$$\begin{aligned} x_i(s) &= x_i + \int_{s_i}^{s'} \cos\theta_i(s) ds' = x_i + \int_{s_i}^{s'} \cos(\theta_i + \kappa_i(s' - s_i)) ds' \\ &= x_i + \frac{1}{\kappa_i}\left[\sin\left(\theta_i + \kappa_i(s - s_i)\right) - \sin\theta_i\right], \end{aligned} \tag{2.11a}$$

$$\begin{aligned} y_i(s) &= y_i + \int_{s_i}^{s'} \sin\theta_i(s) ds' = y_i + \int_{s_i}^{s'} \sin(\theta_i + \kappa_i(s' - s_i)) ds' \\ &= y_i - \frac{1}{\kappa_i}\left[\cos\left(\theta_i + \kappa_i(s - s_i)\right) - \cos\theta_i\right] \end{aligned} \tag{2.11b}$$

which leads to

$$x_{i+1} = x_i + (\sin\theta_{i+1} - \sin\theta_i)/\kappa_i, \qquad y_{i+1} = y_i - (\cos\theta_{i+1} - \cos\theta_i)/\kappa_i \tag{2.12}$$

The last one is the series expansion of the second one. Starting with

$$\begin{aligned} x_{i+1} &= x_i + (\sin(\theta_i + \kappa_i\delta s) - \sin\theta_i)/\kappa_i \\ &= x_i + \left[\sin\theta_i \frac{\cos(\kappa_i\delta s) - 1}{\kappa_i\delta s} + \cos\theta_i \frac{\sin(\kappa_i\delta s)}{\kappa_i\delta s}\right]\delta s \end{aligned} \tag{2.13}$$

$$\begin{aligned} y_{i+1} &= y_i - (\cos(\theta_i + \kappa_i\delta s) - \cos\theta_i)/\kappa_i \\ &= y_i - \left[\cos\theta_i \frac{\cos(\kappa_i\delta s) - 1}{\kappa_i\delta s} - \sin\theta_i \frac{\sin(\kappa_i\delta s)}{\kappa_i\delta s}\right]\delta s \end{aligned} \tag{2.14}$$



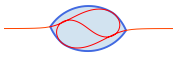

and using the series expansion

$$\frac{\sin x}{x} = 1 + \sum_{i=1}^{\infty} \frac{(-1)^i\, x^{2i}}{(2i+1)!}, \qquad \frac{\cos x}{x} = \sum_{i=1}^{\infty} \frac{(-1)^i\, x^{2i-1}}{(2i)!} \tag{2.15}$$

we can approximate the second integration with series to the order $n$, where $n$ is the maximum $i$ value in the truncated series (2.15). For example, for $n = 2$, we have

$$\begin{cases} \frac{\sin(\kappa_i \delta s)}{\kappa_i \delta s} & \approx 1 - \frac{(\kappa_i \delta s)^2}{6} + \frac{(\kappa_i \delta s)^4}{120} \\ \frac{\cos(\kappa_i \delta s) - 1}{\kappa_i \delta s} & \approx -\frac{\kappa_i \delta s}{2} + \frac{(\kappa_i \delta s)^3}{24} \end{cases} \implies$$
$$\begin{cases} x_{i+1} = x_i + \left[\sin\theta_i(-\frac{\kappa_i \delta s}{2} + \frac{(\kappa_i \delta s)^3}{24}) + \cos\theta_i(1 - \frac{(\kappa_i \delta s)^2}{6} + \frac{(\kappa_i \delta s)^4}{120})\right] \delta s \\ y_{i+1} = y_i - \left[\cos\theta_i(-\frac{\kappa_i \delta s}{2} + \frac{(\kappa_i \delta s)^3}{24}) - \sin\theta_i(1 - \frac{(\kappa_i \delta s)^2}{6} + \frac{(\kappa_i \delta s)^4}{120})\right] \delta s \end{cases} \tag{2.16}$$

### 2.2.3 Super-Clothoid

We introduce the *super-clothoid discretization*, but precise studies and numerical implementations can be found in the work of Bertails-Descoubes (2012), Casati (2015), and Raphaël Charrondière (2021).

For this discretization, the curvature is linear per segment, so each edge is an Euler spiral, also known as a clothoid or Cornu spiral, which gives the name Super-Clothoid. Figure 2.3 shows the discretization. As the curvature is linear per segment, we introduce $\eta_i$, constant per segment, such that

$$\kappa_i(s) = \kappa_i + \eta_i(s - s_i), \quad s \in [s_i, s_{i+1}]. \tag{2.17}$$

And $(\kappa_i, \theta_i, x_i, y_i)$ are defined at the nodes $s = s_i$.

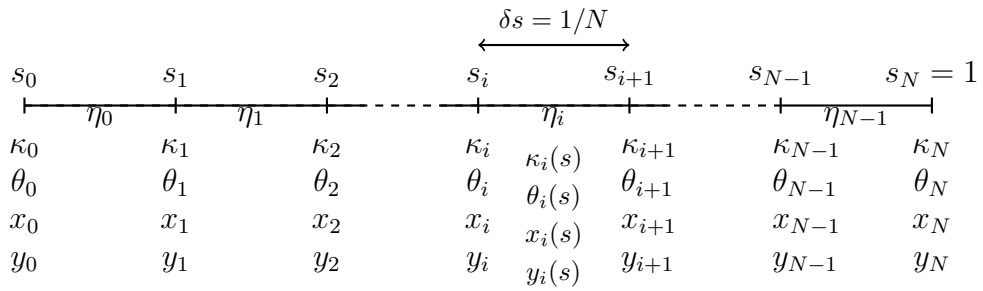


**Figure 2.3: Super-Clothoid Discretization**

With this definition, the total energy of the system is

$$\mathcal{E} = \sum_{i=1}^{N-1} \int_{s_i}^{s_{i+1}} \frac{1}{2} \left[\kappa_i + \eta_i(s - s_i)\right]^2 ds = \sum_{i=1}^{N-1} \kappa_i^2 \delta s + \eta_i \kappa_i \delta s^2 + \eta_i^{2/3} \delta s^3. \tag{2.18}$$

We can derive $\theta_i(s)$ by integrating (2.3a)

$$\theta_i(s) = \int_{s_i}^{s} \kappa_i(s')ds' = \theta_i + \kappa_i(s - s_i) + \frac{\eta_i}{2}(s - s_i)^2. \tag{2.19}$$

Integrating equations (2.3c) and (2.3d) is more difficult than for Super-Helices. We choose to use the Taylor expansion to approximate the exact expression, starting with

$$\begin{aligned}\frac{dx(s)}{ds} &= \cos\theta(s) = \cos\left(\theta_i + \kappa_i\tilde{s} + \frac{\eta_i}{2}\tilde{s}^2\right) \\ &= \cos\theta_i\left[\cos\left(\kappa_i\tilde{s}\right)\cos\left(\frac{\eta_i}{2}\tilde{s}^2\right) - \sin\left(\kappa_i\tilde{s}\right)\sin\left(\frac{\eta_i}{2}\tilde{s}^2\right)\right] \\ &- \sin\theta_i\left[\sin\left(\kappa_i\tilde{s}\right)\cos\left(\frac{\eta_i}{2}\tilde{s}^2\right) + \cos\left(\kappa_i\tilde{s}\right)\sin\left(\frac{\eta_i}{2}\tilde{s}^2\right)\right],\end{aligned} \tag{2.20a}$$

$$\begin{aligned}\frac{dy(s)}{ds} &= \sin\theta(s) = \sin\left(\theta_i + \kappa_i\tilde{s} + \frac{\eta_i}{2}\tilde{s}^2\right) \\ &= \sin\theta_i\left[\cos\left(\kappa_i\tilde{s}\right)\cos\left(\frac{\eta_i}{2}\tilde{s}^2\right) - \sin\left(\kappa_i\tilde{s}\right)\sin\left(\frac{\eta_i}{2}\tilde{s}^2\right)\right] \\ &+ \cos\theta_i\left[\sin\left(\kappa_i\tilde{s}\right)\cos\left(\frac{\eta_i}{2}\tilde{s}^2\right) + \cos\left(\kappa_i\tilde{s}\right)\sin\left(\frac{\eta_i}{2}\tilde{s}^2\right)\right],\end{aligned} \tag{2.20b}$$

where $\tilde{s} = s - s_i$.

The Taylor expansions of $\sin x$ and $\cos x$

$$\sin x = \sum_{n=0}^{\infty}\frac{(-1)^n}{(2n+1)!}x^{2n+1} = x - \frac{x^3}{3!} + \frac{x^5}{5!} - ... \tag{2.21a}$$

$$\cos x = \sum_{n=0}^{\infty}\frac{(-1)^n}{2n!}x^{2n} = 1 - \frac{x^2}{2!} + \frac{x^4}{4!} - ..., \tag{2.21b}$$

are used to write the Taylor expansions of the original expressions (2.20). For example, we consider the component $\cos\left(\kappa_i\tilde{s}\right)\cos\left(\frac{\eta_i}{2}\tilde{s}^2\right)$. Using Taylor expansion, it becomes a multiplication between two polynomials. Multiplying a $\tilde{s}^{2q}$-order term from the expansion of $\cos(\kappa_i\tilde{s})$ with a $(\tilde{s}^2)^{2p}$-order term from that of $\cos(\frac{\eta_i}{2}\tilde{s}^2)$ gives

$$\frac{(-1)^p}{(2p)!}\frac{(-1)^q}{(2q)!} \times \kappa_i^{2q}\left(\frac{\eta_i}{2}\right)^{2p}\tilde{s}^{4p+2q}. \tag{2.22}$$

Integrating it over $[s_i, s_{i+1}]$ gives

$$\frac{1}{4p+2q+1}\frac{(-1)^p}{(2p)!}\frac{(-1)^q}{(2q)!} \times \kappa_i^{2q}\left(\frac{\eta_i}{2}\right)^{2p}\delta s^{4p+2q+1}, \qquad \delta s = s_{i+1} - s_i. \tag{2.23}$$

In the same manner, we can have the Taylor expansion of the other components in (2.20) to any given order, then integrate to obtain $x$ and $y$.

### 2.2.4 Implementation and Mixed formulation

To solve the system as an optimization problem, we use the optimizer IPOPT from the Python package CasADi, which are introduced in section 1.3.2 and section 2.1 respectively. More precisely, we minimize the total energy for each discretization with boundary constraints. Note that the Lagrange multipliers of boundary condition $x(1)$ and $y(1)$ are respectively $P$ and $Q$ in the differential equation (2.3b)

For all the discretization schemes, there are basic variables from which we can deduce other variables through integration. For example, the basic variables are $\theta_i$ for the rod discretization, and $\kappa_i$ for the Super-Helices. Thanks to the computer algebra syntax of CasADi, we can define all the other variables from the basic variables and implement the model as an optimization problem



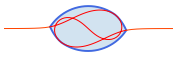

with only the basic variables. However, we can also define all the variables in the solver, integrate along each segment, and relate them by adding continuity constraints in the solver. Following the work of Blumentals (2017) and Raphaël Charrondière (2021), we call the former the *chained formulation* and the latter *mixed formulation*.

As we put our problem in form of an optimization problem, this method can also be understood as the *multiple-shooting* method. In fact, the integrations are used so that we can apply the boundary conditions at $s = 1$. This corresponds to the principle of shooting method that has been explained in section 1.5.2. The multiple shooting method is a variation of the shooting method. It divides the domain into several segments. The integration is accomplished over each segment, therefore giving the name 'multiple'. And we impose continuity conditions at the segment boundaries (nodes). Taking the Super-Helices discretization as example, with only basic variables, the discretized optimization problem of the chained formulation is

$$\begin{aligned} \min_{\kappa_i} \quad & \sum_i \frac{1}{2}\kappa_i^2 ds \\ \text{subject to} \quad & \theta_N[\kappa_i] = 0; \quad x_N[\kappa_i] = 1 - \Delta; \quad y_N[\kappa_i] = 0, \end{aligned}$$

where $\theta_N[\kappa_i]$, $x_N[\kappa_i]$ and $y_N[\kappa_i]$ are expressions of $\kappa_i$.

As for the mixed formulation, the discretized optimization problem is

$$\begin{aligned} \min_{\kappa_i,\theta_i,x_i,y_i} \quad & \sum_i \frac{1}{2}\kappa_i^2 \delta s \\ \text{subject to} \quad & \theta_{i+1} - \theta_i = \kappa_i \delta s \\ & x_{i+1} - x_i = \frac{1}{2}(\cos\theta_{i+1} + \cos\theta_i)\,\delta s \\ & y_{i+1} - y_i = \frac{1}{2}(\sin\theta_{i+1} + \sin\theta_i)\,\delta s \\ & \theta_0 = 0; \quad x_0 = 0; \quad y_0 = 0 \\ & \theta_N = 0; \quad x_N = 1 - \Delta; \quad y_N = 0. \end{aligned} \tag{2.24}$$

Note that the mixed formulation is reminiscent of the methods used in optimal control theory (Trélat, 2012), and detailed discussions can be found in Part II of the these of Blumentals, 2017. The implementation of this optimization problem in Python with CasADi can be found in appendix B.

Intuitively, one may think the mixed formulation takes more time to solve because more variables are introduced in the solver. However, in practice, using $N = 200$ discrete points, the same initial solution and the same solver options, we solved the Planar Elastica problem for a given $\Delta$ on the same computer using the chained formulation and the mixed formulation, and found that the chained formulation takes 1.13 second while the mixed formulation only takes 0.31 second.

Although the mixed formulation introduces more variables, the computational complexity of the mixed formulation is linear, while that of the chained formulation is almost cubic (Charrondière, Neukirch, and Bertails-Descoubes, 2024). As a consequence, when the number of elements is large, the mixed formulation needs much fewer computations, but for a small number of elements, the mixed formulation may be slower than the chained formulation, see section 5 of Charrondière, Neukirch, and Bertails-Descoubes, 2024.

Considering its good performance, we use the mixed formulation to implement different discretization schemes for the following analysis.



### 2.2.5 Results and discussions

To study the accuracy and the convergence of the different discretizations introduced in the former section, we solve the Planar Elastica problem with different schemes for several different numbers $N$ of mesh point, and compare the result with the analytical solution (see appendix C). We fix the end displacement to $\Delta = 0.2$, a value for which the maximum value of $\kappa(s)$ is around 5.85, according to the analytical results.

The accuracy is represented by the $L1$ error

$$\sum_{i=0}^{N} \frac{|u_{i,numerical} - u_{analytical}(s_i)|}{N} \tag{2.25}$$

where $u$ is one of the kinematics variables.

To ensure the comparability between different results, the solver is initialized (warm-start) with the same state, which is the linearized solution of Planar Elastica.

In figure 2.4, we show the solving time and the $L1$ errors for different variables as functions of $N$. Apart from the discretization schemes mentioned earlier, we also add the data generated by the 3D solver MERCI (Charrondière et al., 2020; Charrondière, Neukirch, and Bertails-Descoubes, 2024). This is a solver written in C++, which also uses the optimizer IPOPT, but applies the clothoid-based discretization strategy. It can be understood as an advanced 3D (curvature and twist) version of the Super-Clothoid discretization with higher-order expansion approximation. Generally speaking, the convergence rate of $\kappa$ error is nearly the same for all the schemes. As for $\theta$ error, the rod discretization and all the variations of the Super-Helices have the same convergence rate, but Trapeze integration and the rod discretization have a smaller error. The Super-Clothoid and MERCI have a higher convergence rate and also smaller errors than other schemes. For $x$ and $y$ errors, the convergence rate of the Sinc and Sinc expansion schemes is higher (i.e better) than for the $\theta$ error.

We remark that there is little difference in error magnitude and convergence rate between the trapezoidal integration of the Super-Helices and the rod discretization, the other schemes are more accurate and have higher order of convergence rate. It may seem strange as Super-Helices is a higher order scheme compared to the rod discretization. In fact, for the trapeze integration, we do not make use of $\theta_i(s)$ as a linear function along each segment, but only use its value at the nodes. This is approximately equivalent to considering $\theta$ constant per segment. For the Sinc and order 2 expansion Sinc expansion schemes, the error is smaller, and the convergence rate is higher. These two schemes have the same accuracy when $N$ is sufficiently large. It shows that even when the expansion order is small, we can have virtually the same accuracy as the original Sinc integration. In fact, when $\kappa_i$ is approaching zero, the sinc integration scheme may fail because $\kappa_i \delta s$ appears in the denominator. The Sinc expansion overcomes this inconvenience. Moreover, less computation time is needed for the order 2 Sinc expansion. For higher orders of Sinc expansion ($n \geq 3$), little difference can be observed with the original Sinc integration, even when $N$ is small. As for the solving time, the Sinc expansion needs more computation time when the order $n$ is increased, but it always runs faster than Sinc when $n$ remains moderate ($n < 6$).

Compared to the other schemes, Super-Clothoid provides the best accuracy under the same conditions. For dense discretization (large $N$), we need to change the default tolerance of IPOPT to allow the scheme to continue improving the accuracy. We illustrate this observation with figure 2.5. In figure 2.5, we also see that the scheme converges faster as the expansion order goes higher, but the order 5 expansion has the same accuracy as the order 10 expansion. In figure 2.4, we compare the order 4 Super-Clothoid expansion with the other schemes. It has nearly no difference from the error magnitudes of solver MERCI, except for very small $N$. In fact, when $n = 5$, no difference can be seen even for small $N$. This indicates that for the 2D problem of Planar



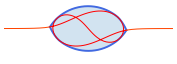

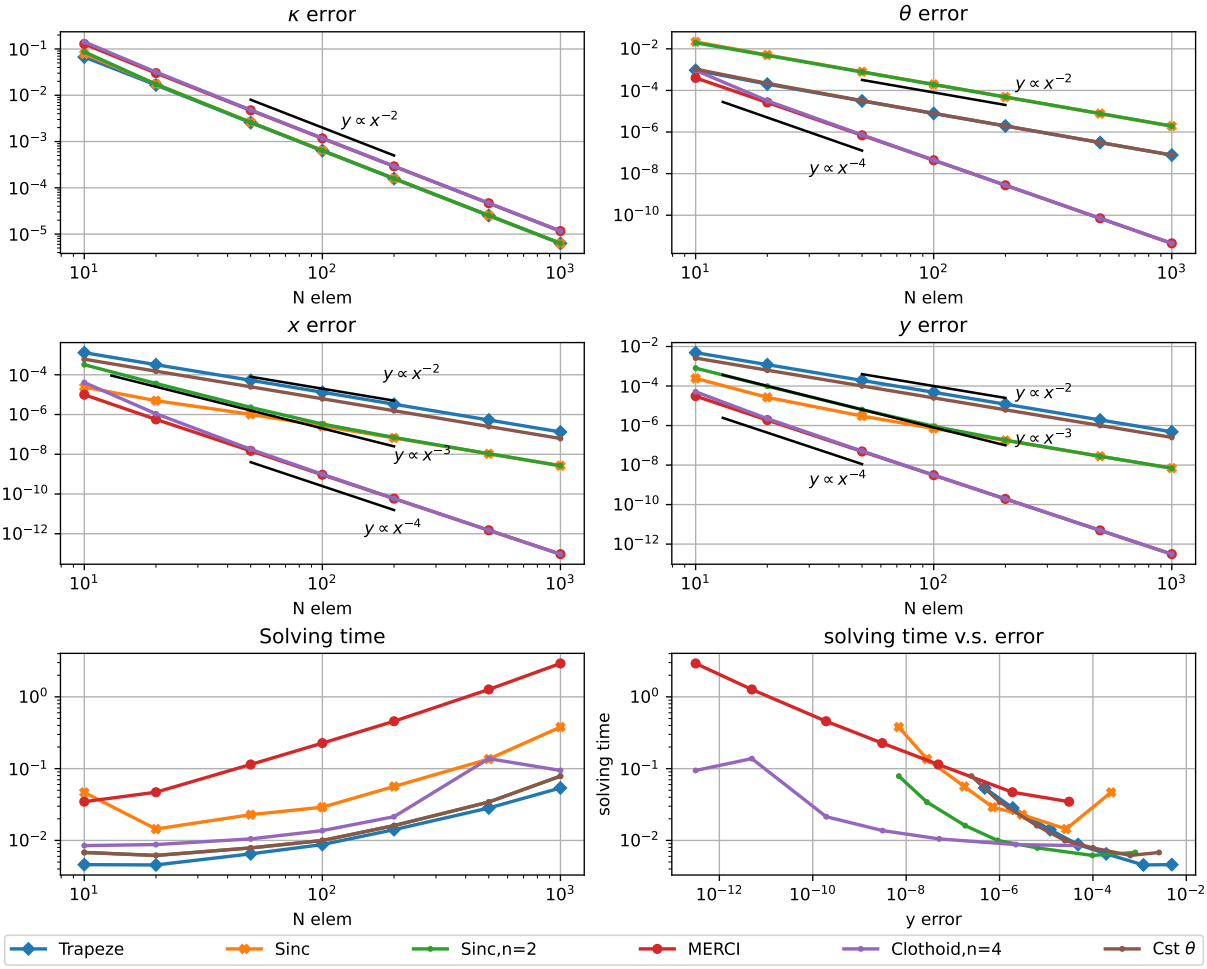


**Figure 2.4: Convergence study : comparison of different numerical integration schemes. *Trapeze*, *Sinc*, and *Sinc,n=2* are respectively the trapezoidal integration, Sinc integration, and the order 2 series expansion of the Sinc integration of the Super-Helices discretization. *MERCI* is the data from solver MERCI. *Clothoid,n=4* is the Super-Clothoid discretization with order 4 series expansion, and *Cst* $\theta$ is the rod discretization.**

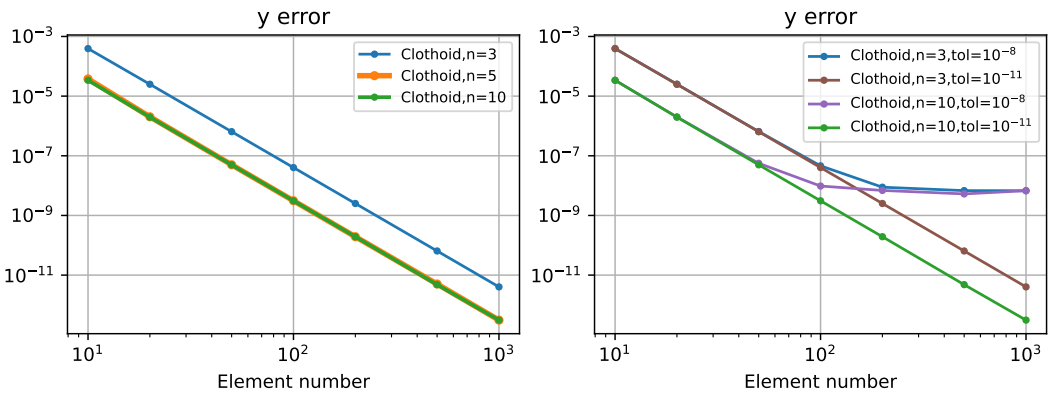


**Figure 2.5: The influence of the *tol* option of IPOPT.**

Elastica, good accuracy can be achieved by a small-order expansion, which saves computational time compared to the higher-order scheme provided by more advanced 3D solvers like MERCI.

As for the solving time, all our schemes need less time than solver MERCI, which is understandable because MERCI uses a higher-order scheme and solves an intrinsically 3D problem (more variables). Apart from MERCI, the Sinc integration is the longest to achieve convergence. This may be caused by the fact that $\kappa_i$ appears in the denominator. The time needed for Trapeze and Sinc expansion is nearly the same and is the smallest. The computational time for the order 4 expansion of Super-Clotoid is a little larger than the Sinc expansion and Trapeze integration, which is impressive as it provides much better accuracy. We remark that when the number of elements is very small, more time may be needed to find a converged solution. This is true for all the schemes, but not shown in figure 2.4.

Finally, the last figure reflects the performance of each scheme. A good integration scheme and a good choice of $N$ should have less error and should need less time to converge, that is lie near the lower left corner of the figure. With this standard, the order 4 expansion of Super-Clothoid is seen to have the best performance.



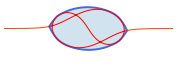

# Chapter 3

# Treatment of contact condition

Contact problems are of great importance for many real applications, including mechanical and civil engineering, as well as environmental and medical research. Most movements that we experience daily involve contact and friction, for example, the simple act of walking or running, driving cars and riding bicycles. In some systems, the nature and characteristics of the contact are in essence for delivering the loads and play a fundamental role in the resulting deformation of the structures. Such systems are often difficult to analyze because the area of the contact as well as the characteristics of friction are not known a priori. Adding the fact that these problems are usually nonlinear, it is difficult to characterize the mechanical aspects of these 'simple' movements.

Before the rapid rise and improvements of modern computer technology, such problems were often addressed by using simple assumptions to describe contact and friction. Nowadays, with the help of increasing computational power, one can deal with contact problems with better accuracy by applying the tools of computational mechanics. However, better accuracy, robustness and efficiency of the computational methods are still a challenge. Researchers are constantly developing new algorithms, and computational contact mechanics has emerged as its own discipline apart from standard computational mechanics (Kikuchi and Oden, 1988; Konyukhov and Izi, 2015; Wriggers, 2006).

Although friction is an important ingredient for contact mechanics, here we limit our discussions to the statics of frictionless contacts. As this thesis deals with slender structures, mainly rods and beams, we focus on the beam contact modelization.

## 3.1 Conditions for contact

When a mechanical system involves contact, one can formulate the contact via different approaches, including the strong formulation (directly finding equations for contact bodies using balance laws), the weak formulation (the approach based on variational principles), and a constrained optimization problem formulation.

The classical Signorini problem (Signorini, 1933) consists in finding the equilibrium of a linearly elastic body in contact with a frictionless rigid foundation, and it is a good example to discuss the general notions related to contact problems, and to show different formulations of contact conditions. For example, chapter 2 of Kikuchi and Oden (1988) and chapter 6 of Wriggers (2006) give the weak formulations of the Signorini problem, which is necessary to address the contact problem in finite element formulation. In the work of Houssein, Garnotel, and Hecht (2022) and Houssein, Garnotel, and Hecht (2019, 2023), the finite element method tool FreeFEM and the optimizer IPOPT are used to compute and solve the contact problem. Note that all of these formulations do not exclude each other, and one can certainly recover one formulation from another.

As we intend to use an optimizer to solve the contact problem, the geometry and kinematics



conditions are the most important ingredients to clearly define the non-penetration condition of the contact, and here we discuss these conditions in 2D.

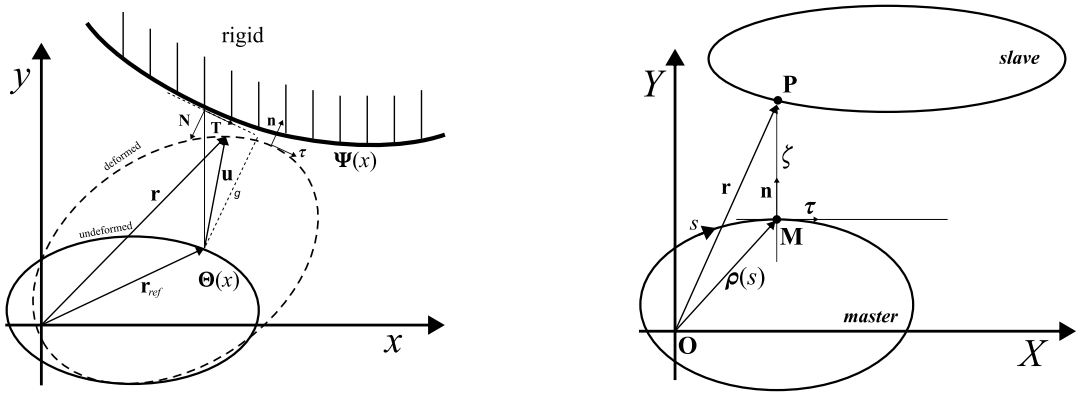


**(a) Contact with a rigid obstacle (Signorini)** **(b) Arbitrary two body contact problem**

**Figure 3.1: Geometry and kinematics of contact problems. Figures adapted from Konyukhov and Izi (2015)**

### 3.1.1 Non-penetration condition of Signorini problem

To begin with, we consider the classical Signorini problem, involving a contact with a rigid obstacle. In figure 3.1a we show the system geometry. The rigid obstacle is described by $y = \Psi(x)$, and the initial state of the deformable object is described by $y = \Theta(x)$. We note $\mathbf{u} = \{u(x), v(x)\}$ the displacement, such that a point $\{x, \Theta(x)\}$ at the initial state moves to $\{x + u, \Theta + v\}$ in the deformed configuration.

The non-penetration condition in the original and deformed configuration are respectively

$$\Theta(x) \leq \Psi(x), \tag{3.1}$$

$$\Theta(x) + v(x) \leq \Psi(x + u). \tag{3.2}$$

We can apply first order Taylor expansion on the second condition, and derive

$$\Theta - \Psi \leq -v + \Psi' u = \begin{pmatrix} u & v \end{pmatrix} \cdot \begin{pmatrix} \Psi' \\ -1 \end{pmatrix} = \mathbf{u} \cdot \mathbf{N}$$

where $\mathbf{N}$ is orthogonal to the tangent vector of the rigid obstacle. Introducing the unit normal vector of the obstacle $\mathbf{n}_{rig} = \mathbf{N}/|\mathbf{N}|$, we have

$$\frac{\Theta - \Psi}{\sqrt{1 + (\Psi')^2}} \leq \mathbf{u} \cdot \mathbf{n}_{rig} \Rightarrow -u_{n_{rig}} - g \leq 0 \tag{3.3}$$

where $u_{n_{rig}}$ is the projection of the displacement onto the normal direction $\mathbf{n}_{rig}$, and $g = \frac{\Psi - \Theta}{\sqrt{1+(\Psi')^2}}$ is the distance along $y$-axis also projected onto $\mathbf{n}_{rig}$, which is called *the normalized initial gap*. This condition can be interpreted as the non-penetration during the deformation. Please note that the normal of the deformable body and the normal of the obstacle coincides when they are in contact, that is $\mathbf{n}_{rig} + \mathbf{n} = 0$.

This condition correlates with the stress, with which we recover the KKT conditions obtained by the constrained optimization problem formulation. Supposing there is no friction, we introduce the stress vector, and split it into the normal and tangential part:

$$\boldsymbol{\sigma} = \sigma_n \mathbf{n} + \sigma_\tau \boldsymbol{\tau}, \tag{3.4}$$



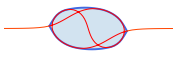

where $\mathbf{n}$ and $\boldsymbol{\tau}$ are the normal and tangential vectors shown in figure 3.1a. The KKT conditions are

$$\begin{cases} u_n - g = 0, \text{ and } & \sigma_n < 0 \quad \text{contact} \\ u_n - g < 0, \text{ and } & \sigma_n = 0 \quad \text{no contact} \end{cases} \Rightarrow \quad \begin{array}{l} \text{Complementary condition:} \\ (u_n - g)\sigma_n = 0 \end{array} \tag{3.5}$$

The Signorini problem is basic but important for computational contact mechanics. For more detailed discussions please refer to (Kikuchi and Oden, 1988).

### 3.1.2 The 'master-slave' approach and the detection of the closest point

In this part, we generalize the contact conditions for an arbitrary two body contact problem, in which the 'master-slave' approach is proved to be very efficient.

Suppose that we have two bodies in the global frame of coordinates $XOY$, shown in figure 3.1b. The two bodies are called respectively *the master* and *the slave*. Sometimes the 'master body' is also called the 'mortar part', and the 'slave body' is called the 'non-mortar part'. To understand the definition, the observer is placed on the master body, on which a local coordinate system is thus defined. Here we use its natural coordinate $s$, also known as the arc-length coordinate. A set of possible contact points on the slave body is monitored so that the two bodies will not penetrate into each other.

In the scope of this thesis, we are interested in the beam-to-beam contact, and Wriggers (2006) argues that the typical distinction in slave and master elements is not needed in this case, but we introduce this notion for the basic knowledge of contact problems, and also to present *the closest point project procedure*, which is related to the 'master-slave' approach. This procedure finds the point on the master body that has the smallest distance to the given slave point.

Suppose the surface of the master body is described by $\boldsymbol{\rho}(s) = \mathbf{OM}$, where $\mathbf{O}$ is the origin and $\mathbf{M}$ is a point on the master body. We would like to find the smallest distance between the master and a given point $\mathbf{P}$ of the slave body. We note vector $\mathbf{OP} = \mathbf{r}$, then finding the point on the master surface that is closest to $\mathbf{P}$ can be reformulated as

$$\text{Find } s, \text{ s.t. } \min_s F(s) = \frac{1}{2}||\mathbf{r} - \boldsymbol{\rho}(s)|| = \frac{1}{2}(\boldsymbol{\rho}(s) - \mathbf{r}) \cdot (\boldsymbol{\rho}(s) - \mathbf{r}). \tag{3.6}$$

At minimum, the derivative of $F(s)$ is zero, that is

$$(\boldsymbol{\rho}(s) - \mathbf{r})\frac{d\boldsymbol{\rho}}{ds} = 0 \Rightarrow (\boldsymbol{\rho}(s) - \mathbf{r}) \cdot \boldsymbol{\tau} = 0, \tag{3.7}$$

where $\boldsymbol{\tau}$ is the tangent vector at point $\mathbf{M}$. This condition means that the position vector of a slave point $\mathbf{r}$ can be expressed as

$$\mathbf{r}(s, \zeta) = \boldsymbol{\rho}(s) + \zeta\, \mathbf{n}. \tag{3.8}$$

where $\boldsymbol{n}$ is the normal vector at point $\mathbf{M}$. This expression is a transformation between the local coordinates $(s, \zeta)$ and the global coordinates $(X, Y)$, and it measures the contact interaction with local coordinates $(s, \zeta)$. The natural or arc-length coordinate $s$, is responsible for the tangential interactions, which is important for problems with friction, while $\zeta$ is related to the normal interaction. When $\zeta$ is positive, the two bodies are not in contact. When $\zeta$ is zero, the slave point $\mathbf{P}$ is on the contact boundary, and a negative $\zeta$ implies interpenetration.

Please note that one can easily reapply the conditions discussed in the Signorini problem to the 'master-slave' system.

## 3.2 Beam-to-beam contact

The conditions that we discussed previously are for general contact mechanics, but here the problems we are interested in involve mainly 1D slender structures. Hence, in this part, we focus on beam-to-beam contacts.

The contact problem of beams is important for science and engineering. Indeed, the main components of many systems are slender rods or fibers, typical examples include racquet strings, industrial webbing, woven fabrics, high-tensile ropes and cables, but also some biological systems such as hair (Daviet, Bertails-Descoubes, and Boissieux, 2011; Derouet-Jourdan et al., 2013), or biopolymer networks. These structures can be identified as 1D solids in space, and they can come into contact during the motion. Compared to contact between 2D or 3D solids, the geometry description of 1D curves in space leads to some specialities in beam-to-beam contact. In section 12.1 of reference Wriggers (2006), the contact kinematics between two beams with circular cross-sections in 3D space are described. The normal contact condition is based on the minimum distance between the two subjects, which is related to the non-penetration condition and the closest point project procedure that was mentioned previously. Further, the tangential contact conditions and the normal contact conditions between two beams with rectangular cross-sections are discussed. More details about the kinematical contact condition and the numerical algorithms can be found in the series work of Litewka and Wriggers (2002a), Litewka and Wriggers (2002b), Wriggers and Zavarise (1997), and Zavarise and Wriggers (2000), where they analyzed the frictional/frictionless contact between circular/rectangular cross-section beams.

When a beam-to-beam contact problem is implemented numerically, the applied numerical method may require particular treatment of the contact between discretized objects, for example, for finite element methods (FEM), the variation of the contact condition is required by the weak formulation. However, most of the numerical models and algorithms of contact have been proposed in a general sense, aiming to improve the detection of the contact point and the computation of the system reaction. A literature survey has been given in the review paper of Repupilli (2012), and several different conditions for beam-to-beam contact in 2D and 3D discretized systems were described. The most popular strategy dealing with slender 1D structures models the contact interaction as a discrete contact force acting on the closest point of the subject, thus it is called *the point-to-point contact formulation*. It is relatively straightforward to implement and has good computational efficiency. However, the existence of the closest point is not always guaranteed, especially when the contact angle is small. To manage this kind of situation, Durville (2005) introduced the notion *zones of approximation*, which are regions where contact may occur, defined by distance criteria. This is a kind of *the point-to-segment formulations*, which are more robust when several contact points exist simultaneously, for example in the case of entangled fibers.

The smoothness of the contact modelling is also a required feature for the development of the algorithm. Litewka (2007) adopted a mesh-smoothing technique for FEM, which adds continuous features to the contact algorithm. Crespel et al. (2024) provides a high-order detection scheme between two smooth curves which gives smoother force responses of the system in motion. Based on the point-to-segment formulation, Meier, Popp, and Wall (2016) proposed the *line-to-line formulation*, in which the contact force law is smooth, and the beam element is $C1$-continuous. In this case, the contact forces are distributed along the beam, which gives the name of the approach and is a robust model in the entire range of possible contact angles. In a later study Meier, Wall, and Popp (2017) proposed a novel formulation taking advantage of the long-existing point-to-point contact model and the line-to-line contact models.

Within the scope of this thesis, only the contact between two 1D objects in 2D space is considered. Although it is a simpler case compared to the literature mentioned previously, many notions and



ideas are adapted from them to improve the efficiency and robustness of our algorithm. Because our implementation uses an optimizer, we do not need to develop the variations of the contact condition as in finite element methods, and our focus lies on the contact kinematics, which are written as inequality constraints in the optimizer.

In the following, we present our contact detection and implementation for the 2D problems.

### 3.2.1 Implementation of the contact condition on beam segments

To solve contact problems by adding the non-penetration condition into the optimizer as inequality constraints, we have two principal ingredients: the detection of points which may come into contact, and the criteria preventing the penetration.


**(a) Detection, or monitoring** **(b) Criteria of segment contact**

**Figure 3.2: Detection and non-penetration condition for the beam segments**

The detection of possible contact points can be seen as the contact monitoring. To achieve this, we adapt the idea of *zones of approximation*. To explain in general terms, we iterate through nodes and segments in question and estimate the distance between each pair. If the distance is smaller than a given value, the node-segment pair is monitored in the following steps. In figure 3.2a, we illustrate the estimation of distance between the point $Q$ and a segment $\mathbf{P}_n\mathbf{P}_{n+1}$, which is the distance between $Q$ and the middle point of the segment. During the process of finding approaching pairs, we also define the position marker $k$ as

$$k = \text{Sign}\left[\mathbf{n}\cdot\mathbf{P_nQ}\right] = \text{Sign}\left[\begin{pmatrix}-(y_{n+1}-y_n)\\ x_{n+1}-x_n\end{pmatrix}\cdot\begin{pmatrix}x_q-x_n\\ y_q-y_n\end{pmatrix}\right], \tag{3.9}$$

where $\mathbf{n}$ is perpendicular to the segment. When $k=1$, the point $Q$ is on one side of vector $\mathbf{P}_n\mathbf{P}_{n+1}$ that is pointed by $\mathbf{n}$, and the other side if $k=-1$. For example, in figure 3.2a, $k=1$.

To explain the inequality constraints of the contact, we first consider two segments $A$ and $B$, shown in figure 3.2b.

Suppose the observer is placed on the segment $B$ and we require the segment $A$ to stay on one side of $B$, and not pass to the other side. Using the notion of 'master-slave' approach, the segment $B$ is the master body, the segment $A$ is the slave body, and we apply the non-penetration condition to a set of points on the slave body, for example the two ends of the segment $A$. Then, the non-penetration condition is

$$k(\mathbf{B}_1\mathbf{A}_1 \wedge \mathbf{B}_1\mathbf{B}_2) \geq 0 \tag{3.10a}$$
$$k(\mathbf{B}_1\mathbf{A}_2 \wedge \mathbf{B}_1\mathbf{B}_2) \geq 0 \tag{3.10b}$$

where $k=1$ or $-1$ is the position marker that we introduced earlier. These conditions mean that the two ends of $A$ stay on the same side as they were originally, not passing to the other side of $B$. Please remark that for each segment, several nodes may be monitored at the same time, and the same is true for each node.

The rest of this chapter show two examples in which we use the numerical contact conditions.

## 3.3 Example : Self-contact Elastica

Self-contact of slender structures such as flexible rods and filaments occurs in a family of problems, and different contact scenarios may occur, examples include knots (Gonzalez and Maddocks, 1999; Johanns et al., 2021) or coiling of biological filaments like DNA (Coleman and Swigon, 2004). Compared to these complex self-contact 3D systems, one simple and classical problem is the self-contact of the planar Elastica, which is discussed in (Flaherty and Keller, 1973), and for which a system of differential equations has been derived. We use this example to test our numerical method for treating beam-to-beam contact.

In figure 3.3, we illustrate the geometry of the system. This is the classical planar Elastica problem that has been discussed in section 1.5, but here we add a self-contact feature, preventing the self-intersection that happens when the end displacement $\Delta$ is large.

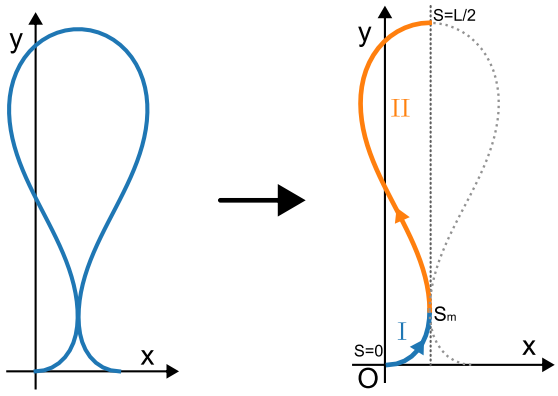


**Figure 3.3: Illustration of the self-contact of a planar Elastica**

In the first place, we derive the differential equations of the system such that the problem can be solved semi-analytically. The results will then be compared with the numerical implementation of the beam-to-beam contact formulation.

### 3.3.1 Analytical result

An Elastica with bending stiffness $EI$ and length $L$ is clamped at the two ends, which are pushed inwards with displacement control. We suppose the Elastica is already in self-contact, and thanks to the symmetry, we only consider half of the system. We use $s_m$ to mark the contact position, and the Elastica is separated into two parts: $s \in [0, s_m]$ and $s \in [s_m, L/2]$. With controlled displacement, we have the boundary conditions :

$$\theta(0) = \theta(L/2) = 0, \qquad x(0) = y(0) = 0, \qquad \theta(s_m) = \frac{\pi}{2}, \qquad x(L/2) = x(s_m) = \frac{L}{2}(1-\Delta) \quad (3.11)$$

The curvature $\kappa(s)$, the angle $\theta(s)$, and the horizontal and vertical positions $x(s)$ and $y(s)$ are all functions of the curvilinear coordinate $s$. They are related by:

$$\theta'(s) = \kappa(s) \qquad x'(s) = \cos\theta(s) \qquad y'(s) = \sin\theta(s) \quad (3.12)$$



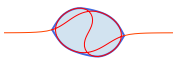

Only bending energy is taken into account for the system, so the total energy is

$$\mathcal{E} = \int_{s=0}^{s_m} \frac{EI}{2} \kappa^2(s)\, ds + \int_{s=s_m}^{L/2} \frac{EI}{2} \kappa^2(s)\, ds \tag{3.13}$$

We would like to minimize this energy under the geometrical constraints using the variational method on the Lagrangian which is constructed by the objective and the constraints with Lagrange multipliers. Computing the variation of Lagrangian and cancelling the terms before the variations of variables, $\bar{x}$, $\bar{\theta}$, and $\bar{s_m}$, we obtain the final system of differential equations with differential equations:

$$x'(s) = \cos\theta(s) \qquad s \in [0, s_m] \text{ if } i = 1 \tag{3.14a}$$
$$y'(s) = \sin\theta(s) \qquad s \in [s_m, L/2] \text{ if } i = 2 \tag{3.14b}$$
$$EI\theta''(s) = n_{xi} \sin\theta(s) \tag{3.14c}$$

competed with geometry constraints (3.12) and boundary conditions (3.11).

Remark that $n_{x1}$ and $n_{x2}$ can be different, indicating the existence of a force jump at the contact point $s_m$. Physically, this force is given by the counterpart due to contact. We note it as

$$F = [\![n_x]\!](s_m) = n_{x2} - n_{x1} \tag{3.15}$$

We solve this system using the shooting method introduced in section 1.5.2.

### 3.3.2 Implementation of the contact method with optimizer

The beam-to-beam contact formulation can also be applied to this system. We reformulate the problem as an optimization problem in order to minimize the elastic energy in the presence of boundary conditions and inequality constraints for the non-penetration condition.

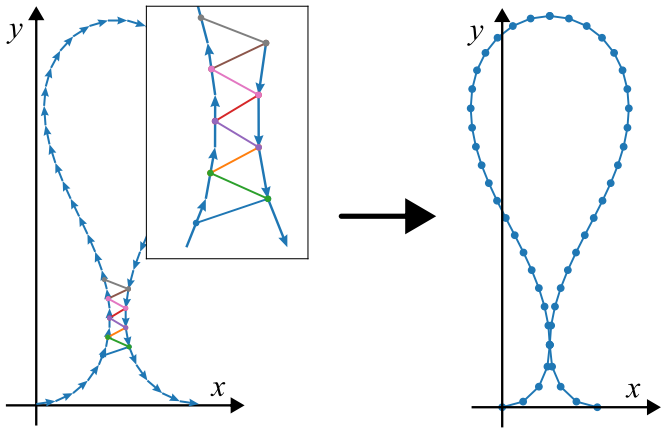


**Figure 3.4: Detection of possible self-contact positions**

Firstly, we adimensionalize the system ($EI = 1$ and $L = 1$) and we discretize the beam into $N$ segments, each segment is associated with $\kappa_i$ and each node with $(\theta_i, x_i, y_i)$, as in the super-helices discretization scheme presented in section 2.2.2. The basic optimization formulation is the same as the planar Elastica problem, but we then add the inequality constraints for the non-penetration conditions.

Figure 3.4 is an illustration of the implementation of our beam-to-beam contact condition on the problem of the self-contacting Elastica. The simulation uses the continuation method with

regard to the displacement $\Delta$. We initiate the system before the occurrence of self-contact, for example the left side of figure 3.4 is a possible initial condition. At this stage, we iterate through segments on the left part of the beam, and for each segment we estimate the distance between the segment and each node on the right part, as mentioned in the previous part. If the distance is smaller than the given criterion, we calculate the position marker with (3.9), and save it with the node-segment pair. For the next step of the continuation, we add the non-penetration condition (3.10) as an inequality constraint, in addition to the basic constraints for the mixed formulation and the boundary conditions. After the solver converges, we refresh the monitored pairs according to the current geometry and consequently change the non-penetration inequality constraints.

### 3.3.3 Results and discussions

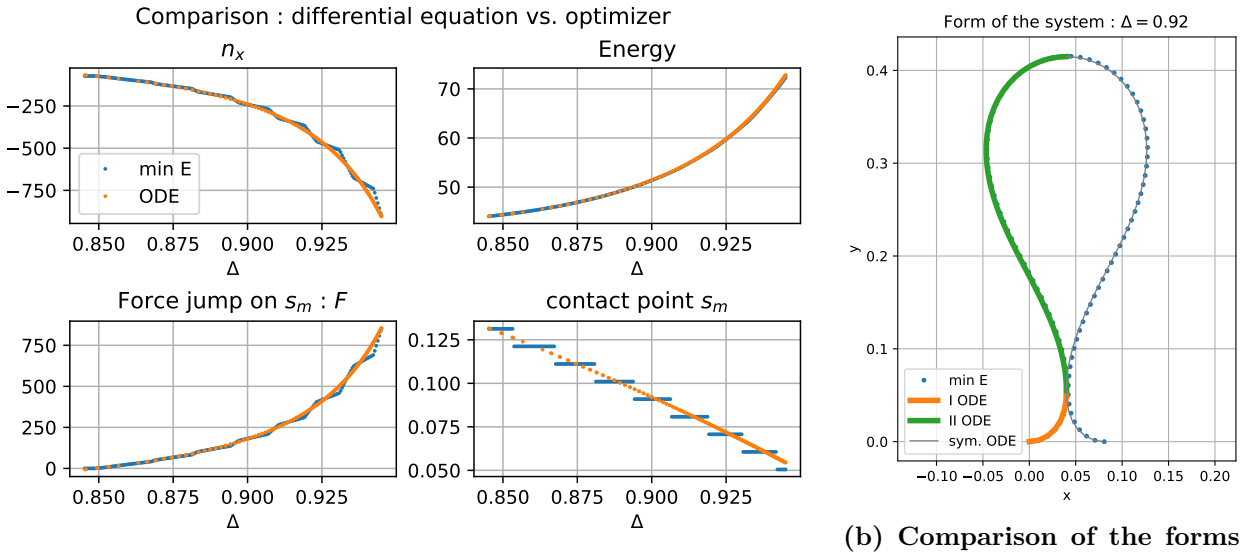


**(a) Comparison of variable values as a functions of $\Delta$**

**(b) Comparison of the forms of the Elastica**

**Figure 3.5: Comparison of the results found by the two methods**

In figure 3.5, we show the results found by the semi-analytical approach (shooting), and compare them to the results of the optimization formulation on the discretized system, with our beam-to-beam contact conditions. In figure 3.5a we compare the values of compression force $n_{x1}$, total energy of the system, the force jump, and the contact point position $s_m$, as functions of $\Delta$. All the results found by the two methods are coherent. However, the results obtained by the discretized system are slightly staggered, especially the $s_m(\Delta)$ curve which has steps. This is due to the non-smoothness related to the discretized system. In fact, the contact position is detected by the closest pair of node-segment, which is not continuous by nature. We chose our method rather for simplicity and efficiency, however more acurate results could be obtained using more sophisticated algorithms from the literature (see section 3.2) In figure 3.5b, the forms of the system found by the 2 methods for a given $\Delta$ value are superimposed upon each other. This comparison also shows good consistency between the 2 methods.

With this relatively simple problem of a beam-to-beam contact problem in 2D, we proved the validity of our implementation of contact conditions as inequality constraints.



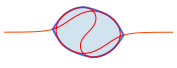

## 3.4 Example: a flexible fiber growing in a deformable ring

In the previous example, there is only one contact point and the monitored contact zone is rather small. Here we give another example in which a large contact zone may appear. A flexible fiber with length $l$ and bending stiffness $k_-$ is inserted into an elastic ring with radius $R$ and bending stiffness $k_+$, see figure 3.6. This problem has been studied by Cutolo et al., 2023 using analytical, experimental, and numerical (FEM) approaches. We would like to use it to test our method of beam-to-beam contact in the case of a broader range of contact length between two beams in 2D.

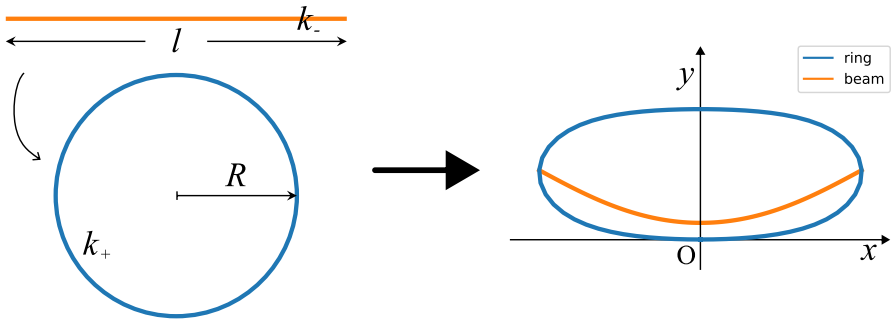


**Figure 3.6: Geometry setup: a flexible fiber in a deformable ring**

After non-dimensionalization by the radius of the ring $R$ and the bending stiffness of the fiber $k_-$, there are two parameters to define the system: $\Lambda = k_+/k_-$ and $\mu = l/R$, which are the ratio between the bending stiffness of the ring and the fiber, and ratio between the length of the fiber and the radius of the ring.

### 3.4.1 Numerical implementation

We discretize the system, and use the optimizer to minimize the total energy of the system with all constraints. More precisely, the ring is discretized into $n$ segments. The middle point of fiber is fixed on the $y$-axis, and the fiber is discretized into $m$ segments at each side, that are $2m$ segments in total. We have chosen $n = 60$ and $m = 60$ in this study. The super-helices discretization scheme is again used, and the geometric variables are the curvature $\kappa_{(\cdot)}$, the deflection $\theta_{(\cdot)}$, the positions $(x_{(\cdot)}, y_{(\cdot)})$, where $(\cdot) = f$ (fiber) or $r$ (ring). The optimization problem to solve is

$$\min \quad \mathcal{E}_{tot} = \mathcal{E}_r + \mathcal{E}_f = \sum_{i=1}^{n} \frac{\Lambda}{2} \kappa_{r_i}^2 \delta s_r + \sum_{i=1}^{2m} \frac{1}{2} \kappa_{f_i}^2 \delta s_f, \tag{3.16a}$$

$$\text{with } \delta s_r = 2\pi/n \text{ and } \delta s_f = \mu/(2m), \tag{3.16b}$$

$$\text{subject to} \quad \text{geometric conditions of the mixed formulation,} \tag{3.16c}$$

$$x_{r_0} = y_{r_0} = x_{r_n} = y_{r_n} = 0, \quad \theta_{r_0} = 0, \quad \theta_{r_n} = 2\pi, \tag{3.16d}$$

$$x_{f_m} = 0, \quad \theta_{f_m} = 0, \tag{3.16e}$$

$$\text{inequality constraints for the contact} \tag{3.16f}$$

Please note that to ensure a good convergence of the solver, we add auxiliary constraints to block some degrees of freedom which may lead to degenerate states. These are the mirror images or symmetric counterparts. Example of the auxiliary constraints include $\theta_{f_{m+1}} \geq 0$, $y_{r_i} > 0$.

As in the self-contact Elastica problem, we monitor the approaching node-segment pairs at each step, and refresh the inequality constraints if there is any change in the registered pairs. But

in this problem, there are two subjects, the ring and the beam, and we need to treat the fiber-ring contact and the self-contact of the fiber at the same time. To do so, we add the monitoring algorithm into the continuation procedure, which goes as

**Continuation algorithm with contact monitoring:**
**Initial**: staring at one state $\mathbf{X}_0$ with less contact zones, detecting the possible node-segment contact pairs $(\mathbf{N}, \mathbf{S})_0$.
**for** each given $\mu_i$ ($\mu$ increases gradually):
Initiate optimizer with $\mathbf{X}_{i-1}$, the solution of the previous step
Solve with the inequality constraints related to $(\mathbf{N}, \mathbf{S})_{i-1}$, find $\mathbf{X}_i$
Detect the possible contact pairs $(\mathbf{N}, \mathbf{S})_i$ with the new solution
**Repeat** until $(\mathbf{N}, \mathbf{S})_{i-1}$ and $(\mathbf{N}, \mathbf{S})_i$ are the same, or the iteration number reaches max:
$(\mathbf{N}, \mathbf{S})_{i-1} \leftarrow (\mathbf{N}, \mathbf{S})_i$, and reset the contact constraints
Solve again with initialization $\mathbf{X}_i$ to find $\mathbf{X}_{new}$
$\mathbf{X}_i \leftarrow \mathbf{X}_{new}$, and reset $(\mathbf{N}, \mathbf{S})_i$ with the new solution

### 3.4.2 Results and discussions

Being a validation test for our beam-to-beam contact treatment, we did not carry out a deep investigation as the original study of Cutolo et al., 2023. In this part, we only show some forms found by our implementation with different values of parameter $\Lambda$ and $\mu$, see figure 3.7. These solutions meet the non-penetration condition and are comparable with the results found in the original study, thus proving our method's ability to treat complex contact conditions, including point contact and zone contact.

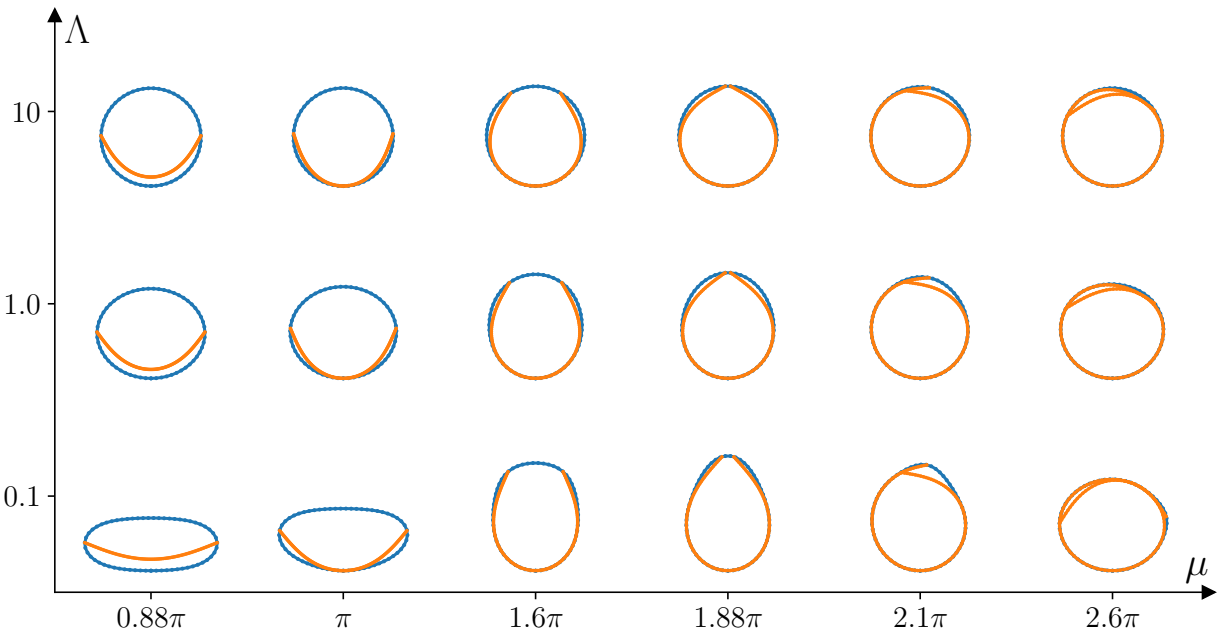


**Figure 3.7: The results found by our algorithm. From left to right, the length of the fiber becomes larger, and from top to bottom, the ring becomes softer.**



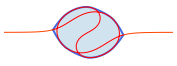

# Chapter 4

# Related concepts

## 4.1 Phase transition

When *phase change* is mentioned, one often thinks about the changes among the states of matters, for example the melting or vaporization. However, phase transition can also occur to some solids, for example the shape-memory alloys. Depending on the microstructure, the same chemical components can exhibit different mechanical properties, and during phase change, the microstructures transform from one to another.

From a macroscopic point of view, the phase transition is related to a non-convex energy potential. In the 19th century, Clerk-Maxwell (1875) proposed an explanation of two phases coexistence in real gas model by considering the stability of the system. His method is now known as the *equal-area construction*, also called the *Maxwell construction*. The theory is not limited to thermodynamics and applies to the broader case of systems exhibiting phase transition, including materials that have non-monotone strain-stress curve corresponding to non-convex elastic potential. Ericksen (1975), one of the pioneers of these studies, showed that a bar with non-monotone strain-stress can have several configurations during deformation, including the phase transition behavior. In section 1.6 of (Bigoni, 2012), examples of elasto-plastic non-linear spring systems are given. While one such spring already exhibits phase transition behavior, the chain composed by three springs has more intricate bifurcation curves and stability properties.

To simply describe the phenomenon, during phase transition, there are two phases of different strain, but the stress is identical in the two phases. As the deformation grows larger, the strain and stress of each phase stay the same, but the proportion of each phase changes to meet the prescribed displacement.

In this section, we explain the phase transition with a simple example of a two-phases beam, inspired by the work of Marko (2007) which treats the coexistence of different deformation states of the DNA molecule.

### 4.1.1 System description

Suppose a beam deforms under displacement control, figure 4.1a. We assume that two possible phases with different elastic potentials can be adopted by the beam, with:

$$\text{Phase 1 (elastic energy per unit length):} \qquad w_1(\varepsilon_1) = \frac{1}{2} E_1 \varepsilon_1^2 \tag{4.1a}$$

$$\text{Phase 2 (elastic energy per unit length):} \qquad w_2(\varepsilon_2) = \delta + \frac{1}{2} E_2 \varepsilon_2^2 \tag{4.1b}$$

where $E_i$ ($i = 1$ or 2) is the modulus of elasticity in tension or compression, $\varepsilon_i$ ($i = 1$ or 2) is the axial strain and $\delta$ is an energy per unit length associated with the phase transition. In phase 2 the

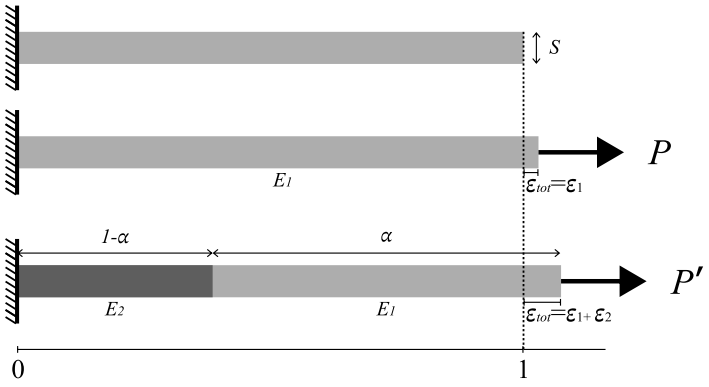


(a) System configuration

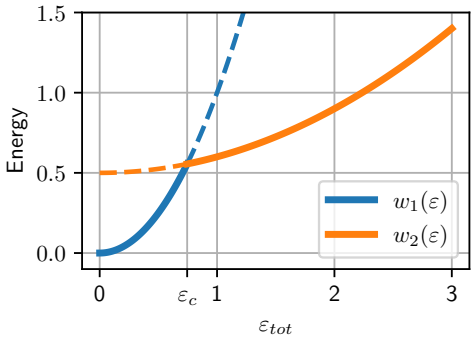


(b) Energy potentials of the two phases

**Figure 4.1: Phase transition: a two-phase beam.**

material becomes more flexible, that is $E_2 < E_1$. As physical systems tend to adopt states with minimal energy, the potential energy of the system can also be considered as a piecewise function

$$w(\varepsilon) = \begin{cases} w_1(\varepsilon) & 0 \le \varepsilon \le \varepsilon_c \\ w_2(\varepsilon) & \varepsilon_c \le \varepsilon \end{cases}, \tag{4.2}$$

where $\varepsilon_c = \sqrt{2\delta/(E_1 - E_2)}$ is the point where the two energy potential curves intersect. Note that this is a non-convex function, which allows the application of Maxwell's construction.

To better illustrate the behaviors of the system, numerical values are applied to parameters related to material properties:

$$E_1 = 2; \quad E_2 = 0.2; \quad \delta = 0.5,$$

and the energy-strain relations are presented in figure 4.1b.

### 4.1.2 Analysis from energy minimization

We suppose the original length of the beam is 1, and the beam extends to $1+\varepsilon$ under displacement control. We use $\alpha$ to indicate the fraction of the two phases, where $\alpha$ is the proportion of phase 1, and $(1-\alpha)$ is that of phase 2. The total energy of the system is the elastic energy of the beam, which is:

$$\mathcal{E}_{tot}(\alpha, \varepsilon_1, \varepsilon_2) = \alpha\frac{1}{2}E_1\varepsilon_1^2 + (1-\alpha)(\delta + \frac{1}{2}E_2\varepsilon_2^2). \tag{4.3}$$

The displacement control is considered as an equality constraint $\alpha\varepsilon_1 + (1-\alpha)\varepsilon_2 = \varepsilon_{tot}$. Because $\alpha$ should be between 0 and 1, we also add the two inequality constraints $\alpha \ge 0$ and $1-\alpha \ge 0$.

Using the optimization theory, we introduce the Lagrangian with unknown variables $\alpha$, $\varepsilon_1$, $\varepsilon_2$:

$$\mathcal{L}(\alpha, \varepsilon_1, \varepsilon_2) = \mathcal{E}_{tot}(\alpha, \varepsilon_1, \varepsilon_2) - \sigma_e(\alpha\varepsilon_1 + (1-\alpha)\varepsilon_2 - \varepsilon_{tot}) - g\alpha - h(1-\alpha), \tag{4.4}$$

where $\sigma_e$, $g$ and $h$ are Lagrange multipliers.

Applying KKT condition to the problem, we have:

$$\frac{\partial\mathcal{L}}{\partial\varepsilon_1} = \alpha(E_1\varepsilon_1 - \sigma_e) = 0, \tag{4.5a}$$

$$\frac{\partial\mathcal{L}}{\partial\varepsilon_2} = (1-\alpha)(E_2\varepsilon_2 - \sigma_e) = 0, \tag{4.5b}$$

$$\frac{\partial\mathcal{L}}{\partial\alpha} = (\frac{1}{2}E_1\varepsilon_1^2 - \frac{1}{2}E_2\varepsilon_2^2 - \delta) - \sigma_e(\varepsilon_1 - \varepsilon_2) - g + h = 0, \tag{4.5c}$$



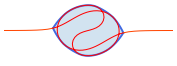

$$\varepsilon_{tot} = \alpha\varepsilon_1 + (1-\alpha)\varepsilon_2, \tag{4.5d}$$
$$0 = g\alpha, \qquad g \geq 0, \qquad \alpha \geq 0, \tag{4.5e}$$
$$0 = h(1-\alpha) \qquad h \geq 0, \qquad 1-\alpha \geq 0. \tag{4.5f}$$

Solving this system consists of considering three cases: $\alpha = 1$, $\alpha = 0$, and $0 < \alpha < 1$.

**Mono-phase cases** When $\alpha = 1$ or 0, the beam only has one phase, and we call them mono-phase cases.

For $\alpha = 0$, the beam is entirely in phase 2, and the relations (4.5a) and (4.5e) are automatically satisfied. Other equations give:

$$\varepsilon_2 = \varepsilon_{tot}; \quad \sigma_e = E_2\varepsilon_{tot}; \quad h = 0; \tag{4.6a}$$
$$g = \frac{1}{2}E_1\varepsilon_1^2 - E_2\varepsilon_{tot}\varepsilon_1 + \frac{1}{2}E_2\varepsilon_{tot}^2 - \delta \geq 0. \tag{4.6b}$$

Note that $\varepsilon_1$ can have any value between 0 and $\varepsilon_c$. For some imposed displacement $\varepsilon_{tot}$, (4.6b) may be violated by an admissible $\varepsilon_1$. This fact leads to the range of $\varepsilon_{tot}$ that has a stable solution of mono-phase-2 state.

We define the function

$$g(\varepsilon_1) = \frac{1}{2}E_1\varepsilon_1^2 - E_2\varepsilon_{tot}\varepsilon_1 + \frac{1}{2}E_2\varepsilon_{tot}^2 - \delta.$$

and we study its sign. When the discriminant is negative, $g \geq 0$ is always satisfied, that is when

$$(E_2\varepsilon_{tot})^2 - E_1\left(E_2\varepsilon_{tot}^2 - 2\delta\right) \leq 0, \quad \Rightarrow \quad \varepsilon_{tot} \geq \sqrt{\frac{2E_1\delta}{E_2(E_1-E_2)}} = \frac{\sqrt{2E_e\delta}}{E_2} > \varepsilon_c,$$

with $E_e = \frac{E_1E_2}{E_1-E_2}$.

When the discriminant is positive, i.e. $\varepsilon_{tot} < \frac{\sqrt{2E_e\delta}}{E_2}$, the equation $g(\varepsilon_1) = 0$ has 2 real solutions

$$\varepsilon_1^{\pm} = \frac{E_2\varepsilon_{tot} \pm \sqrt{2E_1\delta - (E_1-E_2)E_2\varepsilon_{tot}^2}}{E_1}.$$

Consequently, to ensure $g(\varepsilon_1) \geq 0$ for all $\varepsilon_1 \in [0, \varepsilon_c]$, we would need $\varepsilon_1^+ \leq 0$ or $\varepsilon_1^- \geq \varepsilon_c$. Both conditions are impossible, as $\varepsilon_1^+$ is evidently positive, and $\varepsilon_1^- < \sqrt{\frac{E_2}{E_1}}\varepsilon_c < \varepsilon_c$.

To conclude, the mono-phase-2 state can be established when $\varepsilon_{tot} \geq \frac{\sqrt{2E_e\delta}}{E_2}$.

When $\alpha = 1$, the beam is totally in phase 1, and the relation (4.5b) and (4.5f) are automatically satisfied. Other equations give:

$$\varepsilon_1 = \varepsilon_{tot}; \quad \sigma_e = E_1\varepsilon_{tot}; \quad g = 0; \tag{4.7a}$$
$$h = \frac{1}{2}E_1\varepsilon_{tot}^2 + \frac{1}{2}E_2\varepsilon_2^2 + \delta - E_1\varepsilon_{tot}\varepsilon_2 \geq 0. \tag{4.7b}$$

With the same argument as earlier, $\varepsilon_2$ can have any value larger than $\varepsilon_c$, so (4.7b) may be violated depending on the value of $\varepsilon_{tot}$. The analysis on the quadratic function $h(\varepsilon_2)$ leads to the conclusion that a stable mono-phase-1 state can be established when $\varepsilon_{tot} \leq \sqrt{2E_e\delta}/E_1$.

**Two phases coexist** When $1 \geq \alpha \geq 0$, phase 1 and phase 2 coexist in the beam. Equations (4.5a), (4.5b), (4.5e) and (4.5f) give:

$$\varepsilon_1 = \sigma_e/E_1; \quad \varepsilon_2 = \sigma_e/E_2; \quad g = 0; \quad h = 0. \tag{4.8}$$

Injecting these expressions into equation (4.5c) and we have:

$$\delta = \frac{\sigma_e^2}{2}\left(\frac{1}{E_2} - \frac{1}{E_1}\right) = \frac{\sigma_e^2}{2E_e} \qquad \Rightarrow \qquad \sigma_e = \sqrt{\frac{2\delta}{1/E_2 - 1/E_1}} = \sqrt{2\delta E_e} \tag{4.9}$$

with $E_e = \frac{E_1 E_2}{E_1 - E_2}$.

The Lagrange multiplier $\sigma_e$ is identified to be the uniform stress in the beam. $E_e$ is called the equivalent modulus of elasticity, which is a constant, depending only on material properties. When phases 1 and 2 coexist, $\sigma_e$ and the strains $\varepsilon_1$, $\varepsilon_2$ stay the same during phase transition.

Using expression (4.5d), we obtain the fraction indicator $\alpha$:

$$\alpha = \frac{\varepsilon_2 - \varepsilon_{tot}}{\varepsilon_2 - \varepsilon_1} = \frac{E_e}{E_2} - \varepsilon_{tot}\frac{E_e}{\sigma_e} \tag{4.10}$$

Setting $\alpha \to 0$ and $\alpha \to 1$, we obtain the limits between mono-phase and two-phase cases

$$\varepsilon_A = \varepsilon_{tot}|_{\alpha\to 1} = \varepsilon_1|_{1\geq\alpha\geq 0} = \frac{\sqrt{2\delta E_e}}{E_1}, \quad \varepsilon_B = \varepsilon_{tot}|_{\alpha\to 0} = \varepsilon_2|_{1\geq\alpha\geq 0} = \frac{\sqrt{2\delta E_e}}{E_2}. \tag{4.11}$$

We recover the same limits as before. When $\varepsilon_{tot}$ is smaller than $\varepsilon_A$, only phase 1 exists. In contrast, only phase 2 exists when $\varepsilon_{tot}$ is larger than $\varepsilon_B$.

Using these results, the elastic energy as a function of imposed displacement in case $1 \geq \alpha \geq 0$ can be expressed as the following:

$$w_1(\varepsilon_1) = \frac{1}{2}E_1\varepsilon_1^2 = \frac{\sigma_e^2}{2E_1} = \frac{E_e}{E_1}\delta \tag{4.12a}$$

$$w_2(\varepsilon_2) = \delta + \frac{1}{2}E_2\varepsilon_2^2 = (\frac{E_e}{E_2} + 1)\delta \tag{4.12b}$$

$$\mathcal{E}_{tot}(\alpha, \varepsilon_1, \varepsilon_2) = \sigma_e\varepsilon_{tot} - \delta\frac{E_2}{E_1 - E_2} \tag{4.12c}$$

with the constant $\sigma_e$ given by equation (4.9)

Equation (4.12c) is a linear expression of $\varepsilon_{tot}$, so when phase 1 and 2 coexist, the energy varies linearly with the imposed displacement $\varepsilon_{tot}$, not quadratically as in the mono-phase cases.



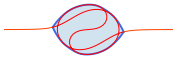

### 4.1.3 Solution and interpretations

Assembling the results of the different cases, the fraction $\alpha$, the elastic energy $\mathcal{E}_{tot}$, and the internal elastic stress can be expressed as a piecewise functions of $\varepsilon_{tot}$:

$$\alpha(\varepsilon_{tot}) = \begin{cases} 1 & (\varepsilon_A \geq \varepsilon_{tot} \geq 0) \\ \dfrac{E_e}{E_2} - \varepsilon_{tot}\sqrt{\dfrac{E_e}{2\delta}} & (\varepsilon_B \geq \varepsilon_{tot} \geq \varepsilon_A) \\ 0 & (\varepsilon_{tot} \geq \varepsilon_B) \end{cases} \tag{4.13a}$$

$$\mathcal{E}_{tot}(\varepsilon_{tot}) = \begin{cases} \dfrac{1}{2}E_1\varepsilon_{tot}^2 & (\varepsilon_A \geq \varepsilon_{tot} \geq 0) \\ \sqrt{2\delta E_e}\varepsilon_{tot} - \delta\dfrac{E_2}{E_1 - E_2} & (\varepsilon_B \geq \varepsilon_{tot} \geq \varepsilon_A) \\ \dfrac{1}{2}E_2\varepsilon_{tot}^2 + \delta & (\varepsilon_{tot} \geq \varepsilon_B) \end{cases} \tag{4.13b}$$

$$\sigma(\varepsilon_{tot}) = \begin{cases} E_1\varepsilon_{tot} & (\varepsilon_A \geq \varepsilon_{tot} \geq 0) \\ \sqrt{2\delta E_e} & (\varepsilon_B \geq \varepsilon_{tot} \geq \varepsilon_A) \\ E_2\varepsilon_{tot} & (\varepsilon_{tot} \geq \varepsilon_B) \end{cases} \tag{4.13c}$$

The analytical results are compared with numerical results found by the numerical optimizer `scipy.optimize.minimize`, in Python using the SLSQP (Sequential Least Squares Programming) optimization method. Figure 4.2 compares the theoretical and analytical results for the elastic energy and the stress. There is a good consistency between theory and numerical values.

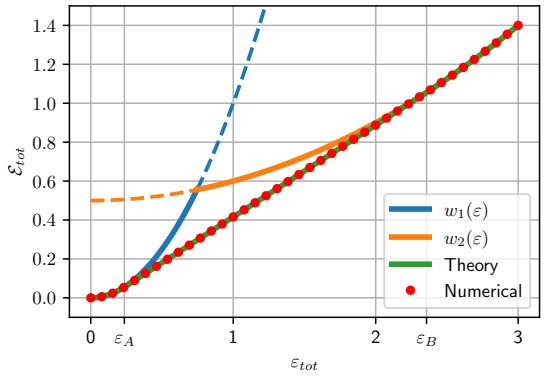


**(a) Energy as a function of the imposed displacement.**

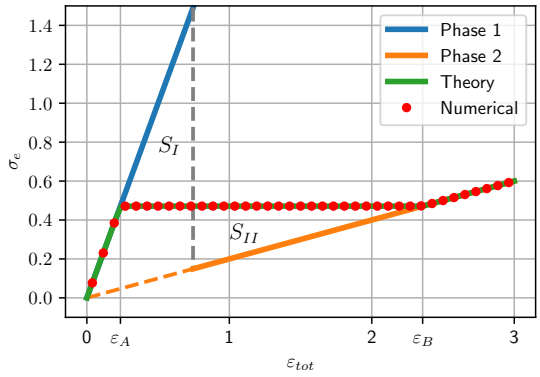


**(b) Stress $\sigma_e$ as a function of the imposed displacement.**

**Figure 4.2: Analytical and numerical results of the phase transition problem**

Our analysis shows that the non-convex potential energy (4.2) gives rise to a phase transition, during which the stress $\sigma_e$ remains constant and is uniform along the beam. This is reflected by the horizontal line in figure 4.2b, known as the *Maxwell line*, separating the non-monotonous stress-strain curve into zones $S_I$ and $S_{II}$ which have the same area. In the work of Ericksen (1975), the establishment of the phase transition and the stability of the system are derived using functional analysis, and the equal-area construction is also well explained. We refer the interested readers to the original work.

The real energy evaluation (4.13b) is the convex envelop of the non-convex energy potential (4.2), and the tangent $dw_1/d\varepsilon$ at $\varepsilon_A$ is equal to tangent $dw_2/d\varepsilon$ at $\varepsilon_B$. As $\mathcal{E}_{tot}(\varepsilon_{tot})$ is strictly below the energy potential $w(\varepsilon)$, one can say that part of energy is lost during the phase transition, this

is also shown by the equation (4.12c) that a portion of energy $\delta\frac{E_2}{E_1-E_2}$ is taken from the elastic energy $\sigma_e\varepsilon_{tot}$.

## 4.2 Configurational force

The *standard forces*, also known as *Newtonian forces*, are associated with the changes of a body's position and/or shape, while the body is smooth and continuous. The *configurational forces*, also generally known as the *material forces* or *energetic driving forces* in modern continuum mechanics, are those forces that are associated by duality with the displacement or motion of whatever may be considered a defect in a continuum field theory, examples including mathematically vanishing support, a dislocation line, a mathematical surface of discontinuity (e.g., a phase-transition front, a shock wave), a material inclusion, a hole, a field singularity such as a crack tip, a strongly localized mathematical field solution (e.g., structured shock waves), and so on (Maugin, 2010). Indeed, in the pioneering work of Eshelby (1951), problems related to the material inhomogeneities and field singularities are investigated based on variational arguments. J. D. Eshelby, who is considered the founder of the field, carried out a series of works thereafter (Eshelby, 1956, 1975, 1999). Based on his ideas, researchers developed a comprehensive theoretical framework for the mechanics of configurational forces, which they call *Eshelbian mechanics*.

While the leading studies use the standard variational approaches, and the configurational forces appear as additional terms to describe phenomena associated with the material itself, Gurtin (2000) proposed to consider configurational forces as basic objects. Effectively, Gurtin, 2000; Maugin, 2010; Podio-Guidugli, 2002 all argue that these forces are observable, and perform work when the defect of the continuum field evolves. Moreover, they are needed to give a complete picture of the body's response during the deformation. In fact, the classical notion of *forces* is related to whatever apparently moves or progresses in the matter in an observable manner, and the mechanics of configurational forces is a true mechanics of forces in the general manner of Newton, as these forces contribute to the dynamics in a local 'conservation' of momentum. They also combine, add, or subtract with one another, and they exhibit moments.

### 4.2.1 Rigid sliding sleeve

Here, we use an example inspired by the work of Bosi et al. (2015), to show how configurational forces appear using the variational method. In the original work, the authors also compared the theoretical analysis with experimental data, which validate the theoretical prediction and illustrate the observable nature of configurational forces.

The system is shown in figure 4.3. An inextensible beam of length $L$ is clamped at one end, and the other end is pushed through a frictionless sliding sleeve with a horizontal compressive force $P$. The distance $D$ between the left clamp and the exit of the sliding sleeve remains constant, and the contour length of the beam between the origin and the exit is $\ell$. The inserted part corresponds well to a system with increasing material, and we expect that an additional force appears due to the varying length $L-\ell$ of the inserted beam.

Now we apply the method of energy minimization, and the total energy of the system is

$$\mathcal{E} = \int_0^\ell \frac{EI}{2}\theta'^2 ds + P\,x(L) = \int_0^\ell \frac{EI}{2}\theta'^2 ds + P\,(x(\ell) + L - \ell) \tag{4.14}$$

with geometric constraints & boundary conditions

$$\theta'(s) = \kappa(s) \qquad x'(s) = \cos\theta(s) \qquad y'(s) = \sin\theta(s) \tag{4.15a}$$

$$\theta(0) = 0 \qquad x(0) = 0 \qquad y(0) = 0 \tag{4.15b}$$

$$\theta(\ell) = 0 \qquad x(\ell) = D \qquad y(\ell) = 0 \tag{4.15c}$$



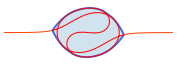

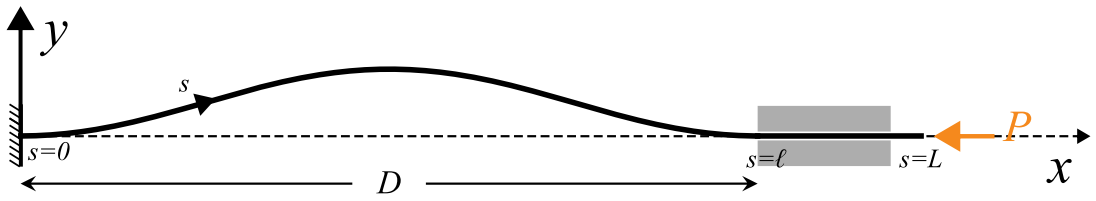


**Figure 4.3: Setup of the rigid sliding sleeve problem. An elastic rod is inserted into a rigid frictionless channel.**

To account for the constraints, we construct the Lagrangian

$$\mathcal{L} = \int_0^\ell \frac{EI}{2}\theta'^2 ds + \int_0^\ell \left[n_x(s)\,(x' - \cos\theta) + n_y(s)\,(y' - \sin\theta)\right] ds + P\,(x(\ell) + L - \ell). \tag{4.16}$$

Compared to the classical Elastica problem, here the boundary $\ell$ is also a variable. As a consequence, the admissible variations at the boundary $s = \ell$ are

$$\bar\theta(\ell) + \bar\ell\,\theta'(\ell) = 0 \qquad \bar x(\ell) + \bar\ell\,x'(\ell) = \bar x(\ell) + \bar\ell = 0 \qquad \bar y(\ell) + \bar\ell\,y'(\ell) = \bar y(\ell) = 0 \tag{4.17}$$

and the variation at $\ell$ for each integrand should also be considered in the variation of $\mathcal{L}$, which is

$$\begin{aligned}\bar{\mathcal{L}} = &\int_0^\ell -EI\theta''\bar\theta + \left[-n_x{}'\,\bar x + n_x\,\sin\theta\,\bar\theta - n_y{}'\,\bar y - n_y\,\cos\theta\,\bar\theta\right] ds \\ &+ EI\theta'(\ell)\bar\theta(\ell) + \bar\ell\frac{EI}{2}\theta'^2(\ell) + n_x(\ell)\,\bar x(\ell) + n_y(\ell)\,\bar y(\ell) + P\,(\bar x(\ell) + \bar\ell\,x'(\ell) - \bar\ell).\end{aligned} \tag{4.18}$$

Using (4.17) to replace the terms $\bar\theta(\ell)$, $\bar x(\ell)$ and $\bar y(\ell)$, $\bar{\mathcal{L}}$ becomes

$$\bar{\mathcal{L}} = \int_0^\ell \left[-EI\theta''\bar\theta - n_x{}'\,\bar x + n_x\,\sin\theta\,\bar\theta - n_y{}'\,\bar y - n_y\,\cos\theta\,\bar\theta\right] ds - \left(\frac{EI}{2}\theta'^2(\ell) + n_x(\ell) + P\right)\bar\ell. \tag{4.19}$$

At the energy minimum, this variation must be zero, which means the factor before each admissible (independent) variation should vanish.

Cancelling the variation of $x$ ($\bar x$) and $y$ ($\bar y$) in the bulk signifies $n_x(s)$ and $n_y(s)$ are constants. Cancelling the variation of $\theta$ ($\bar\theta$) in the bulk leads to

$$EI\theta'' = n_x\,\sin\theta - n_y\,\cos\theta \tag{4.20}$$

which is the classical equation of Elastica. The factor before $\bar\ell$ gives

$$n_x(\ell) = n_x = -\left[\frac{EI}{2}\theta'^2(\ell) + P\right]. \tag{4.21}$$

Compared to the classical Elastica problem shown in 1.5, there is an additional term $\frac{EI}{2}\theta'^2(\ell)$, which is called a *configurational force*.

In appendix D, we show another example of a sliding sleeve, where part of a fiber is inserted into a flexible tube, and the whole structure deforms under external momentum applied to the ends. In this example, jumps of forces and momenta can also be observed due to the varying boundaries.

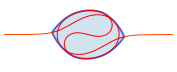

# Part II

# Solid-solid packing : Confined Elastica



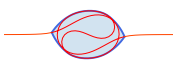

Following the study of the planar Elastica in section 1.5, this part addresses the post-buckling behavior of an elastic beam confined within rigid boundaries.

The deformation of slender elastic rods under lateral constraints has attracted attention since the mid-19th century. Early studies were motivated by challenges in the drilling industry (Lubinski and Althouse, 1962; Miller et al., 2015), but the topic has since broadened to diverse applications, including endoscope–artery interactions in vascular surgery, fiber insertion in the textile industry (Hearle, 2014), DNA coiling in viral capsids (Vetter, Wittel, and Herrmann, 2014), and even geological folding processes (Price and Cosgrove, 1990). This wide range of phenomena has motivated investigations into the deformation processes, force responses, and stability of confined slender structures.

In this thesis, we focus on the packing of a planar, inextensible elastic beam of negligible thickness (the *Elastica*) inside a rectangular cavity. To our knowledge, the first study of this specific problem was carried out by Chateau and Nguyen (1991). Subsequent works explored related configurations: for example, pinned–pinned boundary conditions (Domokos, Holmes, and Royce, 1997), finite-thickness layers (Chai, 1998, 2005), interaction between several layers (Chai and Moshkovitz, 2022), and confined Elastica with variable length (Liakou and Detournay, 2018). Compared to classical buckling of beams, confinement introduces inequality constraints arising from contact conditions (see chapter 3), which lead to non-classical features in the bifurcation diagram (Schulz and Pellegrino, 2000).

Different strategies have been employed to address these constraints. Some studies approximate the walls as soft supports, for example Winkler-type elastic foundations (Chen and Wen, 2019; Hetényi and Hetbenyi, 1946; Judah and Givli, 2024; Katz and Givli, 2015). Others introduce barrier potentials to mimic hard-wall interactions (Manning and Bulman, 2005). Alternatively, the problem can be reformulated as a constrained optimization and solved with interior-point methods (see section 1.3.2). Analytical approaches based on small-deformation, weakly non-linear, or exact Elastica solutions have also been developed (Chai, 1998; Domokos, Holmes, and Royce, 1997; Roman and Pocheau, 1999).

Building on this background, our study focuses on two-dimensional numerical and theoretical analyses of a clamped–clamped Elastica confined within a rigid tunnel. Depending on the position of the clamped extremities, we define two configurations:

- **Wall-attached configuration** (Chapter 5): both ends are clamped to the lower wall.
- **Centered configuration** (Chapter 6): both ends are clamped along the midline between the walls, creating a symmetric confinement.

The emphases and methods differ between the two cases. For the wall-attached configuration, we analyze the deformation process and develop theoretical models based on the Elastica equation. For the centered configuration, we place greater emphasis on bifurcation and stability analyses. In both cases, force responses and energy variations serve as important references of the deformation process. Finally, in Chapter 7, we compare the two configurations, highlighting their similarities and differences, and draw general conclusions on the behavior of clamped Elastica confined in rigid tunnels.

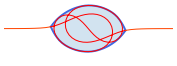

# Chapter 5

# Wall-attached configuration

In this part, we consider an inextensible slender beam (Elastica) of length $L$ and bending stiffness $EI$ confined between two rigid walls separated by a distance $H$, see in figure 5.1.

As shown in the Planar Elastica example, we adimensionalize the system with length unit $L$ and force unit $EI/L^2$ (section 1.5.1). Please recall that the dimensionless system can be considered as a system with $L = 1$ and $EI = 1$. In the following, all parameters are dimensionless.

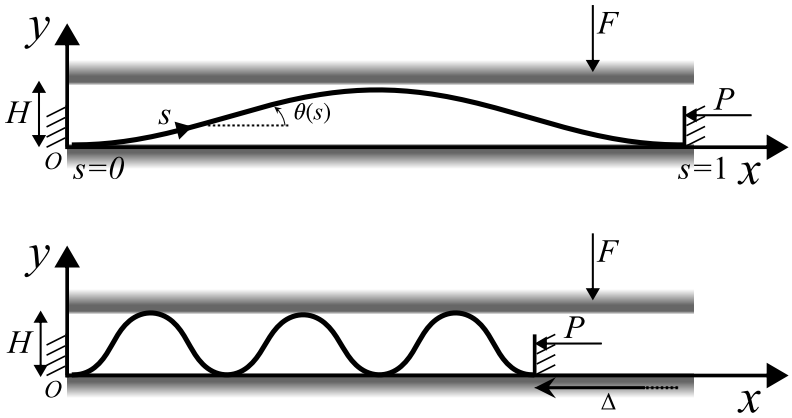


**Figure 5.1: System configuration of the confined beam problem. The**

Both ends of the beam are clamped and attached directly to the lower wall. It deforms under displacement control, and we call $P$ the horizontal force response of the support. As the end displacement $\Delta$ increases, the beam gradually deforms into a wavy configuration due to the geometric constraints imposed by the walls, and we note $F$ the global vertical force response of the wall. The number $N$ of visible arches or undulations along the beam increases with the end displacement. More precisely, we define this number in the following way: the *fold number* $N$ is half the number of free branches that touch both the upper wall and the lower wall. This metric serves as a key indicator of the post-buckling behavior, and is related to the forces $P$ and $F$. An illustration of the definition can be found in figure 5.5.

The present investigations of the problem put emphasis on the beam shape and on the force response. We use different methods, including energy minimization of the discretized system and theoretical analysis, to draw insights on the behaviors of the system. Our theoretical results predict the response of the system under a given displacement $\Delta$. Solving equilibrium with the energy minimization method can be considered as numerical experiments, and the minimization results on the discretized system will be used to be compared to the theoretical prediction.

## 5.1 The whole system simulation: a first glance

Although we can apply the variational method on the Lagrangian to obtain a system of differential equations, actually solving the system is intricate due to the presence of the walls. The system involves inequality constraints and inequality equations, which are difficult to handle. For this reason, we apply the energy minimization method to the discretized system and solve it with the help of CasADi and IPOPT, both presented in chapter 2. This allows us to run simulations as 'numerical experiments', and gives us a first glance at the behavior of the system.

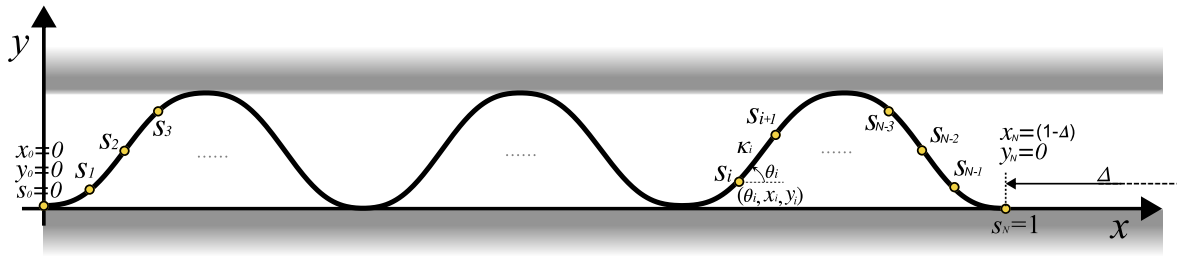


**Figure 5.2: Discretized system used in the optimization procedure.**

Figure 5.2 shows the definition of the discretized system, and we apply the Super-Helices discretization with mixed formulation that has been introduced in section 2.2.2. It is relatively simple and easy to implement, but still very efficient and yields good accuracy.

Thus, the problem, which is eventually sent to CasADi and IPOPT, is

$$\min_{\kappa_i,\theta_i,x_i,y_i} \quad \sum_i \frac{1}{2}\kappa_i^2 \delta s \tag{5.1a}$$

subject to Constraints of mixed formulation,

$$\theta_0 = 0; \quad x_0 = 0; \quad y_0 = 0 \tag{5.1b}$$

$$\theta_N = 0; \quad x_N = 1 - \Delta; \quad y_N = 0. \tag{5.1c}$$

$$y_i \geq 0 \text{ and } H - y_i \geq 0, \quad \forall i = 1, 2, ..., N-1. \tag{5.1d}$$

Please remark that the only difference from the Planar Elastica example shown earlier is the wall constraints (5.1d), which means that regardless of the complexities given by the wall constraints to theoretical analysis, the implementation is extremely simple in the optimizer, showing the interest of using the discretized optimization method.

**The Lagrange multipliers** Thanks to the features of the solver IPOPT and its interface in CasADi, we can obtain the values of Lagrange multipliers in addition to the values of the unknown variables. The Lagrange multipliers reflect the responses of the system to the imposed constraints, among which we are most interested in the force responses. Indeed, the Lagrange multiplier associated with the boundary constraint $x_N = 1 - \Delta$ is the horizontal compression force $P$, and the Lagrange multipliers of the wall constraints are the reaction forces from the walls, which can be proved analytically using the variational method. In figure 5.3, we show one solution given by the solver.

**Solving by continuation method** Because the solution is highly nonlinear when the end displacement $\Delta$ is large, we apply a continuation method with control parameter $\Delta$. Details about the continuation method can be found in section 1.4.3. The algorithm is initialized with a small $\Delta$, such that the linear solution (see for example Neukirch et al. (2021)) is good enough for the



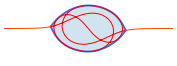

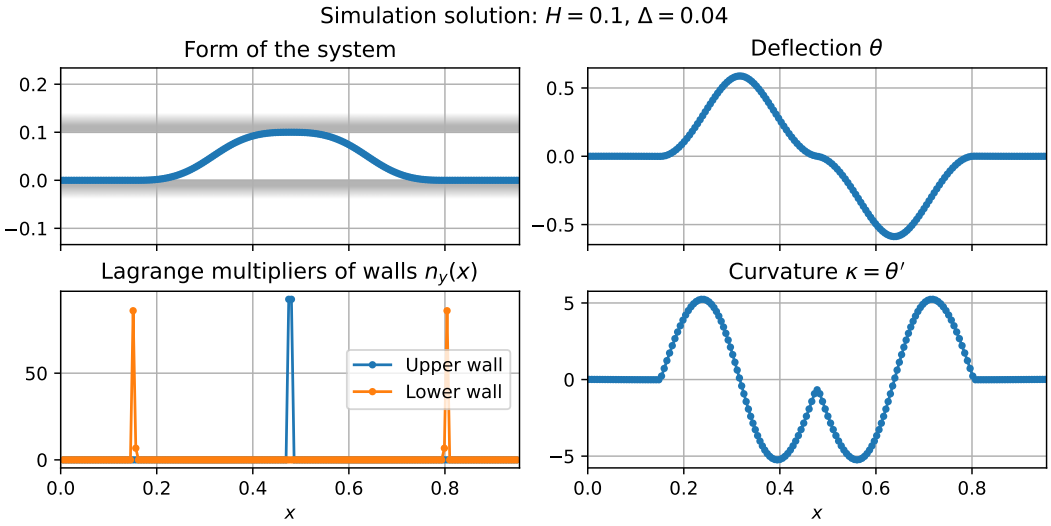


**Figure 5.3: A numerical solution of system (5.1), with 180 discretization points.**

solver to converge. Then we increase $\Delta$ with a given step length, find the solution at this new $\Delta$ using the solution of the previous step as warm-start. In this way, we gradually increase $\Delta$ to reach the target value.

If the step length is too large, the geometry of the beam may change substantially, as if we were pushing the beam abruptly in a real experiment. In fact, multiple stable solutions may coexist for a given load $\Delta$, if the initialization is far from all possible solutions, we cannot predict which solution will actually be found, and the final solution can be very different from the initialization. The same kind of jump between solutions may happen if the parameter `mu_init` of IPOPT solver (see section 1.3.2 and appendix A) is too large. As this parameter modifies the initial problem to deal with the constraints, a larger value means more significant modifications, and more perturbations during the solving process. Examples are given in figure 5.4 where we show two solutions found with the exact same parameters except the `mu_init` of IPOPT. The orange curve is found with a smaller parameter `mu_init`, and one can observe that the curves of forces $P$ and $F$ tend to stick longer to the historical evolution direction before jumping to a state with lower energy, which confirms the above explanation.

In general, *hysteresis* can be observed, which means the solution depends on the loading history.

Due to the properties of IPOPT optimizer, the solutions of the inequality optimization model are energy minima, which are stable solutions, and we cannot find all the equilibria. However, these solutions of the global system are good references for other theoretical models, not only for the geometry and force responses but also for the stability.

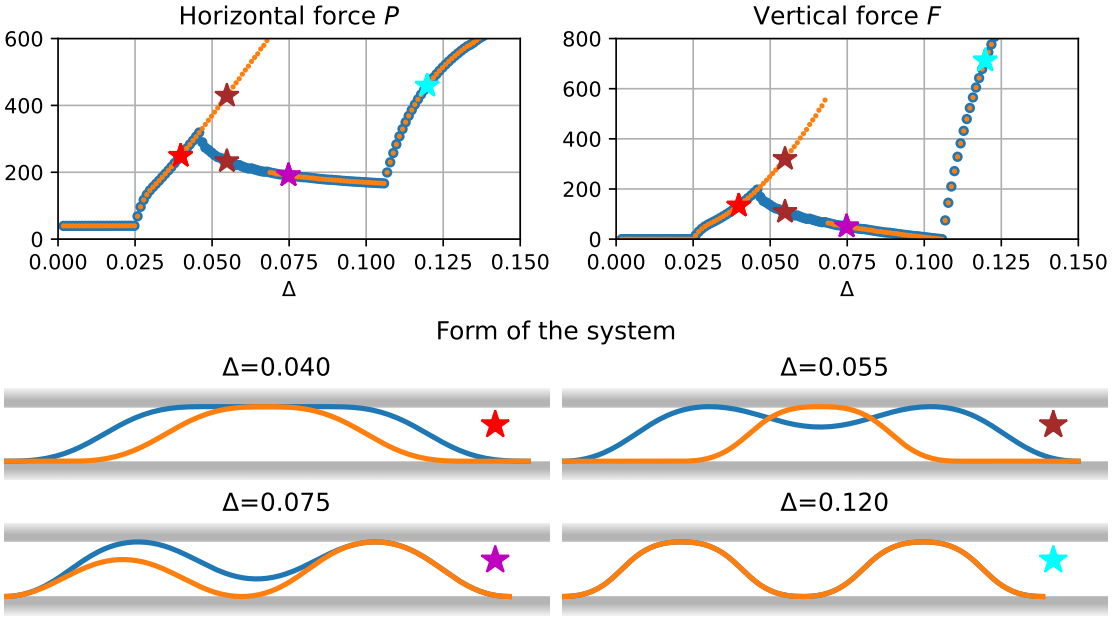


(a) Process from one fold to two folds.

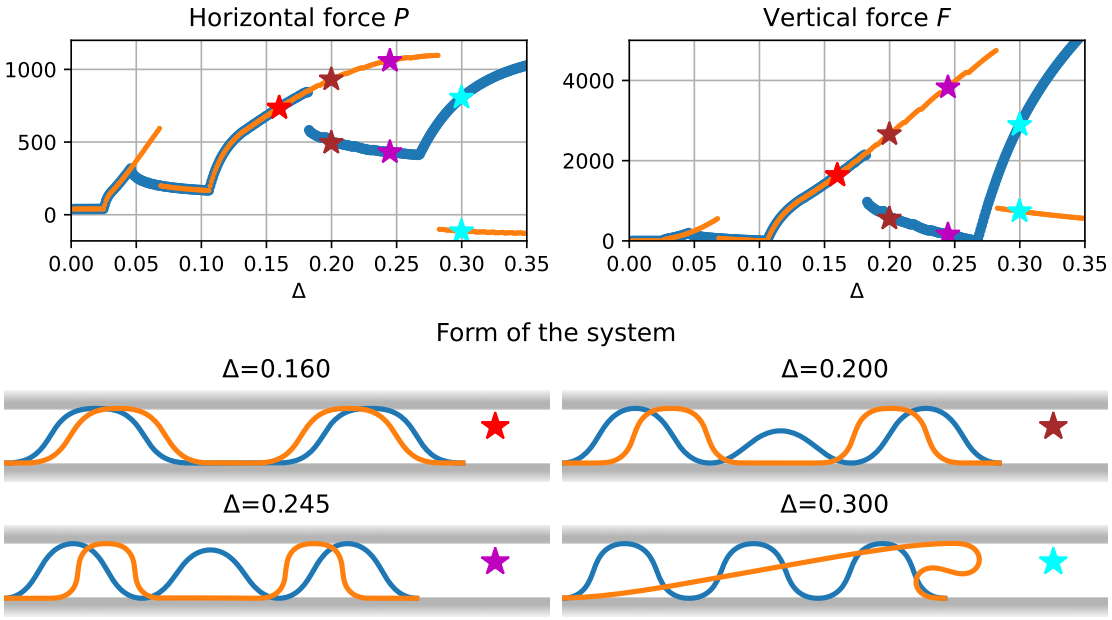


(b) Process from two folds to three folds/spiral.

**Figure 5.4: Comparison between two processes of solving for the increasing Δ experiment. Both solutions are solved using 180 nodes. The blue configuration is obtained with `mu_init`=0.1, while the orange configuration is obtained with `mu_init`=$10^{-5}$.**



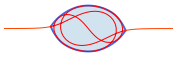

## 5.2 Deformation process and configurations

Results of the optimization model and observation from real experiments show that several configurations can be observed during the insertion of the Elastica. We distinguish them by the names *point-contact state* (PtC), *extended-contact state* (ExtC) and *hanging-fold state* (HgF), see figure 5.5.

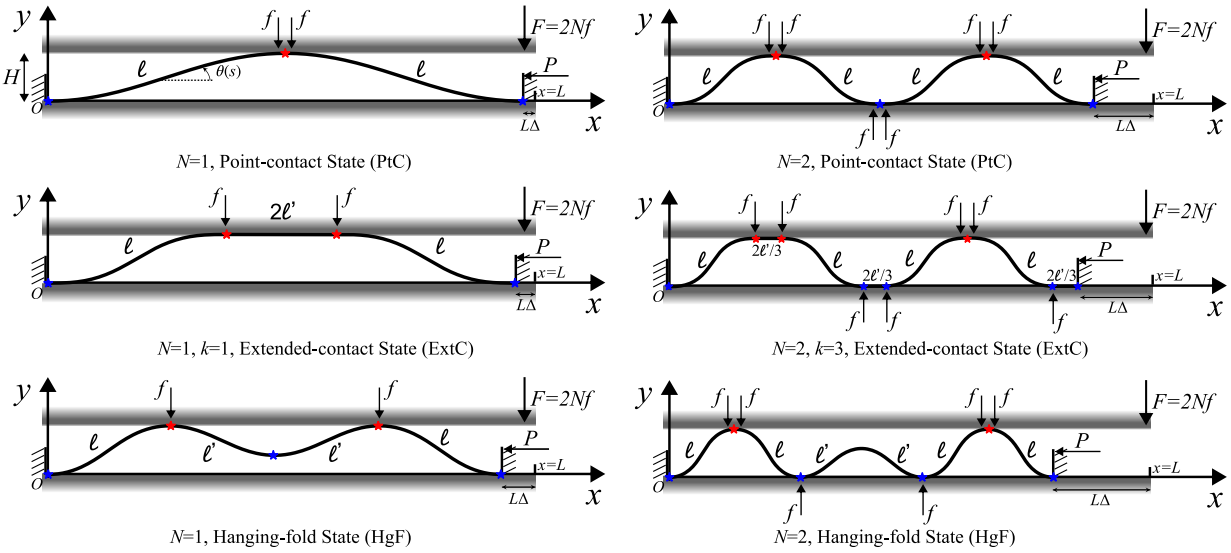


**Figure 5.5: Wall-attached confined Elastica: Illustration of different configurations with different fold numbers $N$**

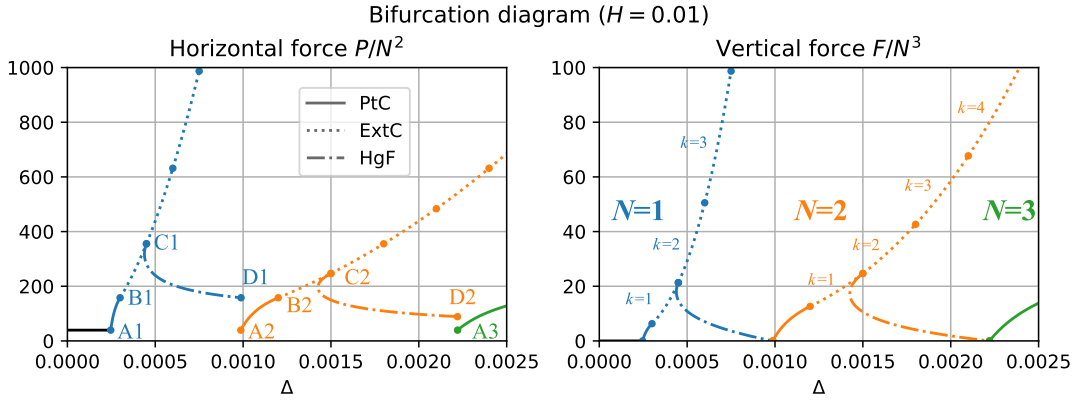


**Figure 5.6: Illustration of the bifurcation diagram ($H = 0.01$). Different types of configuration for the rigidly confined Elastica are marked by the different types of lines. The bifurcation points are marked on the left side. The fold numbers $N$ and the number of the flat region(s) $k$ are marked on the right side.**

Recall that the fold number $N$ is defined as half of the number of free branches that touch both the upper and the lower wall. When the end displacement $\Delta$ increases, $N$ increases monotonously and different configurations appear in an almost periodic manner until the Elastica reaches the spiral state. The transition to spiral shape and beyond are not the main subject in this chapter. A recent study of Deboeuf, Protière, and Katzav (2024) investigated the transition in detail, and appendix E includes a brief presentation of our findings about the spiral state.

To explain the deformation process, we begin with the PtC state, in which the Elastica contacts the upper wall only at isolated point(s). As $\Delta$ increases, the absolute value of curvature at contact points decreases to zero, and the system enters the ExtC state, in which we can observe flat part(s) attached to the upper or lower wall. One interesting fact about a flat region is that there is no force reaction from the wall acting along it, a property also seen in simulations of the entire system. Indeed, the moment and the deflection angle uniformly vanish along each flat region, and the Elastica equation C.1b shows that in this case the vertical component of the internal force should be zero. In the ExtC configuration, the total length of all flat parts attached to the walls increases as the compression increases. Please note that the number of flat parts is not unique, and the length of each part may not be identical, but the elastic energy and the equilibrium condition remain the same (Pocheau and Roman, 2004). In other words, the solution of the problem is not unique, as illustrated for example in figure 5.4. And to enter the HgF state, the compression force $P$ should pass the buckling threshold of the longest flat part $\ell_p$, that is $P = (2\pi/\ell_p)^2$. Then, this flat part buckles and creates a free branch, the two ends of which are attached to the same wall. We call this kind of branch *a hanging fold*, and call the configurations with hanging folds the hanging-fold states (HgF). Because the solution of the ExtC state is not unique, $\ell_p$ is also not unique, and the actual value of $\Delta$ at which the system passes to the HgF state is not fixed and depends on the history of the deformation. In figure 5.4a, the orange solution enters the HgF state with larger $\Delta$ than the blue solution because the flat region is fragmented into more pieces. When the system passes from the ExtC to the HgF states, both the compression force $P$ and the reaction forces of the walls $F$ decrease. When the hanging fold touches one of the walls, a new fold is created, and we enter another cycle of configurations. Note that the deformation process does not follow exactly the order PtC-ExtC-HgF-PtC. The reason will be explained later in this chapter.

## 5.3 Basic idea of analytical models: solving by parts

Although the morphing process is not unique and depends on the history of deformation, each configuration can be described analytically. Indeed, the beam can be separated into free branches and flat regions if there is any. An example is shown in figure 5.7a.

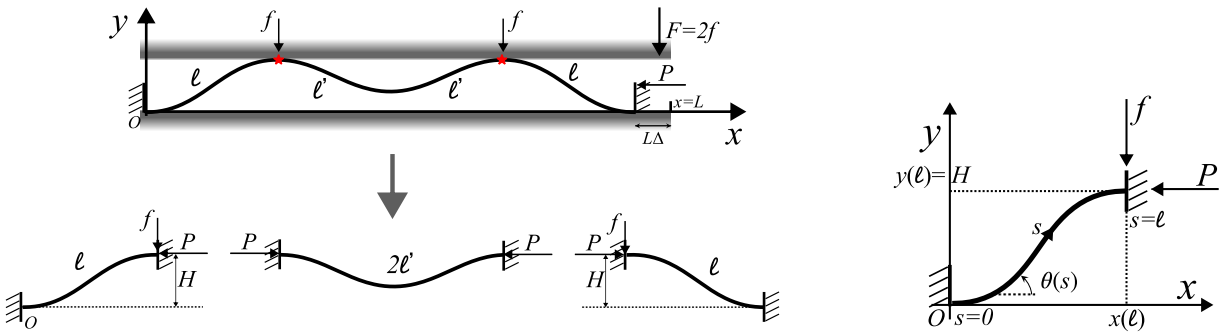


**(a) An example of splitting the system into parts** **(b) The arch solution**

**Figure 5.7: Solving the system by parts, illustration.**

Each free branch (see figure 5.7b) conforms to the equations of the planar Elastica (also introduced in section 1.5 and appendix C):

$$x'(s) = \cos\theta(s), \quad y'(s) = \sin\theta(s), \quad \theta''(s) = -P\sin\theta(s) + f\cos\theta(s), \quad s \in [0, \ell] \tag{5.2}$$



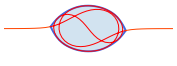

To actually study the confined Elastica by solving the free branch, or arch solution, we need to consider the boundary conditions given by the wall height $H$ and the imposed displacement $\Delta$. Additionally, because the contact between the Elastica and the walls is frictionless, the compression force $P$ is conserved in the entire system. The first integral, also called the Hamiltonian (C.3), is also conserved. Finally, the length of each arch $\ell$ can be found by the conservation of the total length of the Elastica.

### Self-similarity of the Elastica equations

We are interested in the force responses and the shape of the deformed beam. In the first place, even without solving, we can gain some insights from the equations.

It has been shown by Roman and Pocheau (1999) that the system of equations (5.2) present the following self-similar property. If $\theta(s)$, $x(s)$, $y(s)$, $P$ and $f$ verify system (5.2), then do $\widehat{\theta}(\widehat{s})$, $\widehat{x}(\widehat{s})$, $\widehat{y}(\widehat{s})$, $\widehat{P}$ and $\widehat{f}$ also, with

$$\widehat{\theta} = \theta, \quad \zeta\,\widehat{x} = x, \quad \zeta\,\widehat{y} = y, \quad \zeta\,\widehat{s} = s, \quad \widehat{P}/\zeta^2 = P, \quad \widehat{f}/\zeta^2 = f, \quad \widehat{s} \in [0, \ell/\zeta]. \tag{5.3}$$

This means that if the length of an arch is scaled down to $1/k$ of its original length, then the forces are $k^2$ times of their original values. If there are $N$ folds, then the length of an arch is approximately $1/(2N)$, from which we can estimate that the horizontal force responses $P$ increase quadratically with the number $N$ of folds. The total vertical response of the walls $F = 2Nf$ is then seen to follow a cubic dependence on the number $N$ of folds.

## 5.4 Phase diagram

The system depends on two parameters, the end displacement $\Delta$, and the wall height $H$, and we would like to classify the response of the system as a function of these two parameters. This is what is done in the phase diagram of Figure (5.8a), where we present the number $N$ of folds, and Figure (5.8b), where we present the configuration types. In these two figures, we plot (i) results from the total system simulation and (ii) theoretical predictions for the parameter values for which the system experiences a transition (configuration change). Results from the total system simulation approach (Section 5.1) are plotted with points, while results from the theoretical predictions (Sections 5.2, 5.3 and the following analysis) are plotted with lines.

**Transition from $N-1$ to $N$ fold(s)** These lines $H_N(\Delta)$ are related to the 'not touching - touching' transition (point $A_1$ in Figure 5.6) and the HgF-PtC transitions (points $D_{N-1} = A_N$ with $N \geq 2$ in Figure 5.6). For a given $\Delta$, we solve (5.2) with

$$f = 0, \quad \ell = 1/(2N), \quad \theta(0) = \theta(\ell) = 0, \quad x(0) = y(0) = 0, \quad x(\ell) = \ell(1-\Delta), \tag{5.4}$$

and $H_N(\Delta)$ is given by the solution value of $y(\ell)$. The solving can be either done by applying the analytical solution described in Appendix C, or the shooting method that was presented in Section 1.5.2.

Thanks to the self-similarity, the line $H_1(\Delta)$ separating the not touching and the touching region with $\ell = 1/2$, can be scaled to any other $N-1$ to $N$ folds transition, with $\ell = 1/(2N)$ and $H_N(\Delta) = H_1(\Delta)/N$.

**Transition from PtC state to ExtC state** This corresponds to points $B_N$ in Figure 5.6. In the same manner, the lines $H_N^e(\Delta)$ defining the PtC-ExtC transitions are calculated by solving (5.2) with

$$\theta'(0) = \theta'(\ell) = 0, \quad \ell = 1/(2N), \quad \theta(0) = \theta(\ell) = 0, \quad x(0) = y(0) = 0, \quad x(\ell) = \ell(1-\Delta), \tag{5.5}$$

and $H_N^e(\Delta) = y(\ell)$. Once again, $H_N^e$ can be derived by self-similarity, using $H_N^e = H_1^e(\Delta)/N$.

**Transition from ExtC state to HgF state** Different from the two previous types of transition, the ExtC-HgF transition depends on the length of the longest flat region, with the horizontal force $P$ being equal to its buckling force. To simplify the analysis, we suppose the flat regions are segmented into identical $k$ parts. By construction, $1 \le k \le 2N+1$. Given $N$, $k$ and $\Delta$, the lines in the phase diagram $H_N^h(\Delta)$ are found by solving (5.2) with

$$\begin{aligned} &\theta'(0) = \theta'(\ell) = 0, \quad \theta(0) = \theta(\ell) = 0, \quad x(0) = y(0) = 0, \\ &2N\ell + k\ell_p = 1, \quad P = \frac{4\pi^2}{\ell_p^2}, \quad 2N\, x(\ell) = \Delta \end{aligned} \tag{5.6}$$

where $\ell_p$ is the length of each flat part. The transition lines are given by $H_N^h(\Delta) = y(\ell)$.

In this case, the self-similarity cannot be used, and these lines should be solved for each $N$ and $k$.

In figure 5.8, we plot the solutions of the numerical simulations and also the analytical predictions for $H \in [0.05, 0.25]$ and $\Delta \in [0, 0.3]$. Please note that this diagram considers relatively large $H$ and small $\Delta$, such that the number of folds is relatively small. The analytical predictions by

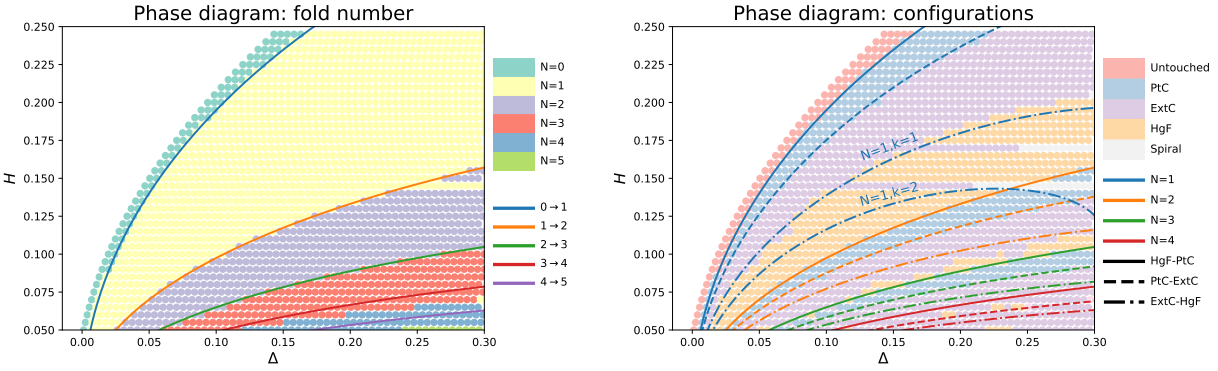


**(a) $H - \Delta$ diagram: fold number** **(b) $H - \Delta$ diagram: configurations**

**Figure 5.8: Phase diagram: the points are solutions of the total system simulations with 200 nodes and default `mu_init`. In each simulation, we fix $H$ and use a continuation method where we increase $\Delta$ with step size 0.005. The lines are theoretical predictions by non-linear arch solutions, see Eqs. (5.4)-(5.5)-(5.6). The ExtC-HgF transition lines are calculated with $k = 1$ except the marked one.**

the non-linear arch solutions, Eqs. (5.4)-(5.5)-(5.6) match well with the total simulation results, especially when the number of folds is small ($N \le 2$). The only mismatches are the two simulations of $H = 0.145$ and $H = 0.170$. In fact, for these two simulations, there are two flat regions, so the ExtC state stays longer than the other cases, and the system enters the spiral state even without passing through the HgF state.

When the fold number is relatively large ($N \ge 3$), the results of the simulation lag behind the predictions (with respect to the increasing $\Delta$), and the configurations tend to stay in the ExtC state. This is due to the multistability of the system. When the fold number is large and the system is in the ExtC state, the flat regions can be fragmented into several pieces, thus the configuration depends on the loading history and hysteresis happens if the loading is reverse, an aspect which the predictions by the arch solutions do not consider.



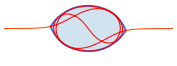

These phase diagrams preliminarily reveal the complexity and rich physics behind the problem of constrained Elastica. In the following, we further investigate the process of the deformation with more details, including the forces and the hysteresis.

## 5.5 Predictions by the von Kármán approximation

Solving by separated parts, we are able to predict the responses of the system. Although the nonlinear planar Elastica equation has analytical solutions, the solutions involve elliptic functions that are cumbersome to get further physical intuition. To bypass this complexity, we apply the von Kármán approximation[1].

The von Kármán approximation is first introduced for the deformation of plates (Eisley, 1964; Kármán, 1907), and in this approximation, the moment balance is linearized, and the strain is approximated by a weakly non-linear expression, which reflects on the kinematics in our system, that is

$$x'(s) = 1 - \frac{1}{2}\theta^2(s), \qquad y'(s) = \theta(s)$$

In the dimensionless system, with the von Kármán approximation, we can again write the Lagrangian and use the variational method to derive the system of equations

$$\theta'(s) = m(s), \tag{5.7a}$$
$$x'(s) = 1 - \frac{1}{2}\theta^2(s), \tag{5.7b}$$
$$y'(s) = \theta(s), \tag{5.7c}$$
$$\theta''(s) = -P\theta(s) + f, \tag{5.7d}$$

with boundary conditions $\theta(0) = \theta(\ell) = 0$, $x(0) = y(0) = 0$ and $y(\ell) = H$, see Figure 5.7b.

The solution of system (5.7) can be explicitly solved

$$m(s) = \frac{f}{\sqrt{P}}\left(\sin\sqrt{P}s - \tan\frac{\sqrt{P}\ell}{2}\cos\sqrt{P}s\right) \tag{5.8a}$$
$$\theta(s) = \frac{f}{P}\left(1 - \cos\sqrt{P}s - \tan\frac{\sqrt{P}\ell}{2}\sin\sqrt{P}s\right) \tag{5.8b}$$
$$y(s) = \frac{f}{P\sqrt{P}}\left(\sqrt{P}s - \sin\sqrt{P}s + \tan\frac{\sqrt{P}\ell}{2}\left[\cos\sqrt{P}s - 1\right]\right) \tag{5.8c}$$

where $\pi \le \sqrt{P}\ell \le 2\pi$, and the length $\ell$ of the arch solution depends on the configuration and on the number of folds. With these expressions, we compute $m(\ell)$, $y(\ell)$, $x(\ell)$ and the energy of one branch:

$$m(\ell) = \frac{f}{\sqrt{P}}\tan\frac{\sqrt{P}\ell}{2} = -m(0) \tag{5.9a}$$
$$y(\ell) = \frac{f}{P\sqrt{P}}\left(\sqrt{P}\ell - 2\tan\frac{\sqrt{P}\ell}{2}\right) = H, \tag{5.9b}$$
$$x(\ell) = \int_0^\ell 1 - (1/2)\,\theta^2(s)ds = \ell - f^2\frac{\sqrt{P}\ell\left[2 + \cos\sqrt{P}\ell\right] - 3\sin\sqrt{P}\ell}{2P^2\sqrt{P}\,(\cos\sqrt{P}\ell + 1)}, \tag{5.9c}$$
$$E_\kappa = \frac{1}{2}\int_0^\ell m^2(s)ds = \frac{f^2}{2P\sqrt{P}}\frac{\sqrt{P}\ell - \sin\sqrt{P}\ell}{1 + \cos\sqrt{P}\ell}. \tag{5.9d}$$

[1]This is also the subject of our article Wang et al. (2025)

These expressions allow us to predict the configuration and the force response for a given pair $(H, \Delta)$.

### 5.5.1 Initial stage to contact

When the Elastica buckles, the horizontal force is $P = 4\pi^2$. As the end is gradually pushed into the tunnel, the Elastica eventually touches the upper wall at $y = H$. It can be predicted by the von Kármán approximation (Bigoni, 2012; Neukirch et al., 2021; Tzokova, 2020), that this happens when $\Delta = (H\pi)^2/4$, and we define

$$H_\Delta := \frac{2}{\pi}\sqrt{\Delta} \tag{5.10}$$

where $H_\Delta$ is a function of the variable $\Delta$.

### 5.5.2 Point contact states (PtC)

Suppose the Elastica is at PtC state with the fold number $N$, then the length of each free branch is $\ell = 1/(2N)$, the vertical response from the walls is $F = 2Nf$, and we have $2Nx(\ell) = 1 - \Delta$. Using the arch solution (5.9), we have

$$H_u = \frac{F_u}{4P_u\sqrt{P_u}}\left(\sqrt{P_u} - 4\tan\frac{\sqrt{P_u}}{4}\right) \tag{5.11a}$$

$$\Delta = {F_u}^2\frac{\sqrt{P_u}\left[2+\cos(\sqrt{P_u}/2)\right] - 6\sin(\sqrt{P_u}/2)}{8{P_u}^2\sqrt{P_u}\left[\cos(\sqrt{P_u}/2)+1\right]} \tag{5.11b}$$

$$\frac{m(\ell)}{N} = -\frac{m(0)}{N} = \frac{F_u}{2\sqrt{P_u}}\tan\frac{\sqrt{P_u}}{4} \tag{5.11c}$$

with

$$H_u = N\,H, \quad P_u = P/N^2, \quad F_u = F/N^3. \tag{5.12}$$

These solution branches each start when $P_u = 4\pi^2$, $F_u = 0$, $H_u = H_\Delta$, and end when $P_u = 16\pi^2$, $F_u = 3^{-1/2}\sqrt{\Delta}$.

### 5.5.3 Extended contact states (ExtC)

Recall that the transition between the PtC state and the ExtC state happens when the value of the moment at the extremities of the free branch becomes zero, that is when $P_u = 16\pi^2$ in von Kármán approximation system (5.7). Then flat parts appear in the system, and for each free branch $m(\ell) = m(0) = 0$. First, we can derive that the Hamiltonian (C.3) is conserved along the Elastica and has the value $I_{nv} = -P$. And, from (5.9a), we have that the value of $\ell$ is fixed to $2\pi/\sqrt{P}$ in the present von Kármán approximation. We note the total length of all the flat parts $2\ell'$ and have $2N\ell + 2k\ell' = 1$. As in the PtC case, we have $F = 2Nf$, and $2Nx(\ell) = 1 - \Delta$ and we obtain

$$H_u = \frac{\pi F_u}{P_u\sqrt{P_u}} \tag{5.13a}$$

$$\Delta = 1 - [2Nx(\ell) + 2\ell'] = \frac{3\pi}{4}\frac{{F_u}^2}{P_u^2\sqrt{P_u}} \tag{5.13b}$$

The branch of solutions ends when one flat part buckles, but the number of flat parts is not a priori determined, so is the length of each part. When the Elastica in ExtC state has $N$ folds, the flat region can be divided into $k$ pieces, with $1 \le k \le 2N+1$. Suppose each flat part has the same



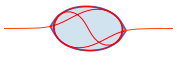

length, then the length of each flat part is $2\ell'/k$, and the branch ends when $P = 4\pi^2/(2\ell'/k)^2$, and we have

$$\ell' = k/(4N + 2k) \text{ and } \ell = 1/(2N + k) \tag{5.14a}$$

$$P_u = 4\pi^2 \left(\frac{2N + k}{N}\right)^2 \tag{5.14b}$$

$$F_u = 8\pi^2 \sqrt{\Delta}\sqrt{2/3} \left(\frac{2N + k}{N}\right)^{5/2} \tag{5.14c}$$

$$H_u = \sqrt{\Delta}\sqrt{2/3}\sqrt{\frac{N}{2N + k}} \tag{5.14d}$$

which means that for large $N$ and with a flat region divided into a maximum number of pieces ($k = 2N + 1$) the vertical force can take values up to $F \simeq 2000\, N^3 \sqrt{\Delta} \simeq 140\, \Delta^2/H^3$, and the horizontal force values up to $P \simeq 600\, N^2 \simeq 100\, \Delta/H^2$.

To sum up, the ExtC branches start at $P_u = 16\pi^2$, $F_u = 64\pi^2\sqrt{\Delta/3}$ and $H_u = \sqrt{\Delta/3}$, and ends when one of the flat segments buckles, that is at $P = 4\pi^2/(2\ell'/k)^2$, where $k$ is the number of flat parts with $1 \leq k \leq 2N + 1$.

### 5.5.4 Hanging fold states (HgF)

After one flat part of the Elastica in the ExtC state buckles, a free branch with two ends in contact with the same wall is created, and the system enters the HgF state. To simplify the analysis, we suppose there is only one flat part ($k = 1$) in the ExtC state with $N$ folds. In such a case, the flat part has length $2\ell'$ and buckles when $P = \pi^2/\ell'^2$. As a consequence, the HgF state starts at $P = 4\pi^2(1 + 2N)^2$, $F = 8\pi^2\sqrt{2\Delta/3}\sqrt{N}(1 + 2N)^{5/2}$, and $H = \sqrt{2\Delta}/\sqrt{3N(1 + 2N)}$. After the flat part buckles, we call the newly created branch the hanging fold, and its length is still noted $2\ell'$. Please note that a configuration having a hanging fold and a flat region is not possible, as it would imply two different values of the Hamiltonian invariant $I_{nv}$: the invariant value for solutions with a flat region is $I_{nv} = -P$ while the invariant value for solutions with a fold is $I_{nv} = -P + (1/2)\,\theta'^2(\ell) > -P$. The vertical force along the hanging fold is zero, that is $f = 0$ in system (5.7). Solving $\theta''(s) = -P\,\theta(s)$ with $\theta(0) = \theta(\ell') = 0$ gives $\theta(s) = c \sin\sqrt{P}s$ with $c$ a constant to be determined and $\sqrt{P}\,\ell' = \pi$. Making use of (5.9a) and the continuity on curvature between the hanging fold and other free branch, we have

$$\theta'(0) = c\sqrt{P} = \frac{f}{\sqrt{P}} \tan\frac{\sqrt{P}\ell}{2} \qquad \Rightarrow \qquad c = \frac{f}{P} \tan\frac{\sqrt{P}\ell}{2}. \tag{5.15}$$

With that, we can calculate the retraction of the hanging fold with $x(\ell')$

$$x(\ell') = \int_0^{\ell'} 1 - (1/2)\,\theta^2(s)ds = \ell' \left(1 - \frac{c^2}{4}\right). \tag{5.16}$$

And the displacement condition is $2[N\,x(\ell) + x(\ell')] = 1 - \Delta$, where $x(\ell)$ is given by (5.9c). Then we can obtain the expressions for the HgF state in the von Kármán approximation

$$H_u = \frac{F_u}{2P_u\sqrt{P_u}} \left(\sqrt{P_u}\ell_u - 2\tan\frac{\sqrt{P_u}\ell_u}{2}\right) \tag{5.17a}$$

$$\Delta = F_u^2 \left\{ \frac{\sqrt{P_u}\ell_u\left[2 + \cos\sqrt{P_u}\ell_u\right] - 3\sin\sqrt{P_u}\ell_u}{4P_u^2\sqrt{P_u}\left(\cos\sqrt{P_u}\ell_u + 1\right)} + \frac{1/2 - \ell_u}{8P_u^2} \frac{1 - \cos\sqrt{P_u}\ell_u}{1 + \cos\sqrt{P_u}\ell_u} \right\} \tag{5.17b}$$

$$P_u = \frac{1}{N^2} \left(\frac{\pi}{1/2 - \ell_u}\right)^2 \tag{5.17c}$$

where $\ell_u = N\ell = 1/2 - \ell' = 1/2 - \pi/(N\sqrt{P_u})$.

This solution ends when the highest (or lowest) point of the hanging fold touches one of the walls. The hanging fold part is now two classic arches, which are the same as the other free branches. We have $\ell = \ell' = 1/(2+2N)$, $P = 4\pi^2\,(1+N)^2$, $F = 0$, and $H = H_\Delta/(1+N)$.

### 5.5.5 Insights from the von Kármán approximation

With the von Kármán approximation, we found that the global solution can be represented by explicit expressions. Moreover, these results are normalized by the fold number $N$, indicating the dependence of the forces on the fold number $N$, which is coherent with our analysis using the self-similarity property of the Elastica equations in section 5.3.

Recall that the system is controlled by $H$ and $\Delta$, with the expressions of von Kármán approximation, we can derive $P_u = P/N^2$ and $F_u/\sqrt{\Delta} = F/(N^3\sqrt{\Delta})$ as functions of $H_\Delta/H = (2\sqrt{\Delta})/(\pi H)$, which is called *the compact ratio*. For each deformation cycle, $P_u$ grows from $4\pi^2$, the buckling threshold, we choose to present $P_u - 4\pi^2$, such that the curve starts from zero, see figure 5.9.

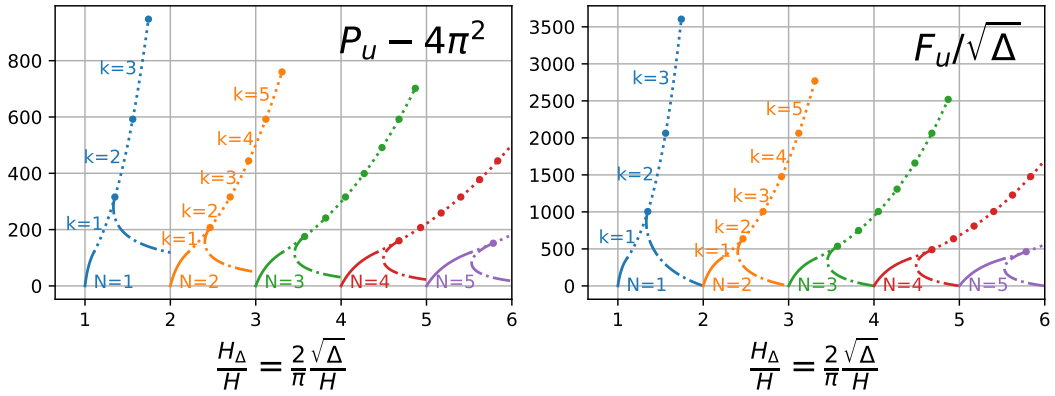


**Figure 5.9: The horizontal and vertical force responses predicted by the von Kármán approximation. The solid lines present the PtC state, the dotted lines for the ExtC state, and the dash-dot lines for the HgF state. Points are added to indicate when the ExtC state ends for different number of flat regions $k$.**

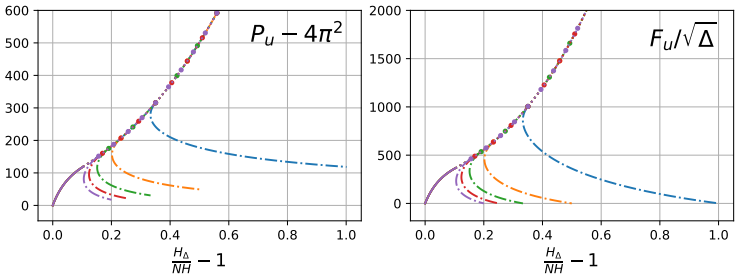


**(a) The horizontal and vertical forces as functions of the rescaled compact ratio $(H_\Delta)/(NH) - 1$**

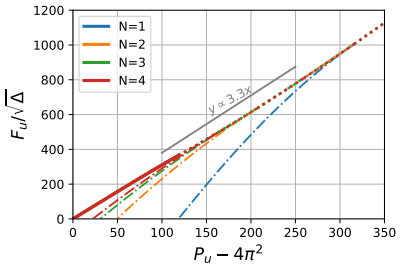


**(b) Almost linear relation between the vertical and horizontal forces.**

**Figure 5.10: Collapse of the curves. The solid lines correspond to the PtC state, the dotted lines to the ExtC state, and the dash-dot lines to the HgF state.**



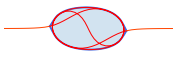

**Universal solution** We show in figure 5.10a that, using the fold number $N$, the PtC branches all collapse on a single master curve, for any $\Delta$ and any $N$. This shows the existence of a universal solution depending on the two parameters $H$ and $\Delta$ only through the rescaled compact ratio, which is also coherent with our analysis of the self-similarity of the Elastica equations. The ExtC branches also collapse, except that the higher limits on these branches are different, because it depends on the maximal number of flat regions $k$, which depends on $N$. There is no collapse for the HgF branches, which can be explained by the presence of $N$ in (5.17c).

In figure 5.10b we plot the vertical force as a function of the horizontal force with rescaled axes. As shown earlier, for PtC and ExtC states there is a universal solution independent of single parameters, and in Figure 5.10b we see the relation between $F$ and $P$ is almost linear. This linear relation implies that $F\,H \sim P\,\Delta$ which means that the work done by the horizontal and vertical loads is comparable.

**Multistability and deformation process** From figure 5.9, we see rather regular variations of the forces. The fold number $N$ increases with the compact ratio $H_\Delta/H$. When the value of $H_\Delta/H$ is larger, the forces grow less rapidly, thus the curves seem to be flattened. For large $N$, a snap-back can be observed in the HgF state. In fact, the expressions of $P_u$ and $F_u$ prove that there is always a snap-back even at $N = 1$, but it is more visible when $N$ is large. Using series expansion around transition point ExtC/HgF for $N = 1$, we find $F = 216\pi^2 H - 3888\pi^2(1/3 - \ell)H + \ldots$ and $\Delta = 9/2H^2 - 27(1/3 - \ell)H^2 + \ldots$, with $\ell$ decreasing from $\ell = 1/3$, which proves the snap-back.

When the Elastica deforms under imposed $\Delta$, the snap-back solutions are unstable, and will not be observed experimentally.

For the ExtC state, when there are more folds, the curves extend to a broader range of $H_\Delta/H$, several stable solutions exist for the same displacement load, and the largest limit pass the range of the HgF state for the same $N$. In addition to that, when the system is in ExtC state and $N$ is large, there are more choices for the number of flat regions $k$ ($1 \leq k \leq 2N + 1$), and $k$ is more likely to be large, thus the buckling of one of the flat regions happens at a larger value of $P$. As a consequence, when $N$ is large, we may pass the hanging fold state and jump to another ExtC state with more folds, see figure 5.11. And this is indeed what we observed in our numerical simulations, see for example the numerical solutions plotted in figure 5.8b.

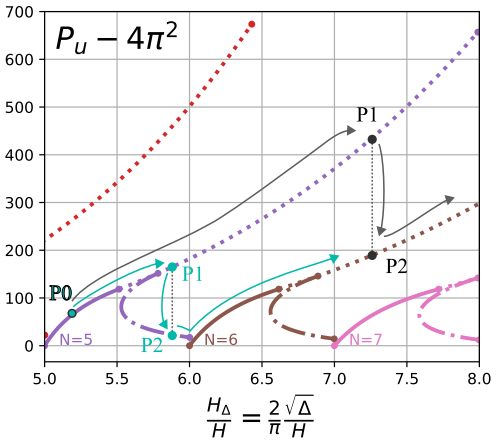


**Figure 5.11: Multistability and evolution: an example. Staring from the same point ($P0$) and increasing $\Delta$, there are more than one possible trajectories, the black and cyan lines are both possible choices. Buckling depends on the number of flat regions $k$. When $k$ is large, buckling happens much later (the black curve) than in the case of small $k$ (the cyan case).**

**Hysteresis** Apart from the multistability and its influence on the deformation process, the solutions of the von Kármán approximation can also explain the hysteresis that was observed in experiences and simulations.

In figure 5.12a, we draw the bifurcation branches of the von Kármán approximation. Supposing

we load the system with increasing $\Delta$, and it jumps from ExtC state at $P0$ ($P2$) to another ExtC state with one more fold at $P1$ ($P3$), just as what was explained earlier. Then we unload the system from $B0 = P3$ with decreasing $\Delta$. Instead of following the path from which the system arrived at $P3$, it will follow $B0 - B1$, passing from the ExtC state to PtC state, then the HgF state until it arrives at the limit point $B1$. For this value of $\Delta$, both $B2$ and $B2'$ are stable solutions, but the system will probably jump to $B2$ state because it is closer to $B1$. Then the system continues the unloading in the PtC state. Thus, when the system is loaded with increasing $\Delta$, it is mainly in the ExtC state, and when it is unloaded, it follows mainly the order of HgF-ExtC-PtC states. The sequence of events is indeed what is found in numerical simulations, see Figure 5.12b. The hysteresis shows that the loading-unloading cycle costs energy even without friction.

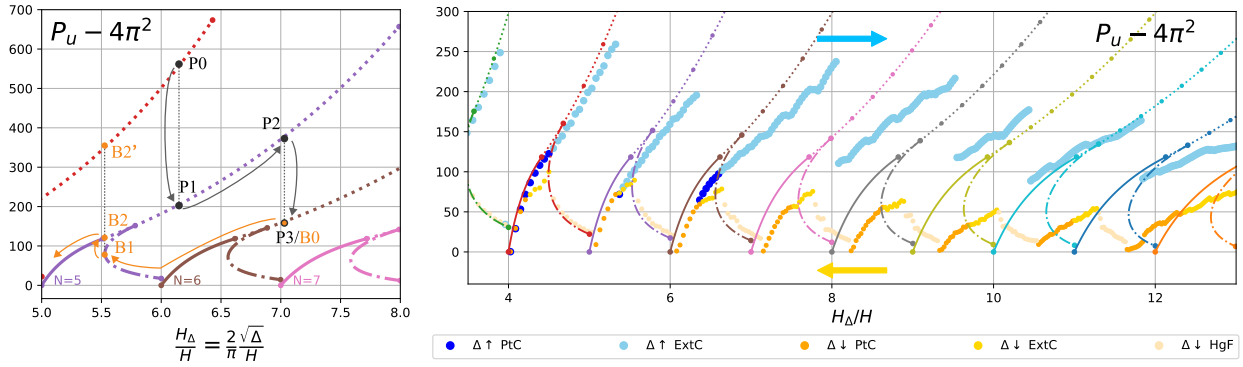


**(a) Prediction** **(b) Comparing with simulation ($H = 0.02$).**

**Figure 5.12: Hysteresis. Using the von Karman approximation, we draw the figure on the left side. We first load the system by increasing $\Delta$ from $P0$ to $P3$, then we unload the system from $B0 = P3$. On the right side, we superimpose the curves of von Kármán approximation with the simulation data. The bluish points are data of a simulation with increasing $\Delta$, while the yellowish points are from a simulation with decreasing $\Delta$.**

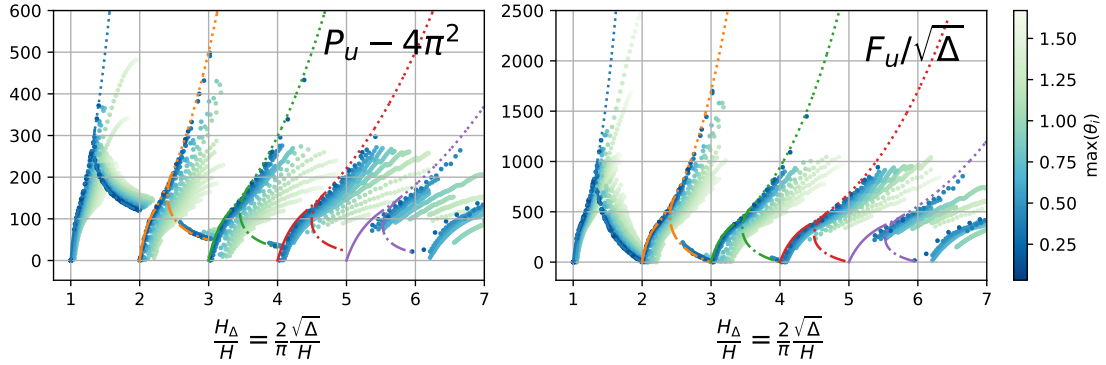


**Figure 5.13: Comparison between the total system simulation and the results from the von Kármán approximation. Each point is given by the simulation and the color of points indicates $\max\theta_i$, the darker color, the smaller $\max\theta_i$.**

**Validity of the von Kármán approximation** The von Kármán kinematic approximation is accurate only when the deformation is small, that it for small values of $\Delta$ and $H$. A measure of the deformation degree is the maximal value of the flexion angle $\theta$ (happening at the inflexion

point $s = \ell/2$), as it is a dimensionless variable related to the geometry of the system. In figure 5.13, we plot the data from the simulations with varying $H$ and $\Delta$, and superimpose the solutions found with the von Kármán approximation. The darker points are associated to smaller $\max\theta_i$, and the figure shows well that the approximation works well when $\max\theta_i$ is small, in other words, the deformation is small. Quantitatively, the approximation works well when $\max\theta_i \lesssim 0.75$.

With (5.8b), we derive

$$\max\theta = \frac{F_u}{2P_u}\left(1 - \frac{1}{\cos\left(\sqrt{P_u}\, l_u/2\right)}\right), \tag{5.18}$$

and with the above solutions, we plot $\max\theta/\sqrt{\Delta}$ as a function of the rescaled compact ratio $H_\Delta/(NH) - 1$ in figure 5.14, from which we see that $2 \leq \max\theta/\sqrt{\Delta} \lesssim 3.7$. With that, we can estimate the von Kármán approximation is valid for $3.7\sqrt{\Delta} < 0.75$, that is $\Delta \lesssim 0.04$.

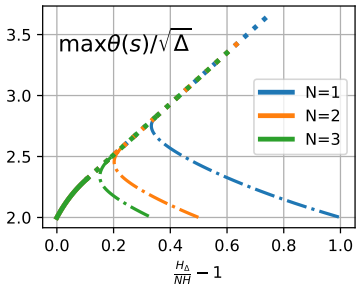


**Figure 5.14: $\max\theta$ with von Kármán approximation**

## 5.6 Cellular models

The analytical models introduced so far were based on the idea of splitting the global system into an integer number of arches. However, to predict the general behaviors of the system without entering into details of morphology, one could lift this restriction and allow the system to be composed of a real number of repeats of the same cell. We call these kinds of models *cellular models*, see figure 5.15.

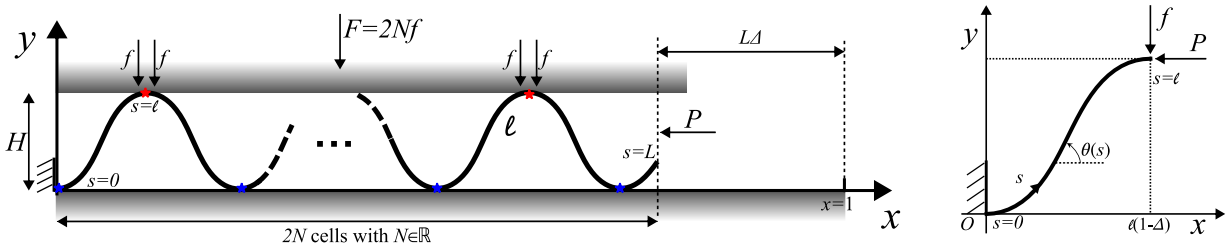


**(a) Cellular model** **(b) One cell**

**Figure 5.15: Cellular model of the wall-attached confined Elastica**

Recall that in the models introduced previously, the length of a branch $\ell$ is determined by the fold number. In the cellular model, the fold number is an unknown real number, so we need to add one more condition into the system of equations to find $\ell$. Here we propose two ways, the first is to use one of the classic conditions for the transition between two different configurations. This is similar to how the transition lines in the phase diagrams are found (see section 5.4). The second is to consider $\ell$ as an unknown when minimizing the total energy of the system.

### 5.6.1 Cellular models for configuration transition

**HgF/PtC transition** At the HgF/PtC transition, the hanging fold just touches one of the walls, and the vertical force of one free branch is zero, see figure 5.16a. Thus, for a given pair of

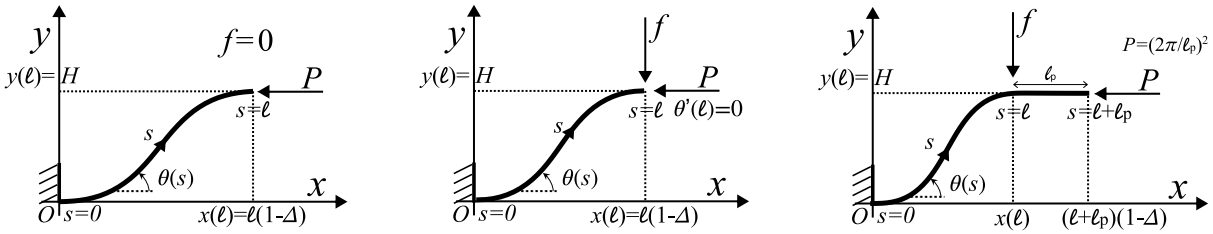


**(a) HgF/PtC transition** **(b) PtC/ExtC transition** **(c) ExtC/HgF transition**

**Figure 5.16: Transitioning cellular models**

$(\Delta, H)$, we solve

$$x'(s) = \cos\theta(s), \qquad y'(s) = \sin\theta(s), \tag{5.19a}$$
$$\theta''(s) = -P\sin\theta(s), \qquad s \in [0, \ell] \tag{5.19b}$$

with boundary conditions

$$\theta(0) = \theta(\ell) = 0, \quad x(0) = y(0) = 0, \quad x(\ell) = \ell(1-\Delta), \quad y(\ell) = H. \tag{5.20}$$

The unknowns of the system are $\theta(s)$, $x(s)$, $y(s)$. In the shooting procedure, we have 6 unknowns: $P$, $\ell$, and 4 initial conditions for the 2 first-order and the second-order ordinary differential equations. This is balanced by the 6 boundary conditions, so the system is closed.

Solving the system gives a prediction for the force responses $P$, and also the fold number, which is derived from $\ell$: $N = 1/(2\ell)$.

**PtC/ExtC transition** At the PtC/ExtC transition, the bending moment at two ends of the free branches becomes zero, see figure 5.16b. From the direct integration of Elastica equation, we have (C.2). As $\theta'(0) = \theta'(\ell) = 0$, then for a given pair of $(\Delta, H)$, we solve

$$x'(s) = \cos\theta(s), \qquad y'(s) = \sin\theta(s), \tag{5.21a}$$
$$\theta'(s) = -P\,y(s) + f\,x(s), \qquad s \in [0, \ell] \tag{5.21b}$$

with boundary conditions

$$\theta(0) = \theta(\ell) = 0, \quad x(0) = y(0) = 0, \quad x(\ell) = \ell(1-\Delta), \quad y(\ell) = H. \tag{5.22}$$

The unknowns of the system are $\theta(s)$, $x(s)$, $y(s)$, $f$, $P$ and $\ell$, and we have 3 first-order ordinary differential equations, 6 boundary conditions, so the system is closed. Please remark that the condition $\theta'(0) = \theta'(\ell) = 0$ disappears from this system, but when it is applied to equation (5.21b), we have $PH = f\ell(1-\Delta)$.

As in the previous case, solving the system gives a prediction for the force responses $P$ $f$, and for the fold number $N = 1/(2\ell)$.

**ExtC/HgF transition** Compared to the previous two cases, we need more assumptions to define the cell model for the ExtC/HgF transition due to the indeterminate distribution of the respective lengths of the flat regions. As the cellular models represent the system by a repetition of the same cell, we assume the cell of ExtC/HgF transition to consist of an arch of length $\ell$ followed by a flat region of length $\ell_p$, see figure 5.16c.

At ExtC/HgF transition, the bending moment at two ends of the free branches still vanishes $(\theta'(0) = \theta'(\ell) = 0)$, same as the PtC/ExtC transition, thus we have the same differential equations



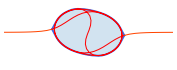

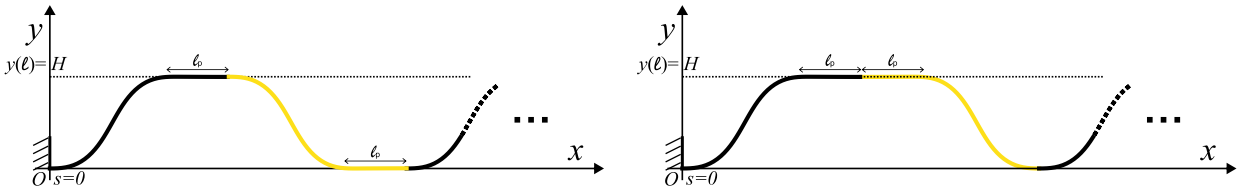


**(a) First way to assemble ExtC/HgF cells.** ($k = 2N$)

**(b) Second way to assemble ExtC/HgF cells.** ($k = N$)

**Figure 5.17: Two ways to assemble ExtC/HgF cells. This affects the computed value of the force $P$.**

(5.21), but the force $P$ is given by the buckling threshold of the flat regions. There are two ways to assemble the cells, see figure 5.17. In the first way (figure 5.17a), the length of each flat region is $\ell_p$, there are in total $k = 2N$ flat regions, and the buckling threshold is $P = 4\pi^2/\ell_p^2$, while in the other way (figure 5.17b), the length of each flat region is $2\ell_p$, there are in total $k = N$ flat regions, and the buckling threshold is $P = \pi^2/\ell_p^2$. Therefore, the transition happens at a smaller $\Delta$ when the second definition is used. It is rarer that the flat regions fragment to a number matching the fold number, thus the first configuration of the ExtC/HgF model is further from simulation results or experimental observations than the second configuration. Thus, only the second configuration is considered for further discussions.

Both ways of assembling have the same boundary conditions

$$\theta(0) = \theta(\ell) = 0, \quad x(0) = y(0) = 0, \quad x(\ell) + \ell_p = (\ell + \ell_p)(1 - \Delta), \quad y(\ell) = H. \tag{5.23}$$

The unknowns of the system are $\theta(s)$, $x(s)$, $y(s)$, $f$, $\ell$ and $\ell_p$. The force $P$ is related to $\ell_p$. We have 3 first order ordinary differential equations, 6 boundary conditions, the system is closed.

The solution of this system of equation gives the force responses $f$ and $P$ (given by $\ell_p$). The number of folds in this case is $N = 1/[2\,(\ell + \ell_p)]$.

**Von Kármán approximation of the transitional cellular model** All the three transitional cellular models have approximated solutions, which are directly derived from the solutions presented in section 5.5. In the following table, we present the results of the forces $P$ and $F$, the fold number $N$, and the total energy $\mathcal{E}_{tot}$ as functions of end shortening $\Delta$ and the height $H$:

| | $P$ | $F$ | $N$ | $\mathcal{E}_{tot} = 2NE_\kappa$ |
|---|---|---|---|---|
| HgF/PtC | $16\frac{\Delta}{H^2}$ | 0 | $\frac{2}{\pi}\frac{\sqrt{\Delta}}{H} \approx 0.64\frac{\sqrt{\Delta}}{H}$ | $16\frac{\Delta^2}{H^2}$ |
| PtC/ExtC | $\frac{16\pi^2}{3}\frac{\Delta}{H^2} \approx 52.6\frac{\Delta}{H^2}$ | $\frac{64\pi^2}{9}\frac{\Delta^2}{H^3} \approx 70.2\frac{\Delta^2}{H^3}$ | $\frac{1}{\sqrt{3}}\frac{\sqrt{\Delta}}{H} \approx 0.58\frac{\sqrt{\Delta}}{H}$ | $\frac{16\pi^2}{9}\frac{\Delta^2}{H^2} \approx 17.6\frac{\Delta^2}{H^2}$ |
| ExtC/HgF | $8\pi^2\frac{\Delta}{H^2} \approx 79.0\frac{\Delta}{H^2}$ | $\frac{32\pi^2}{3}\frac{\Delta^2}{H^3} \approx 105.3\frac{\Delta^2}{H^3}$ | $\frac{\sqrt{2}}{3}\frac{\sqrt{\Delta}}{H} \approx 0.47\frac{\sqrt{\Delta}}{H}$ | $\frac{8\pi^2}{3}\frac{\Delta^2}{H^2} \approx 26.3\frac{\Delta^2}{H^2}$ |

**Table 5.1: Formulas for the forces $P$ and $F$, the fold number $N$ and the total bending energy $2NE_\kappa$ as functions of the end shortening $\Delta$ and the height $H$ in the von Kármán approximation.**

### 5.6.2 Global cellular model

In the global cellular model, we consider an arch solution of unknown length $\ell$, see figure 5.15b. In order to find a condition matching this supplementary unknown, we proceed to minimize the total energy of the problem

$$\min_{\theta(s),x(s),y(s),\ell} \quad \mathcal{E}_{tot} = 2N \cdot \mathcal{E}_{cell} = \frac{1}{\ell}\left[\int_0^\ell \frac{1}{2}\theta'^2(s)\,ds\right] \tag{5.24a}$$

$$\text{subject to} \quad x'(s) = \cos\theta(s), \quad y'(s) = \sin\theta(s), \qquad s \in [0,\ell] \tag{5.24b}$$

$$\theta(0) = \theta(\ell) = 0, \quad x(0) = y(0) = 0, \tag{5.24c}$$

$$x(\ell) = \ell(1-\Delta), \quad y(\ell) = H \tag{5.24d}$$

Here we use the classical variational approach and construct the Lagrangian:

$$\mathcal{L}(\theta, x, y, \ell) = \frac{1}{\ell}\left\{\int_0^\ell \frac{1}{2}\theta'^2(s) + n_x(s)[x'(s) - \cos\theta(s)] + n_y(s)[y'(s) - \sin\theta(s)]\,ds\right\}, \tag{5.25}$$

where $n_x(s)$, $n_y(s)$ are continuous Lagrange multipliers, defined in $s \in [0,\ell]$.

It is similar to the Lagrangian of the Planar Elastica problem, but in this case the boundary is defined by a variable $\ell$. When applying the variational method, one should also consider the variation of the boundary $s = \ell$ in the same way that we have shown with the sliding sleeve example (see equation (4.17)):

$$\bar\theta(\ell) + \bar\ell\theta'(\ell) = 0, \quad \bar x(\ell) + \bar\ell x'(\ell) = \bar x(\ell) + \bar\ell = \bar\ell(1-\Delta), \quad \bar y(\ell) + \bar\ell y'(\ell) = \bar y(\ell) = 0. \tag{5.26}$$

And the variation of the Lagrangian is

$$\begin{aligned}\bar{\mathcal{L}} =& \frac{1}{\ell}\left\{\int_0^\ell \left(-\theta''(s) + n_x(s)\sin\theta(s) - n_y(s)\cos\theta(s)\right)\,\bar\theta(s) - n_x'(s)\,\bar x(s) - n_y'(s)\,\bar y(s)\,ds\right\} \\ &+ \frac{1}{\ell}\left\{-\frac{1}{2}\theta'^2(\ell)\,\bar\ell + n_x(\ell)\underbrace{\bar x(\ell)}_{=-\Delta\,\bar\ell} + n_y(\ell)\underbrace{\bar y(\ell)}_{=0}\right\} - \frac{\bar\ell}{\ell}\mathcal{L}\end{aligned} \tag{5.27}$$

At minimum, $\bar{\mathcal{L}} = 0$ for all the admissible variations, and we have the system of differential / integral equations

$$x'(s) = \cos\theta(s), \qquad y'(s) = \sin\theta(s) \tag{5.28a}$$

$$\theta''(s) = -P\sin\theta(s) + f\cos\theta(s), \qquad s \in [0,\ell] \tag{5.28b}$$

$$\frac{1}{\ell}\int_0^\ell \frac{1}{2}\theta'^2\,ds + \left[\frac{1}{2}\theta'^2(\ell) - P\cdot\Delta\right] = 0, \tag{5.28c}$$

where the Lagrange multipliers $n_x(s) = -P$ and $n_y(s) = -f$ are the $x$ and $y$ components of the internal force.

Just as for the relation C.4 in the appendix C, note that we can use the first order integral C.3 to calculate the integral in equation 5.28c and arrive at the relation

$$\frac{1}{2}\theta'^2(\ell) - P\cdot\Delta + \frac{f}{2}\frac{y(\ell)}{\ell} = 0 \tag{5.29}$$

Solving these equations with boundary conditions (5.24c) and (5.24d), we obtain the general force responses $P$ and $f$, and also a prediction of the fold number with $N = 1/(2\ell)$.



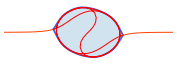

Please note that in addition to the equations of the classical planar Elastica problem, we have the additional equation (5.28c). It comes from the fact that $\ell$ is also a variable in the minimization problem. Moreover, $\ell$ is linked to the varying boundary, similar to the mechanical systems in which *configurational forces* are present, as we mentioned in section 4.2. However, in this case, we cannot conclude that the additional equation is related to some configurational forces, and the physical nature of (5.28c) is still to be discussed.

**The von Kármán approximation** The von Kármán approximation can also be applied to the global cellular model, and the differential equations are the same as (5.7). The only difference from section 5.5 is that here the arch length $\ell$ is an unknown to be solved with the additional equation (5.28c).

Since the solutions (5.9) are calculated by the boundary conditions that are included in the global cellular model, these solutions are also valid here, and we can apply (5.9) in the equation (5.28c) and derive $\ell\sqrt{P} = \tan\left(\ell\sqrt{P}\right)$. Because $0 < \ell\sqrt{P} \leq 2\pi$, we can find $\ell\sqrt{P} \approx 4.5$.

Then, applying boundary conditions on $x(\ell)$ and $y(\ell)$ with (5.9c), (5.9b) and $\ell\sqrt{P} \approx 4.5$, we find

$$f^2\ell^4 = 262.153\,\Delta, \qquad f\ell^3 = 12.984\,H.$$

Please note that the fold number is $N = 1/(2\ell)$, and the total vertical reaction from the walls is $F = 2N\,f = f/\ell$, and the solution may be presented with different variables, see table 5.2

| | $P$ | $F$ | $\mathcal{E}_{tot} = 2NE_\kappa$ | – |
|---|---|---|---|---|
| $(\Delta, H)$ | $31\frac{\Delta}{H^2}$ | $31\frac{\Delta^2}{H^3}$ | $16\frac{\Delta^2}{H^2}$ | $N = 0.62\frac{\sqrt{\Delta}}{H}$ |
| $(\Delta, N)$ | $81\,N^2$ | $130\,N^3\sqrt{\Delta}$ | $40\,\Delta N^2$ | $H = 0.62\frac{\sqrt{\Delta}}{N}$ |
| $(H, N)$ | $81\,N^2$ | $208\,HN^4$ | $104\,H^2N^4$ | $\Delta = 2.6\,H^2N^2$ |

**Table 5.2: Formulas for the forces $P$ and $F$, the total bending energy $2NE_\kappa$, the end shortening $\Delta$, the height $H$, and the fold number $N$ for the cellular model in the von Kármán approximation, as functions of different pairs of variables.**

In figure 5.18, we plot the forces and the fold number found by nonlinear simulations, and the global cellular model in the non-linear setup and in the von Kármán approximation, for $H = 0.1$. Please remark that we especially chose the quantities $P\,H^2$, $F\,H^3$ and $N\,H$. This is because from the expressions shown in table 5.2, these quantities do no depend on the wall distance $H$. Good consistency is observed between the three results. As expected, the von Kármán approximation matches especially well with the non-linear solution when $\Delta$ is small. This proves the validity of the concerned models.

When the pair of variables $(\Delta, H)$ is chosen to express the forces, we see that $P$ varies linearly, and $F$ varies quadratically with $\Delta$. Moreover, in figure 5.19, we compare the force $P$ needed to push the Elastica into a tunnel with wall height $H$ to that of an unconstrained Elastica. For the unconstrained Elastica, $P$ grows approximately linearly with a slope of $2\pi^2$, which can be found by considering the non-linear Elastica equations, see for example Bazant and Cedolin (2010). In the constrained case, the global cellular model predicts that $P$ grows linearly with a slope of $31/H^2$, where $H$ is much smaller than 1. Thus, $P$ grows much more rapidly in the presence of walls.

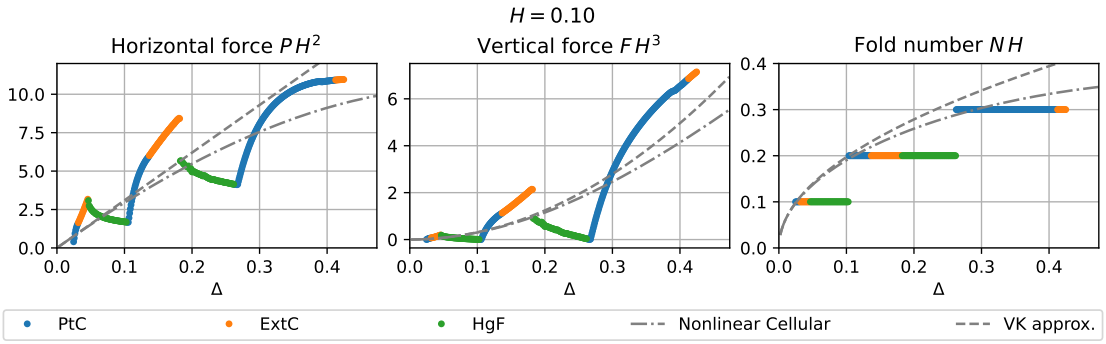


**Figure 5.18: Comparison between the simulation, non-linear solution and von Kármán approximation of the global cellular model.**

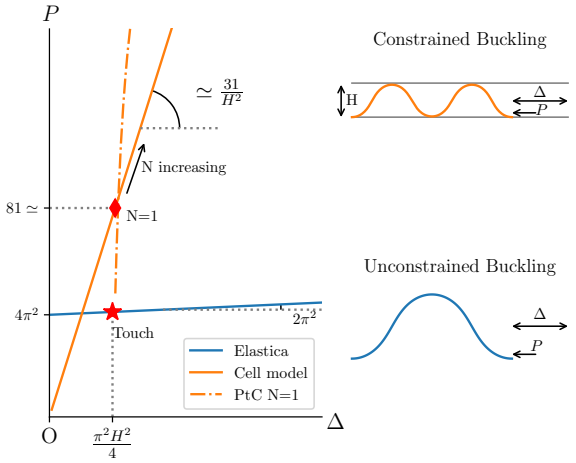


**Figure 5.19: The horizontal force needed to compress a constrained elastic rod predicted by the von Kármán approximation of the global cellular model (orange) and that of an unconstrained Elastica (blue). The solution found by simulation (dash-dot line) is also added. Please note that here we consider the case in which Δ is small.**

### 5.6.3 Self-similarity of the cellular models

In section 5.3, we mentioned that the system of equation of the Elastica is self-similar. The self-similarity also apply to all the cellular models.

We introduce the self-similar variables

$$\widehat{\theta}(\widehat{s}) = \theta(s), \quad \widehat{x}(\widehat{s}) = \frac{x(s)}{\ell}, \quad \widehat{y}(\widehat{s}) = \frac{y(s)}{\ell}, \quad \widehat{P} = P\,\ell^2, \quad \widehat{f} = f\,\ell^2, \quad \widehat{s} = \frac{s}{\ell} \in [0,1], \tag{5.30}$$

to 'scale' the original arch with unknown length $\ell$ to a fixed length $\widehat{\ell} = 1$. Given the dimensionless displacement control $\Delta$, solutions of the self-similar system can be rescaled to any configuration of different wall height $H$. The energy calculated by the self-similar system can also be rescaled back by

$$\mathcal{E} = \widehat{\mathcal{E}}/\ell, \qquad \text{with } \widehat{\mathcal{E}} = \int_0^1 \frac{1}{2}\widehat{\theta}'^2(\widehat{s})\, d\widehat{s} \tag{5.31}$$

Please note that the solutions of the cellular models only concern equilibria, the stability of which needs further investigation. In fact, the stability analysis of the global solution is also valid after rescaling back to configurations with any wall height $H$.

This reduces the solving and analysis for configurations with different $H$, and we call these solutions *the self-similar solutions* or *the global solutions*.

**HgF/PtC and PtC/ExtC transition** Compared to the original model, the self-similar model has one less variable (the length of the arch $\ell$), so one less boundary condition is needed, we choose to remove the condition on $\widehat{y}(1)$, and this is valid for both HgF/PtC and PtC/ExtC cellular models. Thus, the value of $\widehat{y}(1)$ comes from the solution. To rescale the global solution to a configuration with wall height $H$, one find the arch length $\ell$ by

$$\ell = H/\widehat{y}(1), \tag{5.32}$$

with which one can find other variables using (5.30).

**ExtC/HgF transition** The solution of ExtC/HgF cellular model can be derived from the solutions of the self-similar PtC/ExtC cellular model. The length scale $\ell$ is still calculated with the help of (5.32), but a new displacement control parameter $\widetilde{\Delta}$, different from the original $\Delta$, should be derived as follows:

$$\widehat{x}(1) + \hat{\ell}_p = (1 + \hat{\ell}_p)(1 - \widetilde{\Delta}) \quad \Rightarrow \quad \widetilde{\Delta} = 1 - \frac{\widehat{x}(1) + \hat{\ell}_p}{1 + \hat{\ell}_p}, \tag{5.33}$$

where $\hat{\ell}_p = 2\pi/\sqrt{\widehat{P}}$ when cells are assembled as in figure 5.17a, or where $\hat{\ell}_p = \pi/\sqrt{\widehat{P}}$ when cells are assembled as in figure 5.17b.

**The global cellular model** From (5.28)-(5.29), the rescaled equations for the global cellular model are

$$\widehat{x}'(\widehat{s}) = \cos\widehat{\theta}(\widehat{s}), \qquad \widehat{y}'(s) = \sin\widehat{\theta}(\widehat{s}), \tag{5.34a}$$

$$\widehat{\theta}''(\widehat{s}) = \widehat{n}_x \sin\widehat{\theta}(\widehat{s}) - \widehat{n}_y \cos\widehat{\theta}(\widehat{s}), \qquad \widehat{s} \in [0,\, 1] \tag{5.34b}$$

$$\frac{1}{2}\widehat{\theta}'^2(1) - \widehat{P}\cdot\Delta + \frac{\widehat{f}}{2}\widehat{y}(1) = 0 \tag{5.34c}$$

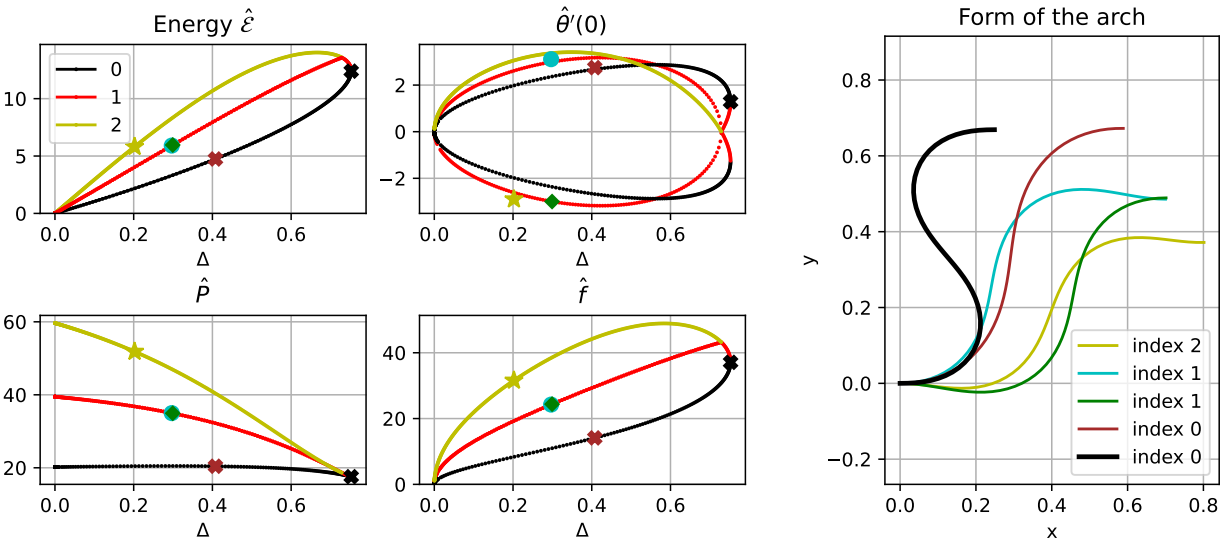


**Figure 5.20: Branches of equilibria of the global cellular model as functions of Δ. The different colors mark different stability indices. Along the branches, 5 points are chosen, and their corresponding shapes are plotted on the right.**

with boundary conditions

$$\widehat{\theta}(0) = \widehat{\theta}(1) = 0, \quad \widehat{x}(0) = \widehat{y}(0) = 0, \quad \widehat{x}(1) = 1 - \Delta. \tag{5.35}$$

We use the same methods presented in section 1.7.2 to calculate the equilibria and the related stability, the results are shown in figure 5.20.

On the left side of figure 5.20, we show the values of the energy, bending moment at $\widehat{s} = 0$ and the forces as functions of Δ. These branches are found by the arc-length continuation method, and several bifurcation points are found.

Recall that the stability index equals the number of negative eigenvalues of the projected Hessian matrix of the discretized system, one equilibrium is stable only if the stability index is zero. As one can see from the figure 5.20, there is only one stable branch, which starts at $\Delta = 0$ and ends at the limit point $\Delta \approx 0.73$.

We plot the form of the arch at 5 chosen points on the branches on the right of figure 5.20. The yellow arch is on an unstable branch (with 2 positive eigenvalues), and the form is symmetric with respect to its middle point. The cyan and green arches have the same value of $\widehat{P}$, $\widehat{f}$ and opposite values of $\widehat{\theta}'(0)$, and their forms are symmetric. In fact, the $\widehat{\theta}'(0)$ branch itself is symmetric, which is related to the symmetry of the system of differential equations. The cyan and green arches reflect how this symmetry manifests in the form. The brown and black points are on the stable branch, which is the most important branch for further analysis. Please notice that no curve passes $\Delta = 0.75$, and the form of the arch at maximum Δ is shown by the black arch.

Please notice that for the self-similar global cellular model, we do not impose any condition on $\widehat{y}(1)$, just as for the self-similar HgF/PtC and PtC/ExtC models. The way to rescale the self-similar solution to that of a configuration with wall height $H$ is the same for the three models: (i) find the arch length $\ell$ with solution $\widehat{y}(1)$ and (5.32), and then (ii) compute the other variables with (5.30).

**Self-similarity and universal solutions** In section 5.5, using the von Kármán approximation, we have found the expressions of forces scaled by the fold number $P_u = P/N^2$, $F_u = F/N^3$ as



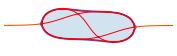

functions of the compact ratio. Earlier in this section, the von Kármán approximation of the global cellular model gives expressions of forces scaled by the wall distance $P\,H^2$, $F\,H^3$ as functions of $\Delta$. These are all closely related to the self-similarity of the Elastica equations, and with the cellular models, we can further express these scaled quantities with the self-similar solutions only.

The key point is the length scale $\ell$ by (5.32), and the real fold number $N$ related to $\ell$. For HgF/PtC, PtC/ExtC and global cellular models, we have

$$N = \frac{1}{2\ell} = \frac{\hat{y}(1)}{2H},$$

and for the ExtC/HgF model, we have

$$N = \frac{1}{2\ell(1+\hat{\ell}_p)} = \frac{\hat{y}(1)}{2H(1+\hat{\ell}_p)}.$$

And we also see that $N\,H$ predicted by the cellular models does not depend on the wall distance $H$.

Then, the forces can be expressed by the self-similar solutions:

$$P = \hat{P}/\ell^2 = 4N^2\hat{P} = \hat{P}\,\hat{y}^2(1)/H^2, \quad \text{(all cellular models)} \tag{5.36a}$$

$$F = 2N\hat{f}/\ell^2 = 8N^3\hat{f} = \hat{f}\,\hat{y}^3(1)/H^3 \quad \text{(HgF/PtC, PtC/ExtC, global)}, \tag{5.36b}$$

$$\text{or} \quad F = 8N^3\hat{f}(1+\hat{\ell}_p) = \frac{\hat{f}\,\hat{y}^3(1)}{H^3(1+\hat{\ell}_p)} \quad \text{(Ext/HgF)}. \tag{5.36c}$$

As a consequence, for all the cellular models, $P\,H^2$, $F\,H^3$, $P/N^2$ and $F/N^3$ are given by the self-similar solutions only: they are independent of the wall distance $H$ and only depend on $\Delta$.

### 5.6.4 Prediction of the cellular models

In this section, we introduced two types of cellular models, the transitional cellular models and the global cellular model.

In figure 5.21, we show the fold number and forces predicted by the cellular models together with the data of the simulation for a fixed wall height $H = 0.1$.

For the forces, we can see that the simulation data stay inside the HgF/PtC and ExtC/HgF cellular models, which are respectively the lower and upper limits. Please note that the ExtC/HgF cell is based on the second configuration, which considers a lesser number of flat regions, $k = N$. However, it still overpredicts the forces, which means that the number of flat regions is also overpredicted.

The curves for the HgF/PtC and PtC/ExtC models pass exactly through the transitional points between different configurations, which is expected from the way these models were constructed. The global cellular model passes through the PtC states, which is also reasonable owing to the model setup.

The cellular models not only capture the global tendency of the forces $P$ and $F$, and of the fold number $N$, but also the shape of the solution. Indeed, when the cellular models predict an integer value of $N$, the cell form can be superimposed on the simulation solutions. This proves the capacity of the relatively simple cellular models to reflect the complex behavior of the whole system.

Figure 5.21 shows the solutions of a case with rather large $H$, thus the maximum number of folds is relatively small. Recall that the multi-stability and hysteresis are more prominent when there are more folds, and this is the case for small $H$.

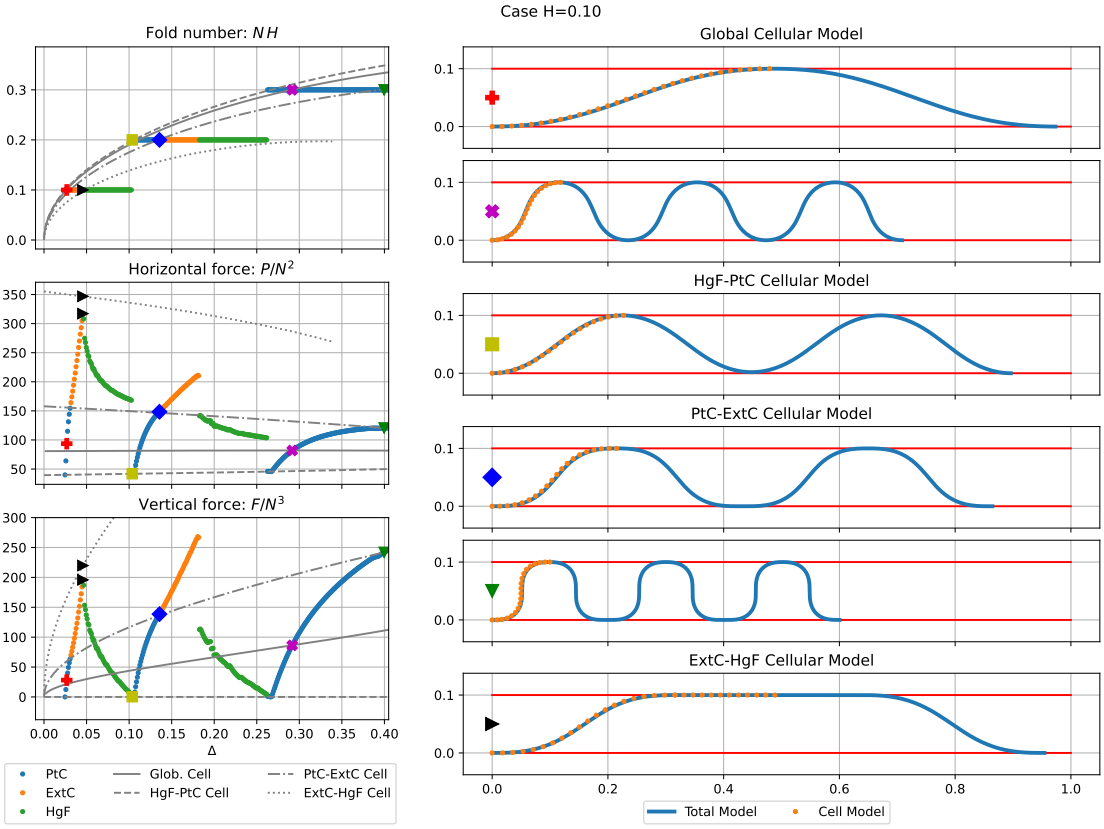


**Figure 5.21: Comparing the cellular models with simulation data for $H = 0.1$. The fold number, the forces are plotted as functions of $\Delta$. Several forms predicted by the cellular models are compared with the simulation results when $N$ of the cellular models is integer, the solutions are marked by the same marker on the left side.**

In figure 5.22, we show the cellular models predictions with the simulation data for $H = 0.01$. While the quantities $N\,H$, $P/N^2$, $F/N^3$, $P\,H^2$ and $F\,H^3$ given by the cellular models are universal, and only depend on $\Delta$, the results of the IPOPT simulation is not. Although the simulation data still stay in the same range as the cellular model predictions, the 'period' of the variation is different. Compared to the data of large $H$ values (for example figure 5.21), the jagged pattern in force variation is denser for small $H$.

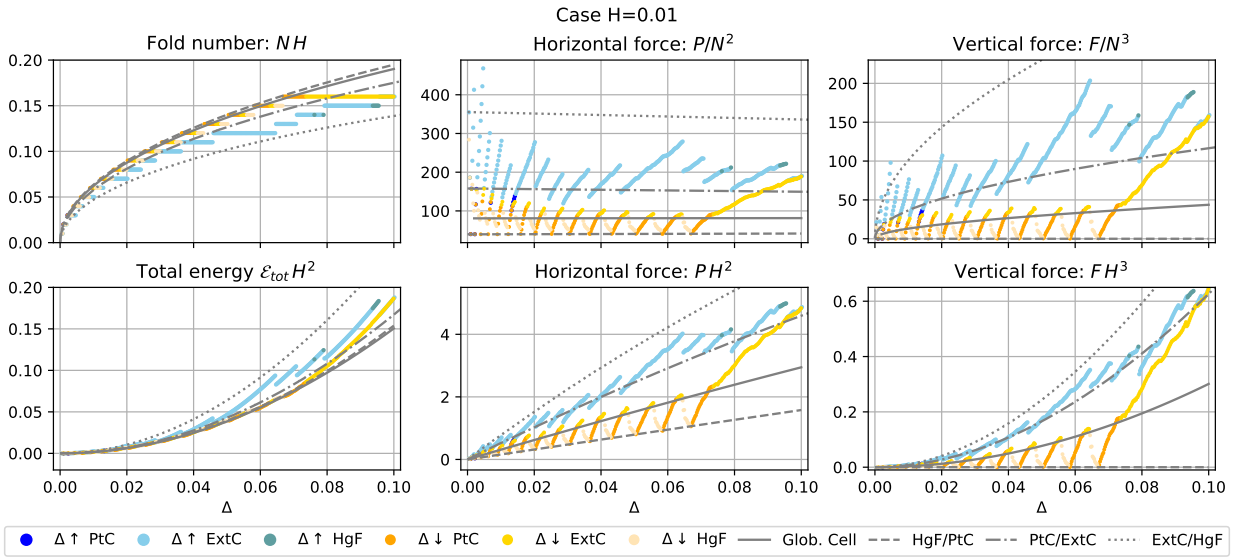


**Figure 5.22: The fold number, the energy and the forces found by the simulation and predicted by the cellular models. The simulation data combines the increasing-decreasing loading process, with** $\max \Delta = 0.1$**.**

For the simulation data with small $H$, hysteresis can be observed. When $\Delta$ increases, the system tends to stay in the ExtC state, thus the value of the forces are larger. And during the unloading process, the system mainly deforms in HgF-ExtC-PtC order, and the forces are smaller compared to the loading process. Nevertheless, the forces given by the simulation data still stay between the HgF/PtC cell and the ExtC/HgF cell prediction. Furthermore, the loading data stay above the global cellular line, while the unloading data stay mostly beneath the global cellular line. Apart from that, the global cellular model has the lowest total energy among all the cellular models, which can be explained by the construction of the model, in which we tried to minimize the total energy with varying $\ell$. Once again, the ExtC/HgF cell overpredicts the forces, which means that during the simulations, the flat region is most likely to be split into $k$ fragments with $k$ smaller than the fold number $N$. As a consequence, the ExtC/HgF model underestimates the fold number and overestimates the total energy of the system. Although the lower limit of the forces still sticks to the prediction from HgF/PtC cell model, the PtC/ExtC line no longer passes through the transitional states of the simulation data. This may be due to the higher level of complexity and multistability when the number of folds is large.

## 5.7 Conclusions

In this chapter, we introduced the problem of an Elastica confined between two rigid walls of distance $H$. More precisely, the two ends of the Elastica are clamped and attached to one of the walls, and it deforms under imposed displacement $\Delta$. To sum up, the system is controlled by a given pair of parameters $(\Delta, H)$.

We have been interested in describing the shape of the beam and the force responses of the system. The investigation employed several approaches, including numerical simulations and theoretical analysis. Several models were proposed, and their predictions were compared with the simulation data. The theoretical models are based on solving by parts, meaning to solve the Elastica equation with imposed constraints for each free branch in the system. Thanks to the self-similarity of the Elastica equation, we can predict without calculations that the force responses of the system scale with fold number $N$. The self-similarity also turned out to be very helpful to other analytical models.

The first application of solving by parts is to find the transition lines in the $(\Delta, H)$ diagrams, with which one is able to predict the fold number $N$ and the configuration of the system for a given pair of $(\Delta, H)$. Furthermore, the von Kármán kinematic approximation was introduced. After applying the approximation, explicit solutions were derived, which were thereafter used to explain in detail the responses of the confined Elastica under relatively small displacement. It has been shown that these solutions are universal, can be scaled with the fold number $N$, and do not depend on individual parameters $\Delta$ and $H$, but rather on the compact ratio $H_\Delta/H$. This is coherent with the self-similarity mentioned earlier, and very useful for the theoretical analysis. The explicit solutions of the von Kármán approximation also show the complexities of the system, including multistability and hysteresis.

After that, we lifted the constraint that the system should be composed by an integer number of free branches, and introduced the cellular models, which consider the number of branches to be a real number instead of an integer. Thanks to the self-similarity, these cellular models can capture the evolution of the deforming system with a universal solution. Regardless of the simplicity, the cellular models turned out to be relevant and informative, and can exactly match the whole system simulations when the predicted fold number $N$ is an integer.

To conclude, we have shown that the physics behind the constrained Elastica problem is rich. There are still a lot of aspects that can be further investigated, including the maximal number of folds that can be reached given a wall height $H$, the post-buckling behaviors after this limit point, not to mention the different ways of loading (loading by forces, vertical compression, etc.) and the different types of fixation. In the next chapter, we will change the position of fixation, and discuss the differences and similarities with the problem of this chapter.



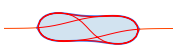

# Chapter 6

# Centered configuration

In the previous chapter, we studied the deformation and force reactions of an Elastica pushed through a tunnel with displacement control. The two extremities of the Elastica were clamped and attached to the lower wall of the tunnel, thus we call it the wall-attached configuration. In this chapter we consider a slightly different case, in which the Elastica is clamped midway between the walls, see figure 6.1, and we call this *the centered configuration*.

Once again, the length and bending stiffness of the Elastica are respectively $L$ and $EI$, and the system is adimensionalized with length unit $L$ and force unit $EI/L^2$. The distance between the upper and lower walls is still marked by $H$, but here the two ends are placed midway between the two walls, thus the distance between the support and one of the walls is $a$, with $H = 2a$. The force responses of the support and the walls are respectively $P$ and $F$, which are the same notations as in the wall-attached configuration.

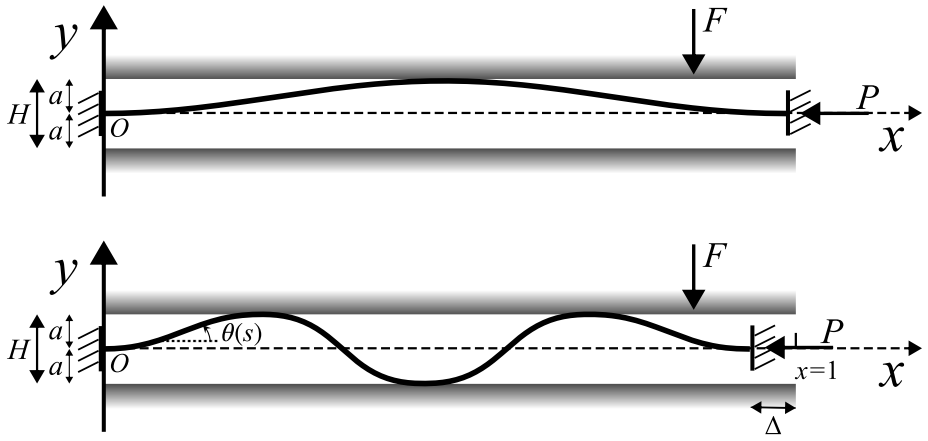


**Figure 6.1: Centered confined Elastica: Illustration of different configurations with different arch number $n$.**

Regarding the boundary conditions, there are numerous variations, including the type of fixation (clamped or pinned), the loading (force or displacement control), the height of the fixation with respect to the walls, etc. Although passing from the wall-attached to the centered configuration is only one small variation, here we will show that it induces some changes that can be generalized to configurations with different fixation heights.

For the centered configuration, we will introduce some new approaches to model the wall constraints. The evolution process of the deformation and the form of the system is no longer emphasized, but the force responses are still one of the focus of the study. Moreover, the stability



of the solutions will be discussed in detail for the centered configuration.

## 6.1 Energy minimization of the discretized system

The discretized system used for the simulations by energy minimization is illustrated in figure 6.2.

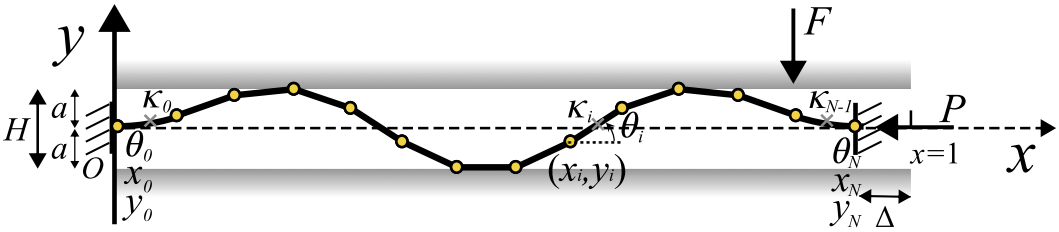


**Figure 6.2: Discretized system of the centered configuration.**

**Minimization with CasADi and IPOPT** When CasADi and IPOPT are used, the implementation is not much different from the wall-attached configuration, except for the definition of the wall constraints. Instead of condition 5.1d, we now have

$$a + y_i \geq 0 \text{ and } a - y_i \geq 0, \quad \forall i = 1, 2, ..., N-1. \tag{6.1}$$

The solving method and the signification of the Lagrange multipliers remain the same as what has been presented in section 5.1.

With the help of CasADi and IPOPT, we are able to run 'numerical experiments' and obtain the equilibrium solutions of the confined Elastica under centered clamps. The results for the case $a = 0.05$ are shown in figure 6.3.

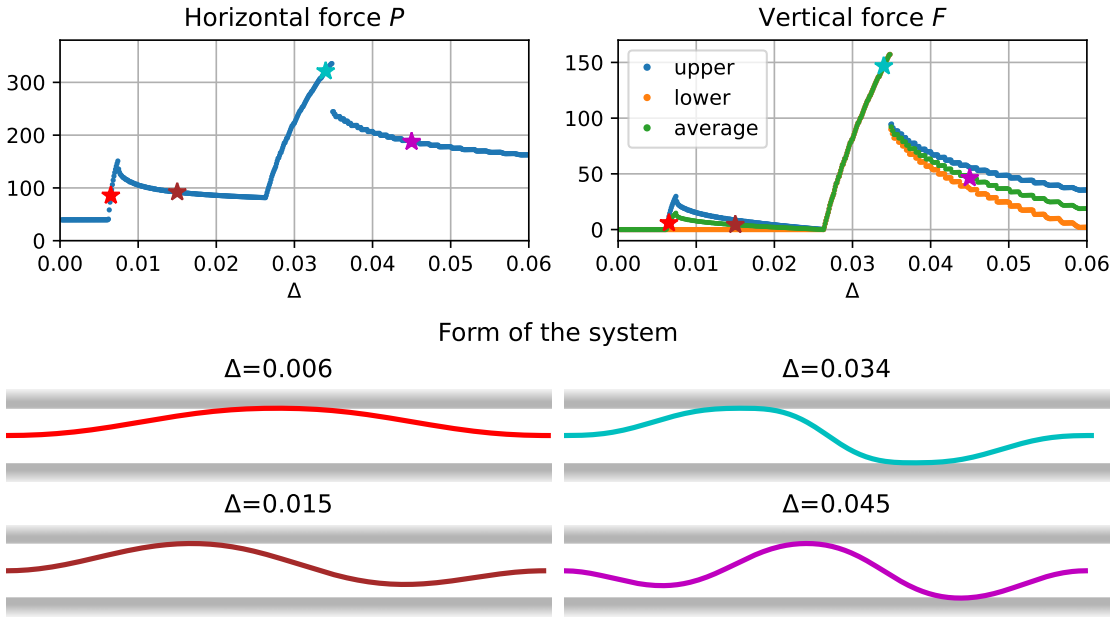


**Figure 6.3: Solution found by energy minimization with CasADi and IPOPT** ($a = 0.05, H = 0.1$)**.**

**A first glance at the behaviors of the centered configuration** From figure 6.3, we see that the evolution of the force responses has a similar repetitive pattern as the wall-attached configuration. However, when we look at the equilibrium shapes, they are less symmetric than those of the wall-attached configurations. For the same reason, the vertical force response of the upper and lower walls may not be the same, and the difference is balanced by the vertical force provided by the supports. In the wall-attached configuration, this force is not distinguished from the vertical force responses from the lower wall. When the form of the system possesses symmetry and the number of touching points to the upper and lower walls is the same, the vertical force responses of the upper and lower walls are the same, see solution marked in cyan. When the system is highly deformed and the Elastica touches the walls at many points, the difference between the vertical force responses of the upper and lower walls becomes less significant, and in the following we use the average value to present the vertical responses from the walls. Additionally, because the folds in the centered configuration are not as homogeneous as those in the wall-attached configuration, the vertical force responses are always strictly positive instead of having some states with zero vertical force $F$.

The simulation results also show how the system deforms as the loading $\Delta$ increases. When the distance between the two walls $H$ is the same as in the wall-attached configuration, the Elastica touches one of the walls at a smaller imposed displacement $\Delta$. Indeed, the first stages of the deformation are the same as the wall-attached configuration, but with wall distance $H/2 = a$. These include the coming-into-contact and the deformation under point contact (PtC) state. At the end of the PtC state, if we continue to load the system with increasing $\Delta$, the system will enter a non-symmetric state, which is shown in brown in figure 6.3. Recall that in the wall-attached configuration, the system will enter the extended contact (ExtC) state, which is not the case for the centered configuration. However, the ExtC state does not violate the constraints and is one equilibrium, because the ExtC state solutions also make the first derivative of the Lagrangian vanish. Here comes our question about the stability of these solutions, which will be discussed in detail in section 6.5.

**Limitation of IPOPT leading to the self-implemented SQP/active-set algorithm** Recall that IPOPT finds only energy minima, which is not enough to study the equilibria and their stability in general. In example 1.7, we have shown that the equilibria, both stable and unstable, and their stability index can be easily calculated for the discretized system with the help of the algorithmic differentiation feature of CasADi. For the confined Elastica, the difficulty comes from the inequality constraints. For a given load, it is difficult to determine which are the active inequality constraints. To handle this, we implemented an algorithm similar to the SQP/active-set method that was presented in section 1.3.1, which is able to find both stable and unstable equilibria under the presence of inequality constraints.

## 6.2 Analytical point of view and bifurcation diagrams

Although less symmetry and homogeneity are present in the centered configuration, it is still possible to separate the system into arches, also called the free branches, and use numerically computed arch solutions to predict the behaviors of the system, as was done for the wall-attached configuration, see section 5.3. Using this method, one is able to find both stable and unstable branches in a bifurcation diagram, and please remark that the solutions presented here are the equilibria, their stability is in question.

Due to the complexity, here we concentrate on the first stages of the deformation, and try to establish the bifurcation diagrams for small values of $\Delta$. In figure 6.4, we show the bifurcation branches found by the arch solutions for the case $a = 0.05$.



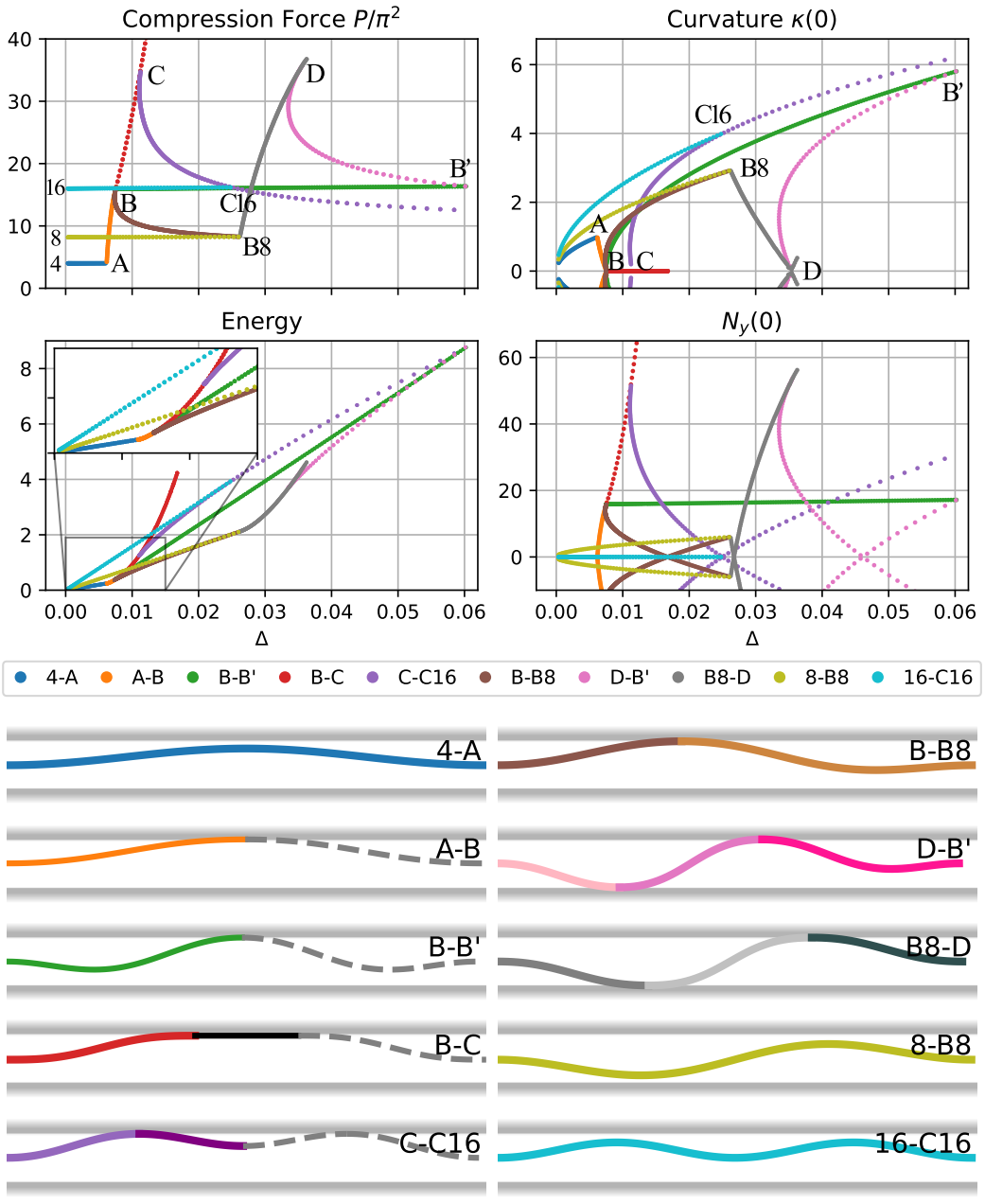


**Figure 6.4: Bifurcation diagram found by shooting and matching arch solutions ($a = 0.05$).**

When the Elastica has not yet touched the walls, the deformation process develops in the same way as a normal buckling problem. When unstable solutions are also considered, every buckling mode has its own branch, emanating from $\Delta = 0$ and evolving until the form violates the wall constraints. Here we choose to show only the first three modes, which are the branches $4 - A$ (mode 1), $8 - B8$ (mode 2), and $16 - C16$ (mode 3). The three branches sequentially reach their bifurcation point at $A$, $B8$ and $C16$.

After the Elastica touches the upper wall, we separate the Elastica into parts connected by the contact points, at which the geometric variables $x(s)$, $y(s)$, $\theta(s)$ are continuous. Thanks to symmetry, we only need to calculate half of the system for the branches $A - B$, $B - B'$, $B - C$ and $C - C16$.

The branches $A - B$ and $B - C$ and $C - C16$ are respectively the PtC, ExtC and HgF states in the wall-attached configuration. Please remark that the point $C16$ connects to the mode 3 branch. Here we specially point out that the branch $16 - C16$ and $B - B'$ are two separated branches. Although they seem to superimpose in the diagram of the horizontal force $P$, they are clearly separated in the bifurcation diagram of the vertical force $F$ and the curvature at $s = 0$.

The asymmetric form that was observed with the IPOPT simulation of figure 6.3 is on the branch $B - B8$, which connect the PtC state to the touching point of mode 2 buckling. At the end of the branch $B - B8$, the Elastica touches both upper and lower walls, and the system then follows the $B8 - D$ branch. At point $D$, the curvature at touching point reaches zero, and the system then continues on the $D - B'$ branch. Both $B8 - D$ and $D - B'$ branches are calculated using three arches. The $D - B'$ branch joins the $B - B'$ branch at point $B'$.

These bifurcation diagrams show the complexity of the existing equilibria for the confined Elastica in centered configuration. Figure 6.4 only considers relatively small values of $\Delta$, and not all the possible bifurcation branches are shown. Please also remark that the turning points and bifurcation points are very sharp. Both features may cause problem for the simple numerical continuation method to find the bifurcation branches.

The analysis with the help of arch solutions shows the branches that are the easiest to find, and makes it possible to present the energy as a function of $\Delta$, as shown in figure 6.4. This energy plot enables one to tell which branch has the lowest energy at a given $\Delta$. However, a branch that has higher energy is not necessarily unstable, it may be locally stable, as mentioned in section 1.4.1, but the stability cannot be easily derived from the shooting approach on the arch solutions.

In the following section, we introduce the soft-wall potential to model the wall constraints. This approach turns the inequality constraints into equations, and smooths out the sharp turning points in the bifurcation diagram, both of which help the stability analysis.

## 6.3 Soft-wall model

Here we introduce another way to model the wall constraints. A comprehensive theoretical study is given by Manning and Bulman (2005) where the soft-wall approach was introduced as a means to study stability in the presence of contact.

Rather than using inequality constraints, we introduce a new term into the minimization objective to penalize the Elastica for approaching the walls. This additional term is usually called a *soft-wall or a barrier potential*, and the minimization problem writes

$$\begin{aligned} \min_{\theta,x,y} \quad & \int_0^1 \frac{1}{2}\theta'^2(s) + b\left[\frac{1}{a - y(s)} + \frac{1}{a + y(s)}\right] ds \\ \text{subject to} \quad & x'(s) = \cos\theta(s), \quad y'(s) = \sin\theta(s), \\ & \theta(0) = \theta(1) = 0, \quad x(0) = y(0) = 0, \quad x(1) = 1 - \Delta, \end{aligned} \tag{6.2}$$

where $b$ is a measure of the intensity of the penalization.

Please remark that the function $1/x$ goes to infinity when $x$ goes to zero, which is valid even a very small coefficient $b$ is used. In this case, the function will take a small value in a larger range of $x$, and will change more abruptly around $x = 0$. Thus, if the soft-wall potential has a smaller parameter $b$, the zone influenced by the soft-wall potential becomes smaller. When $b$ tends to zero, the soft wall tends to the hard wall.

### 6.3.1 The system of differential equations

In this formulation, there are no more inequality constraints, and we are able to obtain a system of equations using a variational method. The Lagrangian of the system is

$$\begin{aligned}\mathcal{L}[\theta, x, y] = &\int_0^1 \frac{1}{2}\theta'^2(s) + b\left[\frac{1}{a - y(s)} + \frac{1}{a + y(s)}\right] ds \\ &+ \int_0^1 n_x(s)\left[x'(s) - \cos\theta(s)\right] + n_y(s)\left[y'(s) - \sin\theta(s)\right] ds\end{aligned} \tag{6.3}$$

From the first derivative of the Lagrangian, we obtain the differential equations :

$$\theta''(s) = n_x(s)\sin\theta(s) - n_y(s)\cos\theta(s) \qquad s \in [0, 1] \tag{6.4a}$$

$$n_x'(s) = 0 \tag{6.4b}$$

$$n_y'(s) = \frac{b}{[a - y(s)]^2} - \frac{b}{[a + y(s)]^2}. \tag{6.4c}$$

The Lagrange multipliers $n_x(s)$ and $n_y(s)$ are respectively the horizontal and vertical components of the internal force along the confined Elastica. The horizontal component $n_x$ is constant, $n_x = -P$, where $P$ is the external force acting on the support to push the Elastica into the tunnel. Adding the soft-wall potential, we find the differential equation (6.4c), indicating that the vertical component of the internal force $n_y(s)$ varies with the $y$ position. With (6.4c) we also see that $n_y$ increases rapidly when $y$ approaches the upper wall ($y = a$) or the lower wall ($y = -a$), and this is how the soft-wall potential models the effects of the confinement. The influence of the walls is present in a diffusing way, $n_y$ changes progressively as $y$ approaches the obstacle, hence the name *soft wall*. The potential strength is controlled by the parameter $b$: as mentioned earlier, when $b$ is large, $n_y$ will be affected in a larger band around the walls, and its impact will be smoother.

**Soft-wall potential of generalized walls** Although it is not required for the confined Elastica problem that we are studying, the soft-wall potential method can also be used to model 'walls' with arbitrary geometry described by functions $H_u(x)$ and $H_l(x)$. In this case, the soft-wall potential becomes:

$$\mathcal{P}(x(s), y(s)) = b\left[\frac{1}{H_u(x) - y} + \frac{1}{y - H_l(x)}\right] \tag{6.5}$$

We can again construct the Lagrangian

$$\mathcal{L} = \int_0^1 \frac{\theta'^2(s)}{2} + \mathcal{P}(x(s), y(s)) + n_x(s)\left[x'(s) - \cos\theta(s)\right] + n_y(s)\left[y'(s) - \sin\theta(s)\right] ds, \tag{6.6}$$

and derive the differential equations in the same way as before. In this case, we have

$$x'(s) = \cos\theta(s), \qquad y'(s) = \sin\theta(s) \tag{6.7a}$$

$$\theta''(s) = n_x(s)\sin\theta(s) - n_y(s)\cos\theta(s), \tag{6.7b}$$

$$n_x'(s) = b\left[\frac{-H_u'(x)}{(H_u(x)-y)^2} + \frac{H_l'(x)}{(y-H_l(x))^2}\right] \tag{6.7c}$$

$$n_y'(s) = b\left[\frac{1}{(H_u(x)-y)^2} - \frac{1}{(y-H_l(x))^2}\right] \tag{6.7d}$$

### 6.3.2 Solving the soft-wall model

To solve the system, one can either use the system of equations and the shooting method that is mentioned in section 1.5.2, or use the algorithmic differentiation feature of CasADi as what is done in the example 1.7. Here we choose the latter because the stability of the solutions can be obtained in a more direct way.

Additionally, the continuation method is applied to find different bifurcation branches. As mentioned earlier, these branches have a number of turning points and bifurcation points. For this reason, we use the arc-length continuation method that was presented in section 1.4.3 to ensure a better performance in searching the bifurcation branches and points.

### 6.3.3 Results of the soft-wall model

In the original problem of the confined Elastica, the system is controlled by two parameters, $a$ and $\Delta$. As for the soft-wall model, we have an additional parameter $b$. In this part, we present the solutions found by the soft-wall model for $a = 0.05$ with different $\Delta$ and $b$. Recall that the results of IPOPT and the predictions by the arch solutions are obtained for the same $a$, which allows us to compare the results from the 3 approaches and helps us to gain insights into the problem in general.

**The influence of parameter $b$** Firstly, we compare the results of the soft-wall model found with different values of $b$ together with the arch predictions and the IPOPT results, see figure 6.5. Compared to the results of IPOPT and arch solutions, the bifurcation branches of the soft-

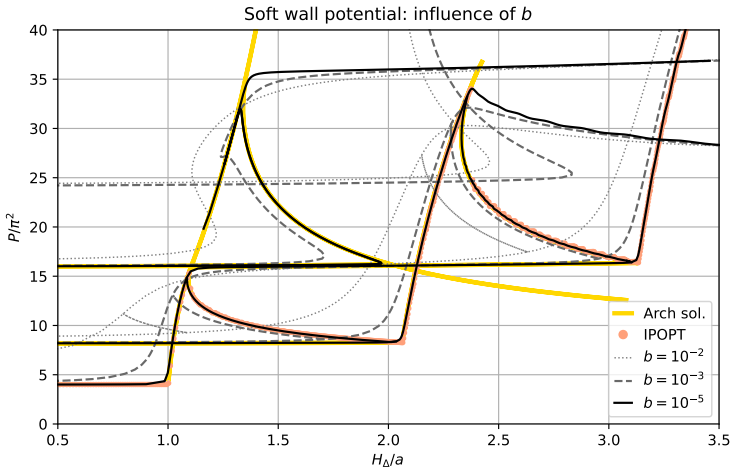


**Figure 6.5: Influence of the parameter $b$.**

wall model are much smoother, which can be explained by the diffusive nature of the soft-wall

potential, and it is a property that helps the continuation method to follow the branches more easily. Solutions with larger $b$ are more smoothened at the sharp turning points, and solutions with smaller $b$ converge to the hard-contact prediction, which is coherent with our explanation in the previous part.

We observe that the continuation algorithm works less well for smaller $b$. There are two possible reasons. First, the turning points of bifurcation branches are sharper, which causes problems if the continuation method cannot handle the jagged bifurcation branches. Secondly, when $b$ is small the soft-wall potential is only effective in a narrow zone around the wall; if the continuation step is too large, the Elastica may pass to the other side of the wall before it is affected by the soft-wall potential. Therefore, when a smaller value of $b$ is chosen for the soft-wall model, one needs smaller continuation steps to follow the bifurcation branches.

Please note that $b$ determines the zone affected by the soft-wall potential in an absolute way, independent of the wall distance parameter $a$. Thus, when $a$ is small, a smaller $b$ is needed to converge the 'soft wall' to the 'hard wall'.

**The bifurcation diagram of the soft-wall model** In figure 6.6, we show the bifurcation branches of the soft-wall model with $b = 10^{-3}$. The shapes of the beam are also shown next to each branch. In addition to the first three modes, a branch initiated with mode 4 is also calculated and presented on the diagram. We see that the four principal branches are connected between them through auxiliary branches. Apart from what was predicted by the arch solutions, there is also a branch connecting the mode 3 and mode 4 curves. This shows the richness of existing equilibria, and one can imagine the presence of a number of other bifurcation branches that are not shown in this diagram.

Recall that the simulation with IPOPT only finds the stable branches, and the prediction by arch solutions needs special consideration to separate the system into arches. Compared to these methods, the soft-wall model is very practical to find both stable and unstable branches in a relatively simple way. Additionally, the stability of the equilibria of the soft-wall model can also be obtained in a relatively easy manner. The results are as follows.

**The stability of the equilibria in the soft-wall model** In figure 6.7, we present the stability index at each point on the bifurcation branches of the soft-wall model with $b = 10^{-3}$ and $b = 10^{-5}$, together with the IPOPT results and the arch predictions. Recall that a zero stability index implies stable solutions, and larger stability indices stand for higher degrees of instability. For both $b = 10^{-3}$ and $b = 10^{-5}$, a stable branch is observed near each IPOPT solution, which is consistent with the fact that IPOPT finds only the stable solutions. As mentioned earlier, there are four main branches, initiated by the first four buckling modes. We can see that the mode 1 solution is stable, and the stability index increases by one as the mode number rises, which is in agreement with the classical theory of buckling. Moreover, the stability changes at each bifurcation point and each limit point, which is consistent with the bifurcation theory of smooth systems.

One important discovery in these diagrams is that, according to the soft-wall model, the solutions near the ExtC and HgF branches are also stable, indicating the multistability character of this problem. These soft-wall branches emanate from the mode 3 buckling point. For the results with $b = 10^{-3}$, we only see the stable solutions (index 0, black) near the HgF branch. The curve turns down a little before going back up. The results with $b = 10^{-5}$ are similar except that the curve continues to go down until nearly reaching the point connecting the PtC and the ExtC branches. When it turns back up, it follows nearly the same path as before, but these are not the same equilibria, and they are unstable (index 2), as shown by the diagram. When we look at the energy predicted by the arch solutions in figure 6.4, we see that when the ExtC ($B - C$) and the asymmetric branch $B - B8$ leave point $B$, the former has a lower energy than the later. In the

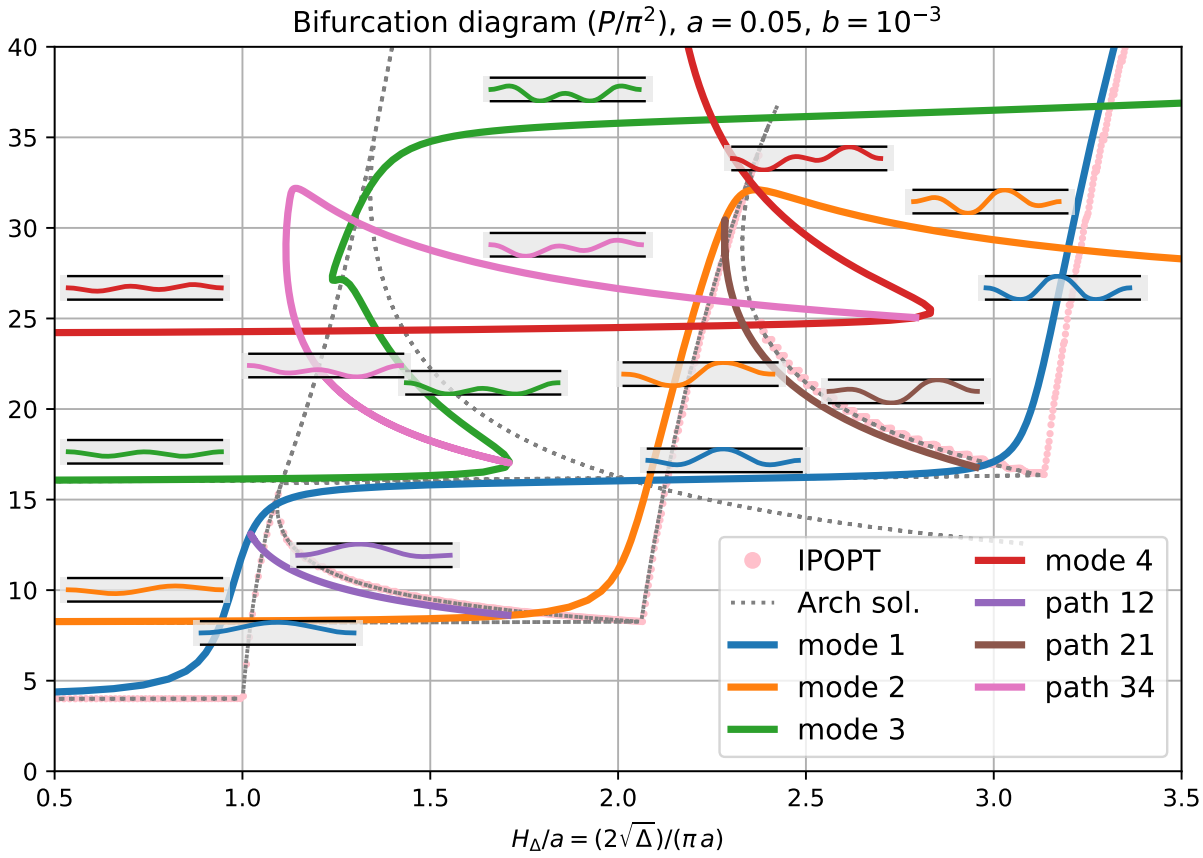


**Figure 6.6: Bifurcation diagram of the soft-wall model with $a = 0.05$, $b = 10^{-3}$.**

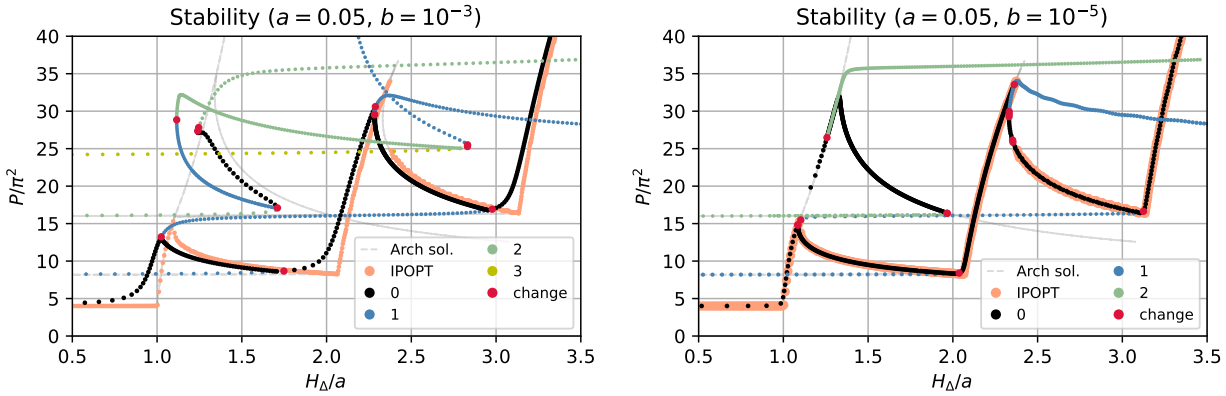


**(a) Soft-wall model with $a = 0.05$, $b = 10^{-3}$** **(b) Soft-wall model with $a = 0.05$, $b = 10^{-5}$**

**Figure 6.7: Stability analysis: the stability index (i.e. the number of negative eigenvalues of the projected Hessian matrix) is presented in different colors. The points at which a branch changes stability are marked in red. The prediction by arches and the IPOPT solutions are also plotted, in gray dashed line and light-salmon points, respectively.**

same manner at point $C$, the ExtC branch has higher energy compared to HgF. Thus, we infer that the stable solutions we found here are the local minima in the admissible solution space, but further investigations are needed to determine whether it is also the case in the original problem with rigid walls, and this is the focus of section 6.5.

In the following section, we will focus on predicting the general force responses with analytical approaches. To achieve this, we propose the cellular model of the confined Elastica in the centered configuration.

## 6.4 Cellular model

When the Elastica is clamped midway between the walls, the system loses homogeneity in its form and the global cellular model presented in section 5.6.2, with a single cell, is no longer suited. In this section we propose the global cellular model for the centered configuration to tackle the inhomogeneity at the boundaries.

The system is considered to be a combination of two types of cells, *Cell 1* describes the arch solution at the two extremities of the Elastica, and *Cell 2* represents the repetitive pattern in the middle, see figure 6.8. The number of Cell 1 is always two, and we assume the number of Cell 2 to be $M$, with $M \in \mathbb{R}$.

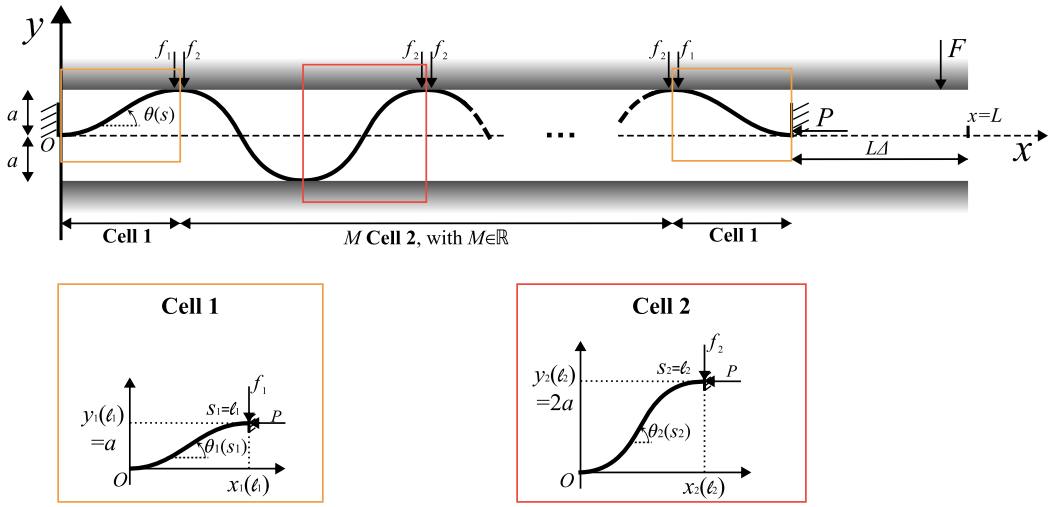


**Figure 6.8: Cellular model of the centered configuration**

The variables of each type of cells are the curvature $\kappa_i$, the deflection $\theta_i$, horizontal and vertical positions $x_i$ $y_i$. They are functions of curvilinear coordinate $s_i \in [0, \ell_i]$, with $i = 1$ for Cell 1 and $i = 2$ for Cell 2. They are related by:

$$\theta_i'(s_i) = \kappa_i(s_i), \quad x_i'(s_i) = \cos\theta_i(s_i), \quad y_i'(s_i) = \sin\theta_i(s_i), \quad s_i \in [0, \ell_i] \quad i = 1 \text{ or } 2. \tag{6.8}$$

The length of the 2 cells, $\ell_1$, $\ell_2$ should conform the total length of the Elastica and the imposed displacement control, leading to the following relations (please remember that we are working in units where the total contour length $L = 1$)

$$2\ell_1 + M\ell_2 = 1 \tag{6.9a}$$

$$2x_1(\ell_1) + Mx_2(\ell_2) = 1 - \Delta \tag{6.9b}$$

The boundary conditions of each cell are

$$\theta_1(0) = \theta_1(\ell_1) = 0 \qquad x_1(0) = y_1(0) = 0 \qquad y_1(\ell_1) = a \tag{6.10a}$$
$$\theta_2(0) = \theta_2(\ell_2) = 0 \qquad x_2(0) = y_2(0) = 0 \qquad y_2(\ell_2) = 2a \tag{6.10b}$$

**Energy and system of equations** As for the global cell model in the wall-attached configuration, we minimize the total energy described by the two cells

$$\mathcal{E}_{tot} = 2\int_0^{\ell_1} \frac{1}{2}\,{\theta_1'}^2\, ds_1 + M\int_0^{\ell_2} \frac{1}{2}\,{\theta_2'}^2\, ds_2\,. \tag{6.11}$$

To find the form of the Elastica, we use the variational method to construct the Lagrangian with the geometrical constraints (6.9) and the boundary conditions (6.10)

$$\begin{aligned}\mathcal{L}\left(\theta_i, x_i, y_i, \ell_i, M\right) = 2&\left\{\int_0^{\ell_1} \frac{1}{2}\,{\theta_1'}^2\, ds_1 + f_1\left(\int_0^{\ell_1} \sin\theta_1\, ds_1 - a\right)\right\}\\ &+ M\left\{\int_0^{\ell_2} \frac{1}{2}\,{\theta_2'}^2\, ds_2 + f_2\left(\int_0^{\ell_2} \sin\theta_2\, ds_2 - 2a\right)\right\}\\ &+ P\left(2\int_0^{\ell_1} \cos\theta_1\, ds_1 + M\int_0^{\ell_2} \cos\theta_2\, ds_2 - (1-\Delta)\right),\end{aligned} \tag{6.12}$$

where $P$, $f_1$ and $f_2$ are the Lagrange multipliers.

To derive the differential equations from the Lagrangian, we compute the variation of the functional $\mathcal{L}$:

$$\begin{aligned}\bar{\mathcal{L}} = 2&\left\{\int_0^{\ell_1} \bar{\theta_1}\,\left[-\theta_1'' - P\sin\theta_1 + f_1\cos\theta_1\right] ds_1 + \theta_1'(\ell_1)\bar{\theta_1}(\ell_1) + \bar{\ell_1}\left(\frac{1}{2}{\theta_1'}^2(\ell_1) + P\right)\right\}\\ +M&\left\{\int_0^{\ell_2} \bar{\theta_2}\,\left[-\theta_2'' - P\sin\theta_2 + f_2\cos\theta_2\right] ds_2 + \theta_2'(\ell_2)\bar{\theta_2}(\ell_2) + \bar{\ell_2}\left(\frac{1}{2}{\theta_2'}^2(\ell_2) + P\right)\right\}\\ -\bar{M}&\left(\int_0^{\ell_2} \frac{1}{2}\,{\theta_2'}^2\, ds_2 + P\int_0^{\ell_2} \cos\theta_2 ds_2\right)\end{aligned} \tag{6.13}$$

where $\bar{(\cdot)}$ is the variation of variable $(\cdot)$.

Note that the constraints (6.9a) and boundary conditions are not taken into the Lagrangian. Thus, we also have the additional relations coming from their variations:

$$\bar{\theta_i}(0) = 0 \qquad \bar{\theta_i}(\ell_i) + \bar{\ell_i}\theta_i'(\ell_i) = 0 \tag{6.14a}$$
$$\bar{x_i}(0) = \bar{y_i}(0) = 0 \qquad \bar{y_i}(\ell_i) + \bar{\ell_i}y'(\ell_i) = \bar{y_i}(\ell_i) = 0 \tag{6.14b}$$
$$2\bar{\ell_1} + M\bar{\ell_2} + \bar{M}\ell_2 = 0 \tag{6.14c}$$

The minimization of the Lagrangian requires $\bar{\mathcal{L}} = 0$ (necessary condition). Grouping terms of variation of $\bar{\theta_i}(s)$, we find the classical Elastica equations for the two cells:

$$\theta_i'' = -P\sin\theta_i + f_i\cos\theta_i, \qquad \forall s_i \in [0, \ell_i],\ \text{with } i = 1 \text{ or } 2 \tag{6.15}$$

It shows that the Lagrangian multipliers $P$, $f_i$ are respectively the horizontal and the vertical components of the internal force of the Elastica in each cell. Note that the horizontal force remains constant for all cells.



As for the other terms in the Lagrangian variation, we use (6.14) to replace all variations with $\bar{\ell_1}$ and $\bar{\ell_2}$, and require $\bar{\mathcal{L}} = 0$. Then we have

$$\theta_1'(\ell_1) = \theta_2'(\ell_2) \tag{6.16a}$$

$$\int_0^{\ell_2} \frac{1}{2}\,{\theta_2'}^2\, ds_2 + \frac{\ell_2}{2}{\theta_2'}^2(\ell_2) - P\,(\ell_2 - x_2(\ell_2)) = 0 \tag{6.16b}$$

**Solving method** We would like to solve for the unknowns $\theta_i(s_i)$, $x_i(s_i)$, $y_i(s_i)$, $\ell_i$, $f_i$ ($i = 1$ or 2), $P$ and $M$ using equations (6.8), (6.15), additional equations (6.16), the geometry conditions (6.9), and the boundary conditions (6.10).

There are 4 first-order differential equations and 2 second-order differential equations, for the 6 variables $\theta_i(s_i)$, $x_i(s_i)$, $y_i(s_i)$ and 6 unknown parameters $\ell_i$, $f_i$, $P$ and $M$. This means 14 conditions are needed to solve all the unknowns, that are the 2 geometry conditions, 10 boundary conditions and 2 additional equations; the system is closed.

More precisely, the shooting method is used. We look for $\theta_i'(0)$, $\ell_i$, $f_i$, $P$ and $M$ (8 unknowns), such that integrating the differential equations from $s_i = 0$ to $s_i = \ell_i$ meets the 4 boundary conditions at $s_i = \ell_i$, the 2 geometry conditions and the 2 additional conditions.

**Comparison with total system simulation** In this part we discuss how the cellular model captures the behaviors of Elastica under displacement control. We again choose the case $a = 0.05$ and we vary the end displacement $\Delta$. The results are compared with IPOPT simulations.

Figure 6.9 shows the forces, the number $M$ of cells of type 2 , and the shape of the beam for 4 $\Delta$ values at which $M$ is an integer. Recall that in the total system simulation, the vertical force reaction of the upper and lower wall can be different. For the cellular model, we define $F = f_1 + Mf_2$, which is the averaging value.

When $M$ of the cellular model is an integer, the form of the system found by the cellular model and the IPOPT simulation exactly match and the values of the forces are also the same, which means that the cellular model can capture the exact behavior of the whole system provided that $M$ is an integer. When it is not, the forms found by the cellular model are not the same as those of the total system simulation, but the cellular model predicts well the general tendency of force reactions, which is the same as what we had for the global cellular model for the wall-attached configuration.

### 6.4.1 The von Kármán approximation of the cellular model

To predict the reactions of the system in a more explicit way, we apply the von Kármán approximation to the cellular model. Recall from section 5.5 that the von Kármán approximation linearizes the moment balance and simplifies the strain in a weakly non-linear way, thus the differential equations for each cell become

$$x_i'(s_i) = 1 - \frac{1}{2}\theta_i^2(s_i) \qquad y_i'(s_i) = \theta_i(s_i) \qquad s_i \in [0, \ell_i] \tag{6.17a}$$

$$\theta_i''(s_i) = -P\theta_i(s_i) + f_i \qquad i = 1 \text{ or } 2 \tag{6.17b}$$

And the additional equation (6.16), the geometry conditions (6.9), and the boundary conditions (6.10) remain the same.

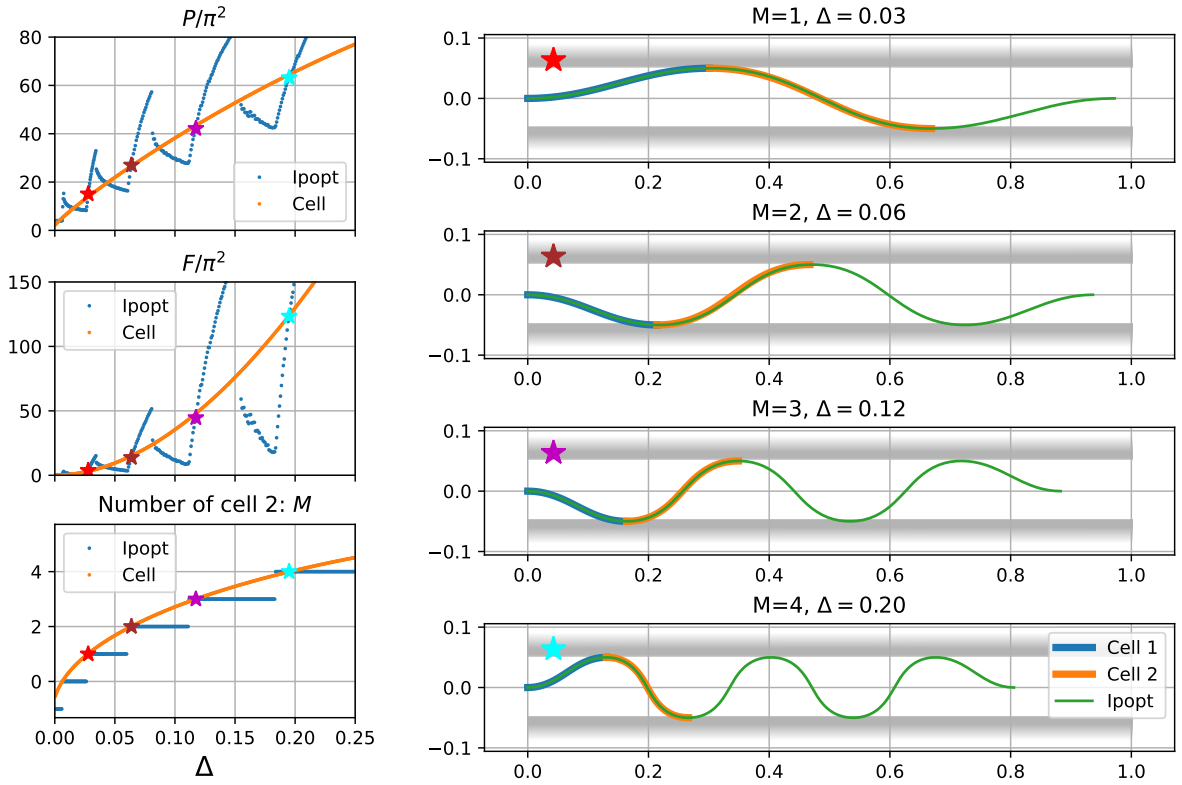


**Figure 6.9: Comparing results from the total system simulation and from the cellular model. Case $a = 0.05$. Left: the forces $(P/\pi^2, F/\pi^2)$ and the number $M$ of cells of type 2 as functions of $\Delta$. The colored stars correspond to the shapes on the right. Right: the shape of the beam for $M = 1, 2, 3, 4$ computed with the total system simulation (IPOPT) and the cellular model.**



**Analytical solution** Because these are the same systems of equations as in section 5.5 the solutions (5.9) and the formulas on $s = \ell$ (5.8) also apply to (6.17). Thus, for the cell $i$, we have

$$x_i(\ell_i) = \ell_i - \frac{f_i^2}{4P^{5/2}}\left(\ell_i\sqrt{P}\tan^2\left(\frac{\ell_i\sqrt{P}}{2}\right) - 6\tan\left(\frac{\ell_i\sqrt{P}}{2}\right) + 3\ell_i\sqrt{P}\right) \tag{6.18a}$$

$$y_1(\ell_1) = \frac{f_1}{P\sqrt{P}}\left(\ell_1\sqrt{P} - 2\tan\left(\frac{\ell_1\sqrt{P}}{2}\right)\right) = a \tag{6.18b}$$

$$y_1(\ell_2) = \frac{f_2}{P\sqrt{P}}\left(\ell_2\sqrt{P} - 2\tan\left(\frac{\ell_2\sqrt{P}}{2}\right)\right) = 2a \tag{6.18c}$$

From (6.16), we have

$$\frac{f_1}{\sqrt{P}}\tan\left(\frac{\ell_1\sqrt{P}}{2}\right) = \frac{f_2}{\sqrt{P}}\tan\left(\frac{\ell_2\sqrt{P}}{2}\right) \tag{6.19}$$

$$\frac{f_2}{\sqrt{P}\cos\left(\frac{\ell_2\sqrt{P}}{2}\right)}\left(\ell_2\sqrt{P}\cos\left(\ell_2\sqrt{P}\right) - \sin\left(\ell_2\sqrt{P}\right)\right) = 0. \tag{6.20}$$

And equations (6.9) are rewritten as

$$2\ell_1 + M\ell_2 = 1 \tag{6.21a}$$

$$2(\ell_1 - x_1(\ell_1)) + M(\ell_2 - x_2(\ell_2)) = \Delta \tag{6.21b}$$

and we replace $\ell_i - x_i(\ell_i)$ using (6.18a).

The equation (6.20) gives $\ell_2\sqrt{P} - \tan(\ell_2\sqrt{P}) = 0$. As $0 < \ell_2\sqrt{P} \leq 2\pi$, we can find $\ell_2\sqrt{P} \approx 4.5$. Injecting this values back into equation (6.18c), we have $f_2 \approx 0.286\, a\, P^{3/2}$. Then, the equation (6.19) gives $-0.8\tan(\ell_1\sqrt{P}/2) = \ell_1\sqrt{P}$. Because $0 < \ell_1\sqrt{P} \leq 2\pi$, we have $\ell_1\sqrt{P} \approx 3.58$, which leads to $f_1 \approx 0.08\, a\, P^{3/2}$. Applying the above expressions into (6.21), we have

$$M = -1.59431 + 0.222548\sqrt{P} \tag{6.22a}$$

$$\Delta = a^2(-0.56468\sqrt{P} + 0.127399P), \tag{6.22b}$$

and we can then derive

$$\sqrt{P} = 4.49341(1.59431 + M) = 2.21619 + 2.80181\sqrt{0.62571 + \frac{\Delta}{a^2}}, \tag{6.23}$$

which means that the horizontal force can be written as a function of $M$ or $\Delta/a^2$. Besides, the vertical force $F$ and the total energy of the system can be written as expressions of $a$ and $P$

$$F = f_1 + Mf_2 = a(-0.37645P^{3/2} + 0.06370P^2) \tag{6.24}$$

$$\mathcal{E}_{tot} = 2E_{\kappa 1} + ME_{\kappa 2} = (0.06370\sqrt{P} - 0.18823)a^2P^{3/2} \tag{6.25}$$

Recall that in table 5.2, we showed that the force responses and the energy can be expressed by two of the variables among $(\Delta, H, N)$. This is also the case here, but the expressions are not as concise as the wall-attached configuration, and for this reason, we do not present the results as a table, but we note here that $M$, $\Delta$ and $a$ can be presented by the two other variables:

$$M = -1.101 + 0.624\sqrt{0.626 + \frac{\Delta}{a^2}} \tag{6.26}$$

$$\Delta = 2.572\left(M^2 + 2.202M + 0.969\right)a^2 \tag{6.27}$$

$$a = \sqrt{0.389\Delta/\left(M^2 + 2.202M + 0.969\right)}. \tag{6.28}$$

**Validation and discussion** We have solved all the unknowns, including $\ell_1$, $\ell_2$, $f_1$, $f_2$, $P$ and $M$, and showed that they can be expressed as functions of the two variables $(\Delta, a)$.

In figure 6.10, we show the solution of the cell model under von Kármán approximation, with $a = 0.05$ ($H = 0.1$). There is good consistency between the IPOPT simulation, the non-linear cellular model and the von Kármán approximation, which validates the expressions of von Kármán approximation. Also, the approximation is better when $\Delta$ is small, which is expected.

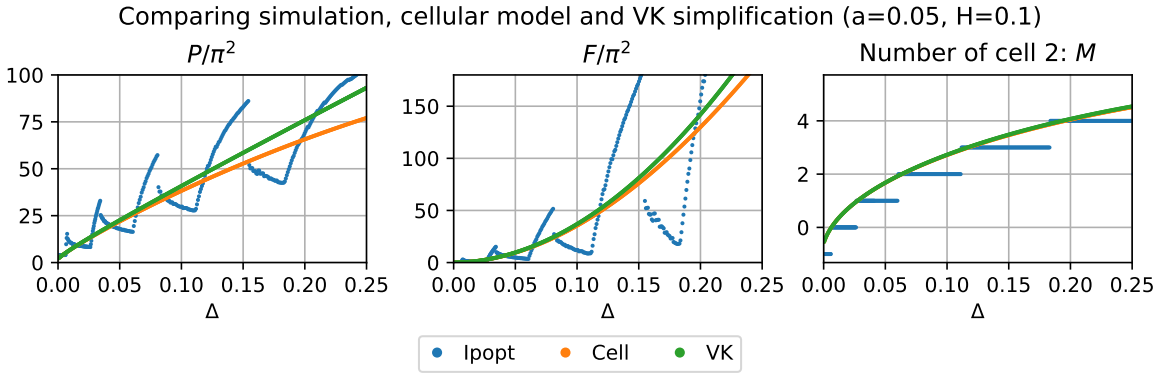


**Figure 6.10: Comparison between the total system simulation, the non-linear cellular model and the von Kármán approximation, for the case of study $a = 0.05$ ($H = 0.1$).**

With (6.23), we see that $P$ depends on the proportion $\Delta/a^2$, which is similar to what is discovered for the wall-attached configuration: the response of the system depends on the aspect ratio $H_\Delta/H = (2\sqrt{\Delta})/(\pi H)$. Moreover, the vertical force $F$ can be written as

$$\frac{F}{\sqrt{\Delta}} = \frac{-0.37645P^{3/2} + 0.06370P^2}{\sqrt{-0.56468\sqrt{P} + 0.127399P}}$$

which is a function only depending on $P$. This means that $F/\sqrt{\Delta}$ is also a function only depending on $\Delta/a^2$, which is similar to the wall-attached configuration case. However, we cannot rescale the forces with the cell number $M$ to have a universal solution. This is due to the inhomogeneity introduced by Cell 1, thus the self-similarity cannot be applied to the centered configuration.

A more detailed discussion between the two configurations can be found in chapter 7.

## 6.5 Stability analysis of the ExtC and HgF branches

From the results of the soft-wall model, we have found stable solutions around the ExtC and HgF branches, which are not found by IPOPT simulation. In this part, we further discuss the stability of these solutions.

### 6.5.1 IPOPT simulation with HgF warm-start

Our first attempt to determine the stability is to warm-start the IPOPT solver with a HgF solution that was found by the wall-attached configuration simulation. The IPOPT optimizer only finds the local minima, which are also the stable solutions. If the solver is able to converge to the HgF solution, we can basically confirm that these solutions are stable.

We especially point out that IPOPT, or the interior-point methods in general, modify the original problem with the barrier parameter $\mu$, see section 1.3.2. This is especially the case for

local minima with small domain of attraction (see section 1.4.1). If the initial value of $\mu$ is too large, the potential well of some local minima may be smoothed out, and the solver may not be able to find these solutions, even though they are stable. As predicted by the arch solutions, the ExtC and HgF branches have higher energy than the asymmetric (asym) branch, so it is very possible that IPOPT misses these solutions if the initial value of $\mu$ is too large. To deal with this issue, we modified the parameters of the IPOPT solver. We used warm-start initialization, set `mu_init`$=10^{-6}$, and set all parameters related to initial distance to bound (for example `warm_start_bound_push`) to $10^{-5}$. With that, we succeeded in finding the HgF solution with IPOPT. We also applied the continuation method with control parameter $\Delta$ to find other solutions following the HgF, ExtC, PtC, and asym branches.

In figure 6.11, we show the solutions found by the IPOPT solver with a warm-start seed marked by the red point and the related branches found by the continuation method. The original IPOPT results starting from $\Delta \simeq 0$ and the arch solutions are also shown in the figure.

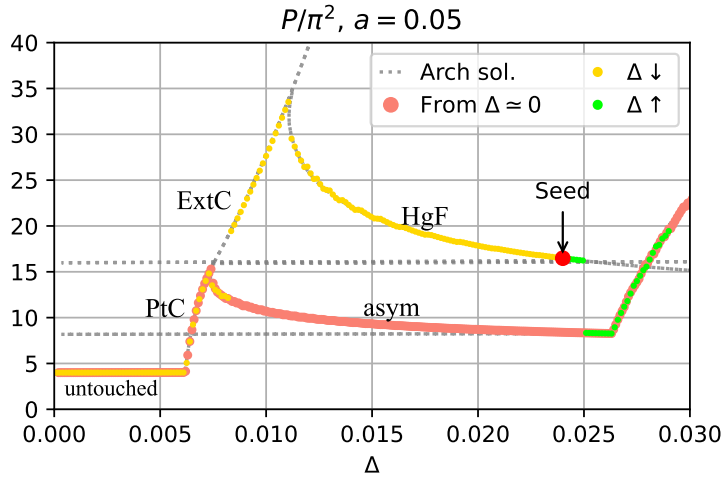


**Figure 6.11: Finding extended contact state with IPOPT. The system is discretized by 200 nodes and solved with modified parameters.**

We observe that IPOPT can successfully find the solutions on the HgF and ExtC branches except near the bifurcation points and the limit point where 'snap-back' happens. This indirectly indicates that the solutions on the ExtC and HgF branches are stable.

### 6.5.2 Stability of the SQP/active-set solutions

In section 6.1, we mentioned the self-implemented SQP/active-set algorithm, which basically solves the first derivative of the Lagrangian of the discretized system, and determines the active inequality constraints with an active-set algorithm. Please recall that the interior-point method treats the inequality constraints by adding barriers, and the final result is the limit when the barrier parameter convergences to zero. Theoretically this gives the solution of the original problem, but considering the computer precision and the tolerance of the algorithm, the values of the Lagrange multipliers of inactive constraints are not exactly zero. On the other hand, the active-set method determines the active constraints in an exact way, which is needed by our stability analysis algorithm. We have explained in section 1.2.2 how to determine whether an equilibrium is a local minimum, which also decides the stability of the solution. Our algorithm is its direct implementation with the help of the algorithmic differentiation of CasADi.

Furthermore, when analyzing the stability with the second-order optimum condition, the strongly active inequality constraints can be considered as equality constraints. As a consequence,

when there are no weakly active constraints, the stability analysis is no different from that of problems with only equality constraints, for example the soft-wall model.

However, in the presence of weakly active constraints, the discussion of the stability is more delicate. Without weakly active constraints, the projection to the admissible subspace can be achieved by the transformation matrix, which is the kernel of the inaccessible directions (see section 1.2.2 and the example 1.7.2). But in the presence of weakly active constraints, the projection cannot be achieved in the same way, because the subspace is defined with some inequalities, see expression (1.8). We call such a subspace a *cone*.

Back to the confined Elastica problem, when the Elastica touches one of the walls, the inequality constraint at this point is active. Recall that the Lagrange multipliers of the wall constraints are physically equivalent to the force reactions from the wall, thus if the force reaction at the contact point is strictly positive, then the constraint is strongly active. On the other hand, if the force reaction is zero at the contact point, the inequality constraint is weakly active.

Accordingly, the HgF states have only strongly active constraints, while the ExtC states have both strongly and weakly active constraints. Therefore, once the nodes having active constraints are known, the stability analysis of the HgF states can be achieved with the original stability analysis algorithm, while the ExtC states need a more advanced method.

**Stability of the HgF states** In figure 6.12, we show the HgF branch found by the SQP/active-set method with the stability index of each solution point. Four different numbers of nodes are

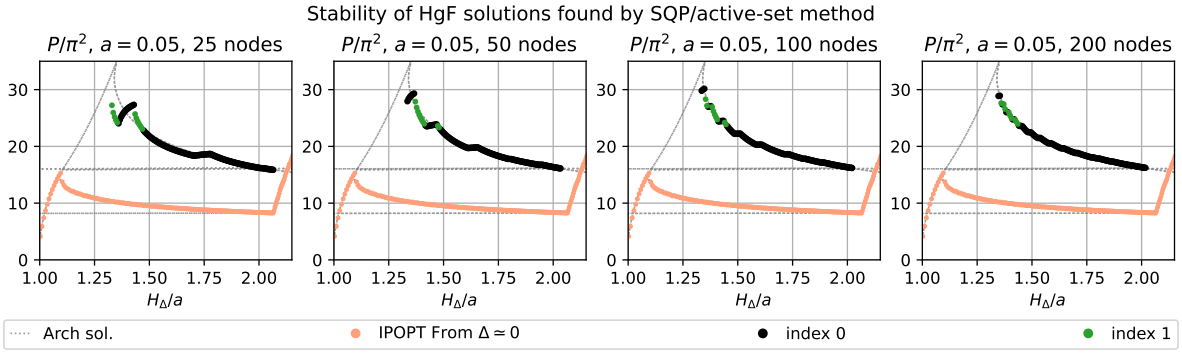


**Figure 6.12: Stability analysis of the HgF solutions found by the SQP/active-set method. The system is discretized by 25, 50, 100, and 200 nodes, and the results are shown separately in the four figures.**

used to discretize the system. From left to right are the results found by using 25, 50, 100 and 200 nodes.

It can be observed that when more nodes are used, the bifurcation branch is smoother. Moreover, approaching the limit point of the HgF branch, some of the solutions are labelled as unstable. In figure 6.13, we show three solutions of the discretized system with 25 nodes to explain the jagged bifurcation branch.

In the continuous system, the wall constraints are defined for a continuous variable $y(s)$, and theoretically, the contacts in the HgF state are punctual. On the other hand, in the discretized system, the wall constraints are directly defined on nodes. The jagged branch is caused by the algorithm passing the contact from one node to the other nodes. Moreover, we see that near the limit point of the HgF branch, when two nodes around a contact point are all active, the system is stable, and if only one node is active, the system is unstable. We assume that this is because a contact point is actually between two nodes, if both nodes are active, the system is more stable.

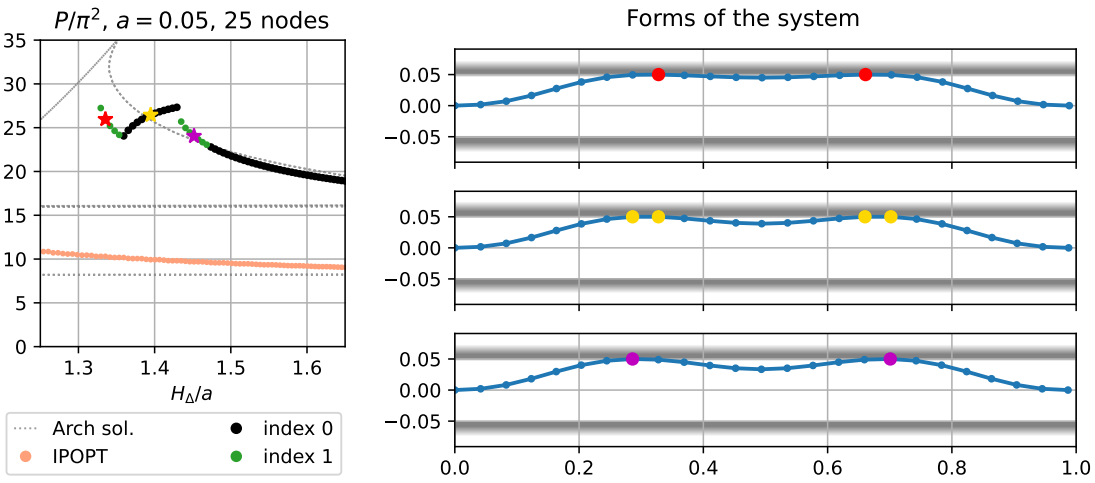


**Figure 6.13: Three solutions on the HgF bifurcation branch of the discretized system with 25 nodes. The contact points are marked by points with different colors, and the solution is marked by a star with the same color on the bifurcation branch.**

Around the limit point, the stability analysis is more sensitive to errors, thus the states in which only one node is active for a contact point are revealed to be unstable.

To this point, we have analyzed the stability of the SQP/active-set solutions on the HgF branch. Although the results are not precise around the limit point of the HgF branch, we see that the HgF states are basically stable, which is relevant to the stability analysis of the soft-wall model. Improvements can be made by adding higher-order contact conditions, see for example Crespel et al. (2024).

### 6.5.3 Weakly active constraints and Pareto eigenvalue problem

As mentioned earlier, to determine the stability of equilibria with weakly active constraints, the projection of the admissible space is different from the case in which only strongly active constraints are present. Nevertheless, the stability analysis can still be achieved by calculating the eigenvalues of the discretized system but with additional conditions.

In this section, we discuss a related problem, *the Pareto eigenvalue problem*, where one seeks eigenvalues of a matrix in a cone:

> ***Pareto eigenvalue problem*** *Given* $\mathbf{A}$*, a real matrix of size* $n \times n$*, find* $\lambda \in \mathbb{R}$*, and a non-zero vector* $\mathbf{y}$*, such that*
>
> $$\mathbb{R}^n_+ \ni \mathbf{y} \perp (\mathbf{A}\mathbf{y} - \lambda\mathbf{y}) \in \mathbb{R}^n_+. \tag{6.29}$$

The expression $\mathbf{y} \perp (\mathbf{A}\mathbf{y} - \lambda\mathbf{y})$ means $\mathbf{y}^T(\mathbf{A}\mathbf{y} - \lambda\mathbf{y}) = 0$.

Pareto eigenvalue problem is closely related to the positivity of matrix $\mathbf{A}$ in the cone $\mathbb{R}^n_+$. If the minimal Pareto eigenvalue of $\mathbf{A}$ is positive, then $\mathbf{A}$ is positive definite in $\mathbb{R}^n_+$.

**Computation of the Pareto spectrum** According to Costa and Seeger (2008), if $\lambda \in \mathbb{R}$ is a Pareto eigenvalue of matrix $\mathbf{A} \in \mathbb{R}^{n\times n}$ if and only if there is an index set $J$, a non-empty subset

of $[1, 2, ..., n]$ and a vector $\xi \in \mathbf{R}^k$, where $k$ is the number of elements of set $J$, such that

$$\mathbf{A}^J \xi = \lambda \xi, \qquad \xi \in \mathbb{R}^k_+ \tag{6.30a}$$

$$\sum_{j \in J} A_{ij} \xi_j \geq 0, \quad i \notin J \tag{6.30b}$$

where $\mathbf{A}^J$ is the principal submatrix of $\mathbf{A}$ formed with the rows and columns of $\mathbf{A}$ indexed by $J$. In this case, the vector $\mathbf{x} \in \mathbb{R}^n$, defined by

$$\mathbf{x} = \begin{cases} \xi_j & \text{if } j \in J \\ 0 & \text{if } j \notin J \end{cases} \tag{6.31}$$

is a Pareto eigenvector of $\mathbf{A}$ and $\lambda$ is the corresponding eigenvalue.

To compute all the Pareto eigenvalues, one has to compute the eigenvalues and eigenvectors of all the principal submatrices of matrix $\mathbf{A}$. If $\mathbf{A}$ is of size $n \times n$, there are $2^n - 1$ ways of choosing the indices, thus $2^n - 1$ principal submatrices to investigate. The number grows exponentially with $n$, which can cause computation difficulties for large matrices.

Note that some submatrices may have zero Pareto eigenvalues and some others may have multiples. At most, each submatrix may have $n$ Pareto eigenvalues, so the total number of Pareto eigenvalues for the matrix $\mathbf{A}$ is less than or equal to $n\, 2^{n-1}$. This upper bound is in fact lower, as it has been shown that a matrix $\mathbf{A} \in \mathbb{R}^{n \times n}$ has at most $n\, 2^{n-1} - n + 1$ Pareto eigenvalues (Costa and Seeger, 2008).

**Pareto eigenvalue problem from an optimization point of view** Analyzing the positivity of an $n \times n$ real matrix $\mathbf{A}$ in the cone $\mathbb{R}^n_+$ is to discuss whether $\mathbf{y}^T \mathbf{A} \mathbf{y}$ is positive for all $\mathbf{y} \in \mathbb{R}^n_+$. We reformulate this problem into an optimization problem. Furthermore, we show the equivalence between the optimization problem and the Pareto eigenvalue problem.

The corresponding optimization problem of the Pareto problem writes

$$\begin{aligned} \text{minimize} \quad & \mathbf{y}^T \mathbf{A} \mathbf{y}, \quad \mathbf{y} \in \mathbb{R}^n \\ \text{subject to} \quad & \mathbf{y} \geq 0 \\ & ||\mathbf{y}|| = \mathbf{y}^T \mathbf{y} = 1 \end{aligned} \tag{6.32}$$

If the minimal objective found in this problem is negative, then it means $\mathbf{A}$ is not positive definite, and the solution found is unstable.

The advantage of this formulation is that we do not have to compute the eigenvalue spectrum to find the minimal eigenvalue, and this can be interesting for problems of large dimension.

**Equivalence to Pareto eigenvalue problem**

To analyze the above optimization problem, we construct the Lagrangian

$$\mathcal{L} = \mathbf{y}^T \mathbf{A} \mathbf{y} - \lambda(\mathbf{y}^T \mathbf{y} - 1) - 2\boldsymbol{\mu}\mathbf{y} \tag{6.33}$$

where $\boldsymbol{\mu}$ is a vector with components $\mu_1$, $\mu_2$, ..., $\mu_n$.

At the minimum point, the gradient of the Lagrangian should be zero. If $\mathbf{A}$ is symmetric, which is the case for the Hessian matrix, then we have

$$\nabla \mathcal{L} = 2(\mathbf{A}\mathbf{y} - \lambda \mathbf{y} - \boldsymbol{\mu}) = \mathbf{0} \quad \Leftrightarrow \quad \boldsymbol{\mu} = \mathbf{A}\mathbf{y} - \lambda \mathbf{y}, \tag{6.34}$$

and also the additional conditions for the inequality constraint $\mathbf{y} \geq 0$

$$\mu_i y_i = 0, \quad y_i \geq 0, \quad \mu_i \geq 0, \qquad \forall i = 1, 2, ... n, \tag{6.35}$$



which leads to the same formulation as the Pareto eigenvalue problem.

Then we apply the second-order sufficient condition, that is

$$\nabla^2 \mathcal{L} = \mathbf{A} - \lambda \mathbb{I} \text{ is positive definite on the subspace } \{\mathbf{y} | \mathbf{y}^T \mathbf{y} = 1, \mathbf{y} \geq \mathbf{0}\}. \tag{6.36}$$

Note that we have the same Hessian matrix as in the case without weakly active constraints (see section 1.2.2). Consequently, proving how the stability of a solution depends on the smallest Pareto eigenvalue is similar.

**Implementation and comparison of the two ways to find the minimal Pareto eigenvalue**

We implemented the enumerating method in Python with SciPy to compute the eigenvalue spectrum. The optimization formulation is on the other hand implemented with IPOPT and CasADi. Random symmetric real matrices of different dimensions are generated, and for each dimension, we apply the two methods to 400 matrices. For each matrix, the minimum found by the enumerating method is considered to be exact, and we compare it with the minimum objective found by IPOPT. To measure the accuracy of the method, we calculate the rate at which the two methods find the same minimum, and this rate is considered the accuracy of the optimization method.

Because the solution of the optimization method depends on the initialization, we have tested 2 initializations. The first one initiates the search with the absolute value of the eigenvector related to the minimal eigenvalue of the matrix in the whole space. The other one initiates the search with a positive random vector of norm 1.

We also compare the computation time needed for the two methods. All the calculations are done on the same computer, and the values are shown in table 6.1. The time needed for both methods is also shown in figure 6.14, the y axis is in log scale.

| | Enumerative | Optimization | | |
|---|---|---|---|---|
| Dimension | Time (s) | Time (s) | Accuracy (1) | Accuracy (2) |
| $3 \times 3$ | 0.19449 | 2.05698 | 98.00 % | 88.75 % |
| $4 \times 4$ | 0.40941 | 2.16418 | 97.00 % | 88.00 % |
| $5 \times 5$ | 0.90781 | 2.33238 | 95.75 % | 90.25 % |
| $6 \times 6$ | 2.00375 | 2.57070 | 97.25 % | 89.75 % |
| $7 \times 7$ | 4.40090 | 2.71495 | 96.25 % | 88.75 % |
| $8 \times 8$ | 9.70279 | 2.84698 | 96.75 % | 89.50 % |
| $9 \times 9$ | 21.35062 | 3.08506 | 93.50 % | 93.25 % |
| $10 \times 10$ | 46.28476 | 3.16813 | 93.25 % | 89.75 % |
| $12 \times 12$ | 220.82297 | 3.51282 | 94.00 % | 91.75 % |

**Table 6.1: Comparison of the two methods. Accuracy (1) is for the eigenvector initialization, and Accuracy (2) is for the random initialization.**

It can be seen that the computation time of the enumerating method grows exponentially with dimension $N$, but for the optimization method, the configuration time grows much more slowly. We also observe that the accuracy depends on the initialization. When initialized with the eigenvector, the accuracy is higher than the random initialization. But when dimension of the problem grows, the accuracy of the eigenvector initialization deceases and that of the random generation increases. It may be explained by the fact that the problem complexity increases when the dimension increases and the eigenvector initialization yields a poorer prediction of the Pareto eigenvector.

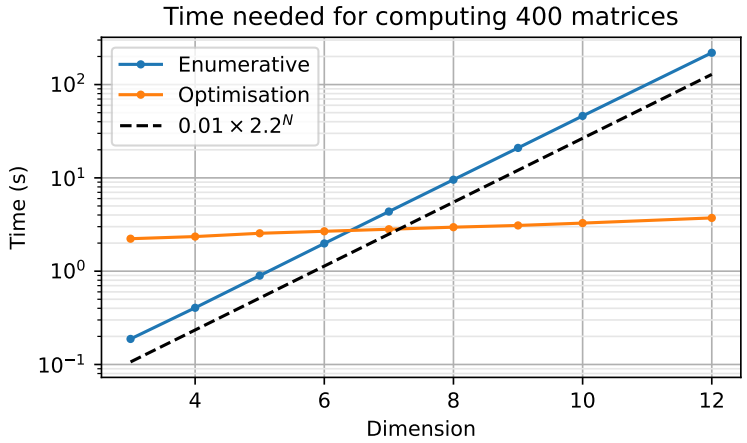


**Figure 6.14: Time needed for computing the minimum Pareto eigenvalue for 400 random symmetric real matrices as a function of the dimension $n$ of the matrices.**

From these observations, we can confirm the interest to use the optimization method for problems of large dimension.

### 6.5.4 Stability in the cone with equality constraints and a few inequality constraints

In the original Pareto problem, all the conditions are inequalities, but for the confined Elastica, there are also equality constraints. In this section, we extend what was learned from the Pareto eigenvalue problem to determine the stability of an equilibrium $\mathbf{x}^*$ with both strongly and weakly active inequality constraints. That is equivalent to discussing the positiveness of a matrix $\mathbf{H}$ in the subspace

$$M = \{\mathbf{y} \,|\, \nabla \mathbf{h}(\mathbf{x}^*)\mathbf{y} = 0,\ \nabla g_j(\mathbf{x}^*)\mathbf{y} = 0,\ \forall j \in J_S,\ \nabla g_j(\mathbf{x}^*)\mathbf{y} \geq 0,\ \forall j \in J_W\}$$

mentioned in section 1.2.2. Please recall that $J_S$ is the index set of all the strongly active constraint, and $J_W$ is the index set of all the weakly active constraints, defined in (1.9).

Our objective is to find whether there is a vector $\mathbf{y}$, such that $\mathbf{y}^T\mathbf{H}\mathbf{y}$ is negative. If so, the Hessian matrix is not positive definite and the solution is unstable. To discuss this problem, we propose two methods, the optimization method and the enumerating method.

#### Optimization method

As its name, we again reformulate the problem as an optimization problem:

$$\begin{aligned} \text{minimize} \quad & \mathbf{y}^T\mathbf{H}\mathbf{y}, \quad \mathbf{y} \in \mathbb{R}^n \\ \text{subject to} \quad & \nabla \mathbf{h}(\mathbf{x}^*)\mathbf{y} = 0, \\ & \nabla g_j(\mathbf{x}^*)\mathbf{y} = 0,\ \forall j \in J_S, \\ & \nabla g_j(\mathbf{x}^*)\mathbf{y} \geq 0,\ \forall j \in J_W \\ & ||\mathbf{y}|| = \mathbf{y}^T\mathbf{y} = 1. \end{aligned} \tag{6.37}$$

The implementation is still achieved with IPOPT and CasADi. If the optimum is negative, then the Hessian matrix is not positive definite and the solution is unstable. We should note that the optimum found by the algorithm depends on initialization and can be a local optimum instead of

the global optimum. Consequently, if the optimum is positive, we do not exclude the possibility of a negative global optimum.

The advantage of this method is the relatively small computational cost even in the presence of numerous weakly active constraints.

**Enumerating method**

We compute all the possible combinations of weakly active constraints supposing the weakly active constraints can be taken into account or not. For each combination, we add the considered weakly active constraints to the strongly active constraints and compute the admissible space and the projected Hessian matrix in the same way as described in part 1.2.2. This practice can be understood as 'blocking' the variational direction from all these constraints, including the added weakly active constraints. Then we calculate all the eigenvalues of the projected Hessian matrix. If there exists one (or more) negative eigenvalue, we project the associated eigenvector $\hat{\mathbf{x}}$ back into the original space $\mathbb{R}^n$ using the transformation matrix $\mathbf{K}$

$$\mathbf{x} = \mathbf{K}\,\hat{\mathbf{x}} \tag{6.38}$$

If all the weakly active inequality constraints are satisfied for $\mathbf{x}$, we find a cone-constrained negative eigenvalue, the Hessian matrix is not positive definite and the solution is unstable. Also, the vector $\mathbf{x}$ corresponds to an unstable variational direction in which the total energy of the system decreases. If some of the weakly active inequality constraints are not satisfied for $\mathbf{x}$, the negative eigenvalue is rejected. In this way, we can compute all the negative eigenvalues of our cone-constrained eigenvalue problem and discuss the stability of the solution.

**Algorithm:**
Initial : compute all the combination $\mathcal{J}$ of weakly active constraints
**for** J **in** $\mathcal{J}$:
    Compute $\mathbf{K}$ by (1.11)
    Project Hessian matrix $\mathbf{H}$ by (1.13)
    Calculate the eigenvalue and eigencectors of projected Hessian matrix $\hat{\mathbf{H}}$
        **if** there is one or more eigenvalue $\lambda < 0$:
            **for** $\lambda$ **in** $\lambda_k < 0$:
                Project the corresponding eigenvector $\hat{\mathbf{x}}$ back to $\mathbf{x}$ by (6.38)
                **if** $\mathbf{x}$ satisfies all the constraints :
                    We have one negative eigenvalue, save $\lambda$ and $\mathbf{x}$

### 6.5.5 Application to the confined Elastica problem

To determine the stability of ExtC state solutions, we apply the two methods that determine the stability of equilibrium with both strongly and weakly active constraints.

Considering the computational time, only 41 nodes are used to discretize the system, and two equilibria in ExtC state found by the SQP/active-set method are chosen for the stability analysis. The geometry of the system is shown in figure 6.15.

The first solution (figure 6.15a) is on the B-C branch of the bifurcation diagram 6.4, and the second solution (figure 6.15b) is beyond point C. The second solution is by nature unstable because the compression force $P$ is larger than the buckling threshold of the flat part. Please note that for wall-attached configurations, to pass above the bifurcation point C, the number of flat regions should be more than one. But here, the flat region is not split, and hence $P$ is necessarily larger than the buckling threshold.

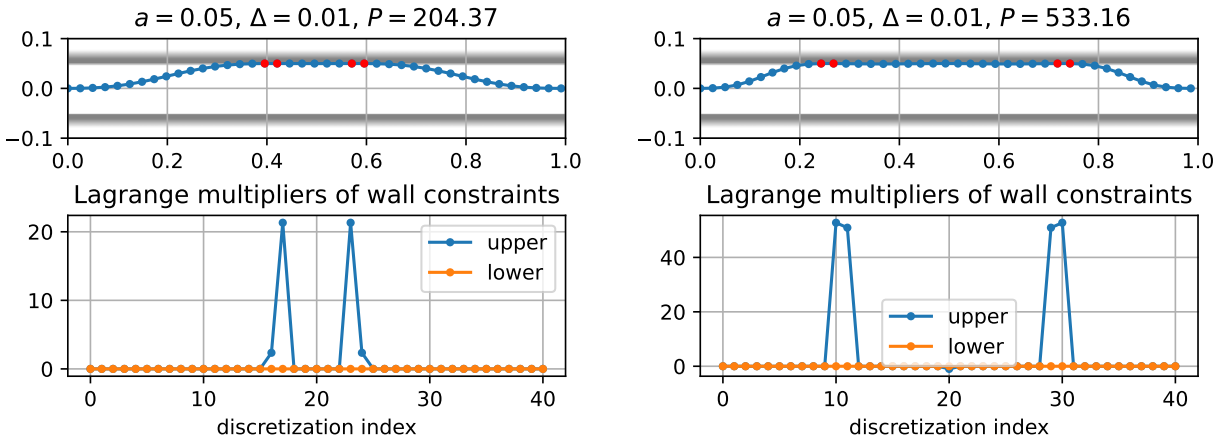


**(a) ExtC P200** **(b) ExtC P500**

**Figure 6.15: Two equilibria in ExtC state. The red points mark the nodes with a strictly positive Lagrange multiplier.**

Both the optimization method and the enumerating method find that the ExtC P200 is stable, and the ExtC P500 state is unstable. Furthermore, the minimal eigenvalues found by the methods are the same, which validates their implementation.

Although the stability of the continuous system needs further investigation (see for example the work of Ro, Chen, and Hong (2010)), with these methods, we can conclude that the ExtC states on the B-C branch of our *discretized* system are stable. Finally, the reason why IPOPT has difficulty converging to these ExtC states still needs further investigation. We assume that it is because the potential well around B-C branch is small and shallow, in other words, the domain of attraction is small (like the local minimum $B$ in figure 1.1b).

### Stability of the mode 3 touching limits

In fact, not only do the ExtC states have weakly active constraints and require calculating eigenvalues in a cone to determine the stability, it is also the case for the mode 3 at the touching limit.

It is known that the stand-alone mode 3 is unstable (the 16-C16 in figure 6.4), but we have shown that the HgF branch (C-C16 branch) is stable, and they are connected at the C16 point. So we question the stability of point C16. Moreover, the Elastica also passes this state in the wall-attached configuration, in which case it is no doubt stable. Regarding this, we selected three different configurations for the wall confinement, see figure 6.16, and analyzed the stability for each setting. Recall that the stability index of buckling mode 3 is 2, which means that the projected Hessian matrix has two negative eigenvalues (and hence two unstable directions), from which we deduce that mode 3 is unstable in the complete absence of contact. Adding walls that do not apply any force to the mode 3 Elastica is equivalent to blocking some variational directions, and the admissible space becomes a cone. Therefore, we need to find the smallest eigenvalue in the cone to determine the stability.

We again applied both the optimization method and the enumerating method, and the results show that the 2U1L setting is stable, which means that the cone constraints have killed both of the two unstable directions. Additionally, the optimum found by the optimization method is the same as the minimal eigenvalue found by the enumerating method. It is actually the HgF/PtC transitional state in the wall-attached configuration, and theoretically proves the stability of this

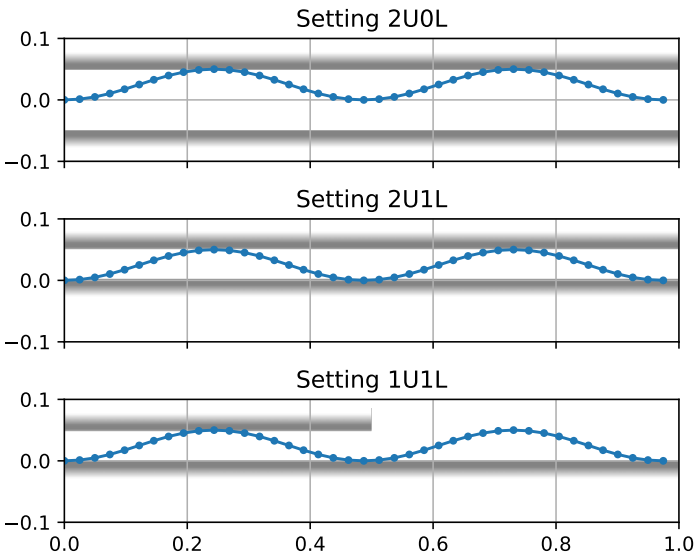


**Figure 6.16: Stability of mode 3 at touching limit. Please remark that here the Elastica touches the walls, but there is no force reaction from the walls at the touching points, meaning $F = f = 0$. Three different ways to place the walls are chosen. 2U0L: two touching points on the upper wall and no touching point on the lower wall. The notation of the other two settings, 2U1L and 1U1L, is chosen in the same manner.**

state. In addition to that, we remark that the walls stabilize the system even without any force from the walls acting on the Elastica. In fact, this is not only the case for mode 3 buckling state. To arrive at any higher buckling modes, one can add external supports, see for example **Fig.** 10.6 *Preventing a column from buckling in a lower mode* in section 10.1 of Bedford and Liechti, 2020. No force is given by these supports, but they constrain the admissible space and thus stabilize the system in its (otherwise) unstable modes.

For 2U0L and 1U1L settings, both methods show that they are unstable. Moreover, as the eigenvector related to a negative eigenvalue is actually a variational direction in which the energy of the system decreases, we show the variations together with the initial state in figure 6.17. For

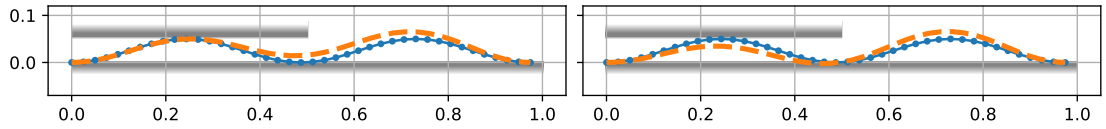


**(a) Setting 1U1L**

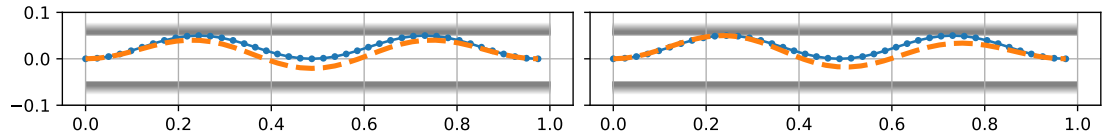


**(b) Setting 2U0L**

**Figure 6.17: The two unstable variational directions for the settings 1U1L and 2U0L.**

each setting, there are two variational directions in which the total energy of the system decreases. And it is equivalent to say that there are two negative eigenvalues, which is the same as the original mode 3 state without walls. With that, we remark that constraining the admissible space does not necessarily reduce the degree of instability.

## 6.6 Conclusions

In this chapter, we have discussed the confined Elastica problem with a slightly different boundary condition: the clamped ends of the Elastica are fixed midway between the walls. Compared to the previous chapter, here we focused on the force responses and on the stability at the early stages of deformation.

With the arch solutions, we first predicted the bifurcation diagram, and it was verified by the IPOPT simulation.

Then, we introduced a new way to model the wall constraints, the soft wall model. We then investigated how the 'soft wall' model converges to the 'hard wall' limit by decreasing the soft wall parameter $b$. This model not only gives the stable equilibria, but also the unstable ones, and the stability can be determined easily with CasADi. Thanks to the results of the soft wall model, we have a more comprehensive view of the confined Elastica problem, especially the richness of equilibria and bifurcation branches. We also recovered the ExtC and HgF branches of the wall-attached configuration, and proved them to be stable in the discretized soft wall model.

Next, a global cellular model was given to predict the general force responses of the system. It is similar to the global cellular model of the wall-attached configuration, but it takes into account the inhomogeneity by adding boundary cells (Cell 1) to the repetitive cells (Cell 2). The solutions of this cellular model proved to be well consistent with the IPOPT simulations, especially when the number of Cell 2 is an integer. We also applied the von Kármán approximation to the cellular model, and obtained explicit expressions of the general force responses as functions of displacement $\Delta$ and wall distance $2a$.

In the last part, we focused on the stability analysis of the ExtC and HgF branches. The solutions used for stability analysis are obtained by the SQP/active-set method, which finds the active inequality constraints in an exact way. With that, the HgF branch is proven to be stable except for the snap-back part. As for the ExtC states, considering the presence of the weakly active constraints, we introduced the Pareto eigenvalue problem, which requires finding eigenvalues of a matrix in a subspace defined by inequalities (a cone). Inspired by the Pareto problem, we give two methods to determine the stability of equilibria with both strongly and weakly active constraints. With this method, the ExtC states of the discretized system are found to be stable. We also discussed the stability of mode 3 at the touching limit with different wall settings, showing more cases to which our methods can be applied.

Further investigations can be carried out, for example, into the general deformation process, the highly deformed states, and also the stability of the continuous system.



# Chapter 7

# Discussions of the confined Elastica problem

In this chapter, we discuss the differences and similarities between the wall-attached and the centered configuration of the confined Elastica.

In figure 7.1, results of the total system simulations are shown together with the predictions of different cellular models. Two different wall heights are chosen, figure 7.1a shows the results for $H = 0.1$, while 7.1b shows the results for a much smaller wall distance $H = 0.01$. For both cases, the horizontal and vertical force responses are presented as functions of $H_0(\Delta)/H$, where $H_0(\Delta)$ is the maximum vertical flexion of the Planar Elastica without contact. It is similar to $H_\Delta$ that was described by (5.10), but here we introduce a higher order term to have a better approximation of $H_0(\Delta)$, with

$$H_0(\Delta) \simeq \frac{2}{\pi}\sqrt{\Delta} - 0.2\,\Delta\sqrt{\Delta} \tag{7.1}$$

Apart from the results and predictions shown in the figures, there are also the explicit expressions from the von Kármán approximation of the global cellular models, see section 5.6.2 and 6.4.1. We will also use these solutions to interpret the observations from the figure.

Recall that $H$ is the wall distance, which is related to $a$ in the centered configuration with $H = 2a$. In both configurations, the force responses $P$ and $F$, and the number of cell/fold depend only on the ratio $\sqrt{\Delta}/H$. Therefore, the behaviors of the two configurations can be easily compared at the same $\sqrt{\Delta}/H$. We use the subscript *wall* and *center* to respectively mark the responses of the wall-attached and centered configuration.

## 7.1 System evolution

From the chapter of the wall-attached configuration, we already know that the HgF-PtC transitional point is at integer values of $H_0(\Delta)/H$, which is again found in the figures. The number $H_0(\Delta)/H$ may then be interpreted as an approximation of the fold number $N \approx H_0(\Delta)/H$. As for the centered configuration, we observe a similar jagged pattern except that the period is about half that of the wall-attached configuration.

Please note that the repetitive patterns are related to the fold number $N$ of the wall-attached configuration and the Cell 2 number $M$ of the centered configuration.

Due to the geometry difference between the two configurations, the relation between the fold number $N$ of the wall-attached configuration and the cell 2 number $M$ is ambiguous. However, some insights can be gained from the definition of the vertical force response $F$. We have $F = 2N\,f$ for

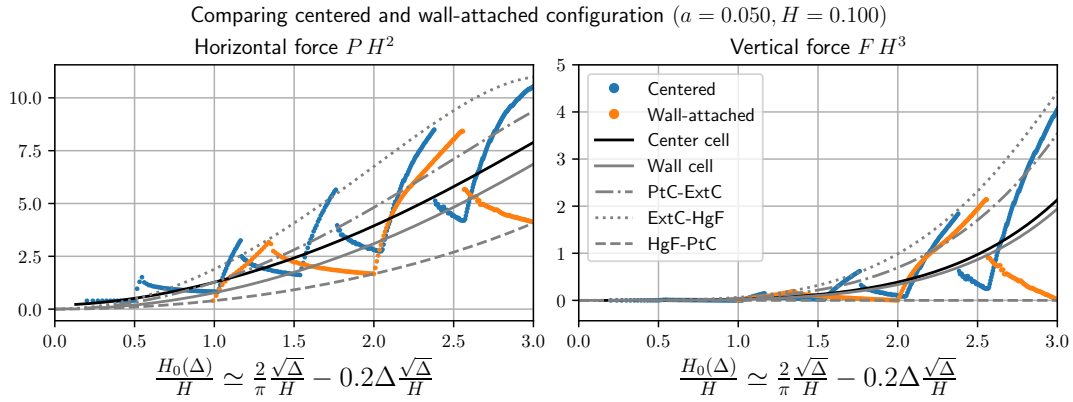


**(a)** $a = 0.05,\ H = 0.1$

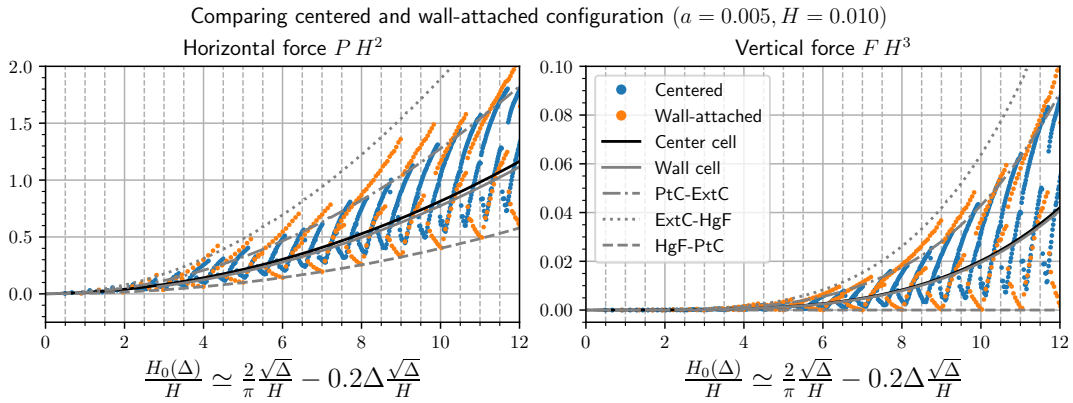


**(b)** $a = 0.005,\ H = 0.01$

**Figure 7.1: Comparing force responses between the wall-attached configuration and the centered configuration. The results of the total system simulation, the predictions of different cellular models are presented together on the diagrams. Considering the remarkable hysteresis phenomenon when the wall distance is small, data for both loading and unloading simulations are shown for the second case.**

the wall-attached configuration and $F = f_1 + M\, f_2$ for the centered configuration, which indicates a correspondence between $M+1$ and $2N$.

We further investigate $M$ and $N$ with the von Kármán approximation. For a given ratio $\sqrt{\Delta}/H$, we have $N = 0.62\sqrt{\Delta}/H = (0.62\sqrt{\Delta})/(2a)$. Replacing $\sqrt{\Delta}/a$ in the expression of $M$, we find

$$M + 1.101 = 0.624\sqrt{0.626 + \left(\frac{2}{0.62}\right)^2 N^2} = 2N\sqrt{1 + \frac{0.06}{N^2}} \simeq 2N. \tag{7.2}$$

This not only proves the correspondence between $M+1$ and $2N$, but also indicates that for a given value of $\sqrt{\Delta}/H$, $M+1$ is approximately equal to $2N$, and this is coherent with what can be observed from the results of the total system simulations.

## 7.2 Force responses

Globally speaking, the values of the forces in both configurations are in the same range. All the simulation results stay between the predictions by ExtC-HgF cellular model and the HgF-PtC cellular model. One can deduce that the force responses for other fixation heights also stay inside these two limits.

For both configurations, the force minima are at the transitional points where $N$ or $M$ increases by one. The forces minima of the centered configuration are all larger than those of the wall-attached configuration. More precisely, the simulation data of the wall-attached configuration touch the HgF-PtC cellular model prediction, but the results of the centered configuration always stay above.

As for the global cellular models for the two configurations, the predicted force responses for the centered configuration are larger than those of the wall-attached configuration. But the difference is not very large, and is smaller when the wall distance is smaller. This can be explained using the von Kármán approximations of both cellular models, from which we have

$$P_{center} - P_{wall} \simeq 9.8 + 0.4\frac{\Delta}{H^2} + 24.8\sqrt{\frac{\Delta}{H^2} + 0.16} \tag{7.3}$$

which means that for a given value of $\sqrt{\Delta}/H$, the horizontal force predicted by the global cellular model of the centered configuration is always larger than the wall-attached configuration, but the difference is not very large because the order of $P$ is around $10^2$ to $10^3$, and the order of $\sqrt{\Delta}/H$ is around 1 to 10. Moreover, multiplying this expression by $H^2$, we see that the difference decreases as $H^2$ when $H$ decreases, which is what is observed in figure 7.1.

Similar comparison can also be applied to the vertical force $F$ and the energy, and we found that the centered configuration has larger $F$ and higher energy for the same $\sqrt{\Delta}/H$, but the difference is not large.

From the force response comparison, we conclude that the inhomogeneity introduced by the centered configuration leads to a slight increase in the force response, but the values still stay in the same order of magnitude.

## 7.3 Universal prediction of the cellular models

In figure 7.1, we presented the force responses as functions of $H_0(\Delta)/H$, and have observed that for a given value of the wall distance $H$, the results of both configurations stay between the ExtC/HgF and HgF/PtC cell predictions.

Indeed, this feature can be extended to a universal prediction of the force responses. In section 5.6.3, we presented the self-similarity of the cellular models for the wall-attached configuration.

The self-similar solutions only depend on $\Delta$, and can be transformed to any given wall distance $H$.

Thanks to the self-similarity, the quantities $P\,H^2$ and $F\,H^3$ of the self-similar cellular models only depend on $\Delta$, which means that these solutions are universal. Furthermore, not only do the simulation data of the wall-attached configuration follow the predictions of the cellular models, but also the centered configuration. In figure 7.2, we show $P\,H^2$ and $F\,H^3$ given by the self-similar solutions as functions of $\Delta$, together with simulation data of the wall-attached and centered configuration at different wall distances $H$.

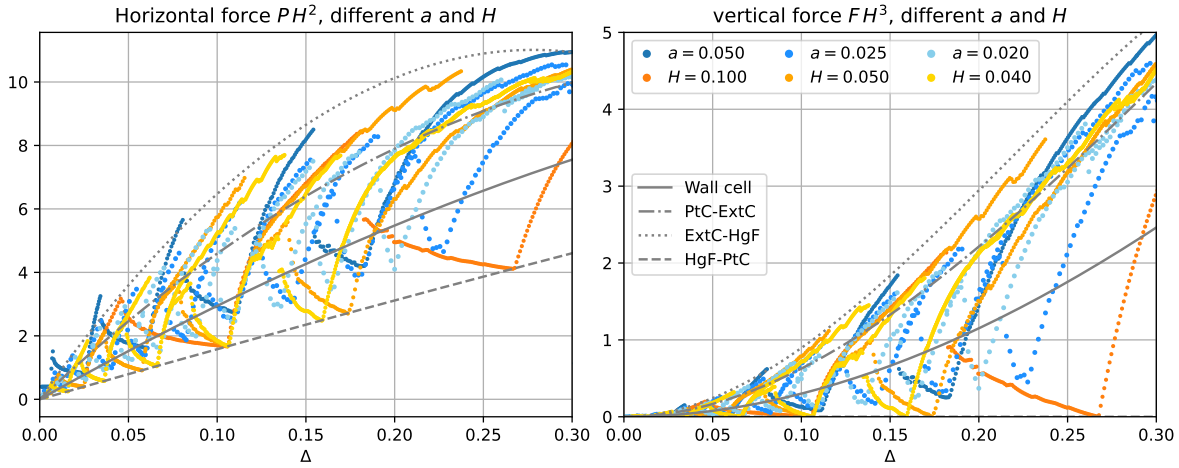


**Figure 7.2: Cellular models: the universal limits of the force responses**

All the data are well enclosed by the self-similar solution of the wall-attached cellular models, which proves our analysis, and we can conclude that these curves are generally relevant to the confined Elastica problem with clamped boundary conditions.

## 7.4 Conclusion and perspectives of the confined Elastica in general

In this chapter, we mainly discussed and compared the force responses of the wall-attached and centered configurations.

Based on the IPOPT simulations, we observed similar repetitive patterns in the force diagrams, but the two configurations have different changing periods. Additionally, the magnitude of the force responses is slightly different. These observations are rationalized when using the von Kármán approximations of both global cellular models. Most importantly, for both wall-attached and centered configuration, we found that the range of the force responses stays between the ExtC/HgF and HgF/PtC cellular models of the wall-attached configuration. Moreover, thanks to the self-similarity, these predictions were generalized to any given wall distance $H$.

All these observations and analysis partially reveals the behaviors of the confined Elastica in general. But there still remains many different aspects for further investigations, for example, how the deformation process changes with the fixation position, including the changing period of the force responses and the geometry of the system.

# Part III

# Liquid-solid packing



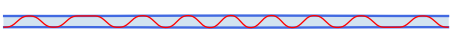

In part II, we examined the behavior of an inextensible slender beam (Elastica) confined between rigid walls. Under solid confinement, the Elastica developed into ordered folds and exhibited characteristic force responses that could be described using self-similar and cellular models. These studies highlighted the essential role of geometry and boundary conditions in determining packing patterns.

Packing phenomena, however, are not restricted to solid confinements. In many natural and synthetic systems, confinement arises from liquid interfaces, where surface tension provides the dominant restoring force. At small scales, capillary forces can exceed elastic resistance, giving rise to the so-called *elasto-capillary effects*. When slender structures are captured or constrained by liquid interfaces, they undergo packing behaviors that are qualitatively different from those observed under rigid walls.

This part of the thesis focuses on such liquid–solid packing problems, exploring how flexible structures interact with deformable liquid boundaries. Two representative systems are studied.

Chapter 8 investigates the coiling of a flexible fiber around a liquid drop, a phenomenon inspired by the natural windlass mechanism of spider silk. Experimental studies (Elettro, 2015; Elettro et al., 2016) demonstrated this effect in both biological and synthetic systems, while theoretical models have analyzed it in two and three dimensions (Elettro, Grandgeorge, and Neukirch, 2017; Elettro et al., 2015). Here, we implement a two-dimensional numerical model using CasADi and IPOPT, considering both rigid and deformable drops, in order to characterize the influence of surface tension and interface geometry on fiber coiling.

Chapter 9 addresses the case of a fibrous elastic membrane saturated with liquid, inspired by the experimental observations of Grandgeorge et al. (2018). In this system, surface tension dominates the global behavior, leading to responses reminiscent of soap films, while local confinement produces wrinkling and phase-transition-like patterns under compression. To capture these effects, we propose a two-dimensional model in which an Elastica is trapped inside a liquid layer, assuming translational invariance along the third dimension. Numerical simulations and theoretical analyses are used to describe the deformation process and to explore the analogy with phase transitions.

Through these two examples, Part III extends the classical framework of packing from rigid to liquid confinements. The results highlight both the similarities and the qualitative differences between solid–solid and liquid–solid systems, emphasizing the role of capillarity as a soft but effective confinement mechanism.



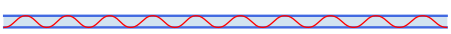

# Chapter 8

# Drop on a fiber

In nature, spiders are well-known for their ability to capture their prey with a web of silk. The spider silk has remarkable mechanical properties such as good ductility and high tensile strength. It was observed that the circumferential 'capture' threads in webs of spider *Araneus diadematus* can be contracted to less than 5% of the original length without slouch, and in the study of Vollrath and Edmonds (1989), this remarkable elasticity is explained by the thin layer of aqueous glue of the capture threads. This liquid layer induces packing of the silk by surface tension, and the viscosity further provides damping energy when the web is under shock.

With that we introduce the elasto-capillary coiling, which is induced by the surface tension difference between air-fiber and liquid-fiber interfaces. This difference yields a capillary force acting on the part of the fiber inside the drop. When the compression force due to capillarity is large enough, the fiber buckles and coils inside the drop. From an energetic point of view, the coiling of the fiber reduces the surface energy and increases the bending energy. If the reduction can compensate for the increase, then coiling occurs. Thanks to the windlass, the extra coiled structures serve as a reservoir and leads to the super-stretchability of the system.

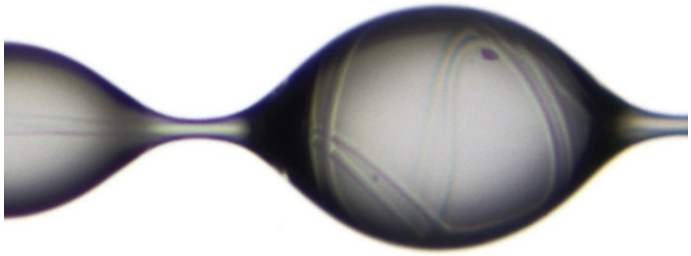

**Figure 8.1: Nephila capture silk coiling inside liquid glue droplets. Reproduced from Elettro et al. (2016).**

The experimental study of Elettro et al. (2016) reproduced the elasto-capillary induced windlass with natural spider silk (see figure 8.1) and also synthetic thin threads. Later, the synthetic system is scaled up by Grandgeorge (2018) (see figure 8.2). Additionally, a simplified 2D model is proposed to predict the behaviors of the drop-fiber system theoretically (Elettro et al., 2015). In this model, the fiber is assumed to be a disk, and a soft-wall potential (see section 6.3) is used to prevent the rod from exiting the liquid confinement. Elettro, Grandgeorge, and Neukirch (2017) then extended the 2D model to 3D. In both 2D and 3D models, it is shown that different coiling configurations exist, and bifurcation curves for the system are computed. Other studies include Schulman et al. (2017), in which experiments were carried out with microfibers and liquid droplets of different sizes, and a minimal model is given to estimate the winding threshold. In another experimental study, Barber et al. (2020) used flexible polymer-based ribbons to modulate interfacial interactions with liquid droplets, and discovered flagellum-like structures in addition to the wrapping. In a more recent study, Chen and Zhang (2022) proposed a numerical method which couples the lattice

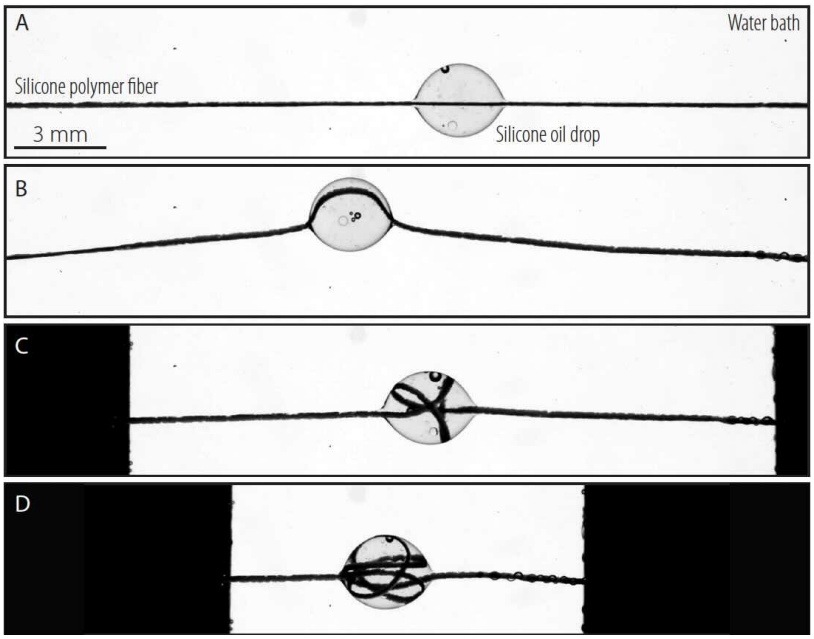


**Figure 8.2: Silicone polymer fiber coiling inside a silicone oil drop, while the whole system is immersed in a water bath. Reproduced from Grandgeorge (2018).**

model and many-body dissipative particle dynamics to simulate the elasto-capillary simulation. With this method, they succeeded in simulating the coiling of a flexible fiber around a droplet.

In this chapter, we implement numerically the drop-fiber system in 2D with CasADi and IPOPT. The interest of our implementation is that the inequality constraints of confinement can be applied directly by the optimizer instead of a soft-wall potential. Firstly, the drop is simplified as a rigid disk, and then we allow the liquid interface to deform. Different system parameters will be introduced, and their effects will be discussed. We will also study the behaviors of the system in general, in order to have a better understanding of the elasto-capillary effects and packing phenomenon for the liquid confinement.

## 8.1 Disk-like drop

In this section, we present a 2D model for a drop-fiber system in which the drop is assumed to be a rigid disk. In 2D, the fiber can be considered as an Elastica as in part II. The fiber is inextensible with length $L$ and bending stiffness $B$ (with unit $N \cdot m$ in 2D). The radius of the disk drop is $R$, and the surface tension of the liquid-vapor, solid-vapor, and solid-liquid are respectively $\gamma_{LV}$, $\gamma_{SV}$ and $\gamma_{SL}$. The gravity is neglected in the system. An illustration is given in figure 8.3.

### 8.1.1 Geometry and modelization

The drop is described by its center $(x_c, y_c)$, and its radius $R$. The left end of the fiber is at the origin, and the right end is controlled by displacement $\Delta L$. We separate the fiber into three parts. The middle part is inside the drop with length $\ell_s$, and the other two parts are of the same length $((L - \ell_s)/2)$, situated on the left and right sides of the drop.

The geometric variables of the fiber are functions of $s$, the curvilinear coordinate. They are $\kappa_{si}(s)$, $\theta_{si}(s)$, $x_{si}(s)$, and $y_{si}(s)$, which are respectively the curvature, the flexion, the horizontal

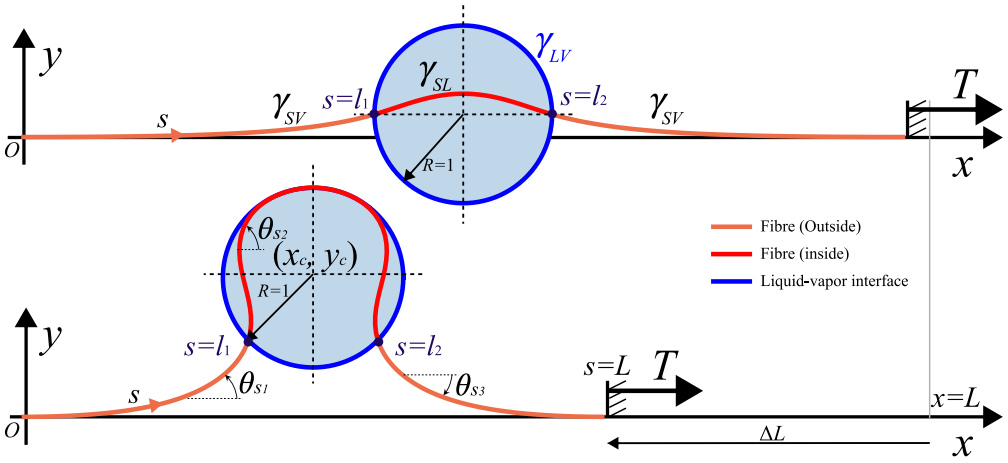


**Figure 8.3: Simplified system: drop coiling inside a circular rigid drop.**

and vertical positions of the part $i$. These variables are related by the differential equations

$$\theta'_{si}(s) = \kappa_{si}(s) \qquad x'_{si}(s) = \cos\theta_{si}(s) \qquad y'_{si}(s) = \sin\theta_{si}(s) \qquad i = 1,\ 2 \text{ or } 3, \tag{8.1}$$

$s \in [0, l_1]$ for the first part, $s \in [l_1, l_2]$ for the second part and $s \in [l_2, L]$ for the third part, where $l_1 = L - l_2 = (L - \ell_s)/2$ and $l_2 - l_1 = \ell_s$. The three parts are related by the following matching conditions at each intersection:

$$\theta_{s1}(l_1) = \theta_{s2}(l_1) \qquad x_{s1}(l_1) = x_{s2}(l_1) \qquad y_{s1}(l_1) = y_{s2}(l_1) \tag{8.2a}$$

$$\theta_{s2}(l_2) = \theta_{s3}(l_2) \qquad x_{s2}(l_2) = x_{s3}(l_2) \qquad y_{s2}(l_2) = y_{s3}(l_2) \tag{8.2b}$$

And the boundary conditions are

$$\theta_{s1}(0) = \theta_{s3}(L) = 0, \qquad x_{s1}(0) = y_{s1}(0) = y_{s3}(L) = 0, \qquad x_{s3}(L) = L - \Delta L. \tag{8.3}$$

To confine the beam inside a disk-like drop, we add the following geometry conditions

$$(x_{s1}(l_1) - x_c)^2 + (y_{s1}(l_1) - y_c)^2 = R^2 \tag{8.4a}$$

$$(x_{s2}(s) - x_c)^2 + (y_{s2}(s) - y_c)^2 \le R^2 \qquad s \in [l_1, l_2] \tag{8.4b}$$

$$(x_{s3}(l_2) - x_c)^2 + (y_{s3}(l_2) - y_c)^2 = R^2 \tag{8.4c}$$

**Formulation from the energetic point of view** The total energy of the system consists of the surface and the elastic energies, which are

$$\mathcal{E}_{surf} = 2\pi R\,\gamma_{LV} + 2\ell_s\,\gamma_{SL} + 2(L - \ell_s)\,\gamma_{SV}, \tag{8.5a}$$

$$\mathcal{E}_{elas} = \int_0^{l_1} \frac{B}{2}\kappa_{s1}^2\,ds + \int_{l_1}^{l_2} \frac{B}{2}\kappa_{s2}^2\,ds + \int_{l_2}^{L} \frac{B}{2}\kappa_{s3}^2\,ds. \tag{8.5b}$$

Under the geometric 'rigid' assumption, the shape of the disk drop does not change, and the term $2\pi R\,\gamma_{LV}$ in the surface energy 8.5a is a constant. Moreover, the total length of the fiber is constant, thus the only variation of the surface energy is actually $2(\gamma_{SL} - \gamma_{SV})\ell_s$. To simplify the notation, we write

$$\Delta\gamma = 2\,(\gamma_{SV} - \gamma_{SL}) \tag{8.6}$$

which has to be positive for coiling to occur. Finally, finding the form and responses of the system involves minimizing the energy

$$\mathcal{E}(\ell_s, \kappa_{si}(s), \theta_{si}(s), x_{si}(s), y_{si}(s)) = \mathcal{E}_{elas} - \Delta\gamma\,\ell_s \tag{8.7}$$

under conditions (8.2), (8.3), and (8.4).

**Non-dimensionalization** We can adimensionalize the system with a length unit and a force unit, here we chose $R$ and $B/R$ respectively.

As opposed to problems involving only an Elastica, here we have the additional parameter $\Delta\gamma$, related to the drop. Applying the non-dimensionalization, we have

$$\Delta\hat{\gamma} = \frac{\Delta\gamma\, R^2}{B}, \tag{8.8}$$

which compares capillarity and elasticity. A large value of $\Delta\hat{\gamma}$ means that the capillarity is strong, and the coiling of the Elastica inside the drop is favorable energetically.

The dimensionless system of equations can also be directly recovered by setting $R = 1$ and $B = 1$ in the original system, and please note that the parameters and variables are all dimensionless in the following sections.

### 8.1.2 Numerical implementation and solving

As in other problems involving the Elastica, we discretize the system using Super-Helices and the mixed formulation, and the implementation is effectuated with IPOPT and CasADi in Python.

There are two main differences with the confined Elastica problem studied in part II. The first is, evidently, the constraints of the liquid confinement, and the second is that the Elastica is divided into three parts of varying lengths. The confinement condition can be achieved by writing the discretized version of (8.4). As for the varying parts, we use the same method as in the flexible sliding sleeve problem, see appendix D. Suppose the number of discretized segments for each part are respectively $N_1$, $N_2$, and $N_3$, the discretized system given to CasADi and IPOPT is

$$\min \quad \sum_{i=0}^{N_1-1} \frac{1}{2}\left(\kappa_{s1}^i\right)^2 \left(\frac{L-\ell_s}{2N_1}\right) + \sum_{i=0}^{N_2-1} \frac{1}{2}\left(\kappa_{s2}^i\right)^2 \left(\frac{\ell_s}{N_2}\right) + \sum_{i=0}^{N_3-1} \frac{1}{2}\left(\kappa_{s3}^i\right)^2 \left(\frac{L-\ell_s}{2N_3}\right) - \Delta\gamma\,\ell_s \tag{8.9a}$$

subject to Constraints of boundary conditions, mixed formulation, and confinement

$$\theta_{s1}^0 = \theta_{s3}^{N_3} = 0, \quad x_{s1}^0 = 0, \quad x_{s3}^{N_3} = L - \Delta L, \quad y_{s1}^0 = y_{s3}^{N_3} = 0; \tag{8.9b}$$

$$\theta_{s1}^{N_1} = \theta_{s2}^0, \quad x_{s1}^{N_1} = x_{s2}^0, \quad y_{s1}^{N_1} = y_{s2}^0; \tag{8.9c}$$

$$\theta_{s2}^{N_2} = \theta_{s3}^0, \quad x_{s2}^{N_2} = x_{s3}^0, \quad y_{s2}^{N_2} = y_{s3}^0; \tag{8.9d}$$

$$\left(x_{s2}^0 - x_c\right)^2 + \left(y_{s2}^0 - y_c\right)^2 = 1; \quad \left(x_{s2}^{N_2} - x_c\right)^2 + \left(y_{s2}^{N_2} - y_c\right)^2 = 1; \tag{8.9e}$$

$$\left(x_{s2}^i - x_c\right)^2 + \left(y_{s2}^i - y_c\right)^2 \leq 1, \quad \forall i = 1, 2, ..., N_2 - 1. \tag{8.9f}$$

Given parameters are $\Delta\gamma$ and $L$, and the discretized system is solved by the continuation method with control parameter $\Delta L$.

The focus of the analysis is the coiling part, and we observe that, except for the part inside the drop, the Elastica only deforms within a small range near the drop. Hence, the system actually depends on the controlled displacement $\Delta L$ rather than the original total length $L$. Practically, the value of $L$ is chosen such that the Elastica keeps straight near the left and right ends during the whole simulation.

As what has been presented in 5.1, we have access to the values of Lagrange multipliers in addition to the variables. In the problem of coiling fiber inside the liquid cavity, the tension $T$ (see figure 8.3) is the Lagrange multiplier of the constraint related to the displacement control $x(L) = L - \Delta L$.

### 8.1.3 Results and discussions

In the study of Elettro et al. (2015), the system is solved with differential equations derived with a variational method based on the continuous energy (8.7) with constraints, thus both stable and unstable solutions are found. With the optimizer IPOPT, we only find stable solutions, corresponding to local minima of the total energy of the system. We found in some simulations that the system is multistable, and the actual solution found by IPOPT depends on the parameters of the solving process, which is similar to what is explained in section 5.1 for the confined Elastica problem.

In figure 8.4, we show the results of two simulations with the same system parameters ($\Delta\gamma = 5$), but different solving parameter `mu_init`. In both simulations, we first decrease ($\Delta L \uparrow$) then increase ($\Delta L \downarrow$) the distance between the two ends. Hysteresis is observed, indicating the existence of energy dissipation during a loading cycle. Please remark that it is different from the energy dissipation due to the viscosity. Axisymmetric and point-symmetric configurations are respec-

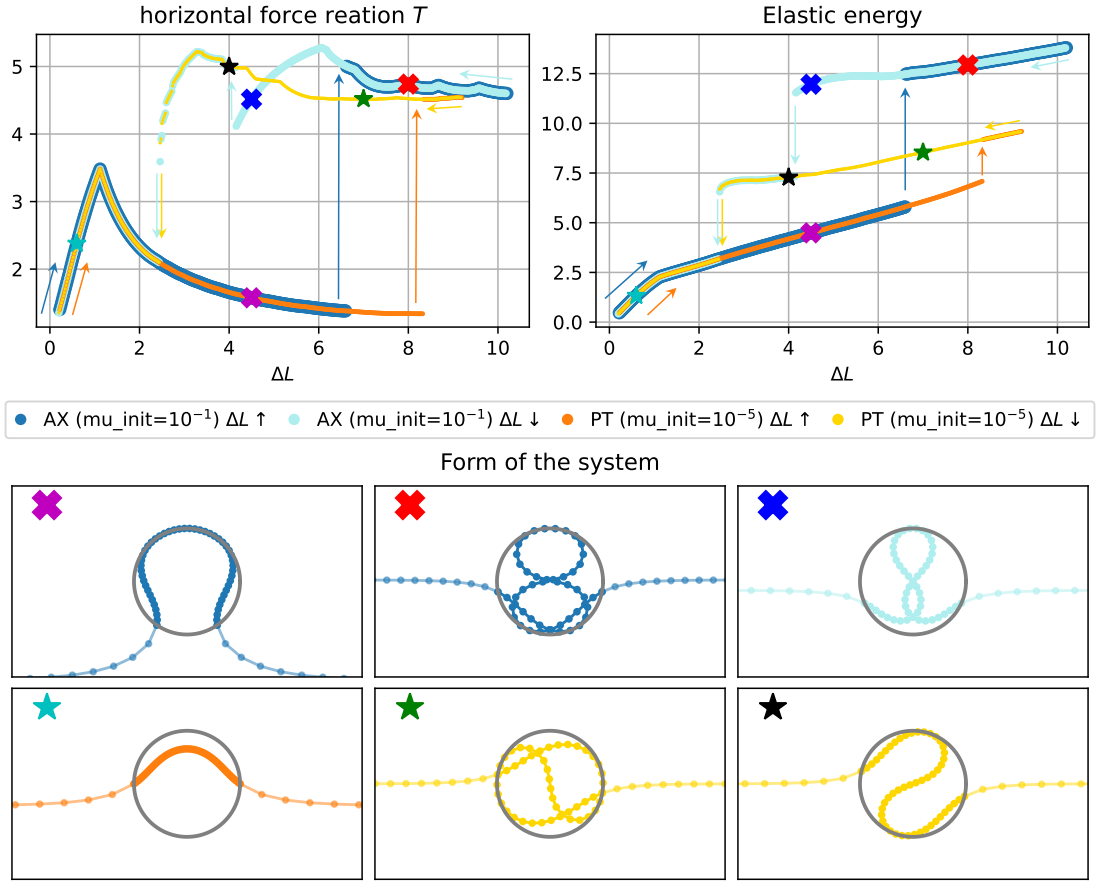


**Figure 8.4: The axisymmetric and point-symmetric configurations.** ($\Delta\gamma = 5$)

tively observed in these two simulations. The one with point-symmetric configuration is found by setting `mu_init`=$10^{-5}$, while the axisymmetric configuration is found by using the default value `mu_init`=0.1. Indeed, the contraction branch of the point-symmetric simulation sticks to the lower branch until a larger value of $\Delta L$. But we remark that a larger value of `mu_init` does not ensure finding the axisymmetric solutions. Since the elastic energy of the axisymmetric configuration is larger than the point-symmetric configuration, the system tends to adapt the point-symmetric configuration, and it is especially the case for large values of $\Delta\gamma$.

In figure 8.5, we show the solutions of simulations with different $\Delta\gamma$. When $\Delta\gamma$ is large,

the capillary effects are more pronounced. As a consequence, the bending related to the liquid interface at the triple point is larger, making the system less likely to stick to the initial buckling regime or pass to the axisymmetric configuration, hence the system jumps to the point-symmetric configuration at a smaller value of $\Delta\gamma$.

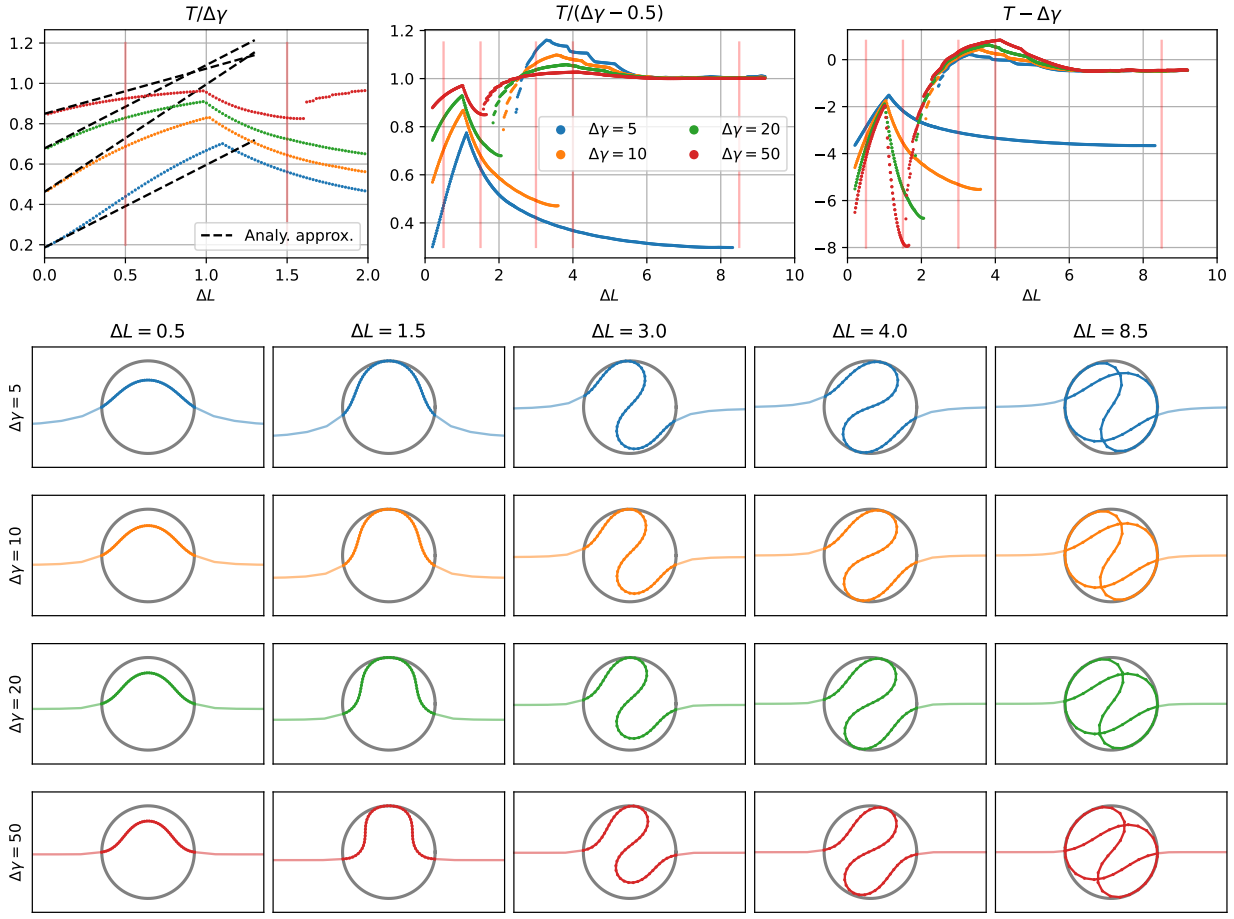


**Figure 8.5: Results of simulations with different values of $\Delta\gamma$. Each simulation includes increasing and decreasing $\Delta L$ process. Horizontal force reaction $T$ is presented with different scalings. The analytical approximations are calculated with the expressions from Elettro et al. (2015). Five values of $\Delta L$ are chosen and marked in the force diagrams with red lines, and we show the form of the system related to solutions on the decreasing $\Delta L$ branch.**

The force diagrams are presented with different scaling in figure 8.5, with the purpose of showing how $\Delta\gamma$ affects the different stages of the deformation. The first plot shows the initial stage of the deformation, including the initial buckling stage. We compare the simulation data with the predictions from Elettro et al. (2015) obtained by asymptotic analysis. The data and the prediction are in good agreement, proving the validity of the numerical implementation.

After the buckling stage, the fiber touches the drop interface and the force $T$ reaches a peak and then decreases with respect to $\Delta L$. From the second and third force diagrams, we see that $T$ scales with $\Delta L$ during this stage. As $T$ continues to decrease, at one point the fiber deforms into an 'S' shape and the force $T$ increases. We call this stage the transitional stage.

When $\Delta L \geq 6$, the horizontal force reaction $T$ reaches a plateau. During these two stages, $T$ is nearly a translation of $\Delta\gamma$, the four curves nearly superimposed in the diagram $T - \Delta\gamma$. The

observations from the forms of the system can indirectly explain the dependency of $\Delta\gamma$.

When the force curve reaches the plateau, each additional insertion of the fiber leads to more coils around the periphery of the drop. For this reason, we also call this stage the *coiling stage*. At this stage, the values of $T$ is approximately $\Delta\gamma - 0.5$ for all values of $\Delta\gamma$. We can explain this value by estimating the energy variation. Supposing $\delta L$ is the length variation of the inserted fiber, then the variation of the elastic energy is approximately $\kappa^2/2\,\delta L$, and the curvature of the additional fibers is approximately the same as the disk drop, that is $\kappa = 1/R = 1$. The work of $T$ is $T\,\delta L$, and the variation of the surface energy is $-\Delta\gamma\,\delta L$. Balancing these three terms, we find $T = \Delta\gamma - 0.5$, which confront the simulation data.

We conclude from the results and observations of the disk drop configuration that the dimensionless parameter $\Delta\gamma$ (8.8) measures the capillary effects of the surface tension with respect to the elastic effects of the fiber. When the value of $\Delta\gamma$ is large, it is more energetically favorable for the fiber to coil inside the drop, and it also reflects in the angle $\theta_s$ at the triple point.

Although this model is in 2D and does not confront the 3D settings in real life, it still demonstrates behaviors similar to the elasto-capillary coiling observed in experiences, for example, the different stages of deformation (Elettro et al., 2016). Additionally, the solutions of our simulations prove the feasibility of modeling the liquid-solid packing problem using a discretized optimization problem formulation.

In the next section, we stay in two dimensions but allow the drop to be deformable, and the numerical implementation is extended to adapt to the deformable interface.

## 8.2 Deformable drop

In the last section, we showed that it is possible to formulate the problem of the fiber coiling inside a circular drop as a discretized optimization problem and implement it using CasADi and IPOPT. We can further remove the geometric assumption of the rigid disk for the drop, and allow the drop to be deformable. The system of the fiber and the deformable drop is shown in figure 8.6. The

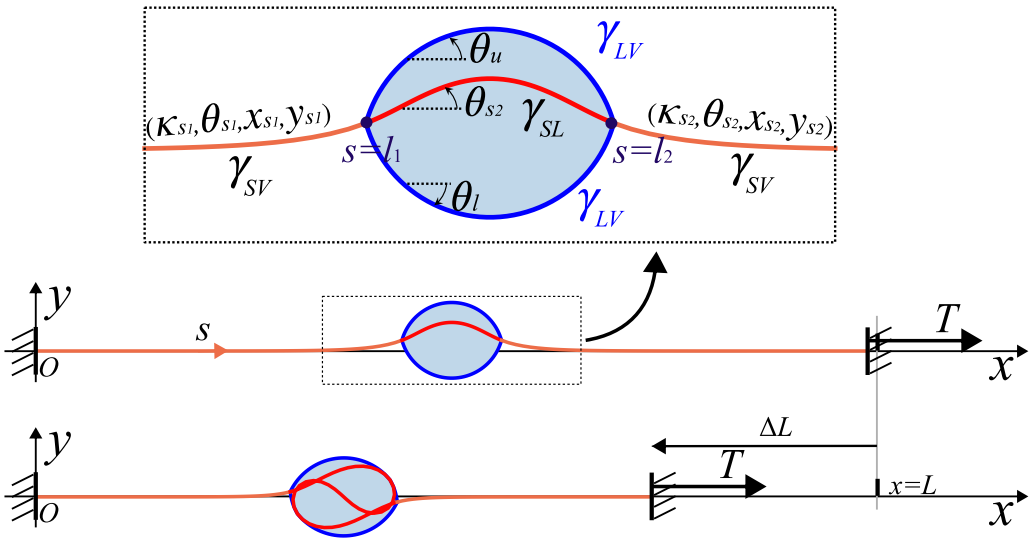


**Figure 8.6: Drop coiling on a deformable drop**

material properties are described with the same symbols as for the rigid-disk drop, and here the gravity is also neglected.

### 8.2.1 Description of the drop and formulation of the problem

The description of the fiber keeps same as in the disk drop case, and here we only present the description of the drop.

As in the example of the hanging drop in section 1.6, the interface of the drop is described using the variable $\sigma \in [0,1]$ which is the reference curvilinear coordinate. The unknowns functions are $(\theta_j(\sigma_j), x_j(\sigma_j), y_j(\sigma_j))$, where $j = u$ for the upper interface and $j = l$ for the lower interface. The length of the upper and lower interfaces are unknown, and we note them $\ell_u$ and $\ell_l$. The variables are related by

$$\frac{dx_j}{d\sigma_j} = {x_j}'(\sigma_j) = \ell_j \cos\theta_j(\sigma_j), \quad \frac{dy_j}{d\sigma_j} = {y_j}'(\sigma_j) = \ell_j \sin\theta_j(\sigma_j), \qquad \sigma_j \in [0,1] \text{ and } j = u \text{ or } l. \tag{8.10}$$

At the triple points, which are the two ends of the second part of the fiber, the upper and lower interfaces are connected together, thus we add continuity conditions

$$x_u(0) = x_l(0) = x_{s2}(l_1), \qquad y_u(0) = y_l(0) = y_{s2}(l_1) \tag{8.11a}$$
$$x_u(1) = x_l(1) = x_{s2}(l_2), \qquad y_u(1) = y_l(1) = y_{s2}(l_2) \tag{8.11b}$$

And the volume of the drop is

$$V = \int_0^1 y_u \cos(\theta_u)\, \ell_u d\sigma_u - \int_0^1 y_l \cos(\theta_l)\, \ell_l d\sigma_l \tag{8.12}$$

To relate the deformable drop to the rigid-disk drop, we assume that $V = \pi R^2$, where $R$ is equivalent to the radius of the disk drop.

The surface energy of the system is

$$\mathcal{E}_{surf} = \gamma_{LV}\,(\ell_u + \ell_l) + 2\ell_s\gamma_{SL} + 2(L - \ell_s)\gamma_{SV}. \tag{8.13}$$

While the term $L\gamma_{SV}$ is still a constant, the surface energy related to the liquid-vapor interfaces is now variable. We again use the symbol $\Delta\gamma$ as in (8.6).

**Constraints of the liquid confinement** Because the liquid interfaces are now deformable, the conditions (8.4) are not applicable anymore. Theoretically, we can express the confinement by

$$y_u(\sigma_u) \geq y_{s2}(s) \geq y_l(\sigma_l), \qquad \text{with } x_u(\sigma_u) = x_{s2}(s) = x_l(\sigma_l). \tag{8.14}$$

However, this formulation is not practical for further analysis. For the numerical implementation, the liquid confinement condition will be reformulated.

**Formulation from the energetic point of view** Similar to the case of the disk drop, the problem can be written as a constrained optimization problem:

$$\begin{aligned} \min \quad & \mathcal{E}_{elas} + (\ell_u + \ell_l)\gamma_{LV} - \Delta\gamma\,\ell_s, \quad \mathcal{E}_{elas} \text{ is given by (8.5b)} \\ \text{subject to} \quad & \text{Differential equations of the geometry (8.1), (8.10)} \\ & \text{Continuation conditions (8.2), (8.11)} \\ & \text{Boundary conditions (8.3)} \\ & \text{Volume condition } V = \pi R^2 \\ & \text{Liquid confinement conditions} \end{aligned} \tag{8.15}$$

**The initial stage of deformation** Suppose initially the fiber stays straight, and we focus on the shape of the drop. Using energy minimization as in section 1.6 or the method of force balance, we can find that the upper and lower interfaces are circular arcs, symmetric with respect to the horizontal and vertical axes. Therefore, we have $\theta_u(0) + \theta_l(0) = 0$, $\theta_u(0) + \theta_u(1) = 0$ and $\theta_u(1) + \theta_l(1) = 0$, and also

$$\Delta\gamma = 2\gamma_{LV} \cos\theta_u(0) = 2\gamma_{LV} \cos\left(\frac{\theta_l(1) - \theta_u(1)}{2}\right). \tag{8.16}$$

Recall that in the example of the simple drop on a substrate, the Young-Dupré law indicates $\Delta\gamma = \gamma_{LV}\cos\theta_0$, where $\theta_0$ is the angle at the intersection of liquid interface and the floor. The relation (8.16) is a modified version of the Young-Dupré law.

From the constant volume of the drop, we can also derive the initial length of the liquid cavity

$$x_u(1) - x_u(0) = 2R\sin\theta_c\sqrt{\frac{\pi}{2(\theta_c - \cos\theta_c\sin\theta_c)}}, \quad \text{with } \theta_c = \theta_u(0). \tag{8.17}$$

**Non-dimensionalization** Similar to the system of rigid-disk drop, we also adimensionalize the system with the length unit $R$ and the force unit $B/R^2$ and, in the following, all variables and parameters are dimensionless.

### 8.2.2 Discretization and numerical implementation

In the deformable-drop case, the discretization of the Elastica is the same as that in the rigid-drop case. For the liquid interfaces, we use the rod discretization scheme, meaning that the angle $\theta_j$ ($j = u$ or $l$) is constant per segment. A more detailed description of the liquid interface can be found in section 1.7.1.

As we apply the optimization method to the discretized system, the conditions are actually transformed into non-penetration conditions (3.10), which were described in section 3.2.1. The discretized interfaces serve as the reference segments (segment $\mathbf{B}_1\mathbf{B}_2$ in equation (3.10a)), and the nodes of the Elastica (equivalent to the node $\mathbf{A}_1$ in equation (3.10a)) is set to stay on one side of the interface segments. More precisely, we define the *confinement matches*, relate each node of the fiber to the closest segment of the upper interface and also to that of the lower interface. The node is then set to remain always at the same side of the segment. To ensure the convergence, several other segments next to the closest segment can be added into the non-penetration condition.

Given a set of parameter $(\gamma_{LV}, \Delta\gamma, L)$, the simulation begins with a weakly deformed stage (a small value of $\Delta L$) and an approximation of the initial solution, we use the continuation method with control parameter $\Delta L$. The algorithm goes as follows:

**Algorithm of the liquid confinement:**
**Initial**: starting from a small $\Delta L$ and the initial state, set the confinement matches.
**for** each given $\Delta L_i$ ($\Delta L$ increases gradually):
  Initiate optimizer with the solution of the previous step
  Apply the equality constraints and the confinement constraints
  Solve the system
  Detect if all the fiber nodes of the second part stay inside the drop
  **Repeat** if any node of part two is outside the drop, or the iteration number reaches max:
    Reset the confinement matches
    Apply the equality constraints and the confinement constraints
    Solve the system
  Reset the confinement matches



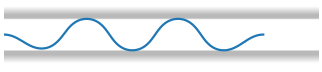

### 8.2.3 Results and discussions

Please recall that the behaviors of the system depend on the (nondimensionalized) parameters $\gamma_{LV}$, $\Delta\gamma$ and $\Delta L$, the last one serving as the control parameter in a simulation. With that, we conducted several simulations with different parameters values. In figure 8.7, simulation solutions with different values of $\Delta\gamma/\gamma_{LV}$ and the same value of $\Delta\gamma$ are presented. In figure 8.8, it is the value of $\Delta\gamma/\gamma_{LV}$ that is kept the same, and the value $\Delta\gamma$ which varies.

Following the analysis of the disk drop, we show the variation of the horizontal force reaction $T$ as a function of $\Delta L$. Physically, $T$ is the externally-applied tension on the fiber at, and numerically it is given by the Lagrange multiplier of the displacement control constraint on $x(L)$. Please remark that tiny jagged patterns can be observed on the force reaction curves. This is due to the discretized non-penetration condition, and can be smoothed by using finer discretization or higher order non-penetration conditions (Crespel et al., 2024).

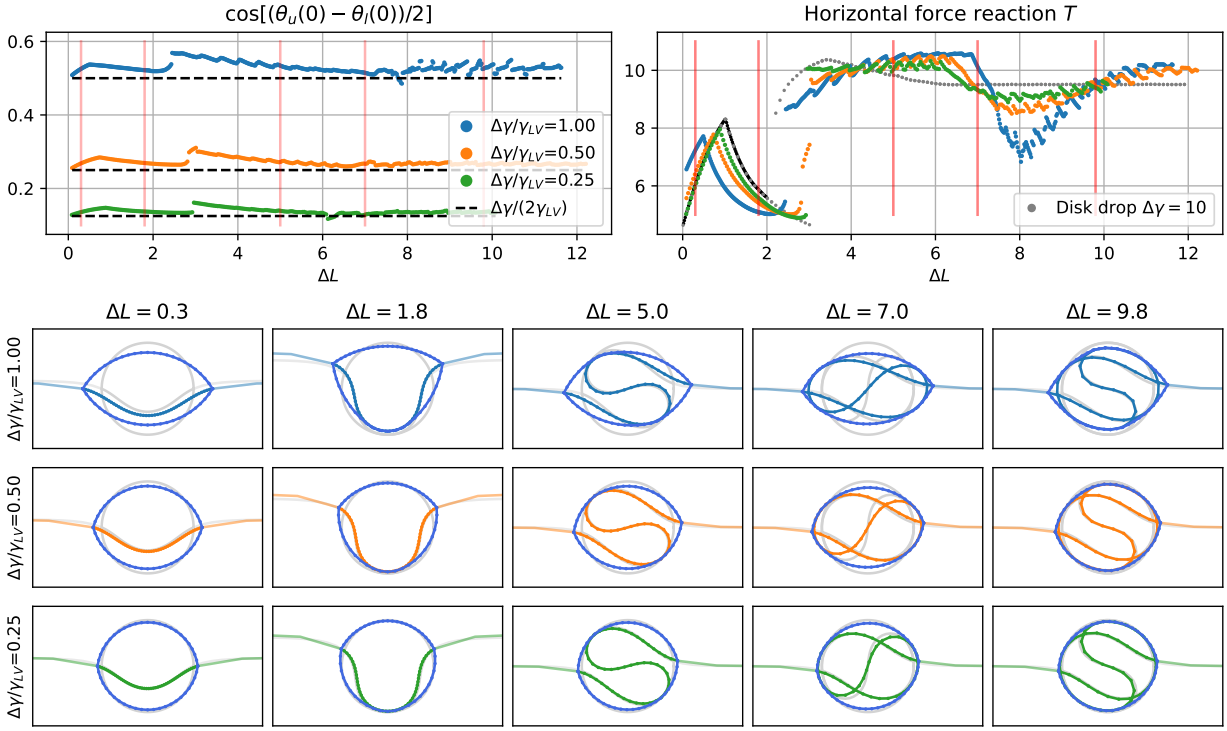


**Figure 8.7: Results of simulations for the deformable drop with $\Delta\gamma = 10$ and different values of $\Delta\gamma/\gamma_{LV}$. (Top-left) Computed 'contact' angle and comparison with the prediction from Eq. 8.16 plotted in dashed-black lines. (Top-right) Reaction force $T$, with the results of the rigid-disk drop plotted in gray for comparison. Five different $\Delta L$ are chosen, marked by the red lines in the force and angle diagrams. (Bottom) The forms of the system are shown below, compared with the rigid-disk solutions in gray.**

In figure 8.7, we show the drop angle and the tension $T$ as functions of $\Delta L$. In the force diagram, we also show the rigid-disk drop results. Below the diagrams, the forms of the system for each simulation at five different values of $\Delta L$ are presented with the rigid-disk drop solution in gray for comparison.

In the preliminary theoretical analysis, we found that $\Delta\gamma/\gamma_{LV}$ determines the contact angle of the drop, and the contact angle is predicted to satisfy (8.16) at the initial stage of deformation.

The values of contact angle $\theta_u(0)$ and $\theta_l(0)$ are estimated with

$$\theta_j(0) \simeq (3\theta_j^0 - \theta_j^1)/2, \qquad (j = u \text{ or } l) \tag{8.18}$$

where $\theta_j^0$ and $\theta_j^1$ are respectively the discretized flexion angle of the first and the second segment. From the angle diagram, the curves of the numerical solutions join the prediction lines at $\Delta L = 0$, and then stay around the prediction for larger displacement. This is coherent with the theoretical prediction, indicating the value of $\Delta\gamma/\gamma_{LV}$ affects the contact angle of the drop. When $\Delta\gamma/(2\gamma_{LV})$ tends to zero, the contact angle tends to $\pi/2$, and the behaviors of the system are more similar to the disk drop case. Conversely, when the value of $\Delta\gamma/(2\gamma_{LV})$ approaching one, the drop becomes flatter. When the value exceeds one, the solid surface is lyophilic, and the drop will spread on the surface.

Comparing the results of the deformable drop and those of the rigid-disk drop, we see differences at each stage of deformation, especially the initial buckling stage and the final coiling stage. At the initial buckling stage, drops with a smaller contact angle buckle with smaller tension $T$, and the peak point is anticipated. This is because the drop is longer and narrower; thus the length of the fiber initially covered by the drop is larger, and a smaller middle point displacement is needed to touch the interface. During the coiling stage, the rigid-disk drop has a constant value of $T$. But for the deformable drop, the value of $T$ sinuates, and the amplitude is larger for drops with smaller contact angles. Detailed discussions about the coiling stage can be found later in this section.

Figure 8.8 presents the solutions with the same $\Delta\gamma/\gamma_{LV}$ and different values of $\Delta\gamma$. We choose $\Delta\gamma/\gamma_{LV} = 1$, a relatively large value, such that the contact angle is small, and the solutions diverge more from the rigid-disk drop case.

From the results of the rigid-disk drop, we know that $\Delta\gamma$ is related to the capillarity effects, the fiber is more likely to coil inside the drop when $\Delta\gamma$ has large values, and this affects the inclination of the fiber at the triple points. For the deformable drop, these effects retain. Moreover, in the rigid-disk drop section we have mentioned that it is more likely to obtain axisymmetric configurations for small values of $\Delta\gamma$, and this is also the case for the deformable drop. The solutions of $\Delta\gamma = 5$ presented in figure 8.8 have indeed the axisymmetric property. For the same value of $\Delta L$, the axisymmetric configuration has higher elastic energy than the point-symmetric configuration. For larger $\Delta\gamma$ values ($\Delta\gamma = 10, 20, 40$), the $T - \Delta\gamma$ curves almost superimpose as soon as the fiber deforms into point-symmetric configurations, and then the system enters the coiling stage. From the forms of the system shown below the diagrams, we observe that after the fiber adapts the point-symmetric configuration, there is little difference between the geometry of solutions with different $\Delta\gamma$ at a given value of $\Delta$. These observations indicate that the variation of $T$ during the coiling stage is closely related to the shape of the drop, which is determined by $\Delta\gamma/\gamma_{LV}$.

We further investigate the coiling stage with simulations for larger values of controlled displacement $\Delta L$. Figure 8.9 shows three solutions of the deformable drop and one solution of the rigid-disk drop.

In the force diagram, we present the force $T - \Delta\gamma$ as a function of $\Delta L/(2\pi)$, and we observe that the sinuosity during the coiling stage is periodic, and the period is approximately $2\pi$, the perimeter of the drop if it is circular. The deformation of the couple system is also observed to be periodic, relevant to the variation of $T$, from which we deduce that the sinuosity observed in the force diagram is due to the non-circular shape of the deformable drop.

The solutions presented in blue and orange have the same $\Delta\gamma/\gamma_{LV} = 1$, which is the same value as the solutions presented in figure 8.8. The force curves are superimposed at the beginning of the coiling stage, then the blue solution, which has a smaller value of $\Delta\gamma$ elongates, and the force curve does not vary much afterward. For the orange solution, the elongation also happens



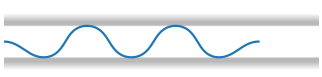

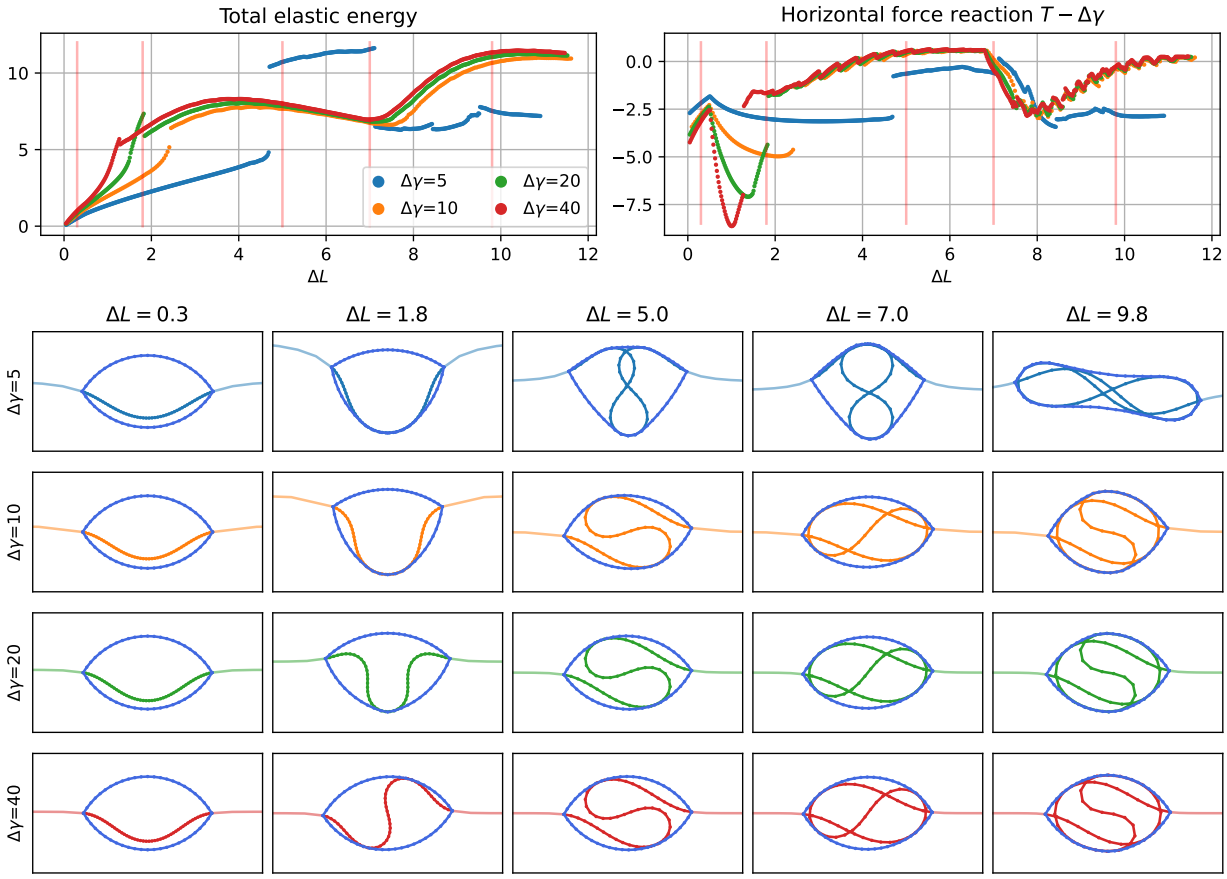


**Figure 8.8: Results of simulations with $\Delta\gamma/\gamma_{LV} = 1$ and different values of $\Delta\gamma$. Five different $\Delta L$ are chosen, marked by the red lines in the force and energy diagrams, and the related forms of the system are shown below.**

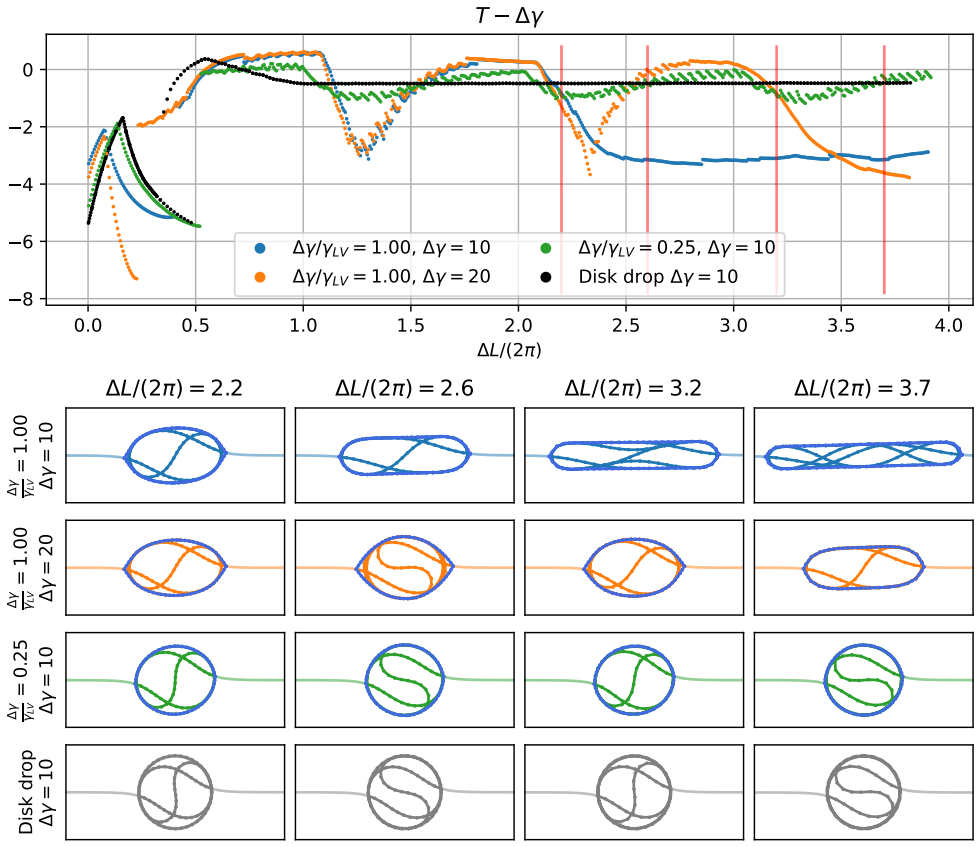


**Figure 8.9: Coiling stage. Three solutions of the deformable drop simulations with different parameter values are shown with one solution of the rigid-disk drop case. Four different $\Delta L$ are chosen, marked by the red lines in the force diagram, and the related forms of the system are shown below.**

but at a larger value of $\Delta\gamma$. In fact, the elongation is also observed for the solution with $\Delta\gamma = 5$ in figure 8.8, so it seems that the smaller $\Delta\gamma$, the smaller the value of $\Delta L$ at which elongation happens. It is possible that this elongation happens when the contact angle is small (large value of $\Delta\gamma/\gamma_{LV}$). The elongated form is energetically favorable for the fiber, as the fiber is less curved in most part, but it costs more interface energy. If the surface tension is not large enough, the drop is not able to trap the fibers anymore, and this deformation happens.

The deformable drop solutions presented in blue and green colors and the rigid-disk solution have the same value of $\Delta\gamma$, but the green solution has a larger contact angle (a smaller value of $\Delta\gamma/\gamma_{LV}$). We observe again that solutions with large contact angles tend to the solutions of the rigid-disk drop case, thus the sinuosity during the coiling stage is smoother. Indeed, when the fiber coils in a drop with a smaller contact angle, the fiber is actually coiling around an ellipse with larger eccentricity, thus the amplitude of the sinuosity is larger.

## 8.3 Conclusion for the drop-fiber packing

In this chapter, we have studied the coiling of an elastic fiber inside a liquid drop by using a numerical optimizer solving the discretized system. Two models in 2D were proposed, and the difference lies in the drop. For the first model, the shape of the drop is fixed to a disk, and for the other model, the drop is allowed to deform.

After non-dimensionalization, the behavior of the disk drop model only depends on $\Delta\gamma$ (8.8) and the loading parameter $\Delta L$. $\Delta\gamma$ measures the capillary effects compared to the elastic effects, directly related to the force reaction $T$, and to the deflection angle of the fiber at the triple point (i.e. point where the three phases meet). The simulation results show different stages of the deformation, including the initial buckling stage, the transitional stage, and the coiling stage. During the transitional stage, two configurations are observed: the axisymmetric and point-symmetric configurations. When the system enters the coiling stage, the force reaction stays constant. These results confirm the theoretical predictions, show the possibility of reproducing the elasto-capillary coiling observed in experiments, and also validate our numerical implementations.

For the deformable drop, we mainly examined the effects given by the contact angle, which depends on $\Delta\gamma/\gamma_{LV}$. A drop with a smaller contact angle has a longer and narrower shape, and this changes the force reaction at each stage of the deformation, especially the coiling stage, in which a periodic sinuosity was observed. The effects of $\Delta\gamma$ observed in the rigid-disk case are retained for the deformable drop, and we further discovered that drops with small values of $\Delta\gamma$ may deform into elongated shapes.

This problem of the elasto-capillary coiling of a fiber inside a drop helped us understand how surface tension affects the slender structure (Elastica) and leads to the packing phenomenon. In the next chapter, we will present and study another form of liquid confinement.



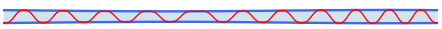

# Chapter 9

# Soaked membrane

The last chapter has shown the elasto-capillary interaction through the coiling of an elastic fiber around a drop. This is basically the packing phenomenon of a flexible fiber inside a liquid cavity that has the natural tendency to 'pull' the slender structure inside. The length of the fiber inside the liquid cavity keeps increasing during the deformation. As more and more matter is added into the cavity and the structure arranges itself in the most energetically favorable way, the fiber finally coils inside the drop.

This is not the only way that a liquid cavity captures and deforms flexible structures. Here we present another system in which an inextensible structure is totally trapped inside the liquid cavity throughout the deformation. Even without adding materials into the liquid cavity, the elasto-capillary interactions are still able to arrange the structure into ordered patterns. This system is composed of a flexible porous membrane, soaked with liquid, realized by Grandgeorge et al. (2018) with polymer fibers through electrospinning, and experimental inspections were made on this membrane. It has been observed that the soaked membrane has extraordinary deformability. Just as spider silk, the membrane can withstand large contractions without sagging. Figure 9.1 shows one of the experiences in which the membrane is contracted in one direction.

At the extended state (see **A**), the surface of the membrane is smooth. A small compression drives the surface to adapt homogeneous wavy patterns (see **B**). As the compression continues to increase, some regions exhibit more compact waves (collapsed) while other parts conserve the initial wavy patterns (see **C**). For even larger compressions (see **D**), it is the proportion of the collapsed regions increases, but the collapsed and wavy patterns remain nearly the same.

This deformation process is similar to the phase transition phenomenon that was described in section 4.1. The wavy and collapsed regions are the two phases. During the phase transition, the two phases coexist, and the change of loading causes one phase to transform into the other.

In the soaked membrane system, three ingredients play a central role: confinement by liquid interfaces, the emergence of wrinkling, and the occurrence of phase-transition-like behavior. As in the fiber–drop system, elasto-capillary effects generate confinement by the liquid interface; however, the wrinkling and phase transitions observed here are distinctive features of the soaked membrane.

Wrinkling instabilities are a common response of thin plates, films, and membranes subjected to compressive stresses. They manifest as periodic, often sinusoidal surface patterns, and are ubiquitous both in nature and in everyday life. Examples include the folded tubular mucosa, the gyrification of the brain cortex (Tan et al., 2020), the edge wrinkles in a lotus leaf or orchid petals (Wang, Yang, and Xu, 2022), and the draping of hanging curtains (Vandeparre et al., 2011).

The specific morphology and evolution of wrinkles depend on the system configuration and on the balance of internal and external stresses. When an elastic plate or membrane floats on a fluid foundation or is attached to a much softer elastic substrate, wrinkles result from a competition



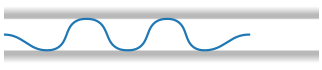

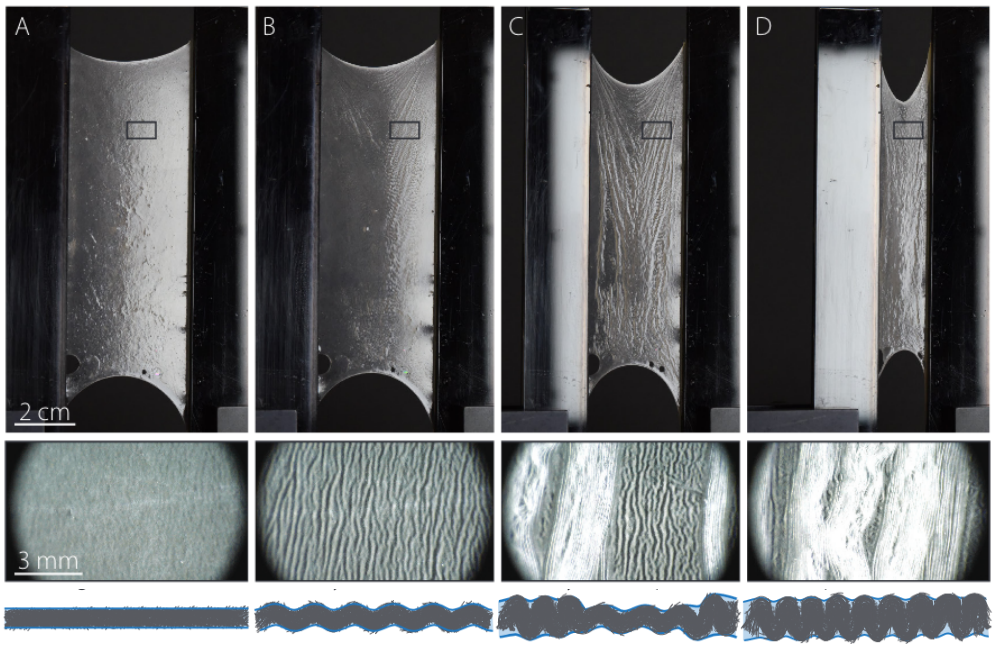


**Figure 9.1: The PAN membrane was soaked with water and compressed. From top to bottom respectively are the macro top view of the system, zooms of the membrane surface, and the assumed side views of the composite system. From left to right, the compression increases, and the deformation of the membrane changes. Figure adapted from Grandgeorge (2018).**

between the membrane's bending energy and either the gravitational potential of the fluid or the elastic energy of the support. The earliest analyses of such systems can be traced back to Hertz (1884) and Föppl (1897). More recently, Pocivavsek et al. (2008) and Brau et al. (2011) reported a variety of complex patterns, ranging from monoperiodic and multiperiodic wrinkles to localized folded states. Building on these observations, Audoly (2011) derived nonlinear envelope equations for localized deformations using two-scale expansions, while Diamant and Witten (2011) described the continuous progression from sinusoidal wrinkles to the formation of a single large fold.

In addition to elastic or gravitational substrates, capillarity can also generate wrinkling in thin membranes. Wrapping, folding, and other surface patterns induced by liquid interfaces have been studied extensively (Huang et al., 2007; Hure, 2011; Vella, Adda-Bedia, and Cerda, 2010). In contrast, the wrinkling of the soaked membrane considered here arises primarily from confinement by liquid interfaces. In this system, wrinkles act as surface reservoirs, enabling the membrane to accommodate large compressive strains and to achieve remarkable stretchability.

This mechanism has analogies with biological systems. White blood cells, such as macrophages and lymphocytes, are able to undergo large deformations despite the fragility of their membranes, which rupture at extensions of only a few percent. Their extraordinary deformability arises from microvilli and membrane reservoirs that unfold under stress (Lam et al., 2009). Furthermore, the effective tension of cell membranes can be modeled analogously to surface tension (Guillou et al., 2016). Understanding wrinkling morphologies in soaked membranes may thus provide insights into cellular mechanics. Beyond biology, similar principles are relevant for the design of stretchable and functional materials, including flexible electronics, soft robotics, and advanced metamaterials.

While elasto-capillary effects, wrinkling instabilities, and phase-transition phenomena have each been studied extensively, their interplay within soaked membrane systems remains poorly un-

derstood. This chapter investigates a theoretical model inspired by experimental observations (Grandgeorge et al., 2018), with the aim of clarifying the mechanisms underlying deformation and phase-transition-like behaviors in liquid-confined membranes.

## 9.1 Modelling and geometric description

To study the membrane-liquid system, we consider a simplified two-dimensional model, assuming translational invariance along the third dimension.

The elastic membrane is confined between two (liquid-air) interfaces, and it is assumed to be inextensible. Its length is denoted by $L$, and its bending stiffness per unit width is denoted by $B$. Gravitational effects are negligible, and therefore not included in the model.

The membrane is supposed to be covered by an incompressible liquid layer, and the surface tension of the liquid-air interface is $\gamma$. During the deformation, the membrane is trapped by the liquid cavity, and does not pierce the liquid-air interface. For this reason, the difference between the solid-liquid and the solid-air surface tension ($\Delta\gamma$ in the drop-fiber problem) does not enter the problem formulation.

The top of figure 9.2 shows the initial configuration of the system, where the membrane and both interfaces are flat. The upper interface is located at $y = H_0$, the lower one is at $y = -H_0$, placing the membrane at the center of the liquid layer. Hence, the initial thickness of the liquid is $2H_0$ and the liquid volume is $2H_0L$. Below, the deformed configuration is illustrated. The membrane deforms under displacement control while remaining confined between the interfaces, and the liquid volume is kept constant.

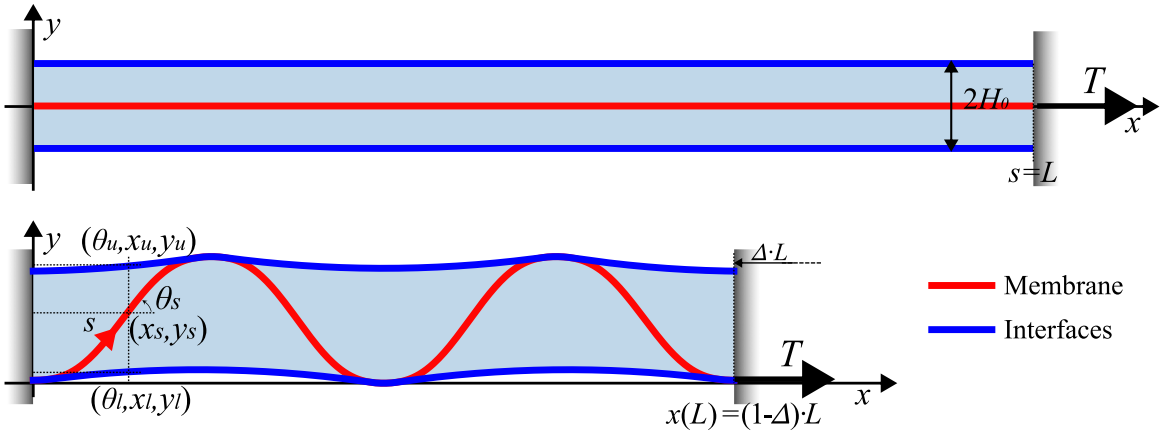


**Figure 9.2: Geometry description of the membrane-liquid system. Top: initial state. Bottom: deformed state.**

The geometry of the system is described by variables which are functions of the curvilinear coordinate $s$ of the membrane. Variables with subscript $s$ (solid) are related to the membrane, and the variables with subscript $u$ (upper) and $l$ (lower) describe the upper and lower liquid-air interfaces respectively.

The functions $\kappa_s(s)$, $\theta_s(s)$, $x_s(s)$, and $y_s(s)$ are respectively the curvature, the deflection angle, and the horizontal and vertical positions of the membrane. They are related by:

$$\theta_s{}'(s) = \kappa_s(s) \qquad x_s{}'(s) = \cos\theta_s(s) \qquad y_s{}'(s) = \sin\theta_s(s) \qquad s \in [0,\, L]. \tag{9.1}$$

The variables of the interfaces include $\theta_k(s)$, $e_k(s)$, $x_k(s)$ and $y_k(s)$, with ($k = u$ or $l$). Note that these are also functions of $s$, the curvilinear coordinate of the membrane. $\theta_k(s)$ is the deflection

angle of the interface, and $x_k(s)$ and $y_k(s)$ are the positions. $e_k(s)$ is the length variation of the interface. They are related by

$$\frac{dy_k}{dx_k} = \tan\theta_k, \qquad (k = u \text{ or } l) \tag{9.2a}$$

$$x_k{}'(s) = \frac{dx_k}{ds} = (1 + e_k)\cos\theta_k, \tag{9.2b}$$

$$y_k{}'(s) = \frac{dy_k}{ds} = (1 + e_k)\sin\theta_k, \tag{9.2c}$$

$$x_k(s) = x_s(s). \tag{9.2d}$$

The last equation connects the variables of the interface to those of the membrane and helps to simplify the formulation of the liquid volume and the no-penetration condition, which will be discussed later in this section.

With these notations, the length of the interfaces can be calculated by

$$L_k = \int_0^L (1 + e_k(s))\, ds \tag{9.3}$$

and the volume of the liquid contained between the 2 interfaces is

$$\mathcal{V}_{liquid} = \int_0^L \left[y_u\,(1 + e_u)\cos\theta_u - y_l\,(1 + e_l)\cos\theta_l\right] ds = 2L\,H_0 \tag{9.4}$$

### 9.1.1 Energetic point of view and optimization problem formulation

To find the responses of the soaked membrane at a given static load, we formulate an optimization problem based on the geometry described above and minimize the total energy under specified conditions.

The total energy of the system is the sum of the elastic energy of the membrane and the surface energy of the interfaces:

$$\mathcal{E}_{tot} = \mathcal{E}_{elas} + \mathcal{E}_{surf} = \int_{s=0}^{L} \frac{B}{2}\,\kappa_s^2(s)\, ds + \gamma\left(\int_0^L (1 + e_u(s))\, ds + \int_0^L (1 + e_l(s))\, ds\right). \tag{9.5}$$

The liquid confinement is interpreted as the no penetration condition

$$y_l(x) \le y_s(x) \le y_u(x).$$

Thanks to condition (9.2d), the above relation can be simply expressed by $s$

$$y_l(s) \le y_s(s) \le y_u(s). \tag{9.6}$$

The membrane is clamped at both ends. Not losing generality, we add periodic conditions for the interfaces. The boundary conditions of the system are

$$\theta_s(0) = 0 \qquad x_s(0) = 0 \qquad y_s(0) = 0 \tag{9.7a}$$

$$\theta_s(L) = 0 \qquad x_s(L) = L\,(1 - \Delta) \qquad y_s(L) = 0 \tag{9.7b}$$

$$y_u(0) = y_u(L) \qquad y_l(0) = y_l(L) \tag{9.7c}$$

The volume of the liquid is constant, interpreted as the volume constraint (9.4).

To sum up, the behaviors of the soaked membrane can be assessed by solving the optimization problem

$$\begin{array}{rl} \min & \mathcal{E}_{tot} \quad \text{given by (9.5)} \\ \text{subject to} & \text{Differential equations of the geometry (9.1), (9.2b), (9.2c)} \\ & \text{Matching condition (9.2d)} \\ & \text{Volume condition (9.4)} \\ & \text{Boundary conditions (9.7a)} \\ & \text{Liquid confinement conditions (9.6)} \end{array} \tag{9.8}$$

### 9.1.2 Dimensionless system

Please note that there are 2 parameters related to the material properties: the surface tension $\gamma$ and the bending stiffness $B$. There are 3 parameters related to the geometry: the membrane length $L$, the initial liquid layer thickness $H_0$, and the end shortening parameter $\Delta$.

$\gamma$ and $B$ are chosen to adimensionalize the other parameters and variables, then the force unit is $\sqrt{\gamma B}$, and the length unit $\sqrt{B/\gamma}$ which is the elasto-capillary length. The elasto-capillary length compares the elasticity with the capillarity, and estimates the characteristic size of slender structures that can be deformed by the surface tension.

After the non-dimensionalization, the 5 parameters are reduced to 3:

$$H_\gamma = H_0\sqrt{\gamma/B}, \qquad L/H_0, \qquad \Delta. \tag{9.9}$$

The parameter $H_\gamma$ reflects the elasto-capillarity, with a large value of $H_\gamma$ signifying strong capillary effects. The parameter $L/H_0$ is the aspect ratio of the liquid volume at the start of the experiment, and it also determines the geometry of the confinement. The last parameter $\Delta$ serves as a control of the loading.

For the simplicity of the notations, we do not introduce new symbols for the dimensionless variables. In the following, if not specially stated, the variables and parameters are all dimensionless. The dimensionless $H_0$ is equivalent to the parameter $H_\gamma$. In the analyses, the system depends on the set of parameters $(H_0, L, \Delta)$. We call $(H_0, L)$ the system parameters, and $\Delta$ the control parameter.

## 9.2 Discretized systems and numerical implementations

As in the other problems discussed previously, our first investigations on the soaked membrane problem rely on numerical methods, discretizing the system and reformulating the problem as a constrained optimization problem which can be solved by CasADi and IPOPT.

Please notice that the 2D model of the soaked membrane is very similar to that of the confined Elastica presented in part II, and the difference comes from the confinement. The wall confinement is rigid in part II, while the liquid interfaces are deformable for the soaked membrane. This contrast is similar to the difference between the rigid-disk drop and the deformable liquid drop, and from the last section we already showed that for deformable confinements, the non-penetration conditions should be treated with more caution. To numerically implement the non-penetration condition, we proposed two discretized systems, which are presented in the following.

### 9.2.1 Direct discretized system

Our first attempt at numerical implementation is directly derived from the continuous model presented in section 9.1, and figure 9.3 shows the discretized system.



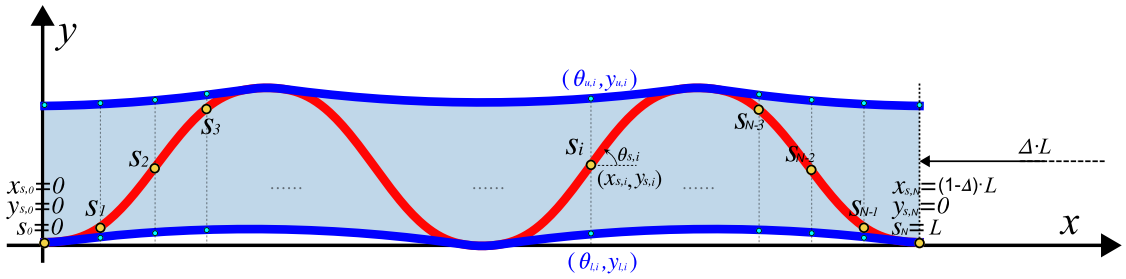


**Figure 9.3: Discretized system directly implemented from the continuous system.**

As mentioned earlier, the 2D model of the soaked membrane is similar to that of the Elastica confined between rigid walls. For the membrane, we apply the same discretization scheme as the confined Elastica, meaning the super-Helices discretization, hence the discretized elastic energy, the mixed formulation constraints, and the boundary conditions remain the same.

For the liquid part, we use the rod discretization, setting the deflection angles ($\theta_u$ and $\theta_l$) and the length variations ($e_u$ and $e_l$) constant per segment. The volume of the liquid is calculated by trapezoidal integration, meaning

$$\mathcal{V}_{liquid} \approx \sum_{i=0}^{N-1} \frac{y_u^{i+1} + y_u^i}{2}(1 + e_u^i)\cos\theta_u^i\,\delta s - \sum_{i=0}^{N-1} \frac{y_l^{i+1} + y_l^i}{2}(1 + e_l^i)\cos\theta_l^i\,\delta s \tag{9.10}$$

Thanks to the definition of interface variables as functions of the curvilinear coordinate $s$ of the membrane, and the matching condition (9.2d), the non-penetration condition can be easily written for the discretized system

$$y_u^i \geq y_s^i \geq y_l^i \quad \forall i \in (0, N) \tag{9.11}$$

However, we remark that relating the interfaces with the membrane brings benefits, but also problems. When the membrane turns backward, meaning the horizontal position $x_s(s)$ is not increasing monotonously, then also the membrane. Figure 9.4 illustrates such a case.

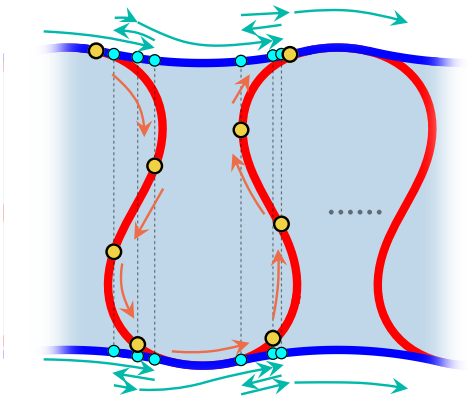

**Figure 9.4: Problem of the direct discretization system: nonphysical overturning of the interfaces. The arrows indicate the increasing order of nodes. When the membrane turns backward, the nodes of the interfaces also, causing nonphysical overlaps of the interfaces.**

Numerically, when this overturning happens, the length variation $e_u$ and $e_l$ defined on the segments in question should adopt a value less than -1 to satisfy the matching condition (9.2d). Please remark that by definition the length variation should be larger than -1, otherwise it means that the material vanishes, breaching the law of mass conservation. This natural condition is not

added into the numerical constraints, because it is self-satisfied when there is no overturning and the volume and the matching constraints are verified. In presence of overturning, the discretized system finds some non-physical directions in which the surface energy can be significantly decreased, which makes the system unstable and the solver cannot converge.

To allow the overturning of the membrane which may happen at large values of $\Delta$, we proposed the decoupled discretized system.

### 9.2.2 Decoupled discretized system

As the name indicates, the decoupled discretized system withdraws the matching condition (9.2d), and defines the membrane and the interfaces separately.

Figure 9.5 illustrates the decoupled discretized system. The mesh points of the membrane, the upper and lower interfaces are defined separately, denoted by $s_i$, $s_{u,i}$ and $s_{l,i}$ respectively.

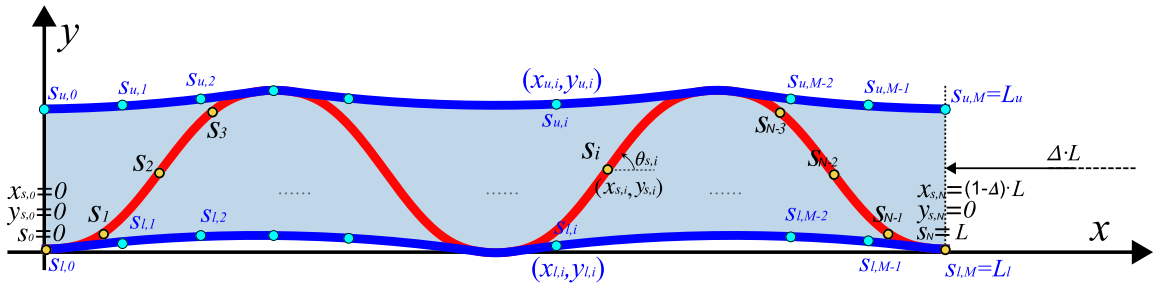


**Figure 9.5: Decoupled discretized system.**

The discretization scheme of the membrane stays the same (super-Helices). The interfaces are still discretized with rod discretization, but the length variations $e_u$ and $e_l$ are now scalars, valid for all the segments of the interfaces. It can be understood as: all segments of the upper (or lower) interface have the same length.

To define the non-penetration condition in the decoupled system, we use the same method as in the discretized system of the deformable drop. The segments of the interfaces still serve as the reference segments, and the nodes of the membrane are set to stay between a certain number of the closest upper and lower interface segments. The details about the numerical beam-to-beam contact conditions can be found in section 3.2.1, and please refer to section 8.2.2 for the implementation of the contact conditions inside the solving algorithm.

In the decoupled discretized system, each object (membrane or interface) can have a different number of nodes. Coarser discretization can be applied to the interfaces as their deformation is not as large as the membrane. This also provides better convergence and requires less computational power.

### 9.2.3 Solving process and the Lagrange multipliers

The solving process for both discretized systems is the same. As the system depends on three parameters, $(H_0, L, \Delta)$, we remark that in each simulation, $(H_0, L)$ is fixed, and the continuation method with control parameter $\Delta$ is used to mimic the experimental control of the contraction.

As other problems solved by IPOPT, in the discretized optimization formulation the Lagrange multipliers provide additional information. Recall that in section 5.1, the physical significance of certain Lagrange multipliers are presented, and the Lagrange multipliers of the soaked membrane system are alike.

The Lagrange multiplier of the boundary constraint $x_s(L) = L(1-\Delta)$ is the horizontal reaction force $T$ of the support, see figure 9.2. And the Lagrange multipliers of the non-penetration constraints are the vertical force reactions from the liquid interfaces, confining the membrane in the liquid. Moreover, the Lagrange multipliers of the mixed formulation, the discretized equivalences of the differential equations (9.1), (9.2b, 9.2c), are the internal moment and force in the membrane and the internal tension of the interfaces.

Compared to the Elastica confined between rigid walls, the soaked membrane system also has a volume constraint. With dimensional analysis, the Lagrange multiplier of the volume constraint has the same dimension as a pressure. An example of the Lagrange multiplier of a volume constraint is given by the simple drop problem in section 1.6. Nevertheless, we remark that in a complex system, expressing the same constraints in different ways leads to different Lagrange multipliers. In the case of the discretized systems of the soaked membrane, we know that it is related to the interior pressure of the liquid cavity, but the two discretization systems define the non-penetration conditions differently, thus the Lagrange multiplier of the volume constraint is not exactly the same for the two systems. For the direct discretized system, we can derive from the discretized formulation that

$$|\mu|\, L(1-\Delta) = \sum_{i}^{N} |f_u^i| + |f_l^i| \tag{9.12}$$

where $\mu$ denotes the Lagrange multiplier of the volume constraint, and $f_u^i$ and $f_l^i$ are the Lagrange multipliers of the non-penetration conditions on the upper and lower interfaces.

For the decoupled discretized system, it is harder to give an exact expression as the constraints are defined on segments and change with the algorithm. Therefore, in the analyses and discussions, we do not take into account the Lagrange multiplier of the volume constraint in the decoupled discretized system.

### 9.2.4 Observations and discussions of the simulation results

To start with, we compare the direct and the decoupled discretized system with the same system parameters and the same loading steps. Before the overturning stage, no difference is observed between the solutions given by the two methods. Then we choose to use the direct discretized system to study the incipient deformation of the soaked membrane model.

We observed that in the early stage of deformation, the membrane buckles and folds are created, similar to what was observed in the confined Elastica problems, and the interfaces do not deform much. Please recall that the system parameters are $H_0$ and $L$, all adimensionalized by the elasto-capillary length, and that $\Delta$ serves as the loading parameter. Depending on the system parameters, the interfaces start to deform at different values of $\Delta$. The behaviors and the responses of the system also vary with the parameters. To further assess these effects, we conducted a parametric study.

In the parametric study, different values of $H_0$ and $L/H_0$ were chosen, and simulations were carried out for each pair of system parameters. We focus on the deformation of the system and the variation of the horizontal force reaction $T$ as $\Delta$ gradually increases.

Nine solutions are chosen and presented in figure 9.6. The three values of $H_0$ (0.1, 1, and 10) represent different orders of magnitude of the intensity of the capillarity effects. And one small (20), one medium (100), and one large (250) value are chosen for the aspect ratio $L/H_0$, forming the nine pairs of system parameters.

Figure 9.6a shows the form of the system given by the simulation at a relatively large value of $\Delta$, illustrating the highly deformed stage before the overturning. Figure 9.6b shows how the horizontal force reaction $T$ changes with $\Delta$ for each pair of the system parameter.

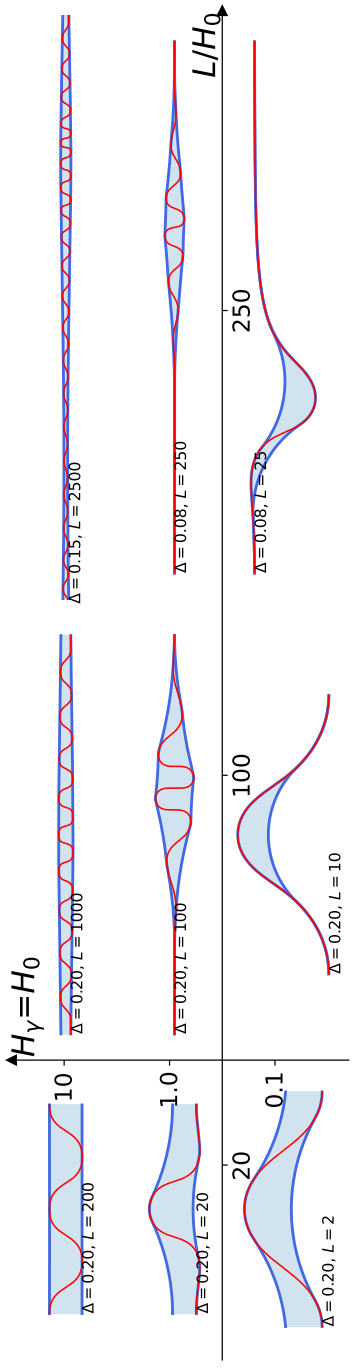


(a) Form of the system for relatively large $\Delta$

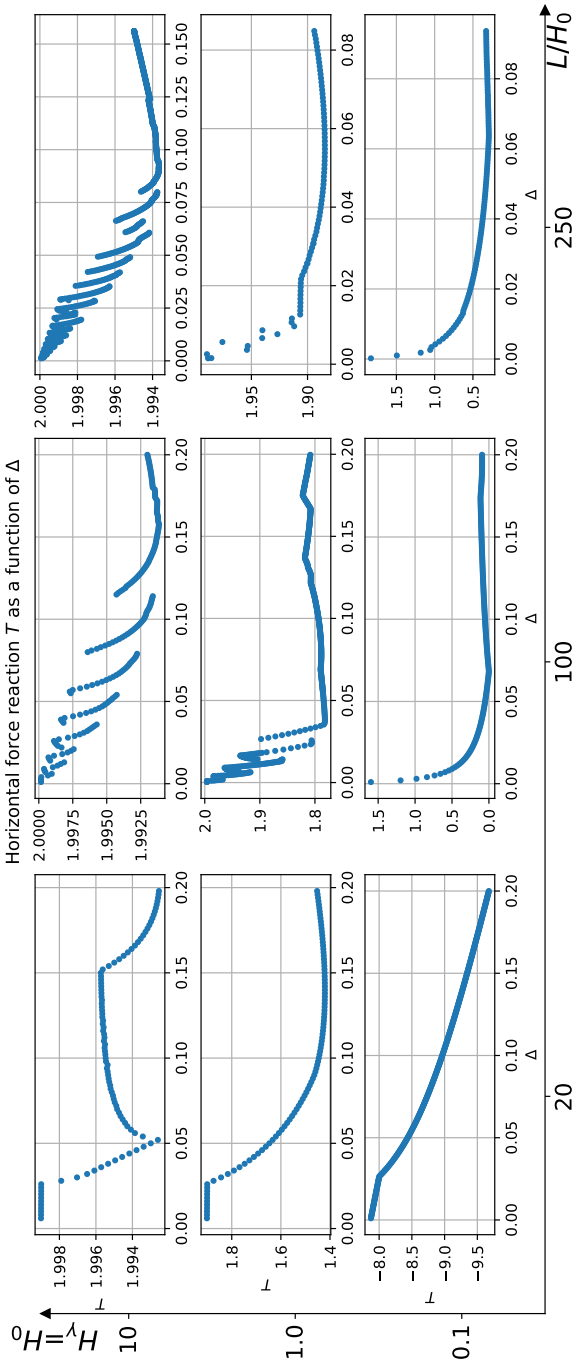


(b) Force reaction $T$ as a function of $\Delta$

**Figure 9.6: Observations from the total system simulations for different $H_0$ and $L/H_0$**

### Influence of the system parameters

Comparing the form of solutions, we see that the interfaces are more flexible when $H_0$ is small. This is expected, because $H_0$ is adimensionalized with the elasto-capillary length $\sqrt{B/\gamma}$, and a small value means that the capillary effects are weak ($\gamma$ small). In this case the interfaces are more likely to be deformed by the membrane inside the liquid cavity.

For $L/H_0$, we know from its definition that it is related to the length of the membrane and the volume of the liquid. A large value of $L/H_0$ means that the liquid layer is relatively thin, i.e. the liquid cavity is narrow compared to the length of the membrane. In fact, $L/H_0$ is equivalent to $1/a$ in the problem of the Elastica confined between rigid walls (chapter 6). We have revealed that more folds are created when the Elastica is pushed into a narrower tunnel, and the period of the folds creation depends on the parameter $1/a$. It is similar in the present case of liquid interfaces, especially during the first stages of deformation.

Coupling the two effects with different values of the system parameters, the responses of the model can be vaguely classified into three categories. In the first category, $H_0$ is large and/or $L/H_0$ is small. In this case, either because the capillarity is too strong or the confinement is too loose, the membrane acts like the Elastica confined between rigid walls. In the second category, $H_0$ is small and $L/H_0$ is large. The capillarity is too weak, and the membrane is barely deformed except at one spot where all the liquid tends to concentrate. The third category groups the rest. During the contraction loading, homogeneous folds are first observed, then the interfaces deform and the folds adopt varying heights. Examples are the four solutions shown in the top right-hand corner of figure 9.6a.

The solutions in this third category are similar to the experimental observations of the soaked membrane, and thus are of the most interest to us. With that, we define the range of the system parameters to be further investigated in the following sections. The parameter $H_0$ should be around 10, and the parameter $L/H_0$ should be in the order of magnitude of hundreds. Considering the precision and the required computational time and power, we limit $L/H_0$ to be less than 500.

### Geometry of the interfaces and capillary pressure

For the solutions with more flexible interfaces shown in figure 9.6a, it can be seen that the parts of interfaces not touched by the membrane (*the free parts* for short) are arc-shaped. Indeed, it is expected from Young-Laplace relation between pressure jump and curvature, and observed in the numerical data that the free parts are actually circular arcs, also meaning the curvature of the free parts are constant, and the angle $\theta$ varies linearly. It is also the case even for the seemingly flat interfaces when $H_0$ is large, but the curvature is too small to make the arc shape visible. Notably, all the free parts have the same curvature, equal to the value given of the Lagrange multiplier of the volume constraint $\mu$, see (9.12). This relation is valid under all circumstances, including the interfaces highly deformed by the membrane. One example is given in figure 9.7.

According to the Young-Laplace equation, which was introduced in the simple drop example in section 1.6, the capillary pressure difference sustained across the interface is given by the product of the surface tension and the local curvature. The observation of the numerical solution confirms our deduction that the Lagrange multiplier of the volume constraint corresponds to the pressure. It also suggests that there are no pressure differences in the liquid cavity across the membrane, which is expected. In our static 2D model, the physics of the fluid only acts on the liquid-air interfaces and the constant volume. There is only one global volume constraint, thus the liquid crossing the membrane does not bring any consequence.

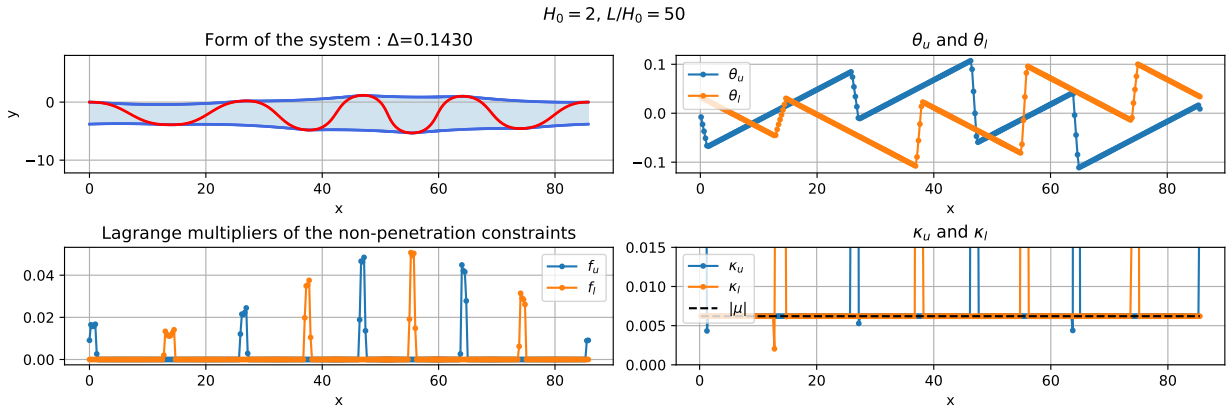


**Figure 9.7: One solution given by the direct discretization system ($H_0 = 2$, $L/H_0 = 50$). We show the form of the solution, the Lagrange multipliers of the non-penetration condition 9.11, the flexion angles of the interfaces, and the curvature of the interfaces calculated from the angles with finite differences. On the curvature diagram, the absolute value of $\mu$, the Lagrange multiplier of the volume constraint is plot in dash-dot black line.**

### Variation of the force reaction $T$

Comparing the force variations as functions of the endshortening $\Delta$ in figure 9.6b, we see a global trend in which $T$ decreases with increasing $\Delta$. $T$ has positive values except in the case $H_0 = 0.1$, $L/H_0 = 20$. Moreover, all positive curves start with $T = 2$ as $\Delta = 0$. We remark that by definition, $T$ is oriented in the opposite direction to the contraction, which is the opposite of the compression force $P$ in the problem of the Elastica confined between rigid walls. Thus, apart from the exceptional case ($H_0 = 0.1$, $L/H_0 = 20$), the supports are held in tension to prevent self-retraction during the displacement control. This is due to the surface tension of the interface. Supposing there is no membrane in the model, then the total energy to minimize during the deformation is only the surface energy, which is the product of the surface tension and the length of the interfaces. If the end displacement changes by $\delta\ell$, then the surface energy variation is $2\gamma\,\delta\ell$ (there are two interfaces), and the work of force $T$ is $-T\,\delta\ell$. Balancing these two terms gives $T = 2\gamma$, which gives the initial value 2 observed from the simulation results in the adimensionalized units. In the presence of the membrane, the buckling of the membrane yields another force opposing the contraction of the interfaces. Please recall that the buckling threshold of an Elastica with length $L$ and clamped at two ends is $(2\pi/L)^2$. In the exceptional case, the length of the membrane is $L = 2$, hence the buckling force is approximately 10, greater than the surface contraction 2. Subtracting 10 from 2 gives -8, which is the starting value of $T$ shown in the diagram, and this means one should push the support to introduce the endshortening $\Delta$. For the other cases, the membrane is so long that the buckling force is very small compared to the surface contraction, which explains why $T$ starts with a value very near 2 in the other force diagrams.

As the displacement loading increases, the deformation of the membrane is more pronounced, and its internal forces grow larger, that is why all $T$ decreases with $\Delta$ in all the force diagrams.

Focusing on the four solutions presented in the top right-hand corner, we see jagged patterns at the beginning of the loading, then the $T$ curve stagnates. We have already explained the deformation process of these solutions. The jagged patterns in the force diagrams correspond to the initial stage of the deformation, during which homogeneous folds are created one after the other. In fact, the internal force reaction $P$ of the membrane can be obtained by transforming

$T$ to $P = 2 - T$, and with that we recover similar force variations as in the case of the Elastica confined between rigid walls. Similar to the confined Elastica, the soaked membrane model also has the self-similar property during the homogeneous wrinkling stage. For the same value of $L/H_0$ and different values of $H_0$, $(2 - T)H_0^2$ as functions of $\Delta$ can be superimposed.

When $T$ is reaching the stagnation range, there is barely any newly created fold, the interfaces start to deform, and rearrangement happens to the existing folds. This stage is the most remarkable difference between the soaked membrane model, and the confined Elastica model discussed in part II, and it is also important to the understanding of the phase transition phenomenon observed in experiments. To discuss when the system enters the second stage, we use $\Delta^*$ to denote the endshortening value for the transition between the homogeneous stage and the inhomogeneous stage.

We remark that hysteresis is also present in the soaked membrane model. In figure 9.8, the results of a simulation with both loading and unloading processes are presented. Apart from the force variation, one solution of the homogeneous stage and one of the inhomogeneous stage are shown on the diagram to help distinguish the branches of the two stages. The force shown in the

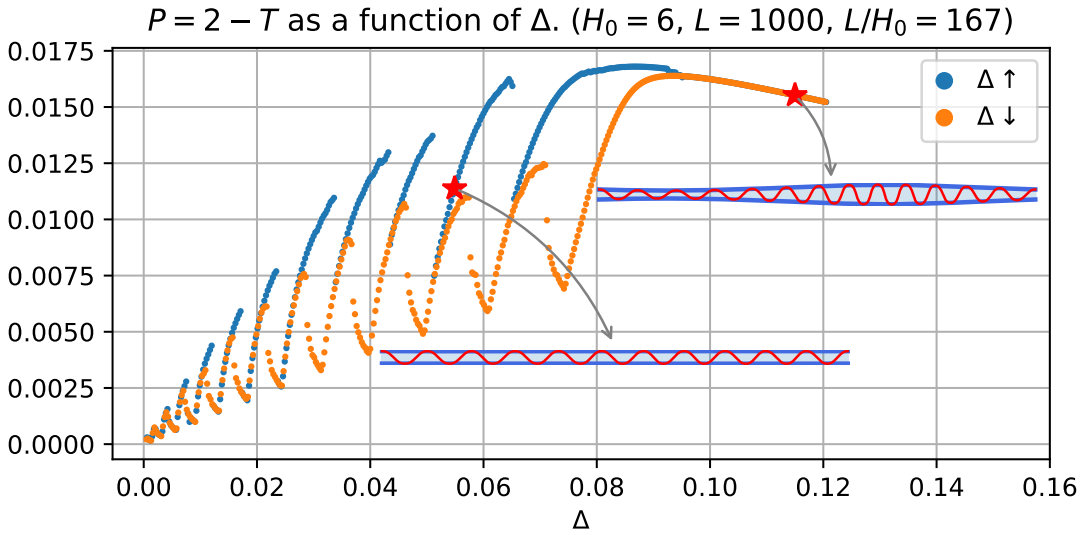


**Figure 9.8: The force diagram of one solution for $H_0 = 6$, $L = 1000$, the simulation contains both the loading and unloading process. For both homogeneous and inhomogeneous stage, one solution is chosen, marked by a red star in the force diagram, and the form of the system is plotted beside (width scaled for display purposes).**

diagram is actually $P = 2 - T$, the horizontal component of the internal force in the membrane. The branches of the homogeneous stage exhibit similar undulating patterns to those of the Elastica confined in rigid channels, and the hysteresis is also similar to the confined Elastica problem. Please notice that during the inhomogeneous stage, the force curves of the loading and unloading processes are superimposed, showing no hysteresis phenomenon.

This is different from the experimental results, in which hysteresis is present during the whole loading and unloading process (Grandgeorge, 2018), and can be explained by the fact that the viscosity and dynamic effects are not included in our model. Nevertheless, the force variation is coherent with the experimental observation: $T$ first decreases rapidly, then reaches a plateau regime.

**When the discretized systems fail and what is next**

Approaching the critical value of $\Delta$ at which the overturning happens, the direct discretized system does not converge. For the decoupled system, a tiny overturning can be observed in one of the folds, then the membrane adapts a shape similar to the spiral shape mentioned in part II and discussed in appendix E. An example is given in figure 9.9.

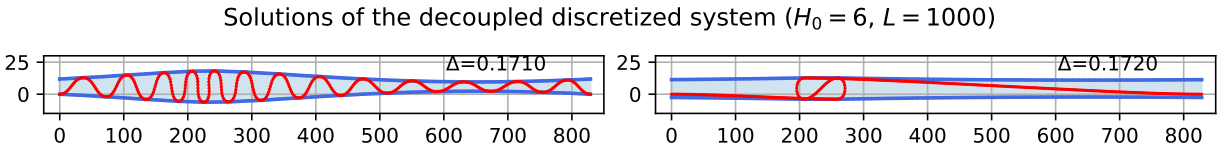


**Figure 9.9: Two solutions found by the decoupled discretized system** ($H_0 = 6, L = 1000$) **(width scaled for display purposes).**

In the proposed model, the spiral solution has significantly lower energy compared to the wrinkling solution (see appendix E), therefore the optimizer converges to the spiral solution. Indeed, in other studies involving the wrinkling of thin film-like structures, the *fold localization* was observed, which looks similar to the spiral shape we have found numerically (Jambon-Puillet, 2016; Pocivavsek et al., 2008). Although the spiral shape has been observed in the experiments of Grandgeorge (2018), this configuration rarely occurred and therefore wasn't investigated systematically (and thus has not been mentioned in literature).

Attempts have been made to avoid the spiral shape by adding self-contact conditions (for the membrane) into the decoupled discretized system, but the algorithm has difficulty converging. At each step inside the self-contact detection loop, the substantial variation of the results makes the constraints defined by the geometry of the previous step no longer applicable in the current step.

We speculate that the violent change comes from omitting the dynamic effects, which also explains the incoherence between the simulation results and the experimental observations. In a static model, all the stable solutions are theoretically admissible, and passing from one solution to any other can be easily achieved by the solver. When dynamic effects are added into the system, a certain time and energy are needed to pass from one state to another. In the static 2D model of the soaked membrane, the omitted dynamic effects especially refer to the dissipation brought by the fluid viscosity, and the diffusion related to the porosity of the membrane. Although the loading motion in the experiences is very slow, the characteristic timescale related to these dynamical effects may be even larger, such that the system never had time to rearrange itself into the spiral shape.

Although the discretized systems were not able to capture all the experimental behaviors of the soaked membrane, the successfully implemented algorithms recovered the formation of the homogeneous wrinkles at the early loading stage, and allowed a parametric study to determine the range of system parameters in which the wrinkling and the phase transition may happen. Moreover, inhomogeneous wrinkling form was observed, which is a promising result to reveal the mechanism of the phase transition phenomenon observed in experiments.

Notably, the creation of the homogeneous folds during the initial loading stage is very similar to the problem of Elastica confined between rigid walls, which was discussed thoroughly in part II. Instead of adding dynamical effects, which may be technically involved and challenging in parameter estimation, we propose to utilize what was learned previously from the confined Elastica problem to try and better understand the phase transition.

In the following section, we present the cellular models based on the same idea of the cellular models discussed in section 5.6.2 to analyze the responses and behaviors of the soaked membrane system.

## 9.3 Single cellular models

Given the creation of the repetitive patterns at the initial stage of deformation, the first analytical models are built with the same idea as the cellular models presented in section 5.6. To begin with, we focus on the homogeneous configuration, and assume that the system is composed of multiple occurrences of the same cell. By this definition, we call these models *single cellular models*.

### 9.3.1 Simplified single cellular model

The observations from the results of the discretized system in section 9.2.4 showed the wrinkling patterns when $H_0$ is relatively large ($H_0 \sim 5$) and the interfaces are almost flat. Even for the inhomogeneous wrinkling forms, the interfaces are approximately flat locally around each fold, regardless of the global undulations. For this reason, our investigations start with the smallest unit: one-half of the fold with interfaces assumed to be flat, that is we recover the cell defined in section 5.6.2.

In part II, we demonstrated the capability of the cellular models to predict the general behaviors of the rigidly confined Elastica. Moreover, these solutions possess a self-similar property, and passing from one value of the wall distance to the other only requires a rescaling (see section 5.6.3). In the following, we will explain how to apply this idea to the cellular model of the soaked membrane.

For the Elastica confined between rigid walls, the distance between the walls is fixed. In the case of the soaked membrane, the distance between the two interfaces is related to the fixed volume of the liquid and the distance between the two supports. Figure 9.10 illustrates how to estimate the distance if the interfaces are assumed to be flat.

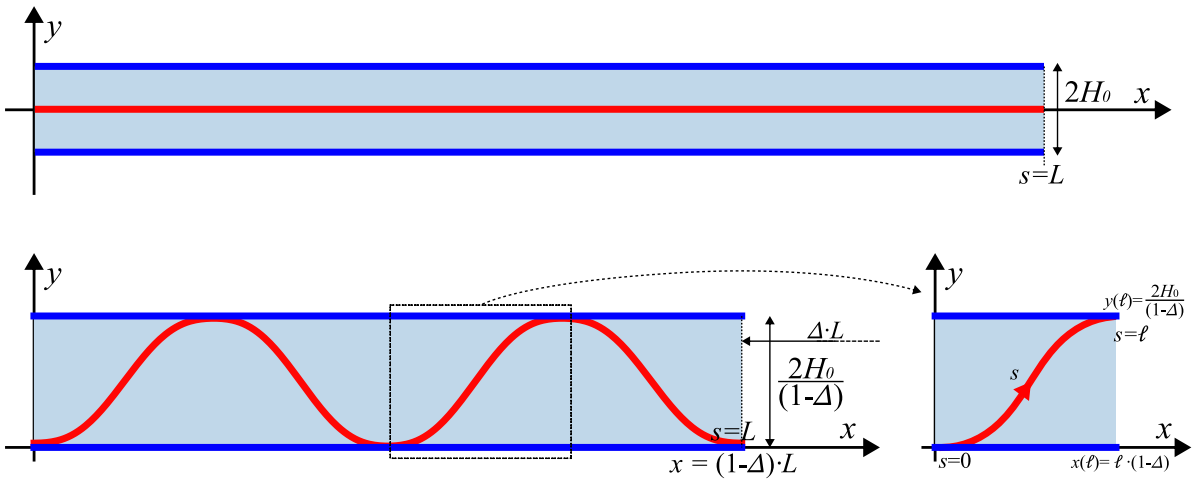


**Figure 9.10: Simplified cellular model**

Recall that the volume of the liquid, $2H_0L$, stays constant during the deformation. At a given contraction load $\Delta$, the length between the two supports is $L(1-\Delta)$. Under the constant volume constraint, the distance between the assumed flat interfaces should be $2H_0/(1-\Delta)$. With that,

we extract the simplified membrane cell, which is described by the same geometric variables, and satisfies the problem definition (5.24), but with a different boundary condition on $y(\ell)$:

$$y(\ell) = \frac{2H_0}{1-\Delta}. \tag{9.13}$$

This change does not affect the deduction of the differential equations and the additional equation of the variable length $\ell$, thus the self-similar solutions of problem (5.34) with boundary condition (5.35) can be directly applied to the soaked membrane problem with the length scale

$$\ell = \frac{2H_0}{1-\Delta}\frac{1}{\hat{y}(1)}, \tag{9.14}$$

and the values of the other variables and the cell energy can be recovered from (5.30) and (5.31).

### 9.3.2 Complete single cellular model

Having established the single cellular model with flat interfaces' assumption, we further improve the cellular model with more realistic interface geometries. As both surface tension theory and simulation results in section 9.2.4 proved that the free parts of the interfaces are circular arcs, the free parts in the cellular model can be modeled by circular arcs. By this means, we propose the *complete single cellular model*. The illustration and the geometric description of this model is given in figure 9.11.

For the purpose of showing their clear physical meaning, dimensional parameters and variables are used in the present derivation of the differential system. Please recall that the bending stiffness of the membrane is $B$, and the surface tension of the interfaces is $\gamma$.

In the single cell shown in figure 9.11, the curvature, the flexion angle, and the positions of the membrane are denoted by $\kappa(s)$, $\theta(s)$, $x(s)$, $y(s)$, and $s$ is the curvilinear coordinate. They are related by:

$$\theta'(s) = \kappa(s), \quad x'(s) = \cos\theta(s), \quad y'(s) = \sin\theta(s), \qquad s \in [0, \ell], \tag{9.15}$$

where $\ell$ is the length of the membrane in one cell. These are the same differential equations as the Elastica and elastic fiber in other problems discussed previously.

The free parts of the liquid surfaces are circular arcs, described by $\beta_i$, $r_i$ and $D_i$ ($i = u$ for *upper* or $l$ for *lower*). And the regions attached to the membrane have the same shape as the membrane.

With the geometry definition, the energy of one cell shown in figure 9.11 is :

$$\mathcal{E}_{cell} = \mathcal{E}_{elas} + \mathcal{E}_{surf} = \int_{s=0}^{\ell} \frac{B}{2}\kappa^2(s)\,ds + \gamma\left(r_u\beta_u + l - D_u + r_l\beta_l + D_l\right) \tag{9.16}$$

The whole length of the membrane is $L$, then there is $N_c = \frac{L}{\ell}$ cell and the total energy is

$$\mathcal{E}_{tot} = N_c\,\mathcal{E}_{cell} = \frac{L}{\ell}(\mathcal{E}_{elas} + \mathcal{E}_{surf}) \tag{9.17}$$

We would like to minimize this energy under the boundary constraints based on the symmetry assumption and the controlled end-displacement:

$$x(D_u) = r_u\,\sin\beta_u, \qquad x(D_l) = x(\ell) - r_l\,\sin\beta_l, \tag{9.18a}$$

$$\theta(0) = \theta(\ell) = 0, \qquad x(0) = y(0) = 0, \qquad x(\ell) = \ell(1-\Delta), \tag{9.18b}$$

and the constraint based on the volume conservation:

$$N_c\,\mathcal{V}^e_{liquid} = \frac{L}{\ell}\mathcal{V}^e_{liquid} = 2\,L\,H_0, \quad \rightarrow \quad \mathcal{V}^e_{liquid} = 2\,\ell\,H_0, \tag{9.19}$$

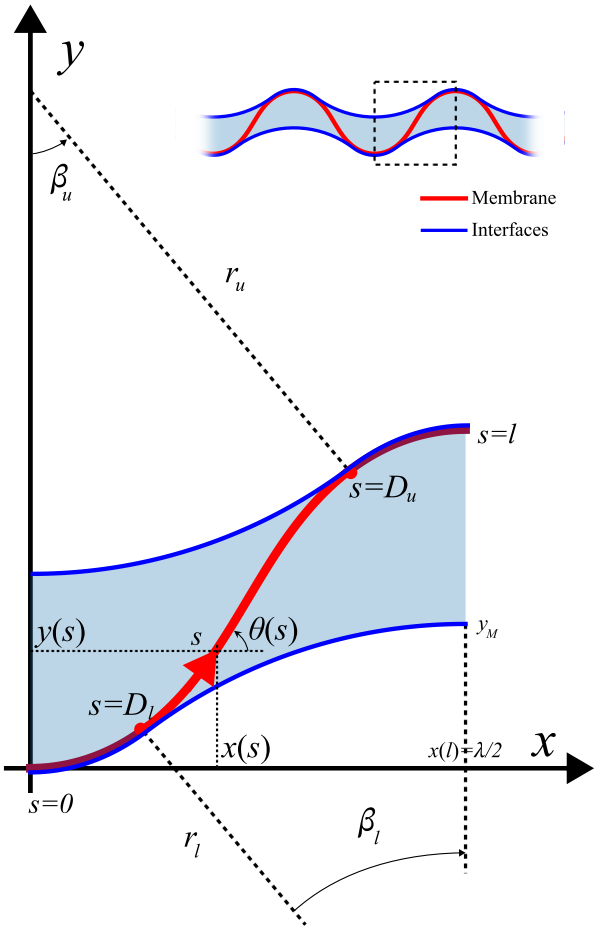


**Figure 9.11: Complete cellular model**

with $\mathcal{V}^e_{liquid}$ the volume of liquid in one cell

$$\begin{aligned}\mathcal{V}^e_{liquid} = &-\int_0^{D_u} y\,x'\,ds + x(D_u)\,y(D_u) - \frac{r_u^2}{2}\left(\beta_u - \frac{1}{2}\sin 2\beta_u\right)\\ &+\int_{D_l}^{\ell} y\,x'\,ds - (x(\ell) - x(D_l))\;y(D_l) - \frac{r_l^2}{2}\left(\beta_l - \frac{1}{2}\sin 2\beta_l\right).\end{aligned} \tag{9.20}$$

The appendix F contains the Lagrangian defined for the complete cellular model and the reasoning for finding the system of equations to solve. We found that the radii of the upper and lower free parts are the same, thus we define $r = r_u = r_l$, and for the angles, we found $\beta_u = \theta(D_u)$ and $\beta_l = \theta(D_l)$.

To summarize, the system of equations is

$$\begin{cases} B\theta''(s) = n_{x1}(s)\sin\theta(s) - n_{y1}(s)\cos\theta(s)\\ n'_{x1} = -p\,y', \qquad n'_{y1} = p\,x' \end{cases} \qquad s\in[0,\,D_l] \tag{9.21a}$$

$$[\![n_x]\!](D_l) = -\gamma\cos\beta_l \quad \& \quad [\![n_y]\!](D_l) = -\gamma\sin\beta_l \tag{9.21b}$$

$$\begin{cases} B\theta''(s) = n_{x2}\sin\theta(s) - n_{y2}\cos\theta(s)\\ n_{x2} \text{ and } n_{y2} \text{ are constants} \end{cases} \qquad s\in[D_l,\,D_u] \tag{9.21c}$$

$$[\![n_x]\!](D_u) = \gamma\cos\beta_u \quad \& \quad [\![n_y]\!](D_u) = \gamma\sin\beta_u \tag{9.21d}$$

$$\begin{cases} B\theta''(s) = n_{x3}(s)\sin\theta(s) - n_{y3}(s)\cos\theta(s)\\ n'_{x3} = p\,y', \qquad n'_{y3} = -p\,x' \end{cases} \qquad s\in[D_u,\,\ell] \tag{9.21e}$$

where $p = -\gamma/r$ is the Lagrange multiplier of the volume constraint, physically the capillary pressure difference.

The variation of length $\ell$ gives the equation

$$\begin{aligned}&\int_0^{\ell}\frac{B}{2}\,\theta'^2(s)ds + \gamma(r_u\beta_u - D_u + r_l\beta_l + D_l\\ &= \ell\left\{\frac{B}{2}\theta'(\ell)^2 + n_{x3}(\ell)\,\Delta - \gamma\cos\beta_l\,(1-\Delta) - p\,[2H_0 - (y(\ell) - y(D_l))\,(1-\Delta)]\right\}\\ &= \ell\left\{-\frac{B}{2}\theta'(\ell)^2 + p\,2H_0 - n_{x3}(\ell) + T\,(1-\Delta)\right\}\end{aligned} \tag{9.22}$$

with

$$T = n_{x3}(\ell) - p\,[y(\ell) - y_M] + 1, \qquad \text{where } y_M = y(D_l) + r(1-\cos\beta_l). \tag{9.23}$$

In addition to the volume condition (9.19), the boundary conditions and the geometric conditions (9.18), there is also

$$n_{y3}(\ell) = 0. \tag{9.24}$$

**Non-dimensionalization and solving method** Being consistent with the previous parts, the system of equations is adimensionalized with $B$ and $\gamma$, and we recall that the system parameters are $(H_0, L)$ and the control parameter is $\Delta$.

The shooting method is used to solve the system of equations for a given set of parameters. The differential equations (9.21) are integrated from $s = 0$ to $s = \ell$, finding the unknown values at $s = 0$ and the unknown parameters, such that all the other given conditions are satisfied. In this system, the unknown initial values are $\theta'(0)$, $n_x(0)$ and $n_y(0)$, and the independent unknown parameters are $r$, $D_l$ and $D_u$. Hence, there are 6 unknowns to be found by the shooting method,

requiring to satisfy the 3 boundary conditions at $s = \ell$, the volume condition (9.19), and the two geometry conditions (9.18a). To sum up, there are 6 unknowns and 6 targets, this system is closed.

Additionally, we remark that the continuation method (with control parameter $\Delta$ and arc-length continuation) is used to find the highly nonlinear solutions.

### 9.3.3 Comparison and discussions of the single cellular models

We have introduced the simplified and complete single cellular models, and in this section, we compare the solutions of these two models with the full simulation results of section 9.2.2.

Please note that the parameter $L$ can be canceled out from the system of equations of the two single cellular models, meaning that the solutions of the cellular models only depend on the system parameter $H_0$. This can be explained in the following way: both cellular models assume that the patterns of the system are identical then, with the same reasoning as the Elastica in wall-attached configuration, these models present an additional self-similarity property. $L$ only intervenes in the cell number $N_c = L/\ell$ of the cellular models.

To discuss the results with the simulation data, the values of the system parameters $H_0$ are chosen such that it is possible to observe the inhomogeneous wrinkling patterns, that is we select $H_0 \simeq 1 \sim 10$, and $L/H_0 \simeq 100$ for the simulations.

In figure 9.12, we show the solutions of the complete single cellular model with different values of $H_0$. These solutions are rescaled with $2H_0/(1-\Delta)$, the approximated height of the liquid layer, and are compared to the simplified single cellular model based on the self-similar solution given in section 5.6.

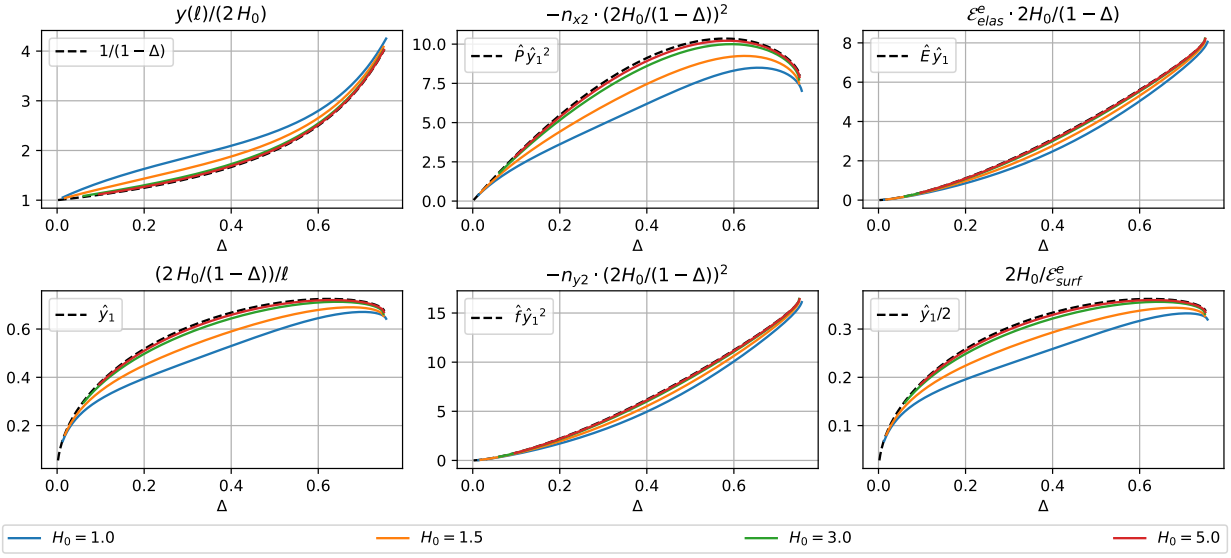


**Figure 9.12: Comparison between the complete single cellular model (see color coding for the value of $H_0$) and the self-similar solution of the simplified single cellular model (dashed black curve).**

It can be observed that as $H_0$ increases, the solutions of the complete cell model converge to the simplified cell model. This is expected, as the capillary effects are strong for larger values of $H_0$, and the interfaces become harder to deform, thus the liquid confinement behaves like the rigid confinement.

Please note that the solutions of the simplified model are already good approximations of the complete model as soon as $H_0 = 3$, which is not a large value in the considered range of $H_0$ ($1 \lesssim H_0 \lesssim 10$). For small values of $\Delta$, the differences between the complete and simplified models

are even smaller. As the single cellular models mainly predict the behaviors of the system during the homogeneous wrinkling stage, that is $\Delta \lesssim 0.2$, the simplified model can very well be used to estimate the responses of the system.

While the solutions in figure 9.12 were found by the continuation method with control parameter $\Delta$, the solutions in figure 9.13 were found by the arc-length continuation method. The value of parameter $H_0$ is chosen to be 5. Four solutions of the complete cellular model are marked on the bifurcation branches, and the related form of the system is given with the same marker in the lower part of figure 9.13. We also show in the figure the bifurcation branches of the simplified cell model which are derived from the self-similar solutions of figure 5.20. Please recall that the stable

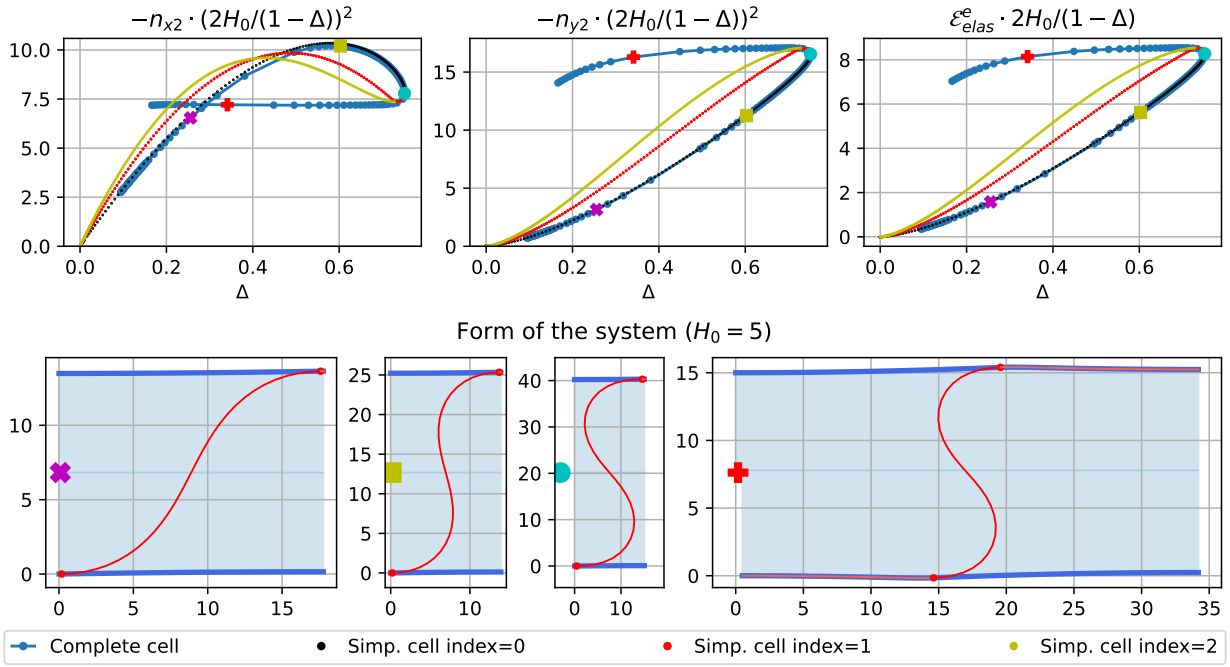


**Figure 9.13: Bifurcation branches of the complete single-cellular model found by the arc-length continuation method, compared with the self-similar solutions presented in figure 5.20. Four solutions of the complete single-cellular model are chosen, marked on the bifurcation diagrams, and the related forms are shown below with the same marker.**

branch (with index 0) of the self-similar solutions is the same as the black dashed branch in figure 9.12. The arc length continuation method is initialized with the same point as the $\Delta$-controlled continuation and, at first, exactly the same solutions as in figure 9.12 are found. At the limit value of $\Delta$ at which the $\Delta$-controlled continuation fails, the arc-length continuation continues finding solutions and constructing a branch that turns back from the $\Delta$ limit to smaller values. A solution on the newly-found branch is shown with the red cross marker. The related form of the system does not have the expected geometry, and it has a higher energy than the solutions on the original branch. Therefore, the solutions on this branch are not taken into account for further analysis.

Notably, the self-similar branch and the complete cell branch turn back at the same point. Although they branch off from each other afterward, we imply from the stability analysis of the self-similar solution that the new branch of the complete cellular model is also unstable. Hence, when $H_0 \gtrsim 5$, the solutions on the stable branch of the simplified cellular model are good approximations of the solutions of the complete cellular model, and the range of $\Delta$ also corresponds to that of the complete cellular model. In addition to that, the simplified cellular model can be used for any

value of $H_0$ provided a rescaling of the self-similar solutions presented in section 5.6, which is very practical. For these reasons, the solutions of the simplified cellular model are used in the following discussions.

**The von Kármán approximation** To repeat, the homogeneous wrinkling patterns are limited to small values of $\Delta$, which means that the von Kármán approximation does not diverge much from the nonlinear solutions. Thus, we transform the expressions found by the von Kármán approximation of the nonlinear global cellular model in section 5.6 to the problem of the soaked membrane.

Please recall that the equivalence of parameters between the confined Elastica in wall-attached configuration and the soaked membrane model under the flat interface assumption is:

| | length scale ($\ell$) | Number of cells |
|---|---|---|
| Elastica | $H/\hat{y}_1$ | $1/\ell = \hat{y}_1/H$ |
| Membrane | $2H_0/[(1-\Delta)\,\hat{y}_1]$ | $L/\ell = (1-\Delta)\hat{y}_1\,L/(2H_0)$ |

**Table 9.1: Parameter equivalence between the confined Elastica and the soaked membrane. $\hat{y}_1 = \hat{y}(1)$ is the self-similar solution of global cellular model.**

With a rescaling of the results in table 5.2, we obtain

$$N_c = 1.25\,L\,\sqrt{\Delta}\frac{1-\Delta}{2H_0} = 0.63\sqrt{\Delta}(1-\Delta)\frac{L}{H_0} \tag{9.25a}$$

$$P = 31.40\,\Delta\left(\frac{1-\Delta}{2H_0}\right)^2 \tag{9.25b}$$

$$F = 31.24\Delta^2(1-\Delta)\left(\frac{1-\Delta}{2H_0}\right)^2\frac{L}{H_0} \tag{9.25c}$$

$$\mathcal{E}^e_{elas} = 12.60\,\Delta\sqrt{\Delta}\,\frac{1-\Delta}{2H_0} \quad \rightarrow \quad \mathcal{E}_{elas} = 15.75\,L\,\Delta^2\left(\frac{1-\Delta}{2H_0}\right)^2 \tag{9.25d}$$

Compared to the expressions of the confined Elastica problem, the expressions of the soaked membrane model are not linearly or quadratically proportional to $\Delta$. Also, the system parameter $L/H_0$ intervenes in the expressions of $N_c$, $F$ and the total elastic energy.

In figure 9.14, we compare the simulation data (see section 9.2.2), the solutions of the simplified cellular model, its von Kármán approximation. We also plot two of the transitional cellular models presented in section 5.6 that we rescaled with the length scale given in table 9.1 in order for them to fit the soaked membrane system. For the chosen pair of the system parameters ($H_0 = 5$, $L/H_0 = 100$), the force reactions predicted by the simplified cellular model are approximately the mean values of the simulation results. Also, the von Kármán approximation is not much different from the nonlinear solution, proving the validity of the expressions (9.25). Both the nonlinear and the von Kármán approximation show that the simplified cellular model is able to predict the global behaviors of the 2D soaked membrane model during the homogeneous wrinkling stage.

In part II, we have demonstrated that the range of the force responses lies between the ExtC/HgF and HgF/PtC transitional cellular models of the wall-attached configuration for both wall-attached and centered configurations. In figure 9.14 we see that the lower bound is still the (rescaled) HgF/PtC transitional cellular model, but we remark that the upper bound is the

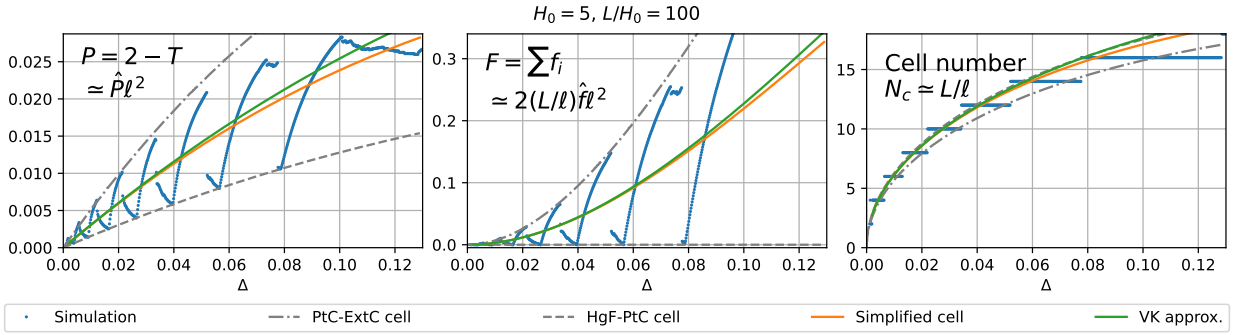


**Figure 9.14: Comparison between the solutions of the discretized system simulation, the simplified single cellular models derived from the confined Elastica in wall-attached configuration, and the von Kármán approximation of the global simplified single cellular model.**

(rescaled) PtC/ExtC transitional cellular model. As a matter of fact, the ExtC configuration is rarely observed in the soaked membrane simulation, which may be due to the deformable liquid confinement.

With these observations, we point out that the packing behavior of the homogeneous wrinkling stage of the soaked membrane is closely related to the problem of the Elastica confined between rigid walls. Moreover, the fact that the self-similar solutions of the confined Elastica problem can be directly applied to the soaked membrane system with a rescaling also reflects the presence of self-similarity during the homogeneous wrinkling stage of the soaked membrane.

**Non-convex total energy** The previous discussions focused on the elastic structure part, and the interfaces were approximated as rigid confinements moving with displacement control $\Delta$. However, further analysis of the total energy predicted by the simplified cellular model can also reveal some aspects of the behaviors beyond the homogeneous wrinkling stage.

Figure 9.15 presents the stable branch and a part of the unstable branch of the simplified single cellular model. To estimate the total energy of the system, the approximated surface energy

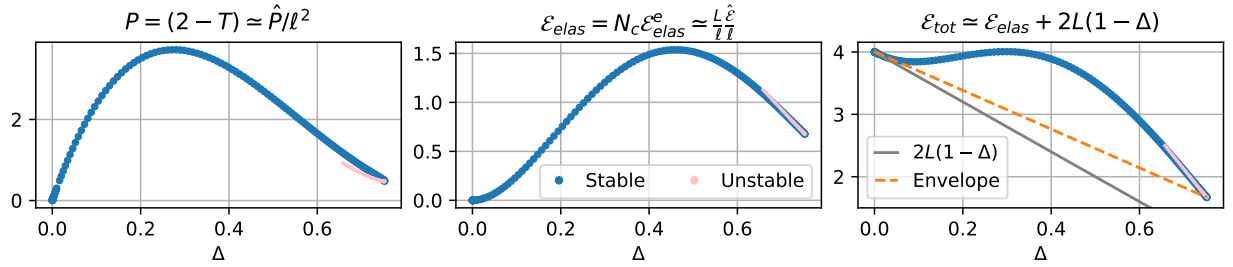


**Figure 9.15: Illustration of the non-convex total energy of the soaked membrane system. The parameters $H_0 = 0.5$ and $L = 2$ are chosen for the better visualization of the non-convex form.**

$2L(1 - \Delta)$ is added to the elastic energy derived from the self-similar solution. The estimated total energy is a non-convex function of the control parameter $\Delta$. Please remark that the system parameters $H_0$ and $L/H_0$ are not in the range chosen by simulation observations. These values are chosen for better illustration of the non-convex total energy, otherwise the surface energy is much higher than the elastic energy, and it is hard to visually observe the non-convex geometry,

but the non-convex nature of the total energy curve does not change for any values of the system parameter due to the self-similar property of the simplified cellular model.

We have discussed in section 4.1 that a physical system with a non-convex energy exhibits phase transition behavior. When the control parameter is in the range where the energy is concave, the global system adapts and presents a solution which is a mix of the two solutions at the intersection with the envelope. These two solutions are the two phases of the system, and the proportion of the two phases changes during the phase transition.

This non-convex total energy reveals the possible phase transition behavior in the soaked membrane system. With the simplified cellular model, the intersections between the energy curve and the envelope are near 0 and $\max(\Delta)$, which means that the phase transition will happen immediately after the controlled displacement is applied, and the two phases are (i) the nearly flat solution near $\Delta = 0$ and (ii) the highly deformed solution at $\max(\Delta)$. This is coherent with the experimental observations that the phase transition starts at very small displacement load $\Delta \gtrsim 5\%$ (Grandgeorge, 2018).

However, in both the simulation and the experiences, the phase transition does not happen right after imposing the displacement control as predicted by the simplified cellular model. We explain this by the exceedingly rough approximation of the surface energy. Suppose the system is in a state of phase transition, then the nearly flat solution and the highly deformed solution have different liquid heights. The additional surface energy due to the geometric passage from one liquid height to the other is not taken into account by the simplified single cellular model. If this energy is added, the two-phase state has indeed more energy, especially for small values of $\Delta$, and thus it will postpone the start of the phase transition to larger values of $\Delta$.

Although the simplified single cellular model gives insights into the problem of the soaked membrane, it cannot give precise predictions of the system behaviors, especially representative solutions during the phase transition. Additionally, there is no solution for $\Delta \gtrsim 0.75$.

The simulation with the discretized full system provides more precise predictions of the system behavior, but is not able to find wrinkling solutions beyond the overturning value. Thus, to study the system for larger values of $\Delta$, we propose the multicellular model, which will be presented in the next section.

## 9.4 Multicellular models

The multicellular, as its name indicates, assumes the system is composed of several cell types instead of a repetition of the same cell.

The basic idea comes from the experimental observations. Suppose there are two phases, represented by two different cells, we would like to find the geometry of each cell such that the total energy of the system is minimized under the given constraints. From the simulation results presented in section 9.2.4, we mentioned the inhomogeneous wrinkling solution, in which the wrinkling patterns cannot be neatly separated into two phases, and the general form is rather a series of folds with smoothly varying heights. Considering both the experimental and numerical observations, we propose two multicellular models:

- **The dictionary cellular model** (section 9.4.1): We suppose there are $A$ phases (the $A$ words in the dictionary) and each phase is represented by one type of cell, the form of which is unknown, and the number of cells in each phase $i = 1 \dots A$ is a real number $N_i$ to be found. When there is only one phase ($A = 1$), it is equivalent to the single cellular model.
- **The integer multicellular model** (section 9.4.2): We suppose there are $N_c$ cells in the system, where $N_c$ is an unknown integer, and the geometry of each cell is also to be found.

This model can be understood as a representation of the wrinkling forms as an assembly of different cells.

The integer multicellular model has more diverse cell types ($N_c$ types of cells instead of $A$ type of cells), hence defined by more variables. The integer multicellular model can be seen as a dictionary cellular model where $A = N_c$ and $N_i = 1\ \forall i$. Regardless of the differences, the two multicellular models define the geometry and energy of each cell in the same way.

**Interface modelling** For the sake of simplicity, we suppose the interfaces in both multicellular models are straight lines, which has proved to be a good approximation for large values of $H_0$. Compared to the simplified single cellular model in which the interfaces are straight horizontal lines, when two adjacent cells in the multicellular model have different heights, an oblique line is used to represent the liquid interface connecting the two cells. This means that the presence of different cells yields an extra energy cost, preventing the immediate ($\Delta \approx 0$) phase transition predicted by the single cellular model.

**Membrane modelling** As in other models, the multicellular models minimize the total energy of the system under given constraints. For the complete and simplified single cellular model, the geometry and the length of the cell is directly derived from the energy with the continuous variables $\theta(s)$, $x(s)$, and $y(s)$. In the presence of several cells, this approach introduces a lot of variables and is therefore technically complicated to solve and implement. Meanwhile, for each cell, only the endshortening $\Delta_i = 1 - x_i(\ell_i)/\ell_i$, the length $\ell_i$, the height $y_i(\ell_i)$, and the energy $\mathcal{E}^{ei}_{elas}$ are needed to define the total energy and the constraints. For this reason, we use the analytical arch solutions of the Elastica presented in appendix C. Given $\mu$ and $Q$, the solution is unique for an arch of unit length. Using the self-similar property of the Elastica equation, the arch solution can be transformed to a cell of length $\ell$. This means that all the required information of a cell can be determined by only three scalars $(\mu, Q, \ell)$ instead of several continuous variables plus $\ell$.

To sum up, given $(\mu, Q, \ell)$, we derive

$$\mathcal{E}^{e}_{elas} = \hat{E}(\mu, Q)/\ell, \qquad \Delta = 1 - \hat{x}_{end}(\mu, Q), \qquad y(\ell) = \hat{y}_{end}(\mu, Q)\,\ell \tag{9.26a}$$

$$P = \hat{P}(\mu, Q)/\ell^2, \qquad f = \hat{f}(\mu, Q)/\ell^2 \tag{9.26b}$$

where $\hat{(\cdot)}$ are the solutions of the unit length arch, and $()_{end}$ are the values at the end point $\hat{s} = 1$. The first three quantities are used to define the optimization problem, and the last two are useful for the post-processing and the discussions of the results.

**The valid $(\mu, Q)$ domain** As the cells are defined by variables $(\mu, Q)$, the valid range of these two variables is chosen with several criteria.

Firstly, the cell shape should be confined in a rectangle in the $(x, y)$ plane defined by the lower-left ($s = 0$) and upper-right ($s = \ell$) corners. This means that the cell shape should be in the point contact state (PtC) mentioned in chapter 5. Then, the liquid interfaces provide a vertical force $f$ opposing the vertical deformation (pushing the cell branch rather than pulling it), that is we have $f > 0$ in the notations of appendix C. Finally, when assembled with other cells, a cell shape should not penetrate its neighbors, that is we have a non-self-penetration condition for the multicellular model.

Please refer to the appendix C for the definition of $Q$ and $\mu$ and how they are related to the horizontal force $P$ and the vertical force $f$. We define the admissible $(\mu, Q)$ domain, shown on the right side of figure 9.16a, with its four boundaries

- $\mathbf{c}_1$ Planar Elastica $f = 0$
- $\mathbf{c}_2$ Small $\Delta$, buckling limit for $f \geq 0$
- $\mathbf{c}_3$ PtC/ExtC limit $\kappa(0) = 0$
- $\mathbf{c}_4$ Self-contact

The $\mathbf{c}_2$ boundary is simply $\mu = 0$. The boundary $\mathbf{c}_1$ and $\mathbf{c}_3$ are defined by analytical expressions, $Q = 4\,F^2(\frac{\pi}{2}, \mu)$ and $Q = 16\,F^2(\frac{\pi}{2}, \mu)$ respectively, where $F$ is the elliptic integral of the first kind. As for the boundary $\mathbf{c}_4$ defining the self-contact limit, it is possible to find an analytical solution, but it is too complex. For this reason, $\mathbf{c}_4$ is defined by a series of solution points.

Figure 9.16b presents the contours of the valid $(\mu, Q)$ domain for the solution of the unit-length arch given in Eqs. (9.26)

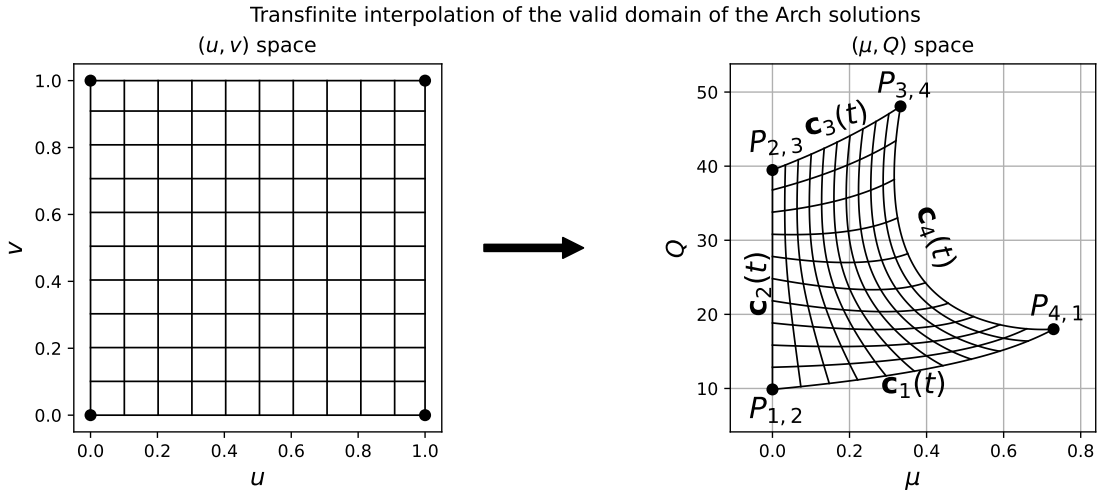


**(a) Transfinite interpolation of the valid $(\mu, Q)$ space.**

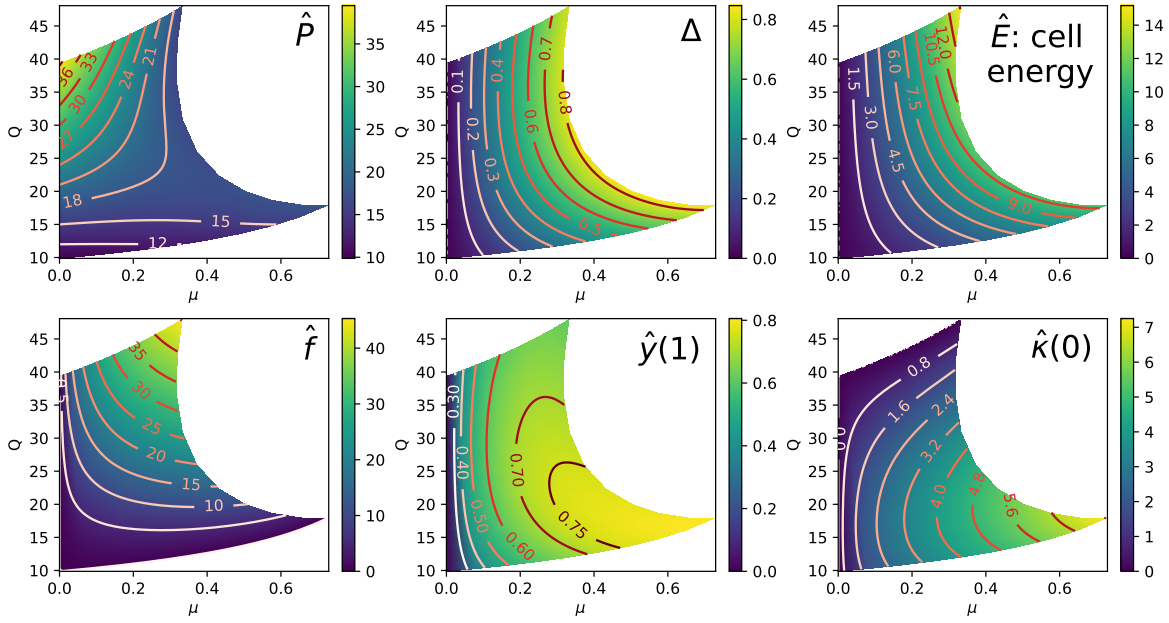


**(b) The contours of the quantities of interest**

**Figure 9.16: The valid domain of $(\mu, Q)$, the transfinite interpolation, and the solutions of the unit-length arch in the valid domain.**

**Interpolations** The boundaries of the valid $(\mu, Q)$ domain and the analytical expressions of the solution, which are both required by the constrained optimization problem, involve elliptic functions. It is technically difficult to put these expressions into CasADi and the IPOPT solver because these elliptic functions are not defined in them.

To define the valid domain, we use transfinite interpolation (Gordon and Hall, 1973), and define the admissible $(\mu, Q)$ domain by a square domain $(u, v) \in [0, 1] \times [0, 1]$, shown in figure 9.16a-left. The transfinite interpolation is widely used in geometric modelling and mesh definition in the finite element method. To match a $(u, v)$ point to a $(\mu, Q)$ point, the following expression is used

$$\begin{aligned}\mathbf{S}(u,v) = &[(1-v)\,\mathbf{c}_1(u) + v\,\mathbf{c}_3(u) + (1-u)\,\mathbf{c}_2(v) + u\,\mathbf{c}_4(v)] \\ &- [(1-u)(1-v)\,\mathbf{P}_{1,2} + uv\,\mathbf{P}_{3,4} + u(1-v)\,\mathbf{P}_{1,4} + (1-u)v\,\mathbf{P}_{3,2}]\end{aligned} \tag{9.27}$$

where $\mathbf{P}_{p,q}$ are the four corner points defined in figure 9.16a, and $\mathbf{c}_i(t)$ are the boundaries expressed by the curvilinear coordinate $t \in [0, 1]$:

$$\mathbf{c}_1(t) = [t \cdot \mathbf{P}_{1,4}[0], 4\,F^2(\frac{\pi}{2}, t \cdot \mathbf{P}_{1,4}[0])], \tag{9.28a}$$

$$\mathbf{c}_2(t) = [0, \pi^2 + t\,3\pi^2], \tag{9.28b}$$

$$\mathbf{c}_3(t) = [t \cdot \mathbf{P}_{3,4}[0], 16\,F^2(\frac{\pi}{2}, t \cdot \mathbf{P}_{3,4}[0])]. \tag{9.28c}$$

The boundary $\mathbf{c}_4(t)$ is defined by a 1D interpolation based on a series of points.

Please note that the curvilinear definition of $\mathbf{c}_i(t)$ is not unique, and it affects how the square in the $(u, v)$ domain is 'stretched' to the shape in the $(\mu, Q)$ domain. We have verified that the domain deformation related to our choice of the boundary definition is well-proportioned. With the transfinite interpolation, the parameters $(\mu, Q)$ become functions of $(u, v)$, and the quantities defined in Eqs. (9.26) also.

The transfinite interpolation fixes the problem of defining the valid $(\mu, Q)$ domain in CasADi and IPOPT, but the arch solutions to be put into the solver still need to be calculated with elliptic functions. To deal with this problem, the 2D Chebyshev interpolation (please refer the section 4.5 of Boyd (2001)) is used. To briefly explain the method, 10 Chebyshev nodes in both directions in $(u, v)$ domain form a $(10 \times 10)$ grid, the values of interest at each point of the grid are computed and then used to find the coefficients of the interpolating polynomial. This can be achieved either by the `numpy` package or through a direct implementation of the theory. Armed with these coefficients and the Chebyshev polynomials, we define the interpolating polynomials, which can be processed by CasADi and IPOPT, but this is not the only choice. Another possible method is the polynomial interpolation, which also gives polynomial approximations. The Chebyshev interpolation is chosen because fewer data points are needed to construct the approximation, and the discrepancy is smaller when the original field is approximated by polynomials of the same order.

In figure 9.17, we show the discrepancy of the 10 nodes Chebyshev interpolation. The three quantities presented in the figure are the ones to be put into the solver. The errors are defined by $|X_{orig} - X_{aprx}|/X_{orig}$, where $X_{orig}$ is the original value, and $X_{aprx}$ is the approximation. The largest errors are near the axis $\mu = 0$, where the values of the solutions tends to zero. The regular patterns in the diagrams are due to the Gibbs effects of the Chebyshev interpolation, but the errors in general are very small, ensuring the accuracy of the interpolated quantities.

### 9.4.1 Dictionary cellular model

Having described the definition of each cell in the multicellular models, we present in this part how to assemble the $A$ phases ('words') in the dictionary cellular model.

The dictionary cellular model can be understood as an extension of the simplified single cellular model. Instead of the only one universal repetitive cell, we suppose there are $A$ kinds of cells, the type $i$ cell $(i = 1, 2, ..., A)$ is repeated $N_i$ times, where $N_i$ is a real number. Please recall that after the transfinite transformation, the variables $(u_i, v_i, \ell_i)$ of each phase leads to the cell energy $\mathcal{E}^{ei}_{elas}$, the local endshortening $\delta_i = 1 - x_i(\ell_i)$, and the cell height $H_i = y_i(\ell_i)$, which are the quantities to

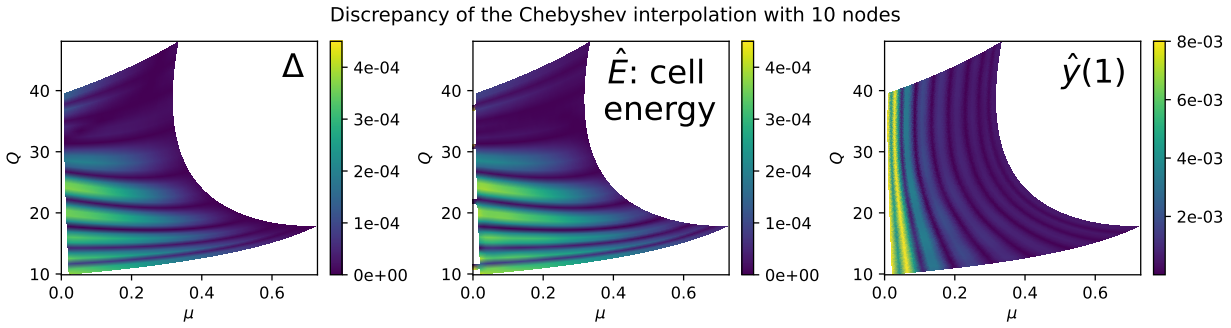


**Figure 9.17: The discrepancy of the Chebyshev interpolation with 10 nodes. Please remark that the approximations are calculated by the polynomials of $(u, v)$.**

be sent to the optimizer. Adding the cell number $N_i$ to the three variables, one phase possesses 4 variables, and there are a total of $4A$ scalar unknowns to be solved for. Figure 9.18 shows an illustration of the dictionary cellular model with 3 words, but other numbers of words can also be chosen. And, to be coherent with the discretized system defined in section 9.2, we assume the system to be left-right symmetric.

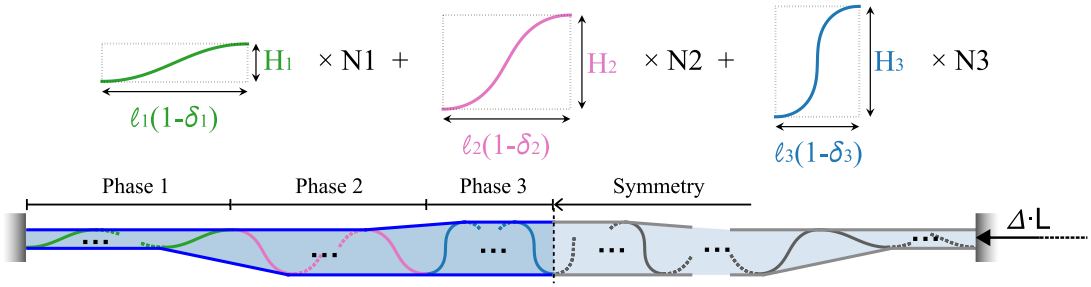


**Figure 9.18: An illustration of the dictionary cellular model with 3 'words'.**

We define the volume of the liquid, the elastic and surface energy in the adimensionalized system as

$$\mathcal{V}_{liqiud} = 2\left(\sum_{i=1}^{A} N_i X_i H_i + \sum_{i=1}^{A-1} (X_{i+1} + X_i)(H_{i+1} + H_i)/2 - (X_{i+1}H_{i+1} + X_i H_i)\right) \tag{9.29}$$

$$\mathcal{E}_{elas} = 2\left(\sum_{i=1}^{A} N_i \mathcal{E}_{elas}^{ei}\right) \tag{9.30}$$

$$\mathcal{E}_{surf} = 2\left(\sum_{i=1}^{A} 2N_i X_i + \sum_{i=1}^{A-1} \left[\sqrt{(X_{i+1} + X_i)^2 + (H_{i+1} - H_i)^2} - (X_{i+1} + X_i)\right]\right) \tag{9.31}$$

where $X_i = \ell_i(1 - \delta_i)$, and the coefficient 2 is due to the left-right symmetry.

In the definition of the liquid volume, it is approximated by the sum of all the rectangles confining the cells, adjusted by the trapezoids at the junctures of two adjacent phases. The surface energy, as mentioned earlier in the interface modelling part, it is approximated by the straight lines relating the extremities of the cells, that are the horizontal lines within one phase, and oblique lines at the junctures of two adjacent phases. Please note that by this definition, the precise ordering of the phases counts. Although reversing the order of phases does not change the volume and surface energy, interchanging two phases in a dictionary cell model of more than three 'words' may lead to different values of energy and liquid volume.

Having defined the liquid volume and the energy, for a given set of parameters $(H_0, L, \Delta)$, we formulate the optimization problem of the dictionary cellular model, and implement it with CasADi and IPOPT:

$$\min_{(u_i, v_i, \ell_i, N_i)} \quad \mathcal{E}_{tot} = \mathcal{E}_{elas} + \mathcal{E}_{surf} \tag{9.32a}$$

$$\text{subject to} \quad \text{The displacement control:} \quad 2\left(\sum_{i=1}^{A} \delta_i \ell_i N_i\right) = \Delta L \tag{9.32b}$$

$$\text{Match of the membrane length:} \quad 2\left(\sum_{i=1}^{A} \ell_i N_i\right) = L \tag{9.32c}$$

$$\text{Constant volume:} \quad \mathcal{V}_{liquid} = 2H_0 L \tag{9.32d}$$

$$\text{Validity of the cells:} \quad 1 \geq u_i \geq 0, \quad 1 \geq v_i \geq 0, \quad \ell_i \geq 0 \tag{9.32e}$$

$$\text{Minimal cell number of each phase:} \quad N_i \geq 1 \tag{9.32f}$$

**Results and discussion** As the basic idea of the dictionary cell model is to separate the system into different phases, to discuss the results we introduce the notion of *cell proportion* $\alpha_i$

$$\alpha_i = 2\, N_i\, \ell_i / L, \tag{9.33}$$

which is the ratio between the length taken by the phase $i$ and the total length of the membrane. A large value of $\alpha_i$ means that the system has a large proportion of phase $i$.

Figures 9.19 and 9.20 illustrate the results of the dictionary cell model with 4 and 10 alphabets respectively for the case $(H_0 = 6, L = 100)$, which are the same parameters as the results given in figures 9.8 and 9.9.

We start from the dictionary cell model with 4 words. In the diagram of the cell number and the diagram of the force on top of figure 9.19, the discretized system simulation data are also plotted to be compared with the results of the dictionary cell model. The blue and orange colors denote the dictionary cell model results related to loading and unloading processes respectively.

For all the models using the variational method, the Lagrange multiplier $T$ of condition $x(L)$ has the same dimension as a force, and is shown in the discretized system to be the external horizontal force reaction. Although we did not deduce the precise relation between $T$ and other unknown variables for the dictionary cell model, it is assumed to have the same meaning. In the force diagram in the top-right corner, the blue and orange curves are obtained by the Lagrange multiplier $T$ with $P = 2 - T$. In the same diagram, the internal horizontal forces of each 'words' $P_i$ are also presented. We observe that $2 - T$ does not match $P_i$. This is different from the discretized system, in which the internal horizontal force of the membrane (the Lagrange multipliers of the mixed formulation related to (9.2b)) is nearly constant (with less than 1% differences) and matches the value of $2 - T$. We assume that this discrepancy is due to the straight interface approximation.

For small values of $\Delta$, all words are the same, but at one point, the words become different, and the system is considered to enter the phase transition stage. Hysteresis takes place only around the transition point thus, for simplicity, we plot (in gray level) the individual data for each 'word' for the unloading process only. When the dictionary cell model has 4 words, the transition point is located at a larger $\Delta$ value than that of the discretized full system simulation. Before the phase transition, the curves of the dictionary cell model pass between the data of the discretized full system. During this stage, all the words are the same, and it is basically the same solution as the single cellular model. Compared to the discretized system which fails at the overturning point, the dictionary cell model achieves our goal of extending the 2D model to larger values of $\Delta$ with assumed wrinkling form.

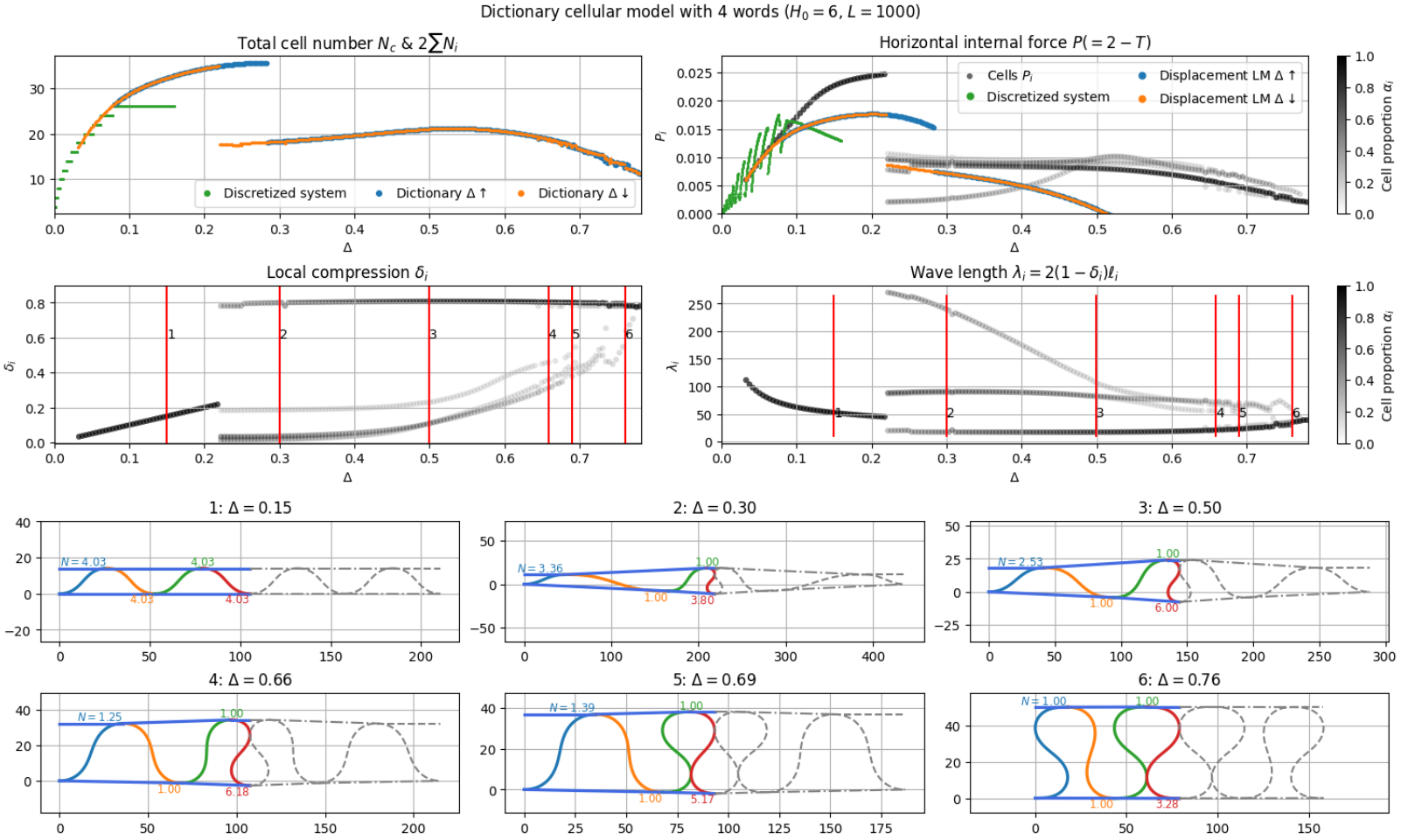


**Figure 9.19: Results of the dictionary cell model with 4 'words' for the case $(H_0 = 6, L = 1000)$. The calculation includes both the loading and unloading processes. In the two diagrams on top, the blue and orange curves correspond to the loading and the unloading respectively, and the results of the discretized full system are presented in green. The grayish points are the solutions related to each 'word' during the unloading process, with the gray level marking the cell proportion $\alpha_i$. Six values of $\Delta$ are marked by red lines in the local endshortening plot and the wavelength diagram, and the corresponding forms are presented at the bottom. The dashed-gray parts present the symmetry, and the cell number $N_i$ is indicated near each cell.**

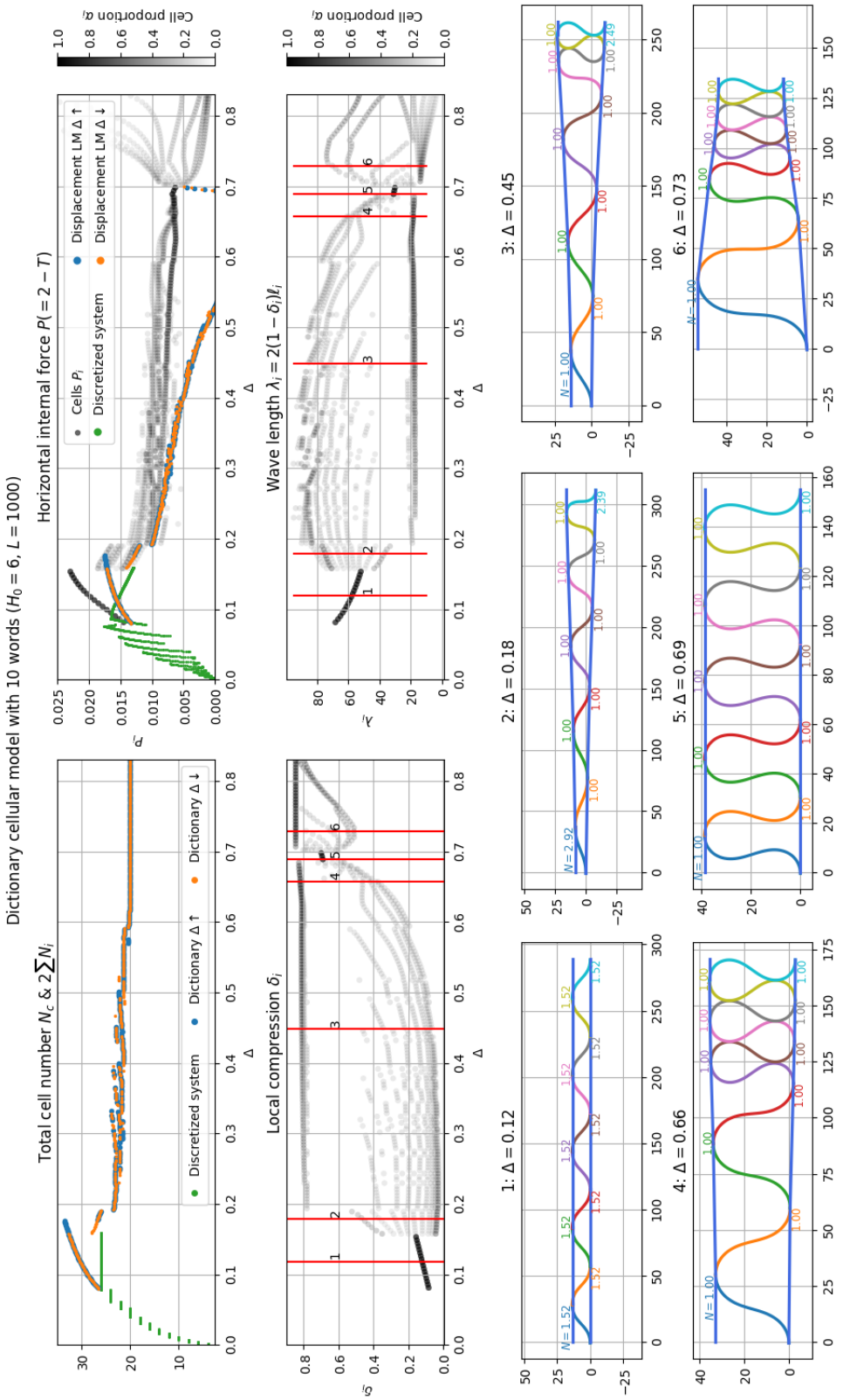


**Figure 9.20: Results of the dictionary cell model with $A = 10$ words for the case $(H_0 = 6, L = 1000)$. Same information as in figure 9.19 is given. The symmetric parts are not plotted for simplicity.**

During the phase transition (solutions 2 - 6), the cell number $N_i$ of the first and last words are larger than one, while $N_i$ of the two words in the middle have the imposed minimum value one. In fact, the middle cells serve as buffers between the first and last cell, such that the general height of the interfaces changes more smoothly and has less surface energy compared to a rough change. From the diagram of wave length $\lambda_i$ with $\lambda_i = 2(1-\Delta)\ell_i$, we observe that one word has a very large value of $\lambda_i$ at the beginning of the phase transition. This is indeed one of the middle words that has a gentle slope and serves as a buffer between the less curved and highly curved words.

As $\Delta$ goes larger, the cell number $N_i$ and the proportions $\alpha_i$ of the words with self-contact increase. The different words have closer cell heights, leading to the decreasing $\lambda_i$ of the buffer word. Regardless of the change in shape, the $\lambda_i$ of the two dominant words stay nearly the same, which looks like the phase transition phenomenon observed experimentally: the wavelengths of the two phases undergo only minor changes. Additionally, compared to the rapid change in cell number during the early stage, the total cell number predicted by the dictionary model stays nearly the same during the phase transition. We conclude that the observation from the discretized system of the nearly constant cell number during the early phase transition is extended to larger values of $\Delta$.

For very large values of $\Delta$, nearly all the cells are in self-contact, which can be understood as the totally collapsed stage. After all the cells are in self-contact, the solving program cannot continue to larger $\Delta$ values for the reason of imposed geometry control. The self-contact mechanism needs to be added in the model to solve for larger values of $\Delta$.

Results of the dictionary cell model with $A = 10$ words for the same values of parameters $H_0$ and $L/H_0$ are shown in figure 9.20. Compared to the previous observations, when there are 10 words, the phase transition happens at a smaller value of $\Delta$, and the hysteresis around the transition point is less apparent. Similar to the model with 4 words, during the phase transition, the cell number of the middle words is always one, meaning they act as buffers between dominant words in the first and the last place of the numerical order. Because there are more buffering cells to share the transition region connecting the dominant phases, none of the cells has a very large length, and the form of the system looks similar to that observed in the discretized full system. In the diagram of $\lambda_i$, there is no longer any word with a very large $\lambda_i$, the wavelength of the buffering cells stays between the wavelengths of the two dominant phases. Nevertheless, the wavelengths $\lambda_i$ still remain nearly unchanged in the range $0.2 \lesssim \Delta \lesssim 0.5$, reflecting the unchanged wavelength and varying phase proportion.

As for the total cell number, the dictionary cell model with $A = 4$ or 10 gives similar cell numbers during the phase transition, which is around 20. But we remark that when there are 10 alphabets, under condition (9.32f), the system has at least 20 cells, and the minimal cell number is reached at $\Delta \sim 0.6$, thus the results for a larger value of $\Delta$ is less trustworthy as the variations related to the cell number is blocked by the model itself. This can explain the strange observation of the convergence of all words around $\Delta \sim 0.7$ and the divergence afterward.

### 9.4.2 Integer multicellular model

Whereas the dictionary cellular model considers the system with different phases, the integer multicellular model does not use the notion of phase, and the cells are individual. Consequently, as the name indicates, the number of cells ($N_c$) is an unknown integer rather than a real number in the dictionary cellular model.

The integer multicellular model can be understood as a representation of the wrinkling forms observed in the simulations as an assembly of individual cells. Figure 9.21 illustrates how the cells are arranged in the integer multicellular model. For the same reason as the dictionary cellular model, the system is considered to be symmetric.

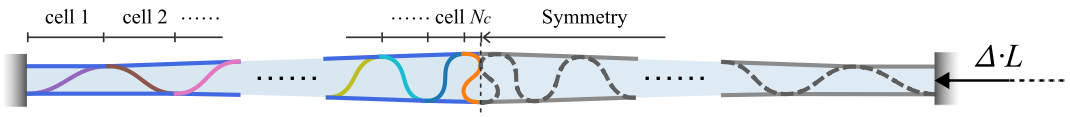


**Figure 9.21: Illustration of the multiple cellular model**

While the definition of each cell remains the same, there is no more $N_i$ associated to each cell because the cells are individual, hence only $(u_i, v_i, \ell_i)$ are needed.

After non-dimensionalization, the volume of the liquid, the elastic and surface energy are similar to that of the dictionary cellular model:

$$\mathcal{V}_{liqiud} = 2\left(\sum_{i=1}^{N_c-1}(X_{i+1}+X_i)(H_{i+1}+H_i)/2 - \sum_{i=2}^{N_c-1} X_i H_i\right) \tag{9.34}$$

$$\mathcal{E}_{elas} = 2\left(\sum_{i=1}^{N_c} \mathcal{E}_{elas}^{ei}\right) \tag{9.35}$$

$$\mathcal{E}_{surf} = 2\left(X_0 + X_{N_c} + \sum_{i=1}^{N_c-1}\sqrt{(X_{i+1}+X_i)^2+(H_{i+1}-H_i)^2}\right) \tag{9.36}$$

where $X_i = \ell_i(1-\delta_i)$, and the coefficient 2 is due to the symmetry assumption. These expressions are derived similarly as for the dictionary cell model, consequently, the numerical order of the cells cannot be interchanged, except a complete reverse of the order.

Then, for a given set of parameters $(H_0, L, \Delta)$, the optimization problem of the integer multi-cellular model to be implemented into CasADi and IPOPT is:

$$\min_{(u_i,v_i,\ell_i)} \quad \mathcal{E}_{tot} = \mathcal{E}_{elas} + \mathcal{E}_{surf} \tag{9.37a}$$

$$\text{subject to} \quad \text{The displacement control:} \quad 2\left(\sum_{i=1}^{N_c}\delta_i\ell_i\right) = \Delta L \tag{9.37b}$$

$$\text{Match of the membrane length:} \quad 2\left(\sum_{i=1}^{N_c}\ell_i\right) = L \tag{9.37c}$$

$$\text{Constant volume:} \quad \mathcal{V}_{liquid} = 2H_0L \tag{9.37d}$$

$$\text{Validity of the cells:} \quad 1 \geq u_i \geq 0, \quad 1 \geq v_i \geq 0, \quad \ell_i \geq 0 \tag{9.37e}$$

Compared to the dictionary cellular model, the difficulty comes from the unknown cell number $N_c$, which means that the number of variables $3N_c$ is itself an unknown.

There are several choices for solving such optimization problems. For example, encoding the presence and absence of variables using binary variables, and then using a Mixed Integer Nonlinear Programming approach (MINLP) to solve the problem. CasADi can be interfaced with the optimization scheme BONMIN (Basic Open-source Nonlinear Mixed INteger programming) which solves general MINLP. Attempts have been made to use BONMIN and the MINLP formulation to find the unknown cell number, but the solver had problems converging. Therefore, we implemented an algorithm based on the idea of *Nested optimization*, in which an outer loop selects the structure of variables and the inner loop solves for optimal values. In our case, the inner optimization problem is solved by CasADi and IPOPT.

More precisely, we define $\mathbf{X}_i = (u_i, v_i, \ell_i)$. Then, for a set of given parameters $(H_0, L, \Delta)$, and an initial solution $\mathbf{X}_{init}$ of $N_c^{init}$ cells, the algorithm goes as following:

**Algorithm to find the optimal number of cells:**
**Initial**: define the optimization problem with fixed cell number $\widetilde{N}_c = N_c^{init}$.
Solve with initialization $\mathbf{X}_{init}$.
Save the solution $\widetilde{\mathbf{X}}$ and the optimum $\widetilde{E}_{opti}$ (the total energy of the system).
**Repeat**
  Define $\mathbf{X}_{init}$ by eliminating from $\widetilde{\mathbf{X}}$ the variables corresponding to the shortest cell
  Define the new optimization problem with fixed $\tilde{N}_c - 1$ cells
  Solve with initialization $\mathbf{X}_{init}$, find the solution $\mathbf{X}$ and the optimum $E_{opti}$
  **If** $E_{opti} > \widetilde{E}_{opti}$:
    **Break**
  **Else:**
    $\tilde{N}_c \leftarrow \tilde{N}_c - 1$; $\widetilde{\mathbf{X}} \leftarrow \mathbf{X}$; $\widetilde{E}_{opti} \leftarrow E_{opti}$
**If** $\tilde{N}_c = N_c^{init}$: (*decreasing cell number does not decrease the total energy*)
  **Repeat**
    Define $\mathbf{X}_{init}$ by duplicating the variables corresponding to the shortest cell branch in $\widetilde{\mathbf{X}}$
    Define the new optimization problem with fixed $\tilde{N}_c + 1$ cells
    Solve with initialization $\mathbf{X}_{init}$, find the solution $\mathbf{X}$ and the optimum $E_{opti}$
    **If** $E_{opti} > \widetilde{E}_{opti}$:
      **Break**
    **Else:**
      $\tilde{N}_c \leftarrow \tilde{N}_c + 1$; $\widetilde{\mathbf{X}} \leftarrow \mathbf{X}$; $\widetilde{E}_{opti} \leftarrow E_{opti}$

Finally, the algorithm finds the optimal cell number $\tilde{N}_c$ and the corresponding solution $\mathbf{X}$ composed by the $3\tilde{N}_c$ variables $(u_i, v_i, \ell_i)$.

In practice, the continuation method with control parameter $\Delta$ is used to simulate the loading process with displacement control,

**Results and discussion** To compare with the other models, we chose the same system parameters ($H_0 = 6, L = 1000$) for the integer multicellular model, and the results are shown in figure 9.22.

Although the diagrams and the form plots look similar to the dictionary cell model, we emphasize that the cells of the integer multicellular model are individual. In the diagrams of cell number and force responses, the integer cellular model covers the data points of the discretized system during the initial stage of deformation. Compared to the dictionary model with 10 alphabets, the transition happens at a smaller $\Delta$ value, and the hysteresis is also less apparent.

In the force diagram, the internal force predicted by the Lagrange multiplier $T$ is the same as the internal force $P_i$ of each cell, and superimposes on the oscillating growth of $P$ given by the discretized simulation. But after the on-set of phase transition, $2 - T$ diverges from the internal forces $P_i$ of each cell, just like the dictionary cell model. In some aspects, this observation supports our assumption that these differences come from the errors brought by the straight interface assumptions. When the system is in the homogeneous wrinkling configuration, the interfaces are globally flat, thus the errors of the straight interfaces is small. For larger deformation, the interfaces should be more curved under the force actions given by the membrane, hence the straight interface assumption is less credible.

In the range $0.2 \lesssim \Delta \lesssim 0.5$, the wavelength diagram of the integer multicellular model has similar patterns as that of the $A = 10$ dictionary model, showing two principal wavelengths with some buffering in between. And the total number of cells is in the same range as $A = 10$ dictionary model. For $0.65 \lesssim \Delta$, the cell number decreases, and there are still two principal wavelengths, unlike the $A = 10$ dictionary model, which presented a converging-diverging change of wavelengths.



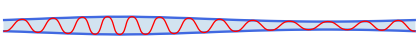

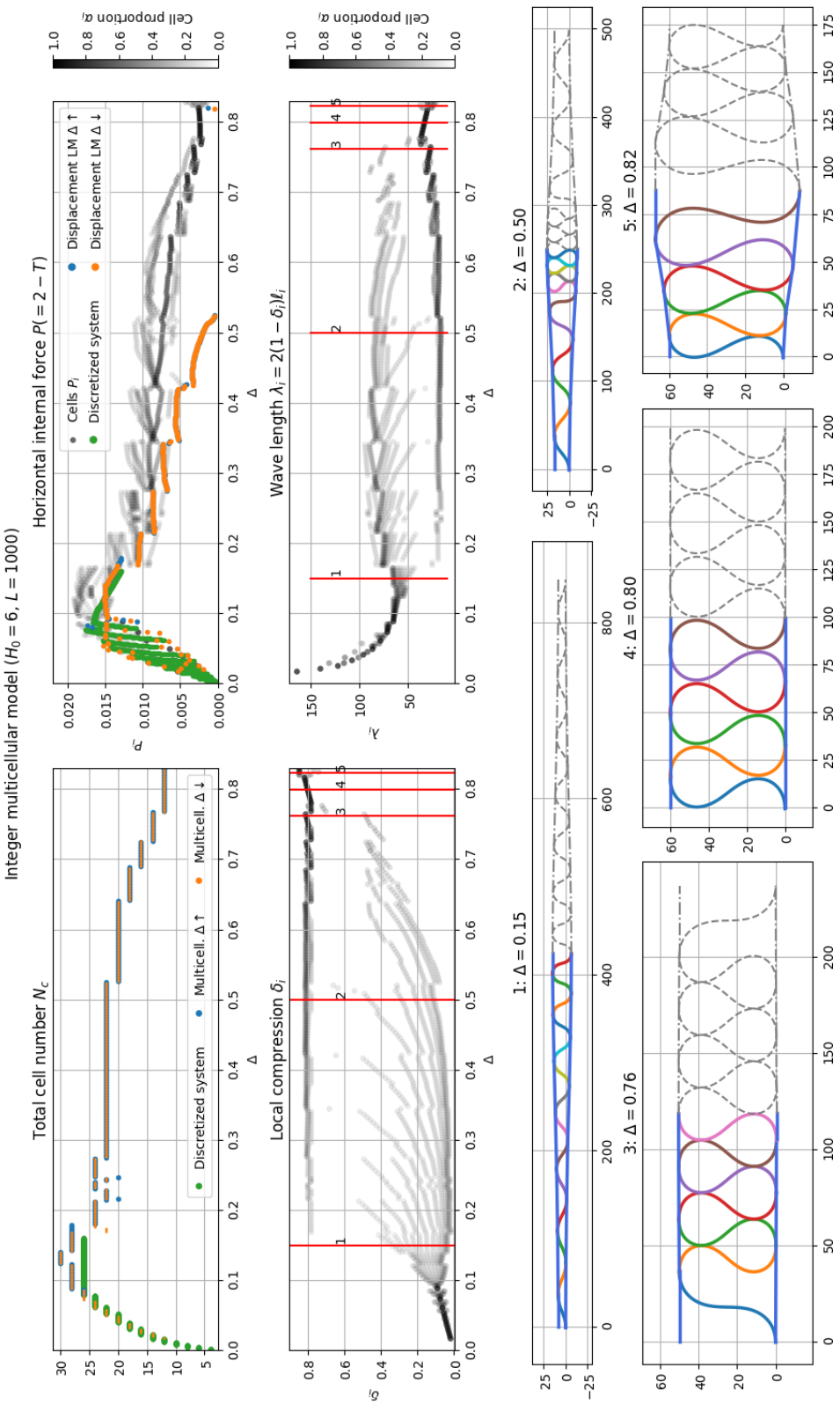


**Figure 9.22: Results of the integer multicellular model for the case ($H_0 = 6, L = 1000$). The calculation includes both loading and unloading process. The results are presented similarly as in figure 9.19. Please remark that the transparency of the grayish cell points is given by the cell number, and is the same for all cell points at the same step, such that the gray level reaches 1 if all the cell points are superimposed.**

When $\Delta \gtrsim 0.78$, all the cells are in self-contact. For even larger value of $\Delta$, the length of each cell increases. In fact, the elastic energy is inversely proportional to the length of an Elastica arch, thus longer arches are energetically favorable, which explains the decrease in the total number of cells.

Because each cell of the integer multicellular model is individual, as opposed to the dictionary model where the number of cells is a real number, the predictions given by the integer multicellular model are closer to the discretized full system. Furthermore, it overcomes the problem of jumping to the spiral shape and gives the predictions for much larger values of $\Delta$. With this model, we observed the wavelength transition similar to the experimental observations.

Conversely, the integer cellular model is still based on some strong assumptions, including the straight interface assumption, the imposed domain of admissible deformation, in which the self-contact is only a geometry assumption without force responses. For this reason, the validity of the solutions at very large values of $\Delta$ is under question.

## 9.5 The critical point of the transition

Based on the 2D model of the soaked membrane shown in figure 9.2, we proposed different models to study the behavior of the system under displacement control. One of the focuses is the phase transition, and an important question is when the phase transition happens.

In section 9.2.4, we observed from the simulation results that when the controlled displacement $\Delta$ passes a certain value, the interfaces are no longer straight, and the system enters the inhomogeneous configuration, which is supposed to be the phase transition stage. We note this critical load $\Delta^*$; it depends on the system parameters $(H_0, L/H_0)$. As the single cellular model lacks an appropriate modeling of the interface between two phases, $\Delta^*$ appears to be zero. For the dictionary cell models, $\Delta^*$ depends on the number of alphabets. Finally, the integer multicellular model behaves similarly to the discretized system and therefore brings no additional insights on $\Delta^*$.

This section presents our investigation of $\Delta^*$ from a more analytical point of view. Because the discretized system is directly derived from the 2D soaked membrane model and is supposed to be most accurate, we use its data as a reference against which we compare our theoretical analyses. A more rigorous definition of $\Delta^*$ is needed for the discussions, especially for the post-processing of the simulation data from the discretized system. Therefore, based on the literal definition, we define the transition criterion as

$$\max\left[y_u(x) - y_l(x)\right] - \min\left[y_u(x) - y_l(x)\right] \geq 0.3\,\frac{2H_0}{1-\Delta}. \tag{9.38}$$

The left-hand side of (9.38) is the difference between the maximal and minimal liquid height, and $2H_0/(1-\Delta)$ is the estimated liquid depth under the straight interface assumption. This criterion means that the phase transition is considered to have started when the proportion between the two quantities exceeds 30%. The value 30% is given by the visual observations of the simulation results, the deformation of the interfaces being perceptible at this value.

We remark that other choices of definition exist. As mentioned in section 9.2.4, when the phase transition begins, the internal force $P$ does not increase anymore. For this reason, $\Delta^*$ can be defined as the $\Delta$ corresponding to the maximal value of $P$, but it has been observed in some case (especially when $H_0$ is large and $L/H_0$ is small) that the interfaces are still flat when $P$ has already begun to decrease. For this reason, the criterion based on the geometry (9.38) is chosen.

In section 1.6 and 1.7, the examples on liquid drops illustrate the Laplace law in which surface tension $\gamma$ links interface curvature to the pressure difference across the interface, balancing external loading, for example gravity. Additionally, in section 9.2.4, we have mentioned that the vertical



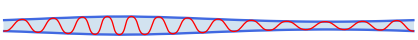

forces applied on the interfaces by the membrane are related to the capillary pressure difference across the interfaces. Therefore, we assume that when the sum of the vertical forces exceeds a certain value, the deformation of the interfaces becomes perceptible. Based on this assumption, we inspected the reactions of a liquid-air interface under vertical forcing, presented in appendix G. We discussed how a liquid-air interface deforms when a pointwise vertical local force $F$ is applied. An expression between $F$ and the interface deflection $\Delta y$ is found.

With these results, we simplify the 2D soaked membrane model to two interfaces under a vertical force $F$ in the middle of the interfaces, and its value is equal to the sum of the vertical forces of the membrane, an illustration is given in figure 9.23.

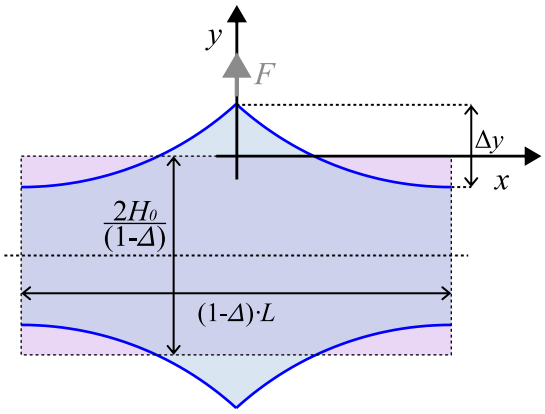


**Figure 9.23: An illustration of the simplified system to estimate $\Delta^*$. The action of the membrane on the upper (resp. lower) interface is simplified to a vertical force $F$ acting at a single point on the interface. The violet and blue regions denote the initial and deformed shapes of the liquid, respectively. Under the volume constraint, they have the same area.**

Before the onset of the phase transition, the soaked membrane acts like the Elastica confined between rigid walls, and we have proved that the cellular models presented in section 5.6 can accurately predict the force reactions of the membrane with the rescaling (9.14). Thus, we use the cellular models to predict the vertical force $F$. Then, $F$ is used to estimate the interface deflection $\Delta$ with equation (G.9) in appendix G. Finally, $\Delta^*$ is calculated with the criterion (9.38). With the scaling $\ell$ defined by (9.14), the force $F$ as a function of $\Delta$ is given by

$$F \simeq \frac{L}{\ell}\frac{\hat{f}(\Delta)}{\ell^2} = L\hat{f}(\Delta)\left(\frac{1-\Delta}{2H_0}\hat{y}_1(\Delta)\right)^3 \tag{9.39}$$

where $\hat{f}(\Delta)$, $\hat{y}_1(\Delta)$ are the self-similar values of the global cellular model presented in section 5.6.2. With $\Delta y$ defined as in figure 9.23, the criterion (9.38) becomes $2\Delta y \geq 0.3\frac{2H_0}{1-\Delta}$. Transforming relation (G.9) into the considered system, we have $\Delta y \simeq 0.5\frac{L(1-\Delta)}{2}\frac{F}{2}$, which leads to

$$\begin{aligned} &2\left(0.5\frac{L(1-\Delta)}{2}\right)\left(\frac{1}{2}L\hat{f}(\Delta)\left(\frac{1-\Delta}{2H_0}\hat{y}_1(\Delta)\right)^3\right) \geq 0.3\frac{2\,H_0}{1-\Delta} \\ \Rightarrow \quad &\frac{1}{2^6}\left(\frac{L}{H_0}\right)^2\left(\frac{1}{H_0}\right)^2\hat{f}(\Delta)\cdot\hat{y}_1^3(\Delta)\cdot(1-\Delta)^5 \geq 0.3. \end{aligned} \tag{9.40}$$

At the critical point of transition $\Delta^*$, we have

$$C(\Delta^*) = \sqrt{\frac{1}{0.3\cdot 2^6}\hat{f}(\Delta^*)\cdot\hat{y}_1^3(\Delta^*)\cdot(1-\Delta^*)^5} = H_0\cdot\frac{H_0}{L} \tag{9.41}$$

which means that the product between $H_0$ and $H_0/L$ is a function of $\Delta^*$.

In figure 9.24, we present the data points of the simulation together with the expression (9.41). Please remark that the black lines is the $C(\Delta^*)$ function multiplied by a factor 1/2. The points

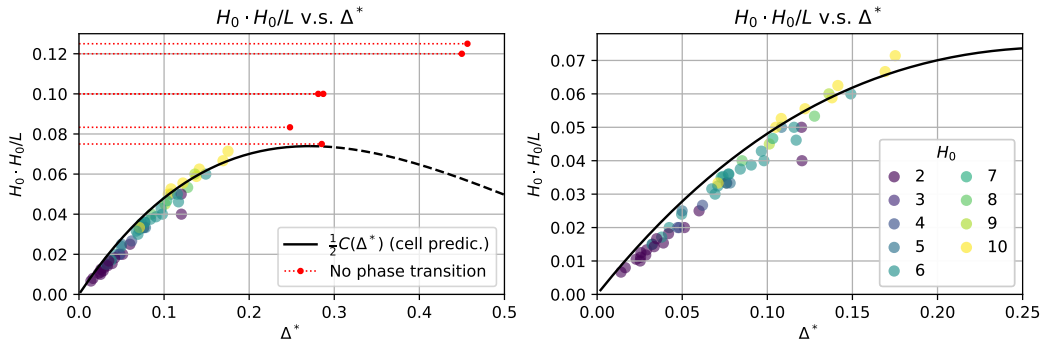


**Figure 9.24: Comparison between the analytical prediction and the simulation data. The back lines are $C(\Delta^*)/2$, where $C(\Delta^*)$ is given by (9.41), and dashed line denotes the decreasing part. Filled circles are points from the simulation data, and the different colors mark the value of parameter $H_0$. The red dotted lines mark the cases in which no phase transition was observed.**

(filled circles) are data from the simulation of the full discretized system. The different colors mark different values of $H_0$, and the red points are related to the simulations in which the criterion (9.38) has never been met, and the red points are the $\Delta$ at which the simulation fails.

Regardless of the 1/2 factor, our analytical approach recovers the global tendency of $\Delta^*$, and also predicts the cases when the phase transition does not occur. The source of the factor 1/2 is under discussion, it may come from the oversimplified model given in figure 9.23. Another possible explanation can be the imprecise prediction of the vertical force $F$ by the cellular model.

## 9.6 Discussions of the soaked membrane

In this chapter, we proposed a 2D model for the soaked membrane system in the one-dimensional compression experiments, aiming to recover the experimental observations of the wrinkling patterns and the phase transition phenomenon. This 2D model assumes an inextensible membrane being confined inside an incompressible liquid layer, and after the dimensional analysis and the non-dimensionalization, we derive that the system depends on the parameters $(H_0, L/H_0, \Delta)$. For further analysis, $(H_0, L)$ serve as system parameters and $\Delta$ is the loading control.

The first approach consisted of using CasADi and IPOPT to solve the discretized system. With this method, a parametric study was performed, which helped us to determine the range of $H_0$ and $L/H_0$, in which the numerical simulations showed similar behaviors as the experiments. These results also gave us the first insights into the behaviors of the 2D soaked membrane model. The homogeneous wrinkling patterns and the forms similar to the early stage of the phase transition were observed, but the first discretized system fails at the overturning limit, preventing further investigations for larger values of $\Delta$. To solve this problem, the decoupled system was proposed, and a spiral shape was found just after the overturning point, which rarely occurred experimentally.

Moreover, analytical approaches were also used. The first category of models is the single cellular model, considering the system as a repetition of the same cell. This model has two variants (i) the simplified single cellular model, and (ii) the complete single cellular model. As the interfaces were observed to be nearly straight in the simulations, we proposed the simplified single cellular model, which can be directly derived from the cellular model of the confined Elastica problem with a different rescaling. The second variant is the complete single cellular model, which has a more precise geometry for the interfaces. Little differences were observed between the two variants for

$H_0 \gtrsim 3$, which is in the chosen range of $H_0$. And the valid solutions of the two models have the same range of $\Delta$, confirming the good approximation of the simplified cellular model. We then compared the predictions of the simplified cellular model with the discretized system simulation and found that the former was yielding an average solution of the latter. Furthermore, it was shown that with a rescaling, the solutions of two transitional cell models (PtC/ExtC and HgF/PtC) of the confined Elastica capture the general variations of the solutions of the soaked membrane in the homogeneous wrinkling stage. After that, the total energy of the system was estimated with the single cellular model, and it turned out to be a non-convex function, indicating the possible occurrence of a phase transition. According to this energy potential, the phase transition should happen as soon as the imposed contraction is applied, which is not the case for both the discretized system simulations and the experimental observations. Assuming that this discrepancy came from the lack of local variability of both the membrane and the interfaces, we then proposed the multicellular model.

As the name indicates, the multicellular models use more than one cell type to model the wrinkling pattern. More precisely, we proposed two multicellular models, the dictionary cell model and the integer multicellular model. The former is based on the idea of phases, and the latter separates the whole system into individual cells. For both models, the interfaces are assumed to be piecewise straight, and the different cells of the membrane are represented by the interpolated analytical solutions of the planar Elastica. It turned out that both models could find solutions for larger values of $\Delta$, but the solutions of the dictionary cell model depend on the imposed phase number, which blocks some degrees of freedom of the model, while the number of cells in the integer multicellular model is, by construction, an unknown integer, and does not have this problem. Notably, for the two multicellular models, we observed that beyond the homogeneous wrinkling stage, a large proportion of the membrane was either spent in the less deformed cells (low height) or the highly curved (self-contact) cells (high height). Between these two are the transitional cells with gradually increasing height. As $\Delta$ increases, the proportion of self-contact cells increases. Besides, the wavelengths of the two dominant phases stay nearly the same, in agreement with the experimental observations. However, we remark that no transitional zone was observed in experiments, and the side view of the membrane under large $\Delta$ is not available experimentally, due to a lack of proper techniques. Thus, whether our models represent what happened experimentally is still to be discussed.

Considering all the results of the different models mentioned above, we assume that in the experiments it was a dynamical transition that occurred when the system arrived at the overturning point. For the theoretical 2D model, the fluid can rearrange freely across the membrane instantaneously when one of the folds skews, and the membrane easily passes to the spiral shape. Conversely, in the experiments, the porosity of the membrane hindered the flow of the liquid and the snap toward the spiral shape. We conjecture that the folds then adapt to the self-contact geometry, eventually leading to the compact packing of the collapsed region.

Finally, we discussed how the critical point of the phase transition $\Delta^*$ depends on the system parameters $H_0$ and $L/H_0$. The criterion of $\Delta^*$ was given with the geometry of the interfaces. Then, with the help of a simplified representation of the interfaces and the solution of the simplified single cell model, we found a relation between $H_0 \cdot H_0/L$ and $\Delta^*$. It was revealed that this prediction is in close agreement with the simulation data, given a factor $1/2$ which needs to be understood.

The disagreements between the numerical results and the experiments could be one of the future investigations. The assumption that dynamical effects preventing the fluid from crossing the membrane instantaneously can be tested by adding conditions on the local liquid volume related to each cell. A more comprehensive improvement is to add dynamical effects like viscosity and diffusion into the discretized simulation. And it is also interesting if any experimental technique can be developed to observe the side view of the soaked membrane during the phase transition.



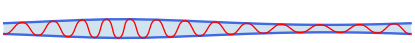

# Conclusion and perspectives

This thesis investigated the packing of slender structures under both solid and liquid confinements, motivated by applications ranging from the deformation of cables in industry to the mechanics of biological systems such as spider silk and cell membranes. The interplay between geometry, elasticity, and confinement governs a wide spectrum of physical behaviors. The central objective of this work was to establish theoretical and numerical frameworks capable of describing packing phenomena across two classes of confinement: rigid boundaries (solid–solid packing) and deformable liquid interfaces (liquid–solid packing).

## Methodological and theoretical contributions

Several methods were applied across the thesis, for both confinement types:

- **Numerical approaches:** formulation and implementation of constrained optimization problems; treatment of beam-to-beam contact; integration of stability and bifurcation analysis.
- **Theoretical tools:** dimensional and self-similar analyses; variational formulations; cellular models for repetitive packing patterns; von Kármán approximations and exact analytical solutions of the Elastica.

These tools enabled systematic exploration of confined Elastica systems and their extensions to liquid-mediated confinements.

## Solid–solid packing

The first part of the thesis focused on the Elastica confined between rigid walls under two boundary conditions: wall-attached and centered configurations. Simulations provided quantitative references for theoretical analyses.

For the wall-attached configuration, we established phase diagrams, explained deformation processes, and introduced cellular models. A key feature was the self-similarity of the problem, which allowed predictions to be generalized for any wall height and which provided universal scaling laws for packing responses.

For the centered configuration, attention was given to bifurcation and stability. A soft-wall potential method was introduced, and the stability of hanging-fold and extended-contact states was investigated. While stability of the extended-contact state was confirmed in the discretized system, questions remain for the continuous limit.

A comparative analysis demonstrated that the boundary conditions primarily affect the period of variation in force responses, while the global magnitude of the force responses remains similar. The universality of the self-similar solutions was confirmed across the two configurations.



**Outlook (solid–solid case):** Future work could address the onset of spiral formations, provide a more detailed study of boundary effects in the centered configuration, and extend stability analyses to continuous systems.

## Liquid–solid packing

The second part of the thesis addressed confinement by liquid interfaces, motivated by experimental observations of drop–fiber systems and soaked membranes.

In the drop–fiber system, we studied elasto-capillary buckling and coiling. Numerical models reproduced known behaviors of 2D disk-like drops, and were extended to deformable drops, revealing how surface tension and interface geometry influence force responses and trapping efficiency.

In the soaked membrane system, simulations reproduced early-stage wrinkling behaviors and indicated the possibility of phase transitions consistent with experiments.

The self-similar solution of the cellular models originally developed for solid confinement was adapted to the soaked membrane model with an appropriate rescaling, successfully capturing the general behaviors of the membrane during the wrinkle creation stage. At larger deformations, multicellular models captured two dominant wavelengths, offering a framework to interpret observed phase-like transitions.

**Outlook (liquid–solid case):** Open questions include understanding why the spiral state rarely occurred experimentally. To verify our assumptions, dynamical effects such as viscosity and diffusion can be added to the model. Another perspective is to validate our models with advanced experimental imaging techniques. Extensions to three-dimensional geometries and applications in material design also represent promising directions.

## Overall significance

Taken together, the results of this thesis extend classical theories of slender-body confinement by incorporating elasto-capillary interactions and demonstrating how liquid interfaces can serve as adaptive confinement reservoirs. The key contributions can be summarized as follows:

- Frameworks for studying slender-structure packing across rigid and liquid confinements.
- Insights into self-similarity and universality in solid confinement, enabling general predictions of deformation and force responses.
- Use of cellular models in systems with liquid confinement, providing tools for interpreting experimental observations of the soaked membrane.

In conclusion, the thesis contributes to the broader understanding of packing phenomena by bridging solid–solid and liquid–solid confinements within a unified theoretical and numerical framework. By elucidating the roles of elasticity, capillarity, and geometry, it advances both fundamental knowledge and applied perspectives in soft-matter physics and engineering.



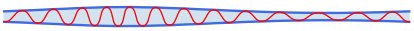

# Appendix



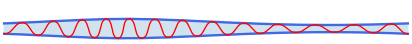

# Appendix A

# Some important IPOPT parameters

- `tol`: Desired convergence tolerance. This is the $\epsilon_{tol}$ of equation (6) in Andreas Wächter and Biegler (2004). This criterion measures the optimality error for the original problem, ensuring the non-violation of the constraints. It is the main criterion that terminates the algorithm. Other criteria, including criteria related to constraints and barrier parameter, are complementary to this criterion. (the default value is $10^{-8}$)
- `mu_target`: Desired value of complementarity. This is a parameter only to be changed when one want to terminate the algorithm for strictly positive barrier parameter $\mu$ in problem (1.24). (the default value is 0)
- `mu_init`: The initial value of barrier parameter. (the default value is 0.1)
- `mu_min`: Minimum value for barrier parameter. Remark that it is not a criterion of termination. (the default value is $10^{-11}$)
- `bound_frac`: Desired minimum relative distance from the initial point to bound. This is $\kappa_2$ in section 3.6 of reference Andreas Wächter and Biegler (2004). (the default value is 0.01)
- `bound_push`: Desired minimum absolute distance from the initial point to bound. This is $\kappa_1$ in section 3.6 of reference Andreas Wächter and Biegler (2004). (the default value is 0.01)
- `slack_bound_frac`, `slack_bound_push`: These are similar to `bound_frac` and `bound_push`, but related to the initial slack variables.
- `warm_start_init_point`: Indicates whether use a warm start initialization, where values of primal and dual variables are given. Possible values are "yes", "no". The primal variables are the unknowns of the problem and the dual variables are the Lagrange multipliers of the constraints and the slack variables. This definition comes from the notion of linear programming. If not warm starting, only primal variables are initialized. Related initialization setting starts with `warm_start`, like `warm_start_bound_push`, `warm_start_bound_frac`, they are the same as the parameters for the regular initialization. (the default value is "no")

For more detailed description of the options, please vist the website of IPOPT documentation[1].

[1] https://coin-or.github.io/Ipopt/OPTIONS.html



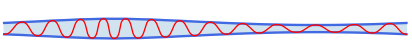

# Appendix B

# Implementation of mixed formulation in Python with CasADi

Here we show an example of the implementation of optimization problem (2.24) using programming language Python and the package CasADi.

We first define the solver using CasADi opti stack, which is a collection of CasADi helper classes:

```
import casadi, time; import numpy as np
import matplotlib.pyplot as plt

###############----- mesh points -----###############
nb_s = 100; s = np.linspace(0, 1, nb_s); ds = s[1]
#####----- set casadi optimisation problem -----#####
opti = casadi.Opti()
########## Variables & parameter ##########
# variables : curvature, angle, position x and y
kappa = opti.variable(nb_s-1); theta = opti.variable(nb_s)
x = opti.variable(nb_s); y = opti.variable(nb_s)
delta = opti.parameter()  # parameters: end-shortening
################ constraints ################
opti.subject_to([ # trapezoidal Super-Helices & mixed formulation
  theta[1:]-theta[:-1]==ds*kappa,
  x[1:]-x[:-1]==ds*(casadi.cos(theta)[:-1]+casadi.cos(theta)[1:])/2,
  y[1:]-y[:-1]==ds*(casadi.sin(theta)[:-1]+casadi.sin(theta)[1:])/2])
BC_cdt = [ # boundary conditions
  x[0] == 0, y[0] == 0, theta[0] == 0,
  x[-1] == 1-delta, y[-1] == 0, theta[-1] == 0]
opti.subject_to(BC_cdt)
################# objective ################
energy = 0.5*casadi.sum1(kappa**2)*ds; opti.minimize(energy)
###### Set solver method and options ######
opti.solver('ipopt', {'ipopt.print_level': 0, 'print_time': 0})
```

Then we set the endshortening $\Delta$, initialize and solve the problem with:

```
delta_value = 0.2  # value of endshortening
opti.set_value(delta, delta_value)  # set values for delta
# the initial guesses of all variables
k_v0 = 4*np.pi*np.sqrt(delta_value)*np.cos(2*np.pi*s[1:])
t_v0 = np.insert(np.cumsum(k_v0)*ds,0,0)
# set initial guess
opti.set_initial(kappa, k_v0.tolist()); opti.set_initial(theta, t_v0.tolist())
```

```
start_time = time.time(); res = opti.solve() # call casadi to solve the problem
print("Solved in %.4f seconds" %(time.time() - start_time))
print(r"Number of variables: ", opti.x.shape)
print(r"Number of Lagrange multipliers: ",opti.lam_g.shape)
# show results
plt.figure(); plt.plot(res.value(x), res.value(y))
plt.xlabel("x"); plt.ylabel("y"); plt.grid(True)
plt.title("shape of the Elastica")
plt.gca().set_aspect('equal'); plt.show()
# Horizontal force P (Lagrange multiplier of condition x(1)=1-delta) and energy
print("P: %.3f, Energy: %.3f"%(res.value(opti.dual(BC_cdt[3])),res.value(energy)))
```

**Outputs:**[1]

Solved in 0.0110 seconds

Number of variables: (399, 1)

Number of Lagrange multipliers: (303, 1)

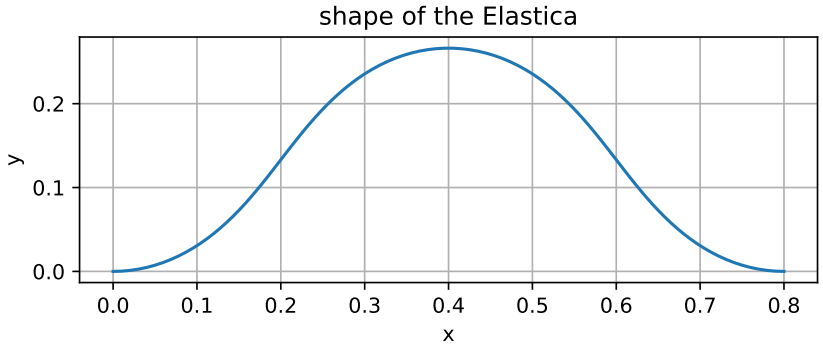


P: 43.914, Energy: 8.320

[1]Platform: macosx-10.9-x86_64, Python version: 3.9.18 (packaged by conda-forge), CasADi version: 3.6.4

# Appendix C

# Analytical solution of the planar Elastica

We consider a branch of Elatica clamped at two ends. The system is adimensionalized with bending stiffness $EI$ and the length of Elastica $L$. The Elastica deforms under horizontal force $P$ and vertical force $f$, shown in figure C.1.

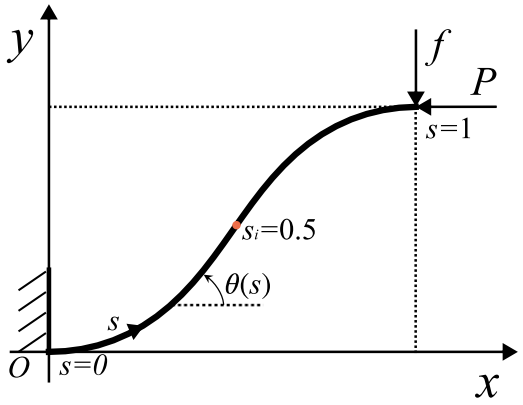


**Figure C.1: A branch of Elastica**

The differential equations of Elastica are

$$x'(s) = \cos\theta(s), \qquad y'(s) = \sin\theta(s) \tag{C.1a}$$

$$\theta''(s) + P\,\sin\theta(s) - f\,\cos\theta(s) = 0, \tag{C.1b}$$

with boundary conditions $x(0) = y(0) = 0$ and $\theta(0) = \theta(1) = 0$.

## C.1 Integrals of the Elastica equation

The above system can be integrated and give some useful relations. Here we limit to 2D configuration. In the work of Kehrbaum and Maddocks (1997), a more comprehensive study of elastic rods in 3D gives the integrals of different rod descriptions.

### C.1.1 Direct integration

From (C.1), we can reformulate (C.1b) as

$$\theta''(s) + P\,y'(s) - f\,x'(s) = 0$$

Integrating from $s = 0$ to an arbitrary $s$ gives

$$\theta'(0) = \theta'(s) + P\, y(s) - f\, x(s) \tag{C.2}$$

### C.1.2 First order integration

Another integral can be obtained by integrating equation (C.1b) multiplied with $\theta'(s)$:

$$\int \theta''\theta' + P\,\theta' \sin\theta - f\,\theta' \cos\theta\, ds = \int \frac{d}{ds}\left(\frac{1}{2}\theta'^2 - P\,\cos\theta - f\,\sin\theta\right) = 0,$$

which leads to a constant along the Elastica

$$I_{nv} = \frac{1}{2}\theta'^2(s) - P\,\cos\theta(s) - f\,\sin\theta(s). \tag{C.3}$$

This constant $I_{nv}$ is usually called *the Hamiltonian* (Dichmann, Li, and Maddocks, 1996; Kehrbaum and Maddocks, 1997). Using this conserved quantity with boundary conditions $\theta(0) = \theta(1) = 0$, we have

$$\frac{1}{2}\theta'^2(0) - P = \frac{1}{2}\theta'^2(1) - P,$$

and this leads to the equality between the absolute curvature at the two ends of the Elastica: $\theta'^2(0) = \theta'^2(1)$. And we can again use equation (C.1a) and deduce a relation about the bending energy of the system

$$\int_0^1 \theta'^2(s)\, ds = \frac{1}{2}\theta'^2(1) - P(1 - x(1)) + f\, y(1). \tag{C.4}$$

## C.2 Analytical solution

The equation (C.1b) is an analogy with the equation of pendulum. With the nice symmetric property of the equation, adding the fact that the boundary conditions are symmetric, the solution is symmetric around $s = s_i = 0.5$, and $\theta'(s_i) = 0$.

We define

$$Q = \sqrt{P^2 + f^2}; \tag{C.5a}$$

$$\cos\bar{\theta} = \frac{P}{\sqrt{P^2+f^2}} = \frac{P}{Q}, \qquad \sin\bar{\theta} = \frac{f}{\sqrt{P^2+f^2}} = \frac{f}{Q}. \tag{C.5b}$$

With a change of variable $\alpha(s) = \theta(s) - \bar{\theta}$, then the Elastica equation can be written as

$$\alpha''(s) + Q\,\sin\alpha(s) = 0. \tag{C.6}$$

Multiplying this equation by $\alpha'(s)$ and integrate, we have

$$\frac{1}{2}\left(\frac{d\alpha}{ds}\right)^2 - Q\cos\alpha = \text{constant} = -Q\cos\alpha_i \tag{C.7}$$

where $\alpha_i = \alpha(s_i)$.

$\alpha'(s)$ is equal to $\theta'(s)$ and is positive for $s \in [0, 0.5]$, thus, we have

$$\frac{d\alpha}{ds} = \sqrt{2Q}\sqrt{\cos\alpha - \cos\alpha_i} = 2\sqrt{Q}\sqrt{\sin^2\frac{\alpha_i}{2} - \sin^2\frac{\alpha}{2}}. \tag{C.8}$$

We introduce $\sigma(s)$, such that

$$\sin\sigma(s) = \frac{\sin\frac{\alpha(s)}{2}}{\sin\frac{\alpha_i}{2}}. \tag{C.9}$$

Then the previous equation becomes

$$\frac{d\sigma}{ds} = \sqrt{Q}\sqrt{1-\mu\sin^2\sigma} \tag{C.10}$$

with $\mu = \sin^2\frac{\alpha_i}{2}$. And we have

$$ds = \frac{1}{\sqrt{Q}}(1-\mu\sin^2\sigma)^{-1/2}d\sigma \tag{C.11}$$

To solve this, we introduce the first and second kind of elliptic integral

$$F(\phi, m) = \int_0^\phi (1-m\sin^2\theta)^{-1/2}d\theta, \tag{C.12}$$

$$K(\phi, m) = \int_0^\phi (1-m\sin^2\theta)^{1/2}d\theta, \tag{C.13}$$

and also the Jacobian elliptic functions

$$\phi = \mathrm{am}(u,m), \quad \sin\phi = \mathrm{sn}(u,m), \quad \cos\phi = \mathrm{cn}(u,m), \quad \text{given } u = F(\phi,m) \tag{C.14}$$

From the boundary conditions, we know $\sigma(1/2) = \pi/2$. We suppose $\sigma(\bar{s}) = 0$, and we know $F(0,m) = 0$. Then with equation (C.10),

$$F(\pi/2, \mu) = \sqrt{Q}\left(\frac{1}{2} - \bar{s}\right), \tag{C.15}$$

$$F(\sigma(s), \mu) = \sqrt{Q}\,(s-\bar{s})\,. \tag{C.16}$$

In fact, given $\mu$ and $Q$, the system has a unique solution. Here we express the solution $\theta(s)$, other geometry functions ($\kappa(s)$, $x(s)$, $y(s)$), and the forces $P$, $f$ as functions of $\mu$ and $Q$.

Knowing $\mu$ and $Q$, equation (C.15) gives $\bar{s}$, and we can solve for any $\sigma(s)$ for $s \in [0, 1/2]$ with equation (C.16), which leads to the expression of $\alpha(s)$.

$$\sigma(s) = \mathrm{am}(\sqrt{Q}\,(s-\bar{s})\,,\,\mu) \tag{C.17}$$

$$\sin\frac{\alpha}{2} = \sqrt{\mu}\,\sin\sigma(s) = \sqrt{\mu}\,\mathrm{sn}(\sqrt{Q}\,(s-\bar{s})\,,\,\mu) \tag{C.18}$$

From definition, $P = Q\cos\bar{\theta}$. Because $\theta(0) = 0$, $P = Q\cos\bar{\alpha}(0)$, and we have

$$P = Q\left(1 - 2\sin^2\frac{\alpha_0}{2}\right) = Q\left(1 - 2\mu\,\mathrm{sn}^2(-\sqrt{Q}\bar{s},\,\mu)\right). \tag{C.19}$$

Then $f$ is simply $\sqrt{Q^2 - P^2}$.

The geometry functions are related by differential equations

$$\kappa(s) = \theta'(s) = \alpha'(s), \tag{C.20}$$

$$x'(s) = \cos\theta(s) = \cos\alpha\cos\bar{\theta} - \sin\alpha\sin\bar{\theta}, \tag{C.21}$$

$$y'(s) = \sin\theta(s) = \sin\alpha\cos\bar{\theta} + \cos\alpha\sin\bar{\theta}. \tag{C.22}$$

With equation (C.8) and (C.18), we have the expression of $\kappa(s)$

$$\kappa(s) = \alpha'(s) = 2\sqrt{Q}\sqrt{\mu\left(1 - \mathrm{sn}^2(\sqrt{Q}\,(s-\bar{s})\,,\,\mu)\right)} \tag{C.23}$$

To calculate $x(s)$ and $y(s)$, we need to integrate $\cos\alpha$ and $\sin\alpha$ using the elliptic integrals and relation (C.11) for the change of variables

$$\begin{aligned}
\int_0^s \cos\alpha\, ds &= \int_0^s 1 - 2\mu\sin^2\sigma\, ds = 2\left[\int_0^s 1 - \mu\sin^2\sigma\, ds\right] - s \\
&= \frac{2}{\sqrt{Q}}\left[\int_{\sigma(0)}^{\sigma(s)} \left(1-\mu\sin^2\sigma\right)^{1/2} d\sigma\right] - s \\
&= \frac{2}{\sqrt{Q}}\left[K(\sigma(s),\mu) - K(\sigma(0),\mu)\right] - s,
\end{aligned} \tag{C.24}$$

$$\begin{aligned}
\int_0^s \sin\alpha\, ds &= \int_0^s 2\sin\frac{\alpha}{2}\cos\frac{\alpha}{2}\, ds = 2\int_0^s \sqrt{\mu}\sin\sigma\sqrt{1-\mu\sin^2\sigma}\, ds \\
&= \frac{2\sqrt{\mu}}{\sqrt{Q}}\int_{\sigma(0)}^{\sigma(s)} \sin\sigma\, d\sigma = \frac{2\sqrt{\mu}}{\sqrt{Q}}\left[\cos\sigma(0) - \cos\sigma(s)\right] \\
&= \frac{2\sqrt{\mu}}{\sqrt{Q}}\left[\mathrm{cn}(-\sqrt{Q}\bar{s},\,\mu) - \mathrm{cn}(\sqrt{Q}\,(s-\bar{s})\,,\,\mu)\right].
\end{aligned} \tag{C.25}$$

Then $x(s)$ and $y(s)$ are

$$x(s) = \cos\bar{\theta}\int_0^s \cos\alpha\, ds - \sin\bar{\theta}\int_0^s \sin\alpha\, ds, \tag{C.26}$$

$$y(s) = \cos\bar{\theta}\int_0^s \sin\alpha\, ds + \sin\bar{\theta}\int_0^s \cos\alpha\, ds. \tag{C.27}$$

We can also derive the bending energy of the system

$$\begin{aligned}
\mathcal{E} &= \int_0^1 \frac{\theta'^2}{2} ds = 2\int_0^{1/2} \frac{\alpha'^2}{2} ds = \int_0^{1/2} 4Q\mu(1-\sin^2\sigma) ds \\
&= \int_{\sigma(0)}^{\sigma(1/2)} 4\sqrt{Q}(1-\mu\sin^2\sigma)^{1/2} d\sigma + 2Q(\mu-1) \\
&= 4\sqrt{Q}\left[K(\frac{\pi}{2},\mu) - K(\sigma(0),\mu)\right] + 2Q(\mu-1)
\end{aligned} \tag{C.28}$$

# Appendix D

# Flexible sliding sleeve

In section 4.2.1, we have presented an example showing how an additional term appears when the material of the system varies, and here we use another example of sliding sleeve to show how to numerically implement problems with varying boundaries. The setup of the example is shown in figure D.1. Part of a fiber (orange) of length $L$ and bending stiffness $a_1$ is inserted into a flexible

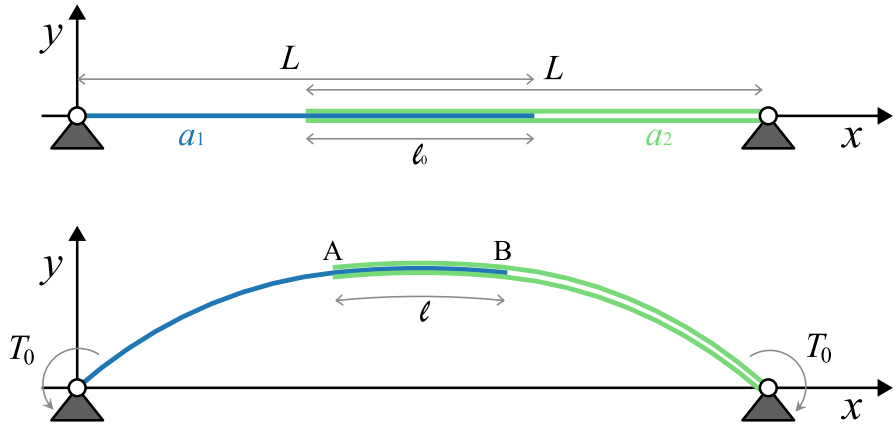


**Figure D.1: Setup of the flexible sliding sleeve problem. A elastic fiber is inserted into a flexible tube, the whole system deforms under the momentum $T_0$ imposed at the extremities.**

tube (green) of the same length and bending stiffness $a_2$.

The positions of the two ends are fixed with distance $L - \ell_0$, where $\ell_0$ is the length of the insertion when the fiber and the tube are in their undeformed shape. The same momentum $T_0$ is imposed at both ends. As the fiber and tube deform, the length of the overlapping region varies, we use $\ell$ for the length after deformation.

This system can be considered as four physical parts, the fiber inside/outside the tube, the tube with/without the fiber, but for the analysis we will treat the overlapping region as one part, then the three parts all have varying length, which leads to the possible appearance of the 'configurational force' similar to the rigid sliding sleeve example.

To implement this problem numerically, we can use one of the discretization schemes of section 2.2, for example the Super-Helices or Super-Clothoid, and apply it to the three parts of the system, see figure D.2a. We consider $N_1$ edges in the part $I$, and we use $(\cdot)_i^I$, $(i = 0, ..., N_1)$ to mark the discrete variable, the same is done with $N_2$ and $N_3$ for the two other parts. The key point is the varying length. To tackle this, we define a fixed mesh grid $\sigma_i$, with $\sigma_0 = 0$ and $\sigma_{N_k} = 1$, where $k = 1, 2$ or 3, and the mesh for the deformed shape is obtained by scaling the fixed mesh with factor

$\ell_k$, the actual length of part $k$, see figure D.2b. Then, the element length $\delta s$ of the discretization scheme is actually $\ell_k \delta\sigma$.

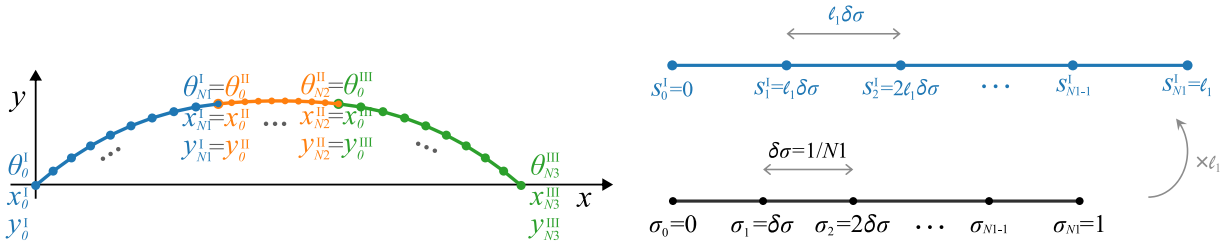


**(a) Illustration : the discretized system** **(b) Curvilinear transformation**

**Figure D.2: Numerical implementation of the flexible sliding sleeve**

We formulate the optimization problem of the discretized system:

$$\begin{aligned}
\min \quad & \mathcal{E}_{tot} = \mathcal{E}_1 + \mathcal{E}_2 + \mathcal{E}_3 - T_0\,\theta_0^I + T_0\,\theta_{N_3}^{III}, && \text{(D.1a)}\\
\text{subject to} \quad & \text{geometry conditions for the mixed formulation}, && \text{(D.1b)}\\
& x_0^I = y_0^I = 0, \quad x_{N_3}^{III} = 2L - \ell_0, \quad y_{N_3}^{III} = 0, && \text{(D.1c)}\\
& \theta_{N_1}^I = \theta_0^{II}, \quad x_{N_1}^I = x_0^{II}, \quad y_{N_1}^I = y_0^{II}, && \text{(D.1d)}\\
& \theta_{N_2}^{II} = \theta_0^{III}, \quad x_{N_2}^I = x_0^{III}, \quad y_{N_2}^I = y_0^{III}, && \text{(D.1e)}\\
& \ell_1 + \ell_2 - L = 0, \qquad \ell_2 + \ell_3 - L = 0, && \text{(D.1f)}
\end{aligned}$$

where $\mathcal{E}_k$ is the elastic energy of part $k$, a function of the geometry variables and the part lengths $\ell_k$.

As there is no inequality constraints, we can implement the problem with CasADi, requiring the first derivative of the Lagrangian to be zero. Further we can calculate the eigenvalues of the projected Hessian for the stability analysis. This implementation is similar to that of the hanging drop example in section 1.7.2.

The forces and momenta of the system hides behind the Lagrange multipliers. The Lagrange multipliers of the discrete geometry condition $\theta' = \kappa$ are the momenta along each part, and the Lagrange multipliers of the discrete geometry condition on $x'$ and $y'$ are respectively the horizontal and vertical internal forces, we note them $n_{x_i}^p$ and $n_{y_i}^p$, where $p = I$, $II$, or $III$, and $i \in [1, 2, ..., N_p]$. Because there is no external forces applied along the structures, and $x$ and $y$ only enter the problem as boundary conditions, $n_{x_i}^p$ have the same value, also for $n_{y_i}^p$, meaning the internal forces are constant along each part. The Lagrange multipliers of boundary conditions of $\theta$, $x$ and $y$ are respectively the momentum, horizontal and vertical forces given by the support. Because of the geometrical continuity conditions (D.1d) and (D.1e), the forces and momenta are continuous for the three parts, and the relative Lagrange multipliers are the forces and momenta at the transition points. Finally, the Lagrange multipliers of the conditions D.1f have the same dimension as forces, They are the constant of Elastica equation, called the *Hamiltonian* in some literatures. The Hamiltonian defines as

$$\frac{a}{2}\kappa^2 + n_x \cos\theta + n_y \sin\theta, \tag{D.2}$$

where $a$ is the bending stiffness and $n_x$ and $n_y$ are the constant internal forces. In the comprehensive study of Neukirch, Corso, and Vetyukov, 2025, it has been shown that the Hamiltonian is conserved both along the tube and fiber, even for the overlapping part.

Next, we show the numerical solutions of some setups with different parameter values. In the first place, solutions of symmetric configurations are given, meaning the fiber and tube have the same length and the same bending stiffness. After that, we introduce non-symmetry, setting the bending stiffness to be different for the fiber and the tube. Note that the numerical values are calculated with dimensionless system with length scale $L$ and force scale $a_2/L^2$.

## D.1 Symmetric case

First, we set the symmetric configuration with $a_1 = a_2$ and $\ell_0 = 0.5$, solutions of different $T_0$ are calculated with the arc-length continuation method presented in section 1.4.3, the length of overlapping part and the maximal y position as functions of $T_0$ are shown on the left of figure D.3, and we also mark the stability indices on the curve. On the right side, three solutions with of different $T_0$ are plotted. Increasing $T_0$ from the unloaded configuration, we can see that the

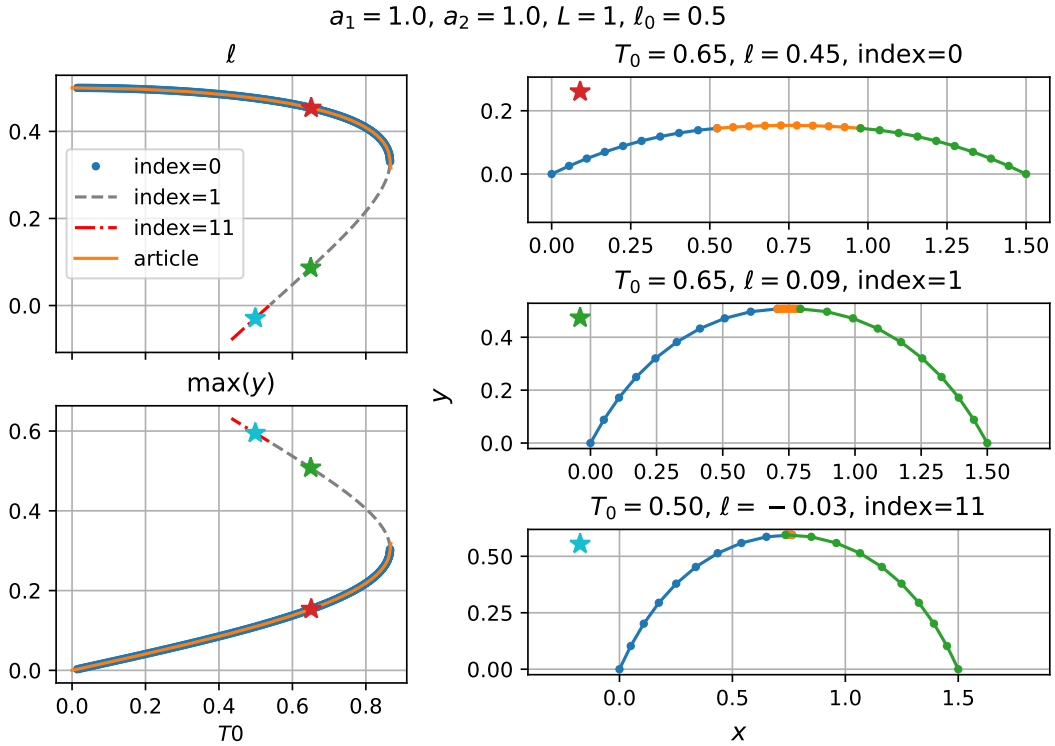


**Figure D.3: Solutions of the flexible sliding sleeve with $a_1 = a_2$ and $\ell_0 = 0.5$. On the left, evolution of $\ell$ and maximal height are plotted with the stability index, and are compared to the results of reference. On the right, we show the forms of three solutions marked by stars on the branches.**

overlapping length $\ell$ decreases while the maximal height increases. This is expected and conforms to the intuition. However, when $T_0$ reaches to the turning point, the solutions become unstable (index=1), while the overlapping part still exists. This can be understood as a sudden 'popup' of the fiber from the tube. Further on the branch, the length of the overlapping region becomes negative, and the stability index suddenly increases to 11.

In figure D.4, we change the initial length of the overlapping part $\ell_0$ to 0.1. In this case there is no more unstable branch with non-negative overlapping length. This means that the fiber is pushed out of the tube as $T_0$ increases, without the sudden 'popup'.

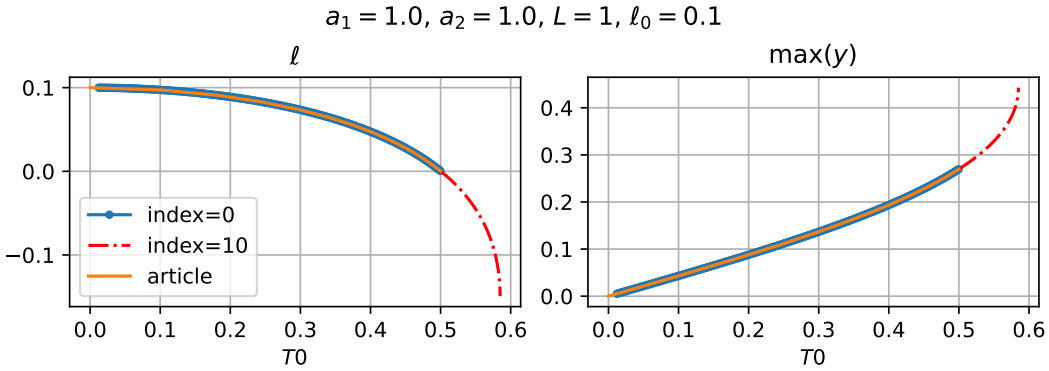


**Figure D.4: Evolution of $\ell$ and maximal height of the flexible sliding sleeve with $a_1 = a_2$ and $\ell_0 = 0.1$.**

## D.2 Asymmetric case

Asymmetries can be introduced by selecting different values for the bending stiffnesses of the fiber and the tube. Here we choose $a_1/a_2 = 1.5$, and keep $\ell_0 = 0.5$, the solutions are shown in figure D.5.

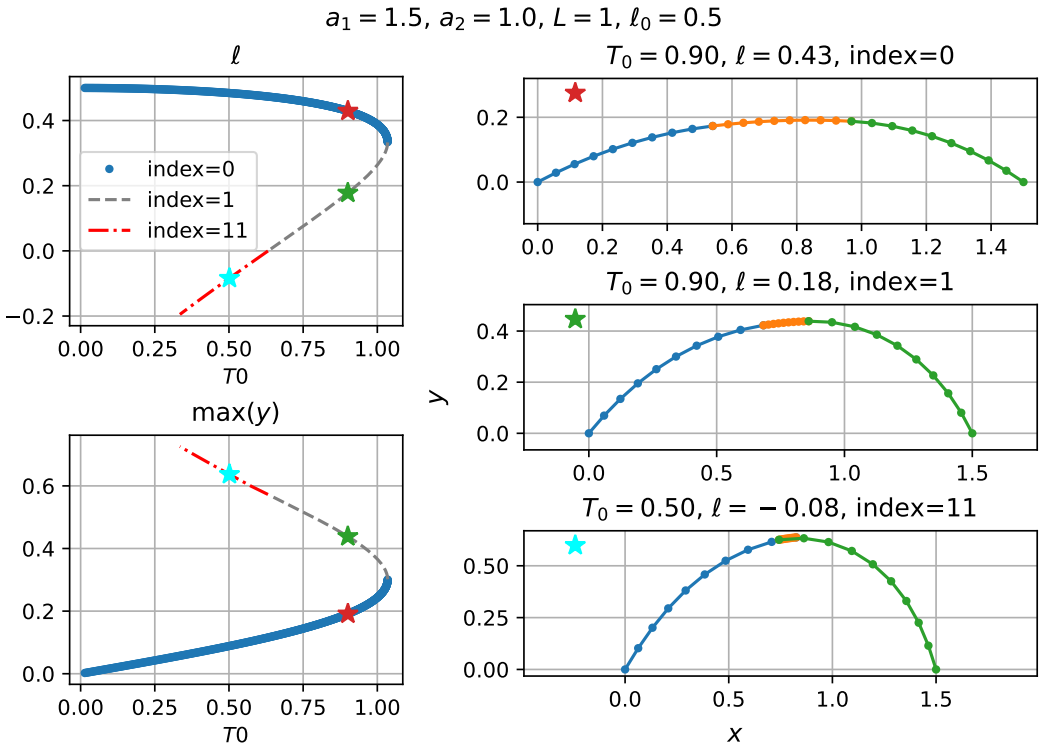


**Figure D.5: Solutions of the flexible sliding sleeve with $a_1/a_2 = 1.5$ and $\ell_0 = 0.5$. On the left, evolution of $\ell$ and maximal height are plotted with the stability index, and are compared to the results of reference. On the right, we show the forms of three solutions marked by stars on the branches.**

Same as the symmetric case with $\ell_0 = 0.5$, there are unstable solutions with positive $\ell$ after the

turning point, indicating the possible occurrence of a sudden popup of the fiber. The difference in the bending stiffnesses leads to non-symmetric shapes, shown on the right side of figure D.5.

We show one of the solutions for the configuration $a_1/a_2 = 1.5$ and $\ell_0 = 0.5$ in figure D.6, and jumps can be observed in forces and bending momenta. In section 4.2, we mentioned that the *configurational forces* appear when the system has moving boundaries. In this case, this is the reason for these jumps.

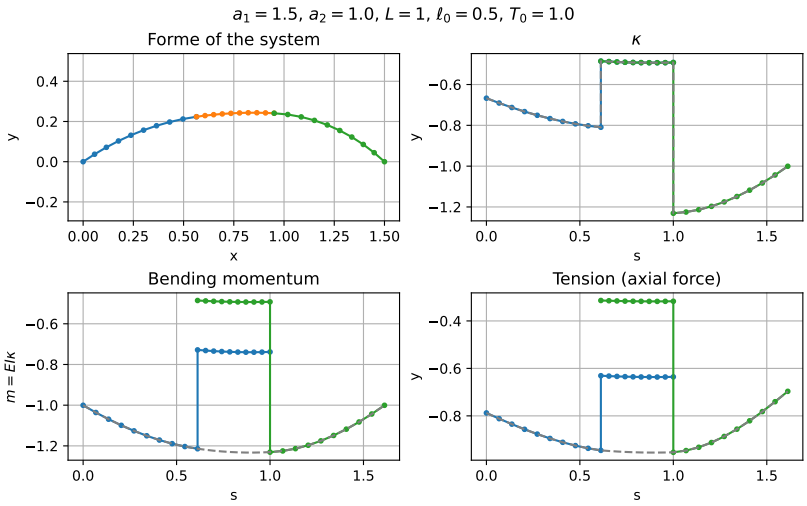


**Figure D.6: The geometry, momenta and axial forces of case $a_1/a_2 = 1.5$ $\ell_0 = 0.5$, and $T_0 = 1$.**

Although we have explained that the forces and bending momenta are continuous for the three parts, the overlapping part is indeed a composite of the fiber and the tube. When consider separately, both the fiber and the tube have forces and momenta jumps between the external part and the overlapping part. Because the momentum is continuous between the external parts and the composite part, which have different bending stiffness, there are jumps of the curvature $\kappa$ for both the fiber and the tube. Thus, there are jumps in momentum when the fiber and the tube are considered separately.

We also plot the internal axial forces $n^p_{x_i} \cos\theta^p_i + n^p_{y_i} \sin\theta^p_i$ in figure D.6. This is calculated by the fact that the Hamiltonian (D.2) is conserved for both the fiber and the tube. Once again, the axial force is continuous when the overlapping part is considered as a whole and jumps appear when it is separated into the fiber and the tube.

Although it is still controversial to use the term *configurational forces* to explain the these jumps, this example shows the force and bending momentum discontinuities when the structures have moving boundaries.

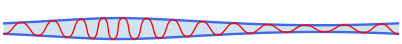

# Appendix E

# Spiral form of the confined Elastica

In the wall-attached confined Elastica problem, we mainly study the formation and different configurations of the wavy patterns. When the end displacement $\Delta$ is large enough, the wavy patterns will be replaced by one large fold, as it is more energetically favorable than the wavy pattern. Because its 'S' shape, we call this state *the spiral*, see figure E.1. The Elastica in the spiral state can

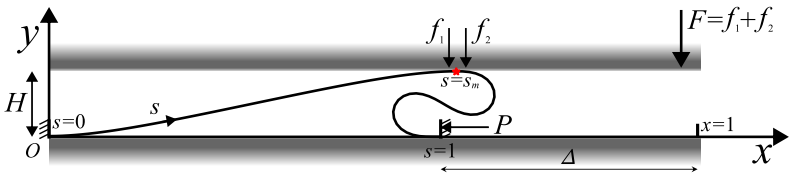


**Figure E.1: Musch compressed state of confined Elastica : spiral state.**

be considered as two branches of free Elastica joined at the point attached to the upper wall. For this reason, we write out the system of equations for the dimensionless system

$$x'(s) = \cos\theta(s), \tag{E.1a}$$
$$y'(s) = \sin\theta(s), \tag{E.1b}$$
$$\theta''(s) = -P\sin\theta(s) + f_1\cos\theta(s) \qquad s \in [0, s_m] \tag{E.1c}$$
$$\theta''(s) = -P\sin\theta(s) - f_2\cos\theta(s) \qquad s \in [s_m, 1] \tag{E.1d}$$

with boundary and continuity conditions

$$\theta(0) = 0 \qquad x(0) = 0 \qquad y(0) = 0, \tag{E.2a}$$
$$\theta(1) = 0 \qquad x(1) = 1 - \Delta \qquad y(0) = 0. \tag{E.2b}$$

At the conjunction point $s = s_m$, the geometry variables $\kappa = \theta'$, $\theta$, $x$ and $y$ are continuous, and $\theta(s_m) = 0$. Remark that $f_1$ and $f_2$ are different, and the force jump at the contact point $s_m$ is given by the upper wall, that is $F = f_1 + f_2$.

We use the shooting method to solve this system of equation. We choose $H = 0.1$, and on the left side of figure E.2, we compare the shooting results total energy, $P$ and $F$ with that obtained by energy minimization with IPOPT. The form of Elastica found by system (E.1) for several chosen $\Delta$ are drawn on the right.

Firstly, the solutions found by ODE system (E.1) coincide well with that of energy minimization method. The energy curve proves that the energy of spiral is much lower than the wavy form when $\Delta$ is large. For this reason, when solved by minimization method with decreasing $\Delta$, the curve sticks longer to the spiral state, the phenomenon is also known as the hysteresis.

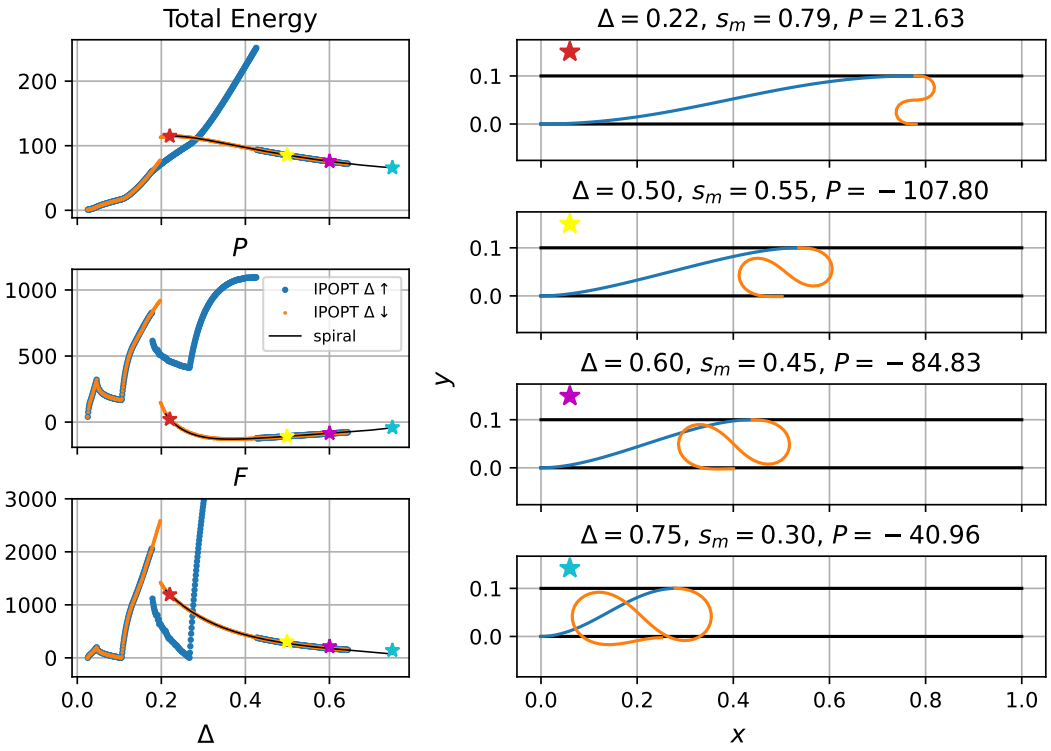


**Figure E.2: Solutions of the spiral model. On the left, the solutions are compared with IPOPT solutions, the stars mark the form of Elastica shown on the right.**

For the forces, we can see that they are much lower than the wavy state, which means a smaller impact on the walls. This may be interesting for applications searching for packing forms with smaller impact on the wrap. Moreover, the horizontal force $P$ is in general negative for the spiral, which means we are not pushing the Elastica into the channel, but holding it from retraction. In fact, the less curved part is 'pulled' by the highly curved 'S' part, this is also related to the transition from the wavy state to the spiral: one highly curved part has the tendency to 'devour' other parts and form the spiral.

Finally, the two parts ODE model is very simplified, and it is representative for the real situation only for a small range of $\Delta$, For example, the third form in figure E.2 exhibits the problem of self-penetration, and the fourth form is moreover passing outside the walls. To find solutions more relevant to reality, we apply the contact constraints described in section 3.2 to the spiral, please see the next part for more details.

## E.1 IPOPT solving with self-contact constraints

Although using CasADi and IPOPT solving the problem by optimization problem formulation 5.1 confines the Elastica between the walls, it does not prevent self-penetration. To conform the real experiments when solving the problem numerically, we restrict the Elastica to stay in the space defined by its left and right ends, and we use the contact algorithm described in section 3.2 to prevent self-penetration, the implementation of which is similar to that of section 3.4.1.

In figure E.3, we superimposed the energy and forces curves found by the contact algorithm to that of other methods. To better illustrate the solutions, we choose three forms with self-contact feature at different $\Delta$, and plot them on the right side of the figure.

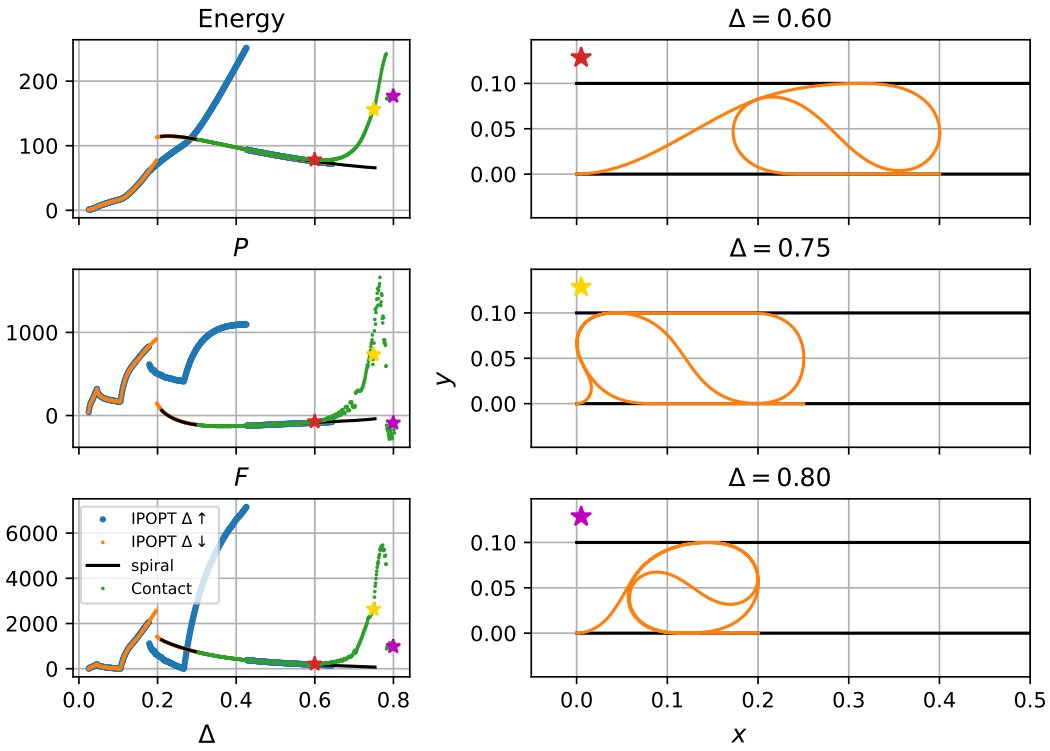


**Figure E.3: Solutions of IPOPT adding self-contact constraints (the green lines). Some solutions, marked by the stars, are shown on the right.**

When self-contact is present, the energy curve is above the curves found without self-contact feature, and the same is true for the curves of horizontal and vertical forces. This is expected, because when there is self-contact, the Elastica bends harder to fit the non-penetration constraints, thus the elastic energy is larger. As for the forces, the self contact point also gives force responses, which we have already observed in the self-contact Elastica problem in section 3.3. However, when the Elastica is highly packed, for example in the state marked by the magenta star, the force responses decrease compared to the slightly packed state. The highly packed stage is out of the scope of this study, and may be a subject for the future investigation.

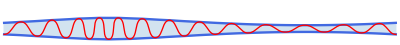

# Appendix F

# The total cellular model: Lagrangian and equations

With the definition of the energy and the constraints defined in section 9.3.2, we apply the variational method and construct the Lagrangian $\mathcal{L} = \mathcal{L}[\theta(s), x(s), y(s), r_u, \beta_u, r_l, \beta_l, D_l, D_u, \ell]$:

$$
\begin{aligned}
\mathcal{L} = \frac{L}{\ell}\Bigg\{ & \int_0^\ell \frac{B}{2}\,\theta'^2(s)\,ds + \gamma\left(r_u\beta_u + r_l\beta_l + D_l - D_u\right) \\
& + \int_0^{D_l} n_{x1}(s)\left(x' - \cos\theta\right) + n_{y1}(s)\left(y' - \sin\theta\right)ds \\
& + \int_{D_l}^{D_u} n_{x2}(s)\left(x' - \cos\theta\right) + n_{y2}(s)\left(y' - \sin\theta\right)ds \\
& + \int_{D_u}^{\ell} n_{x3}(s)\left(x' - \cos\theta\right) + n_{y3}(s)\left(y' - \sin\theta\right)ds \\
& - p\Bigg[ - \int_0^{D_u} yx'ds + x(D_u)\,y(D_u) - \frac{1}{2}r_u^2(\beta_u - \sin\beta_u\cos\beta_u) \\
& \qquad + \int_{D_l}^{\ell} yx'ds + \left[x(D_l) - x(\ell)\right]y(D_l) - \frac{1}{2}r_l^2(\beta_l - \sin\beta_l\cos\beta_l) - 2\ell H_0\Bigg] \\
& - \eta_u\left[x(D_u) - r_u\,\sin\beta_u\right] - \eta_l\left[x(D_l) - x(\ell) + r_l\,\sin\beta_l\right] - T[x(\ell) - \ell(1-\Delta)]\Bigg\}
\end{aligned}
\tag{F.1}
$$

with the continuous Lagrange multipliers $n_{xi}$, $n_{yi}$ ($i = 1$, 2, or 3) and scalar Lagrange multipliers $p$, $\eta_u$, $\eta_l$, $T$. Please remark that the physically $n_{xi}$, $n_{yi}$ are the internal forces along the membrane, and it has been discussed in the example of planar Elastica in section 1.5. The Lagrange multiplier of the volume constraint $p$ has the same dimension as the pressure, and the Lagrange multipliers $\eta_u$, $\eta_l$ and $T$ has the same dimension as a force.

We now compute the first variation of $\mathcal{L}$ and require it to vanish for all admissible variations.



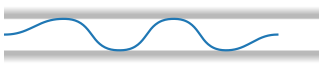

After integration by parts we obtain

$$
\begin{aligned}
\bar{\mathcal{L}} = 0 = &-\frac{L}{\ell^2}\,\bar{\ell}\left\{\int_0^{\ell}\frac{B}{2}\,\theta'^2(s)\,ds + \gamma\left(r_u\beta_u + r_l\beta_l + D_l - D_u\right)\right\}\\
&+\frac{L}{\ell}\left\{\bar{\ell}\frac{1}{2}\,B\,\theta'^2(\ell) + \int_0^{\ell} -B\,\theta''\bar{\theta}ds + B[\theta'\bar{\theta}]_0^{\ell}\right.\\
&\quad+\gamma\left(\bar{r}_u\beta_u + r_u\bar{\beta}_u + \bar{r}_l\beta_l + r_l\bar{\beta}_l + \bar{D}_l - \bar{D}_u\right)\\
&\quad+\int_0^{D_l}\left[-n'_{x1}\bar{x} + n_{x1}\bar{\theta}\sin\theta - n'_{y1}\bar{y} - n_{y1}\bar{\theta}\cos\theta\right]ds + [n_{x1}\bar{x}]_0^{D_l} + [n_{y1}\bar{y}]_0^{D_l}\\
&\quad+\int_{D_l}^{D_u}\left[-n'_{x2}\bar{x} + n_{x2}\bar{\theta}\sin\theta - n'_{y2}\bar{y} - n_{y2}\bar{\theta}\cos\theta\right]ds + [n_{x2}\bar{x}]_{D_l}^{D_u} + [n_{y2}\bar{y}]_{D_l}^{D_u}\\
&\quad+\int_{D_u}^{\ell}\left[-n'_{x3}\bar{x} + n_{x3}\bar{\theta}\sin\theta - n'_{y3}\bar{y} - n_{y3}\bar{\theta}\cos\theta\right]ds + [n_{x3}\bar{x}]_{D_u}^{\ell} + [n_{y3}\bar{y}]_{D_u}^{\ell}\\
&\quad-p\Big[-\bar{D}_u y(D_u)x'(D_u) - \int_0^{D_u}\bar{y}x'ds + \int_0^{D_u}y'\bar{x}ds - [y\bar{x}]_0^{D_u}\\
&\qquad+\bar{x}(D_u)\,y(D_u) + \bar{D}_u x'(D_u)\,y(D_u) + x(D_u)\,\bar{y}(D_u) + x(D_u)\,y'(D_u)\bar{D}_u\\
&\qquad-\bar{r}_u r_u(\beta_u - \sin\beta_u\cos\beta_u) - \frac{1}{2}r_u^2\bar{\beta}_u(1-\cos 2\beta_u)\\
&\qquad-\bar{D}_l y(D_l)x'(D_l) + \bar{\ell}y(\ell)x'(\ell) + \int_{D_l}^{\ell}\bar{y}x'ds - \int_{D_l}^{\ell}y'\bar{x}ds + [y\bar{x}]_{D_l}^{\ell}\\
&\qquad+[x(D_l) - x(\ell)]\,\bar{y}(D_l) + [x(D_l) - x(\ell)]\,y'(D_l)\,\bar{D}_l\\
&\qquad+[\bar{x}(D_l) - \bar{x}(\ell)]\,y(D_l) + [x'(D_l)\bar{D}_l - x'(\ell)\bar{\ell}]\,y(D_l)\\
&\qquad-\bar{r}_l r_l(\beta_l - \sin\beta_l\cos\beta_l) - \frac{1}{2}r_l^2\bar{\beta}_l(1-\cos 2\beta_l) - 2H_0\bar{\ell}\Big]\\
&\quad-\eta_u\left(\bar{x}(D_u) + x'(D_u)\bar{D}_u - \bar{r}_u\,\sin\beta_u - r_u\,\bar{\beta}_u\cos\beta_u\right)\\
&\quad-\eta_l\left(\bar{x}(D_l) + x'(D_l)\bar{D}_l - \bar{x}(\ell) - x'(\ell)\bar{\ell} + \bar{r}_l\,\sin\beta_l + r_l\,\bar{\beta}_l\cos\beta_l\right)\\
&\quad\left.-T\left[\bar{x}(\ell) + x'(\ell)\bar{\ell} - \frac{\bar{\ell}}{\ell}x(\ell)\right]\right\}
\end{aligned}
\tag{F.2}
$$

Firstly, from the variation of the continuous variables $\theta(s)$, $x(s)$ and $y(s)$, we obtain the differential equations:

$$
\begin{cases}
B\theta''(s) = n_{x1}(s)\sin\theta(s) - n_{y1}(s)\cos\theta(s)\\
n'_{x1} = -py' \quad \& \quad n'_{y1} = px'
\end{cases}
\qquad s\in[0,\,D_l] \tag{F.3a}
$$

$$
\begin{cases}
B\theta''(s) = n_{x2}\sin\theta(s) - n_{y2}\cos\theta(s)\\
n_{x2} \text{ and } n_{y2} \text{ are constants}
\end{cases}
\qquad s\in[D_l,\,D_u] \tag{F.3b}
$$

$$
\begin{cases}
B\theta''(s) = n_{x3}(s)\sin\theta(s) - n_{y3}(s)\cos\theta(s)\\
n'_{x3} = py' \quad \& \quad n'_{y3} = -px'
\end{cases}
\qquad s\in[D_u,\,\ell] \tag{F.3c}
$$

These equations can also be derived by using the Euler–Lagrange method.



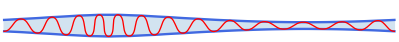

Requiring $\bar{\mathcal{L}} = 0$ for all $\bar{x}(D_u)$, $\bar{x}(D_l)$, $\bar{y}(D_u)$ and $\bar{y}(D_l)$ yields

$$n_{x3}(D_u) - n_{x2}(D_u) = -\eta_u \tag{F.4a}$$
$$n_{x2}(D_l) - n_{x1}(D_l) = -\eta_l \tag{F.4b}$$
$$n_{y3}(D_u) - n_{y2}(D_u) = -p\,x(D_u) \tag{F.4c}$$
$$n_{y2}(D_l) - n_{y1}(D_l) = -p\,[x(D_l) - x(\ell)], \tag{F.4d}$$

which are the force jumps.

The variations of interface parameters $r_{\ell,u}$, $\beta_{\ell,u}$ and $D_{\ell,u}$ gives :

$$p\,r_u\frac{1-\cos 2\beta_u}{2} + \eta_u\cos\beta_u + \gamma = 0 \tag{F.5a}$$
$$\gamma\beta_u + p\,r_u(\beta_u - \sin\beta_u\,\cos\beta_u) + \eta_u\sin\beta_u = 0 \tag{F.5b}$$
$$-\gamma - p\,x(D_u)y'(D_u) - \eta_u x'(D_u) = 0 \tag{F.5c}$$
$$p\,r_l\frac{1-\cos 2\beta_l}{2} - \eta_l\cos\beta_l + \gamma = 0 \tag{F.5d}$$
$$\gamma\beta_l + p\,r_l(\beta_l - \sin\beta_l\,\cos\beta_l) - \eta_l\sin\beta_l = 0 \tag{F.5e}$$
$$\gamma - p\,[x(D_l) - x(\ell)]y'(D_l) - \eta_l x'(D_l) = 0 \tag{F.5f}$$

with further simplification, these equations yield

$$p = -\frac{\gamma}{r_u} = -\frac{\gamma}{r_l} = -\frac{\gamma}{r} \quad \text{with} \quad r_u = r_l = r \tag{F.6a}$$
$$\eta_u = -\gamma\cos\beta_u, \qquad \eta_l = \gamma\cos\beta_l, \tag{F.6b}$$
$$\cos[\beta_u - \theta(D_u)] = 1 \quad \rightarrow \quad \beta_u = \theta(D_u), \qquad \cos[\beta_l - \theta(D_l)] = 1 \quad \rightarrow \quad \beta_l = \theta(D_l). \tag{F.6c}$$

The variations of $x(s)$, $y(s)$ and $\theta(s)$ on the end point $s = \ell$ gives

$$T = -p\,[y(\ell) - y(D_l)] + \eta_l + n_{x3}(\ell) \tag{F.7a}$$
$$n_{y3}(\ell) = 0. \tag{F.7b}$$

Introducing the point $y_M = y(D_l) + r_l(1 - \cos\beta_l)$, the vertical position of the lower interface at $s = \ell$, shown in figure 9.11, then the force $T$ becomes

$$T = n_{x3}(\ell) - p\,[y(\ell) - y_M] + \gamma \tag{F.8}$$

which is a horizontal force balance at $s = \ell$.

And the variation of $\ell$ gives

$$\frac{1}{\ell}\left\{\int_0^\ell \frac{B}{2}\,\theta'^2(s)ds + \gamma(r_u\beta_u - D_u + r_l\beta_l + D_l)\right\} = -\frac{B}{2}\theta'(\ell)^2 + p\,2H_0 - n_{x3}(\ell) + T\,(1-\Delta) \tag{F.9}$$

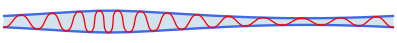

# Appendix G

# Force-induced interface deformation

This problem is set up to explain the deformation of the interfaces in the problem of soaked membrane in chapter 9, an illustration is given in figure G.1.

Some incompressible fluid with volume $V_0$ is confined between $x = 0$ and $x = L$. A localized vertical forcing $F$ is acting on the liquid-air interface of surface tension $\gamma$. Using variational method, we are going to find the shape of the deformed interface.

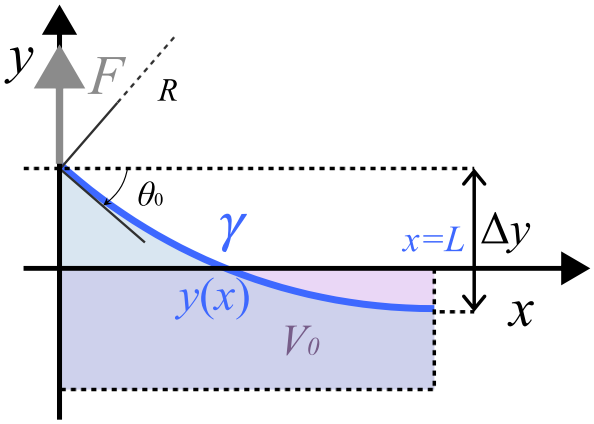


**Figure G.1: Problem setup: a liquid-air interface deforms under a localized vertical force $F$ situated at $x = 0$. The violet and blue parts mark the original and deformed liquid, and they have the same area for the fixed volume.**

The interface is supposed to stay initially at $y = 0$. After deformation, its geometry is described by $y(x)$ with $x \in [0, L]$. Then the energy of the system and the volume of the liquid is

$$\mathcal{E} = \int_0^L \gamma\sqrt{1+y'^2}\,dx - F \cdot y(0), \tag{G.1}$$

$$\mathcal{V} = \int_0^L y\,dx + V_0. \tag{G.2}$$

Building the Lagrangian

$$\mathcal{L} = \int_0^L \gamma\sqrt{1+y'^2}\,dx - F \cdot y(0) - p\left(\int_0^L y\,dx + V_0 - V_0\right) \tag{G.3}$$

and the variation of the Lagrangian is

$$\begin{aligned}\bar{\mathcal{L}} &= \int_0^L \gamma\frac{y'\bar{y}}{\sqrt{1+y'^2}}\,dx - F \cdot \bar{y}(0) - p\int_0^L \bar{y}\,dx \\ &= \gamma\frac{y'(1)}{\sqrt{1+y'^2(1)}}\bar{y}(1) - \left(\gamma\frac{y'(0)}{\sqrt{1+y'^2(0)}} + F\right)\bar{y}(0) - \int_0^L \left(\gamma\frac{y''}{\left(1+y'^2\right)^{3/2}} + p\right)\bar{y}\,dx,\end{aligned} \tag{G.4}$$

from which we obtain the system of equations and the boundary conditions of the interface:

$$y'' = -p\left(1 + y'^2\right)^{3/2} \tag{G.5a}$$

$$\int_0^L y\,dx = 0 \tag{G.5b}$$

$$\gamma\frac{y'(0)}{\sqrt{1+y'^2(0)}} = -F \;\Rightarrow\; y'(0) = \frac{-F}{\sqrt{\gamma^2 - F^2}}, \qquad y'(L) = 0 \tag{G.5c}$$

Introducing the deflection angle of the interface $\theta(s)$ where $s$ is the curvilinear coordinate of the interface, then we have

$$y' = \frac{dy}{dx} = \tan\theta, \qquad y'' = \frac{d^2y}{dx^2} = \frac{1}{\cos^3\theta}\frac{d\theta}{ds}. \tag{G.6}$$

With $\theta(s)$, the equation (G.5a) and the boundary conditions (G.5c) writes

$$\frac{d\theta}{ds} = -p, \qquad \gamma\sin\theta(0) = -F, \qquad \tan\theta(x = L) = 0 \tag{G.7}$$

From (G.7), we see that the geometry of the interface is arc-shaped, and the vertical projection of the surface tension at $x = 0$ balances $F$.

Suppose the radius of the arch is $R$ and note $\theta(0) = \theta_0$, then we can calculate the interface deflection $\Delta y$ by

$$-R\sin\theta_0 = L, \quad \Delta y = R\left(1 - \cos\theta_0\right), \quad \Rightarrow \quad \Delta y = \frac{L\left(1-\cos\theta_0\right)}{-\sin\theta_0} = \frac{L}{F}\left(\gamma - \sqrt{\gamma^2 - F^2}\right) \tag{G.8}$$

Generating a power series expansion for $\Delta y$ about the point $F_\gamma = F/\gamma = 0$, we have

$$\Delta y = L\left(\frac{F_\gamma}{2} + \frac{F_\gamma^3}{8} + \mathcal{O}(F_\gamma^5)\right) \approx 0.5L\,F_\gamma \tag{G.9}$$

which can be used to estimate the deformation of an interface under a given vertical force $F$.



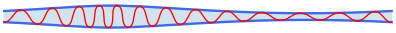

# Bibliography


Andersson, Joel A. E., Joris Gillis, Greg Horn, James B. Rawlings, and Moritz Diehl (Mar. 2019). "CasADi: a software framework for nonlinear optimization and optimal control". In: *Mathematical Programming Computation* 11.1, pp. 1–36. DOI: 10.1007/s12532-018-0139-4 (cit. on p. 27).

Andreas Wächter and Lorenz T. Biegler (Mar. 2004). *On the Implementation of an Interior-Point Filter Line-Search Algorithm for Large-Scale Nonlinear Programming*. URL: https://optimization-online.org/?p=9506 (cit. on pp. 10, 177).

Antman, Stuart S. (2005). *Nonlinear Problems of Elasticity*. Second Edition. Applied Mathematical Sciences, 107. New York: Springer. ISBN: 978-0-387-27649-6 (cit. on p. 15).

Audoly, B. (July 2011). "Localized buckling of a floating elastica". In: *Physical Review E* 84.1, p. 011605. DOI: 10.1103/PhysRevE.84.011605 (cit. on p. 136).

Barber, Dylan M., Zhefei Yang, Lucas Prévost, Olivia du Roure, Anke Lindner, Todd Emrick, and Alfred J. Crosby (2020). "Programmed Wrapping and Assembly of Droplets with Mesoscale Polymers". In: *Advanced Functional Materials* 30.36, p. 2002704. DOI: 10.1002/adfm.202002704 (cit. on p. 121).

Bazant, Zdenek P. and Luigi Cedolin (2010). *Stability of Structures: Elastic, Inelastic, Fracture, and Damage Theories*. World Science Publishing (cit. on p. 79).

Bedford, Anthony and Kenneth M. Liechti (2020). *Mechanics of Materials*. 2nd ed. Cham: Springer International Publishing. ISBN: 978-3-030-22081-5. DOI: 10.1007/978-3-030-22082-2 (cit. on pp. 15, 110).

Bertails, Florence, Basile Audoly, Marie-Paule Cani, Bernard Querleux, Frédéric Leroy, and Jean-Luc Lévêque (2006). "Super-Helices for Predicting the Dynamics of Natural Hair". In: *ACM Transactions on Graphics* 25.3, pp. 1180–1187. DOI: 10.1145/1141911.1142012 (cit. on p. 31).

Bertails-Descoubes, Florence (May 2012). "Super-Clothoids". In: *Computer Graphics Forum* 31.2, pp. 509–518. DOI: 10.1111/j.1467-8659.2012.03030.x (cit. on p. 33).

Bico, José, Étienne Reyssat, and Benoît Roman (2018). "Elastocapillarity: When Surface Tension Deforms Elastic Solids". In: *Annual Review of Fluid Mechanics* 50, pp. 629–659. DOI: 10.1146/annurev-fluid-122316-050130 (cit. on p. 1).

Bigoni, Davide (2012). *Nonlinear Solid Mechanics: Bifurcation Theory and Material Instability*. Cambridge: Cambridge University Press. ISBN: 978-1-107-02541-7. DOI: 10.1017/CBO9781139178938 (cit. on pp. 49, 70).

Blumentals, Alejandro (July 2017). "Numerical modelling of thin elastic solids in contact". PhD thesis. Université Grenoble Alpes. URL: https://theses.hal.science/tel-01682985 (cit. on p. 35).

Bosi, F., D. Misseroni, F. Dal Corso, and D. Bigoni (Sept. 2015). "Development of configurational forces during the injection of an elastic rod". In: *Extreme Mechanics Letters* 4, pp. 83–88. DOI: 10.1016/j.eml.2015.04.007 (cit. on p. 54).

Boyd, John Philip (2001). *Chebyshev and Fourier spectral methods*. 2nd edition revised. Mineola (N.Y.): Dover Publ. ISBN: 978-0-486-41183-5 (cit. on p. 159).




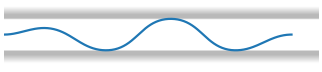

Brau, Fabian, Hugues Vandeparre, Abbas Sabbah, Christophe Poulard, Arezki Boudaoud, and Pascal Damman (Jan. 2011). "Multiple-length-scale elastic instability mimics parametric resonance of nonlinear oscillators". In: *Nature Physics* 7.1, pp. 56–60. DOI: 10.1038/nphys1806. URL: https://www.nature.com/articles/nphys1806 (cit. on p. 136).

Byrd, Richard H., Mary E. Hribar, and Jorge Nocedal (Jan. 1999). "An Interior Point Algorithm for Large-Scale Nonlinear Programming". In: *SIAM Journal on Optimization* 9.4, pp. 877–900. DOI: 10.1137/S1052623497325107 (cit. on p. 10).

Cappello, Jean, Benoit Scheid, Fabian Brau, and Emmanuel Siéfert (Jan. 2023). "Bioinspired shape shifting of liquid-infused ribbed sheets". In: *Proceedings of the National Academy of Sciences* 120.1, e2216001120. DOI: 10.1073/pnas.2216001120 (cit. on p. 1).

Casati, Romain (June 2015). "Quelques contributions à la modélisation numérique de structures élancées pour l'informatique graphique". PhD thesis. Université Grenoble Alpes. URL: https://theses.hal.science/tel-01502808 (cit. on p. 33).

Chai, Herzl (July 1998). "The post-buckling response of a bi-laterally constrained column". In: *Journal of the Mechanics and Physics of Solids* 46.7, pp. 1155–1181. DOI: 10.1016/S0022-5096(98)00004-0 (cit. on p. 59).

— (Mar. 2005). "On the Crush Worthiness of a Laterally Confined Bar Under Axial Compression". In: *Journal of Applied Mechanics* 73.5, pp. 834–841. DOI: 10.1115/1.2047595 (cit. on p. 59).

Chai, Herzl and Dov Moshkovitz (Dec. 2022). "On the post-buckling behavior of laterally constrained multilayers". In: *International Journal of Solids and Structures*. Special Issue in the honour Dr Stelios Kyriakides 257, p. 111827. DOI: 10.1016/j.ijsolstr.2022.111827 (cit. on p. 59).

Champneys, Alan R., Timothy J. Dodwell, Rainer M. J. Groh, Giles W. Hunt, Robin M. Neville, Alberto Pirrera, Amir H. Sakhaei, Mark Schenk, and M. Ahmer Wadee (2019). "Happy Catastrophe: Recent Progress in Analysis and Exploitation of Elastic Instability". In: *Frontiers in Applied Mathematics and Statistics* 5. DOI: 10.3389/fams.2019.00034 (cit. on p. 13).

Charrondière, Raphaël, Florence Bertails-Descoubes, Sébastien Neukirch, and Victor Romero (June 2020). "Numerical modeling of inextensible elastic ribbons with curvature-based elements". In: *Computer Methods in Applied Mechanics and Engineering* 364, p. 112922. DOI: 10.1016/j.cma.2020.112922 (cit. on p. 36).

Charrondière, Raphaël, Sébastien Neukirch, and Florence Bertails-Descoubes (2024). "Merci: Mixed curvature-based elements for computing equilibria of thin elastic ribbons". In: *ACM Transactions on Graphics* 43.5. Publisher: Association for Computing Machinery, pp. 160.1–160.26. DOI: 10.1145/3674502 (cit. on pp. 35, 36).

Charru, François (2011). *Hydrodynamic instabilities*. Cambridge texts in applied mathematics. Cambridge University Press. DOI: 10.1017/CBO9780511975172 (cit. on p. 12).

Chateau, X. and Q. S. Nguyen (1991). "Buckling of elastic structures in unilateral contact with or without friction". In: *European Journal of Mechanics - A/Solids* 10.1, pp. 71–89 (cit. on p. 59).

Chen, Chao and Teng Zhang (July 2022). "Coupling lattice model and many-body dissipative particle dynamics to make elastocapillary simulation simple". In: *Extreme Mechanics Letters* 54, p. 101741. DOI: 10.1016/j.eml.2022.101741 (cit. on p. 121).

Chen, Jen-San and Zheng-Shun Wen (Sept. 2019). "Deformation and vibration of a buckled beam constrained by springy walls". In: *European Journal of Mechanics - A/Solids* 77, p. 103791. DOI: 10.1016/j.euromechsol.2019.05.006 (cit. on pp. 1, 59).

Clerk-Maxwell, James (Mar. 1875). "On the Dynamical Evidence of the Molecular Constitution of Bodies". In: *Nature* 11.279, pp. 357–359. DOI: 10.1038/011357a0 (cit. on p. 49).

Cline, Douglas (Aug. 2017). *Variational Principles in Classical Mechanics*. River Campus Libraries. ISBN: 978-0-9988372-5-3 (cit. on p. 6).



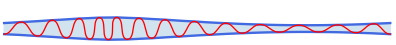

Coleman, Bernard D. and David Swigon (2004). "Theory of self-contact in Kirchhoff rods with applications to supercoiling of knotted and unknotted DNA plasmids". In: *Philosophical Transactions of the Royal Society A: Mathematical, Physical and Engineering Sciences* 362, pp. 1281–1299. DOI: 10.1098/rsta.2004.1393 (cit. on p. 44).

Costa, A. Pinto da and A. Seeger (2008). "Cone-constrained eigenvalue problems: theory and algorithms". In: *Comput. Optim. Appl.* 45.1, pp. 25–57. DOI: 10.1007/s10589-008-9167-8 (cit. on pp. 104, 105).

Crespel, Octave, Emile Hohnadel, Thibaut Metivet, and Florence Bertails-Descoubes (July 2024). "Contact detection between curved fibres: high order makes a difference". In: *ACM Trans. Graph.* 43.4, 132:1–132:23. DOI: 10.1145/3658191 (cit. on pp. 42, 104, 130).

Cutolo, Arsenio, Massimiliano Fraldi, Gaetano Napoli, and Giuseppe Puglisi (2023). "Growth of a flexible fibre in a deformable ring". In: *Soft Matter* 19 (18), pp. 3366–3376. DOI: 10.1039/D3SM00348E (cit. on pp. 47, 48).

Daviet, Gilles, Florence Bertails-Descoubes, and Laurence Boissieux (2011). "A Hybrid Iterative Solver for Robustly Capturing Coulomb Friction in Hair Dynamics". In: *ACM Transactions on Graphics (TOG)* 30.6, art. 139. DOI: 10.1145/2070781.2024173 (cit. on p. 42).

Deboeuf, Stéphanie, Suzie Protière, and Eytan Katzav (2024). "Yin-Yang spiraling transition of a confined buckled elastic sheet". In: *Phys Rev Res* 6.1, p. 013100. DOI: 10.1103/PhysRevResearch.6.013100 (cit. on p. 65).

Derouet-Jourdan, A., F. Bertails-Descoubes, G. Daviet, and J. Thollot (Nov. 2013). "Inverse Dynamic Hair Modeling with Frictional Contact". In: *ACM Trans. Graph.* 32.6, 159:1–159:10. DOI: 10.1145/2508363.2508398 (cit. on p. 42).

Diamant, Haim and Thomas A. Witten (Oct. 2011). "Compression Induced Folding of a Sheet: An Integrable System". In: *Physical Review Letters* 107.16. Publisher: American Physical Society, p. 164302. DOI: 10.1103/PhysRevLett.107.164302 (cit. on p. 136).

Dichmann, D. J., Y. Li, and J. H. Maddocks (1996). "Hamiltonian Formulations and Symmetries in Rod Mechanics". In: *Mathematical Approaches to Biomolecular Structure and Dynamics*. Ed. by J. P. Mesirov, K. Schulten, and D. W. Sumners. Vol. 82. The IMA Volumes in Mathematics and Its Applications. Springer Verlag, pp. 71–113. DOI: 10.1007/978-1-4612-4066-2_6 (cit. on p. 182).

Domokos, G. (1994). "Global description of elastic bars". In: *Z. Angew. Math. Mech* 74.4, T289–T291. DOI: 10.1002/zamm.19940740410 (cit. on p. 18).

Domokos, G., P. Holmes, and B. Royce (1997). "Constrained Euler buckling". In: *Journal of Nonlinear Science* 7.3, pp. 281–314. DOI: 10.1007/BF02678090 (cit. on pp. 1, 59).

Dugas, René (Jan. 1988). *A History of Mechanics*. Courier Corporation. ISBN: 978-0-486-65632-8 (cit. on p. 6).

Duprat, C., S. Protière, A. Y. Beebe, and H. A. Stone (Feb. 2012). "Wetting of flexible fibre arrays". In: *Nature* 482.7386, pp. 510–513. DOI: 10.1038/nature10779 (cit. on p. 1).

Durville, Damien (Nov. 2005). "Numerical simulation of entangled materials mechanical properties". In: *Journal of Materials Science* 40.22, pp. 5941–5948. DOI: 10.1007/s10853-005-5061-2 (cit. on p. 42).

Eisley, Joe G. (1964). "Nonlinear vibration of beams and rectangular plates". In: *Zeitschrift für angewandte Mathematik und Physik (ZAMP)* 15.2, pp. 167–175. DOI: 10.1007/BF01602658 (cit. on p. 69).

Elettro, Hervé (July 2015). "Elasto-capillary windlass : from spider silk to smart actuators". PhD thesis. Université Pierre et Marie Curie - Paris VI. URL: https://tel.archives-ouvertes.fr/tel-01232392 (cit. on p. 119).

Elettro, Hervé, Paul Grandgeorge, and Sébastien Neukirch (Apr. 2017). "Elastocapillary Coiling of an Elastic Rod Inside a Drop". In: *Journal of Elasticity* 127.2, pp. 235–247. DOI: 10.1007/s10659-016-9611-4 (cit. on pp. 119, 121).

Elettro, Hervé, Sébastien Neukirch, Fritz Vollrath, and Arnaud Antkowiak (2016). "In-drop capillary spooling of spider capture thread inspires hybrid fibers with mixed solid–liquid mechanical properties". In: *Proceedings of the National Academy of Sciences of the USA* 113.22, pp. 6143–6147. DOI: 10.1073/pnas.1602451113 (cit. on pp. 1, 119, 121, 127).

Elettro, Hervé, Fritz Vollrath, Arnaud Antkowiak, and Sébastien Neukirch (Oct. 2015). "Coiling of an elastic beam inside a disk: A model for spider-capture silk". In: *International Journal of Non-Linear Mechanics*. Instabilities and Nonlinearities in Soft Systems: From Fluids to Biomaterials 75, pp. 59–66. DOI: 10.1016/j.ijnonlinmec.2015.03.008 (cit. on pp. 119, 121, 125, 126).

Ericksen, J. L. (Nov. 1975). "Equilibrium of bars". In: *Journal of Elasticity* 5.3, pp. 191–201. DOI: 10.1007/BF00126984 (cit. on pp. 49, 53).

Eshelby, J. D. (1951). "The Force on an Elastic Singularity". In: *Philosophical Transactions of the Royal Society of London. Series A, Mathematical and Physical Sciences* 244.877, pp. 87–112. URL: https://www.jstor.org/stable/91488 (cit. on p. 54).

— (Jan. 1956). "The Continuum Theory of Lattice Defects". In: *Solid State Physics*. Ed. by Frederick Seitz and David Turnbull. Vol. 3. Academic Press, pp. 79–144. DOI: 10.1016/S0081-1947(08)60132-0 (cit. on p. 54).

— (Nov. 1975). "The elastic energy-momentum tensor". In: *Journal of Elasticity* 5.3, pp. 321–335. DOI: 10.1007/BF00126994 (cit. on p. 54).

— (1999). "Energy Relations and the Energy-Momentum Tensor in Continuum Mechanics". In: *Fundamental Contributions to the Continuum Theory of Evolving Phase Interfaces in Solids: A Collection of Reprints of 14 Seminal Papers*. Ed. by John M. Ball, David Kinderlehrer, Paulo Podio-Guidugli, and Marshall Slemrod. Berlin, Heidelberg: Springer, pp. 82–119. ISBN: 978-3-642-59938-5. DOI: 10.1007/978-3-642-59938-5_5 (cit. on p. 54).

Flaherty, Joseph E. and Joseph B. Keller (1973). "Contact Problems Involving a Buckled Elastica". In: *SIAM Journal on Applied Mathematics* 24.2, pp. 215–225. URL: https://www.jstor.org/stable/2099677 (cit. on p. 44).

Föppl, August (1897). *Vorlesungen über technische Mechanik*. Vol. 3. BG Teubner (cit. on p. 136).

Gonzalez, Oscar and John H. Maddocks (Apr. 1999). "Global curvature, thickness, and the ideal shapes of knots". In: *Proceedings of the National Academy of Sciences* 96.9, pp. 4769–4773. DOI: 10.1073/pnas.96.9.4769 (cit. on p. 44).

Gordon, William J. and Charles A. Hall (1973). "Construction of curvilinear co-ordinate systems and applications to mesh generation". In: *International Journal for Numerical Methods in Engineering* 7.4, pp. 461–477. DOI: 10.1002/nme.1620070405 (cit. on p. 159).

Grandgeorge, Paul (Feb. 2018). "Le flambage élasto-capillaire de fibres et de membranes fibreuses fines pour la conception de matériaux étirables". PhD thesis. Sorbonne Université. URL: https://tel.archives-ouvertes.fr/tel-02078788 (cit. on pp. 121, 122, 136, 146, 147, 156).

Grandgeorge, Paul, Natacha Krins, Aurélie Hourlier-Fargette, Christel Laberty-Robert, Sébastien Neukirch, and Arnaud Antkowiak (2018). "Capillarity-induced folds fuel extreme shape changes in thin wicked membranes". In: *Science* 360.6386, pp. 296–299. DOI: 10.1126/science.aaq0677 (cit. on pp. 1, 119, 135, 137).

Griewank, Andreas and Andrea Walther (2008). *Evaluating Derivatives*. Second Edition. Society for Industrial and Applied Mathematics. DOI: 10.1137/1.9780898717761. URL: https://epubs.siam.org/doi/abs/10.1137/1.9780898717761 (cit. on p. 27).



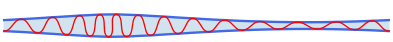

Groh, R. M. J., D. Avitabile, and A. Pirrera (Apr. 2018). "Generalised path-following for well-behaved nonlinear structures". In: *Computer Methods in Applied Mechanics and Engineering* 331, pp. 394–426. DOI: 10.1016/j.cma.2017.12.001 (cit. on p. 12).

Guillou, Lionel, Avin Babataheri, Michael Saitakis, Armelle Bohineust, Stéphanie Dogniaux, Claire Hivroz, Abdul I. Barakat, and Julien Husson (Nov. 2016). "T-lymphocyte passive deformation is controlled by unfolding of membrane surface reservoirs". In: *Molecular Biology of the Cell* 27.22, pp. 3574–3582. DOI: 10.1091/mbc.E16-06-0414 (cit. on pp. 1, 136).

Gurtin, Morton E (2000). *Configurational forces as basic concepts of continuum physics*. Applied mathematical sciences. New York: Springer. ISBN: 978-0-387-98667-8 (cit. on p. 54).

Hagberg, A. and E. Meron (Jan. 1998). "Propagation failure in excitable media". In: *Physical Review E* 57.1, pp. 299–303. DOI: 10.1103/PhysRevE.57.299 (cit. on p. 11).

Hearle, John W. S. (2014). "The 20th-Century Revolution In Textile Machines And Processes. Part 2: Textured Yarns And Other Technologies". In: *Industrial Archaeology Review* 36.1, pp. 32–47. DOI: 10.1179/0309072814Z.00000000028 (cit. on pp. 1, 59).

Hertz, H. (1884). "Ueber das Gleichgewicht schwimmender elastischer Platten". In: *Annalen der Physik* 258.7, pp. 449–455. DOI: 10.1002/andp.18842580711 (cit. on p. 136).

Hetényi, Miklós and Miklbos Imre Hetbenyi (1946). *Beams on elastic foundation: theory with applications in the fields of civil and mechanical engineering*. Vol. 16. University of Michigan press Ann Arbor, MI (cit. on p. 59).

Houssein, Houssam, Simon Garnotel, and Frédéric Hecht (2022). "A Symmetric Algorithm for Solving Mechanical Contact Problems Using FreeFEM". In: *Advances in Computational Methods and Technologies in Aeronautics and Industry*. Ed. by Dietrich Knoerzer, Jacques Periaux, and Tero Tuovinen. Cham: Springer International Publishing, pp. 235–250. ISBN: 978-3-031-12019-0. DOI: 10.1007/978-3-031-12019-0_17 (cit. on p. 39).

Houssein, Houssam, Simon Garnotel, and Frédéric Hecht (Nov. 2019). "Frictionless contact problem for hyperelastic materials with interior point optimizer". URL: https://hal.science/hal-02355429 (cit. on p. 39).

— (Aug. 2023). "Frictionless Signorini's Contact Problem for Hyperelastic Materials with Interior Point Optimizer". In: *Acta Applicandae Mathematicae* 187.1, p. 3. DOI: 10.1007/s10440-023-00598-y (cit. on p. 39).

Huang, Jiangshui, Megan Juszkiewicz, Wim H. de Jeu, Enrique Cerda, Todd Emrick, Narayanan Menon, and Thomas P. Russell (2007). "Capillary Wrinkling of Floating Thin Polymer Films". In: *Science* 317.5838, pp. 650–653. DOI: 10.1126/science.1144616 (cit. on pp. 1, 136).

Hure, Jérémy (2011). "Wrapping an Adhesive Sphere with an Elastic Sheet". In: *Physical Review Letters* 106.17. DOI: 10.1103/PhysRevLett.106.174301 (cit. on p. 136).

Jambon-Puillet, Etienne (Oct. 2016). "Folds in floating membranes : from elastic sheets to granular rafts". Theses. Université Pierre et Marie Curie - Paris VI. URL: https://theses.hal.science/tel-01481288 (cit. on p. 147).

Johanns, Paul, Paul Grandgeorge, Changyeob Baek, Tomohiko G. Sano, John H. Maddocks, and Pedro M. Reis (Feb. 2021). "The shapes of physical trefoil knots". In: *Extreme Mechanics Letters* 43, p. 101172. DOI: 10.1016/j.eml.2021.101172 (cit. on p. 44).

Judah, Nitzan and Sefi Givli (Feb. 2024). "The Post-Buckling Behavior of a Beam Constrained by Nonlinear Springy Walls". In: *Journal of Applied Mechanics* 91.061004. DOI: 10.1115/1.4064684 (cit. on p. 59).

Katz, Shmuel and Sefi Givli (2015). "The post-buckling behavior of a beam constrained by springy walls". In: *Journal of the Mechanics and Physics of Solids* 78, pp. 443 –466. DOI: 10.1016/j.jmps.2015.02.004 (cit. on pp. 1, 59).

Kehrbaum, S. and J. H. Maddocks (Nov. 1997). "Elastic rods, rigid bodies, quaternions and the last quadrature". In: *Philosophical Transactions of the Royal Society of London. Series A:*

*Mathematical, Physical and Engineering Sciences* 355.1732. Publisher: Royal Society, pp. 2117–2136. DOI: 10.1098/rsta.1997.0113 (cit. on pp. 181, 182).

Kikuchi, N. and J. T. Oden (1988). *Contact problems in elasticity: a study of variational inequalities and finite element methods*. SIAM studies in applied mathematics. Philadelphia. ISBN: 978-0-89871-202-5. DOI: 10.1137/1.9781611970845 (cit. on pp. 39, 41).

Konyukhov, Alexander and Ridvan Izi (2015). *Introduction to computational contact mechanics : a geometrical approach*. Wiley series in computational mechanics. Chichester. ISBN: 978-1-118-77065-8 (cit. on pp. 39, 40).

Kármán, Th. von (1907). "Festigkeitsprobleme im Maschinenbau". In: *Encyklopädie der Mathematischen Wissenschaften*. Ed. by F. Klein and C. Müller. Mechanik. Vieweg+Teubner Verlag, Wiesbaden, pp. 311–385. DOI: 10.1007/978-3-663-16028-1_5 (cit. on p. 69).

Lam, Jonathan, Marc Herant, Micah Dembo, and Volkmar Heinrich (Jan. 2009). "Baseline mechanical characterization of J774 macrophages". In: *Biophysical Journal* 96.1, pp. 248–254. DOI: 10.1529/biophysj.108.139154 (cit. on p. 136).

Lanczos, Cornelius (Apr. 2012). *The Variational Principles of Mechanics*. Courier Corporation. ISBN: 978-0-486-13470-3 (cit. on p. 6).

Lazarus, Arnaud, Corrado Maurini, and Sébastien Neukirch (2015). "Stability of discretized nonlinear elastic systems". In: *Extremely Deformable Structures*. Ed. by Davide Bigoni. Vienna: Springer Vienna, pp. 1–53. ISBN: 978-3-7091-1877-1. DOI: 10.1007/978-3-7091-1877-1_1 (cit. on p. 12).

Levyakov, S. V. and V. V. Kuznetsov (Apr. 2010). "Stability analysis of planar equilibrium configurations of elastic rods subjected to end loads". In: *Acta Mechanica* 211.1, pp. 73–87. DOI: 10.1007/s00707-009-0213-0 (cit. on p. 16).

Liakou, Anna and Emmanuel Detournay (Mar. 2018). "Constrained buckling of variable length elastica: Solution by geometrical segmentation". In: *International Journal of Non-Linear Mechanics* 99, pp. 204–217. DOI: 10.1016/j.ijnonlinmec.2017.12.001 (cit. on p. 59).

Litewka, P and P Wriggers (2002a). "Frictional contact between 3D beams". In: *Computational mechanics* 28.1, pp. 26–39 (cit. on p. 42).

Litewka, Przemyslaw (2007). "Smooth Frictional Contact between Beams in 3D". In: *IUTAM Symposium on Computational Methods in Contact Mechanics*. Springer, Dordrecht, pp. 157–176. DOI: 10.1007/978-1-4020-6405-0_10 (cit. on p. 42).

Litewka, Przemysław and Peter Wriggers (2002b). "Contact between 3D beams with rectangular cross-sections". In: *International Journal for Numerical Methods in Engineering* 53.9, pp. 2019–2041 (cit. on p. 42).

Lubinski, Arthur and W.S. Althouse (1962). "Helical Buckling of Tubing Sealed in Packers". In: *Journal of Petroleum Technology* 14.06, pp. 655–670. DOI: 10.2118/178-PA (cit. on pp. 1, 59).

Luenberger, David G. and Yinyu Ye (2008). *Linear and Nonlinear Programming*. Vol. 116. International Series in Operations Research & Management Science. New York, NY: Springer US. ISBN: 978-0-387-74502-2. DOI: 10.1007/978-0-387-74503-9 (cit. on p. 5).

Manning, Robert S and George B Bulman (Aug. 2005). "Stability of an elastic rod buckling into a soft wall". In: *Proceedings of the Royal Society A: Mathematical, Physical and Engineering Sciences* 461.2060. Publisher: Royal Society, pp. 2423–2450. DOI: 10.1098/rspa.2005.1458 (cit. on pp. 1, 59, 91).

Marko, J. F. (2007). "Torque and dynamics of linking number relaxation in stretched supercoiled DNA". In: *Physical Review E* 76, p. 021926 (cit. on p. 49).

Maugin, Gerard A. (Nov. 2010). *Configurational Forces: Thermomechanics, Physics, Mathematics, and Numerics*. New York: Chapman and Hall/CRC. ISBN: 978-0-429-06614-6. DOI: 10.1201/b10356 (cit. on p. 54).



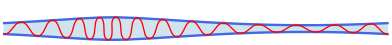

Meier, Christoph, Alexander Popp, and Wolfgang A. Wall (2016). "A finite element approach for the line-to-line contact interaction of thin beams with arbitrary orientation". In: *Computer Methods in Applied Mechanics and Engineering* 308, pp. 377–413. DOI: 10.1016/j.cma.2016.05.012 (cit. on p. 42).

Meier, Christoph, Wolfgang A. Wall, and Alexander Popp (Mar. 2017). "A unified approach for beam-to-beam contact". In: *Computer Methods in Applied Mechanics and Engineering* 315, pp. 972–1010. DOI: 10.1016/j.cma.2016.11.028 (cit. on p. 42).

Michael, D. H. and P. G. Williams (1976). "The Equilibrium and Stability of Axisymmetric Pendent Drops". In: *Proceedings of the Royal Society of London. Series A, Mathematical and Physical Sciences* 351.1664, pp. 117–127. DOI: 10.1098/rspa.1976.0132 (cit. on p. 21).

Miller, J. T., T. Su, E. B. Dussan, J. Pabon, N. Wicks, K. Bertoldi, and P. M. Reis (2015). "Buckling-induced lock-up of a slender rod injected into a horizontal cylinder". In: *International Journal of Solids and Structures* 72, pp. 153 –164. DOI: 10.1016/j.ijsolstr.2015.07.025 (cit. on pp. 1, 59).

Neukirch, Sébastien, Francesco Dal Corso, and Yury Vetyukov (2025). "The frictionless flexible sliding sleeve". In: *Journal of the Mechanics and Physics of Solids* in the press.-, p. 106330. DOI: 10.1016/j.jmps.2025.106330 (cit. on p. 186).

Neukirch, Sébastien, Morteza Yavari, Noël Challamel, and Olivier Thomas (May 2021). "Comparison of the Von Kármán and Kirchhoff models for the post-buckling and vibrations of elastic beams". In: *Journal of Theoretical, Computational and Applied Mechanics*. DOI: 10.46298/jtcam.6828 (cit. on pp. 62, 70).

Nocedal, Jorge and Stephen J. Wright (2006). *Numerical Optimization*. Second Edition. Springer Series in Operations Research and Financial Engineering. New York: Springer. ISBN: 978-0-387-30303-1. DOI: 10.1007/978-0-387-40065-5 (cit. on pp. 5, 6, 9).

Padday, J. F. (Feb. 1971). "The Profiles of Axially Symmetric Menisci". In: *Philosophical Transactions of the Royal Society of London. Series A, Mathematical and Physical Sciences* 269.1197, pp. 265–293. DOI: 10.1098/rsta.1971.0031 (cit. on p. 21).

Padday, J. F. and A. R. Pitt (1973). "The Stability of Axisymmetric Menisci". In: *Philosophical Transactions Mathematical Physical & Engineering Sciences* 275.1253, pp. 489–528. DOI: 10.1098/rsta.1973.0113 (cit. on p. 21).

Pocheau, A. and B. Roman (2004). "Uniqueness of solutions for constrained Elastica". In: *Physica D: Nonlinear Phenomena* 192.3-4, pp. 161–186. DOI: 10.1016/j.physd.2003.12.013 (cit. on p. 66).

Pocivavsek, Luka, Robert Dellsy, Andrew Kern, Sebastián Johnson, Binhua Lin, Ka Yee C. Lee, and Enrique Cerda (2008). "Stress and Fold Localization in Thin Elastic Membranes". In: *Science* 320.5878, pp. 912–916. DOI: 10.1126/science.1154069 (cit. on pp. 136, 147).

Podio-Guidugli, P. (Nov. 2002). "Configurational forces: are they needed?" In: *Mechanics Research Communications* 29.6, pp. 513–519. DOI: 10.1016/S0093-6413(02)00295-1 (cit. on p. 54).

Price, Neville J and John W Cosgrove (1990). *Analysis of geological structures*. Cambridge University Press (cit. on p. 59).

Py, C., R. Bastien, J. Bico, B. Roman, and A. Boudaoud (2007). "3D aggregation of wet fibers". In: *Europhysics Letters* 77.4, p. 44005. DOI: 10.1209/0295-5075/77/44005 (cit. on p. 1).

Raj, Shikhar and Biplab Bose (Nov. 2024). *Pitchfork Bifurcation In A Coupled Cell System*. DOI: 10.48550/arXiv.2411.16400 (cit. on p. 11).

Raphaël Charrondière (Oct. 2021). "Modélisation numérique de rubans par éléments en courbures". PhD thesis. Université Grenoble Alpes. URL: https://hal.inria.fr/tel-03545017v1 (cit. on pp. 33, 35).

Repupilli, Massimiliano (2012). "A Robust Method for Beam-to-Beam contact Problems Based on a Novel Tunneling Constraint". PhD thesis. UCLA. URL: https://escholarship.org/uc/item/7xc298tq (cit. on p. 42).

Ro, Wei-Chia, Jen-San Chen, and Shau-Yu Hong (Aug. 2010). "Vibration and stability of a constrained elastica with variable length". In: *International Journal of Solids and Structures* 47.16, pp. 2143–2154. DOI: 10.1016/j.ijsolstr.2010.04.015 (cit. on p. 109).

Roman, B. and A. Pocheau (1999). "Buckling cascade of thin plates: Forms, constraints and similarity". In: *Europhysics Letters* 46.5, p. 602. DOI: 10.1209/epl/i1999-00306-3 (cit. on pp. 1, 59, 67).

Schulman, Rafael D., Amir Porat, Kathleen Charlesworth, Adam Fortais, Thomas Salez, Elie Raphaël, and Kari Dalnoki-Veress (Jan. 2017). "Elastocapillary bending of microfibers around liquid droplets". In: *Soft Matter* 13.4, pp. 720–724. DOI: 10.1039/C6SM02095J (cit. on pp. 1, 121).

Schulz, M. and S. Pellegrino (2000). "Equilibrium Paths of Mechanical Systems with Unilateral Constraints I. Theory". In: *Proceedings: Mathematical, Physical and Engineering Sciences* 456.2001. Publisher: Royal Society, pp. 2223–2242. DOI: 10.1098/rspa.2000.0610 (cit. on pp. 11, 59).

Seydel, R., F. W. Schneider, T. Küpper, and H. Troger, eds. (1991). *Bifurcation and Chaos: Analysis, Algorithms, Applications*. Basel: Birkhäuser. ISBN: 978-3-0348-7006-1. DOI: 10.1007/978-3-0348-7004-7 (cit. on p. 13).

Seydel, Rüdiger (2010). *Practical Bifurcation and Stability Analysis*. Vol. 5. Interdisciplinary Applied Mathematics. New York, NY: Springer. ISBN: 978-1-4419-1739-3. DOI: 10.1007/978-1-4419-1740-9 (cit. on pp. 12–14).

Shimizu, Masaki and Paul Manneville (Nov. 2019). "Bifurcations to turbulence in transitional channel flow". In: *Physical Review Fluids* 4.11, p. 113903. DOI: 10.1103/PhysRevFluids.4.113903 (cit. on p. 12).

Signorini, Antonio (1933). "Sopra alcune questioni di statica dei sistemi continui". In: *Annali della Scuola Normale Superiore di Pisa-Scienze Fisiche e Matematiche* 2.2, pp. 231–251 (cit. on p. 39).

Strogatz, Steven H. (1994). *Nonlinear Dynamics and Chaos*. Perseus Books (cit. on p. 13).

Style, Robert W., Anand Jagota, Chung-Yuen Hui, and Eric R. Dufresne (2017). "Elastocapillarity: Surface Tension and the Mechanics of Soft Solids". In: *Annual Review of Condensed Matter Physics* 8.1, pp. 99–118. DOI: 10.1146/annurev-conmatphys-031016-025326 (cit. on p. 1).

Tan, Yinlong, Biru Hu, Jia Song, Zengyong Chu, and Wenjian Wu (Apr. 2020). "Bioinspired Multiscale Wrinkling Patterns on Curved Substrates: An Overview". In: *Nano-Micro Letters* 12.1, p. 101. DOI: 10.1007/s40820-020-00436-y (cit. on p. 135).

Trélat, Emmanuel (2012). "Optimal Control and Applications to Aerospace: Some Results and Challenges". In: *J. Optim. Theory. Appl.* 154, pp. 713–758. DOI: 10.1007/s10957-012-0050-5 (cit. on p. 35).

Tzokova, Petia Svetomirova (2020). "Confined wrinkling of thin elastic rods, sheets and cones". PhD thesis. University of Cambridge. DOI: 10.17863/CAM.57977 (cit. on p. 70).

Vandeparre, Hugues, Miguel Piñeirua, Fabian Brau, Benoit Roman, José Bico, Cyprien Gay, Wenzhong Bao, Chun Ning Lau, Pedro M. Reis, and Pascal Damman (June 2011). "Wrinkling Hierarchy in Constrained Thin Sheets from Suspended Graphene to Curtains". In: *Physical Review Letters* 106.22, p. 224301. DOI: 10.1103/PhysRevLett.106.224301 (cit. on p. 135).

Vella, D., M. Adda-Bedia, and E. Cerda (Nov. 2010). "Capillary wrinkling of elastic membranes". In: *Soft Matter* 6.22, pp. 5778–5782. DOI: 10.1039/C0SM00432D (cit. on p. 136).

Verhulst, Ferdinand (1996). *Nonlinear differential equations and dynamical systems*. 2nd., revised and expanded edition. Universitext. Berlin: Springer. ISBN: 978-3-540-60934-6 (cit. on pp. 12, 13).

Vetter, R., F. K. Wittel, and H. J. Herrmann (2014). "Morphogenesis of filaments growing in flexible confinements". In: *Nature Communications* 5, p. 4437. DOI: 10.1038/ncomms5437 (cit. on pp. 1, 59).

Vollrath, Fritz and Donald T. Edmonds (July 1989). "Modulation of the mechanical properties of spider silk by coating with water". In: *Nature* 340.6231. Publisher: Nature Publishing Group, pp. 305–307. DOI: 10.1038/340305a0 (cit. on pp. 1, 121).

Wachter, Andreas and Lorenz T. Biegler (2006). "On the implementation of an interior-point filter line-search algorithm for large-scale nonlinear programming". In: *Math. Program. Ser. A* 106, pp. 25–57. DOI: 10.1007/s10107-004-0559-y (cit. on p. 10).

Wang, Jiayu, Stéphanie Deboeuf, Arnaud Antkowiak, and Sébastien Neukirch (2025). "Constrained Euler buckling: The von Kármán approximation". In: *International Journal of Solids and Structures* 313, p. 113279. DOI: 10.1016/j.ijsolstr.2025.113279 (cit. on p. 69).

Wang, Ting, Yifan Yang, and Fan Xu (July 2022). "Mechanics of tension-induced film wrinkling and restabilization: a review". In: *Proceedings of the Royal Society A: Mathematical, Physical and Engineering Sciences* 478.2263. Publisher: Royal Society, p. 20220149. DOI: 10.1098/rspa.2022.0149. (Visited on 11/29/2023) (cit. on p. 135).

Wriggers, P and Giorgio Zavarise (1997). "On contact between three-dimensional beams undergoing large deflections". In: *Communications in numerical methods in engineering* 13.6, pp. 429–438. DOI: 10.1002/(SICI)1099-0887(199706)13:6%3C429::AID-CNM70%3E3.0.CO;2-X (cit. on p. 42).

Wriggers, Peter (2006). *Computational Contact Mechanics*. Springer. ISBN: 978-3-540-32608-3. DOI: 10.1007/978-3-540-32609-0 (cit. on pp. 39, 41, 42).

Wächter, Andreas (2002). "An Interior Point Algorithm for Large-Scale Nonlinear Optimization with Applications in Process Engineering". PhD Thesis. Carnegie Mellon University (cit. on p. 10).

Zavarise, Giorgio and P Wriggers (2000). "Contact with friction between beams in 3-D space". In: *International Journal for Numerical Methods in Engineering* 49.8, pp. 977–1006 (cit. on p. 42).